Contents

Introduction

0.1 A short historical overview of particle physics

The research field called 'particle physics' started in 1897 with the discovery of the electron by J.J. Thomson in his study of the deflection of cathode rays under the influence of electric and magnetic fields. It was the first elementary particle to be discovered. The second elementary particle introduced, this time by Einstein, was the photon (1905). A notion that was able to explain the photo emission of electrons from metals and that was based on Planck's idea of the quanta of energy.

In 1911 Rutherford proposed his model of the atom based on the observation that when a thin gold foil is irradiated with α particles, most of them fly right through the foil, but a number of them is scattered over a large angle, some even over an angle of 180^0. He concluded that the atoms had a positive core with a radius of about $10^{-15}m$ and that the electrons were orbiting around this nucleus on circular paths with a radius of $10^{-10}m$. To solve the problem of energy loss due to acceleration along circular paths, Bohr (1913) proposed that the electron could only reside in some discrete energy states when orbiting the nucleus. When they would transit from one level to another, they would emit light with a frequency given by $\Delta E = h\nu$.

In 1919 Rutherford discovered that the nucleus was made out of even smaller constituents, namely protons. However, two problems arose: 1) the protons accounted for the total net charge of the nucleus, but only for half of the mass and 2) what kept the nucleus together when the electric repel force for so closely packed positive charge is huge. Both issues were solved by Chadwick. In 1921 he observed that the scattering of α particles in hydrogen could not only be accounted for by the electromagnetic force, leading to the first evidence that the strong interaction was distinct from the electromagnetic force. In 1932 he discovered the neutron, a particle with no net electrical charge and that could account for the missing mass inside the nucleus.

In the mid 20's, theoretical advance was made in the form of quantum mechanics. This theory was able to predict the light spectra emanating from the atoms, and give insight in the atomic structure. The deterministic view used in the macroscopic world had now to be abandoned and replaced with a probabilistic one. The main flaw of the theory is that it is not relativistically covariant. Dirac rewrote the Schrodinger equation so that it would be. The solutions of his new equation naturally introduced spinors, an intrinsic component of the angular moment of the particle. Furthermore it predicts the existence of a sea of negative energy levels. These energy levels were to be completely filled with electrons, but were not visible to us. When an electron is excited to a positive energy state, it will become visible to us. In addition, the void left is attributed to a particle with a mass identical to the electron, but that has an opposite charge, the positron. This particle was discovered in 1932 by Anderson in his experiments with cosmic rays.

An other approach to make quantum mechanics covariant was carried out by Klein and Gordon. Where Dirac found an equation describing the free field behavior of the electron, they found a free field theory describing the behavior of spin 0 particles. Their theory too is plagued with negative energy levels, and where Dirac could use the Pauli exclusion principle (stating that no two electron can be in the same state at the same time) to prevent the electrons to all fall down to the lowest energy level, Klein and Gordon could not use this as the principle is not valid for integer spin particles.

The solution came in what is known as the second quantisation. The equations are no longer

viewed as the equations for the wave function of the particles, but as the equations for field functions, which when quantized give the particles and the antiparticles of the field. The quantization is done via commutation relations between the field and its canonical conjugate and gives rise to creation and annihilation operators, that exist both for particles and antiparticles.

One of the strangest particles around was to be discovered via the β decay of atoms (emission of an e^- by the atom). A number of measurements showed that, although the nucleus undergoing the β transformation was in a definite state, and the product nucleus was also in a definite state, the emitted β particles had a continuous energy distribution. This points to a violation of the principle of conservation of energy. In 1930 Pauli postulated that a third particle must be involved with no rest mass, no net charge and it had to be a spin $\frac{1}{2}$particle. He called his particle the neutrino. Recently it was discovered that the neutrino has a (very small) mass.

Around 1940, the studies of cosmic rays revealed a number of new particles with a mass that was about 200 times the electron mass and with the same charge as the electron. Since their mass was between that of the electron and the proton, they were called mesotrons (now shortened to mesons). Some were seen to interact only weakly with matter and others strongly. They are now called the muon and the pion, respectively.

In the 50's and 60's a great number of mesons and of hyperons (heavier particles) were experimentally discovered through resonances (enhancements) in the cross section. It was noted that some particles could decay into a nucleon (proton or neutron) and some not. This was explained by the introduction of a new quantum number that had to be conserved in decays: the baryon number. However, this was not sufficient to explain all the observed decay and production mechanisms. It was for instance noticed that the $K^{0,+,-}$ is always produced in association with a Λ or Σ when produced via the strong interaction. For this and other reasons, Gell-Mann and Nishijima introduced yet an other quantum number called strangeness.

As the number of new particles continued to increase, the idea grew that the observed particles were not at all elementary but merely composite. In 1961 Gell-Mann and Ne'eman proposed to fit all these particles in the octet representation of SU(3). Three years later Gell-Mann and Zweig proposed the constituent quark model, where the quarks are the SU(3) triplets. A meson would be build up of a quark and an anti-quark, and a baryon is made up of 3 quarks. These quarks now have a fractional baryon number of $1/3$ and a fractional charge . Three quarks needed to be introduced to explain the observed particle variety: the up, down and strange quark. The need for an additional quantum number (now called color) carried by quarks was needed to resolve the conflict with Fermi statistics for ground state baryons. As an analogy to the electromagnetic interaction, Nambu (1966) proposed that strong interactions are mediated by massless vector fields whose quanta are now called gluons. This is the beginning of what is now called QCD (quantum chromo dynamics).

In 1961 Goldstone demonstrated that if a global symmetry of the Lagrangian for some system is spontaneously broken, then a massless boson must appear. Using the same principle, Higgs, Englert and Brout constructed a field theory in which massive bosons are generated via spontaneous symmetry breaking. It introduces a new scalar particle: the Higgs boson. Salam, Weinberg and Glashow will later use this property to generate the masses in a theory that unifies electromagnetism and the weak interaction. This theory predicts that besides the two charged weak gauge bosons W^+ and W^- there exists a neutral counterpart, the Z^0 with similar mass and a comparable coupling to fermions. This would lead to weak neutral currents that were discovered using the Gargamelle bubble chamber. The W^+, W^- and Z^0 were discovered in 1983 at CERN.

In 1975 a third lepton, the τ lepton was found. But only recently a direct observation of its associated neutrino was made[1].

By the advent of accelerators capable of reaching ever higher energies, new particles were created. In 1977 the bottom quark was discovered and in 1995 the top quark was experimentally observed.

[1]The Tau neutrino was discovered by the DONUT experiment in 2001[5].

0.2 Present status

The present understanding of the fundamental structure of matter is one with only 12 particles (and their associated anti-particle) that are all fermions. They are subdivided in leptons and quarks, and each subdivision comes in three (mass) generations. The interactions are mediated by gauge bosons that are exchanged between the particles. A summary of all the elementary particles and some of their properties is given in table 1.

Fermions	Symbol	Q (e)	m (MeV/c^2)
Leptons	e^-	-1	0.511
	ν_e	0	<3eV
	μ^-	-1	105
	ν_μ	0	<0.19
	τ	-1	1777
	ν_τ	0	<18.2
Quarks	u	2/3	1 to 5
	d	-1/3	3 to 9
	c	2/3	1.15 to 1.35GeV
	s	-1/3	75 to 170GeV
	t	2/3	168 to 174GeV
	b	-1/3	4 to 4.4GeV

Bosons	spin	interaction	m (GeV/c^2)
γ	1	EM	0
W^+, W^-	1	Weak	80
Z^0	1	Weak	91
g	1	Strong	0
H	0		>114.1

Table 1: Fundamental particles properties

All particles have experimentally been observed. The top quark was only recently discovered in 1995 at the Tevatron in Fermilab with a mass of $175 GeV/c^2$.

The present theoretical understanding of the micro-world is given by the standard model which is a collection of gauge theories. The part that describes the electromagnetic and weak interactions is based on the SU(2)XU(1) symmetry group. The left-handed fermions form SU(2) doublets, while the right handed ones are in SU(2) singlets. Via spontaneous breaking of gauge symmetry, three of the four original gauge fields acquire mass and become the massive W^+, W^- and Z^0, while the photon is left massless. The quark sector of the model is based on the SU(3) symmetry group. Here, the strong interaction is mediated by quanta of the color field, called gluons.

The spontaneous symmetry breaking in the electroweak sector of the standard model also predicts the existence of a massive gauge boson associate with the Higgs field: the Higgs boson.

0.3 Future

A lot of interest has gone to the discovery of the only particle predicted by the standard theory that still has not been experimentally observed: the Higgs boson.

Therefore CERN has decided to build a new proton-proton collider with a center of mass energy of 14TeV. The protons will be accelerated in two separate storage rings and will collide in four dedicated interaction regions. Around two of these interaction points, general purpose detectors will be built. One of them is the Compact Muon Solenoid (CMS). Around the two other interaction points, dedicated experiments will be built.

The main problem that these new experiments are facing is the incredible high rate of particles that will traverse the detectors. A high luminosity ($10^{34} s^{-1} cm^{-2}$) is needed since the cross section for production of the Higgs boson is small. This leads to two experimental constraints: first the detectors used have to be radiation hard, or said differently, they will have to be able to cope with the high particle fluxes present in the detector for its entire lifetime. Secondly, it will only be possible to write events to tape with a speed of $100 Hz$. This sets the need for a good 'trigger' system that will be able to discard events coming from known physics and keep the events coming from potentially new physics.

The contribution of the Brussels group is located in the heart of the detector: the tracker. The role of the tracker is to precisely determine the momentum of the charged particles and to help in the identification of the diverse particles. The key to the good momentum resolution of the tracker is the 4T magnetic field in which it will be plunged. This field will be generated by a super conducting solenoid.

Originally it was foreseen to equip the tracker with three technologies: Si-pixel detectors, Si-strip detectors and Micro Strip Gas Chambers (MSGC).

0.4 Subject of the thesis

The present work is a study of the MSGCs and their operation in LHC like conditions. MSGCs are proportional gas counters for which the electrode pattern is engraved on a solid substrate. This allows for a small inter anode distance (typically $200\mu m$) allowing the construction of detectors with the small granularity needed to cope with the high track density at LHC. Furthermore the signal readout of the MSGCs is much faster than their ancestors, the multiwire chambers.

We have contributed to the optimisation of the process flow for MSGC substrate production. In this particular scheme 1.6μ thick electrodes are produced. The electrodes are composites made of a sputtered layer of Cu ($0.8\mu m$), an electroless plated layer of Ni ($0.7\mu m$) and a thin electroless plated layer of Au ($0.1\mu m$). The main challenge was to adapt the process flow in such a way that 98% of the anodes are found suitable for detection. In chapter 3 we will prove that this is possible in laboratory conditions.

Next, we have tested detectors equipped with substrates made with the electroless plating technique in different experimental conditions. In a first test, we irradiated the detectors with an $8GeV/c$ pion beam to investigate the general properties of the substrates. Next, the detectors were subjected to a high flux of $350MeV/c$ pions. These conditions are very close to the ones expected at the LHC, this is an important test of the technology. These two test are the subject of chapter 4.

In chapter 5 we will describe a large scale test of MSGC+GEM detectors in a $350MeV/c$ pion beam. This test was mainly aimed at a study of the production scheme of the MSGC+GEM and its long term behavior under a high flux of particles. As, for the first time, a large number of MSGC+GEM detector were put together in a beam, we tried to evaluate their tracking capabilities and studied some properties like the efficiency and signal to noise ratio under a high flux of particles.

In the last chapter of the thesis, we report on the study we made on primary vertex reconstruction using the CMS all silicon tracker. We developed, implemented, and tested two methods for primary vertex finding. We report on the spatial resolution on, and efficiency to find the primary vertex. Also some attention is paid to the time used by the different algorithms.

Chapter 1

The Large Hadron Collider and the Compact Muon Solenoid detector

1.1 Introduction

One of the most challenging research topics in physics today is the search for the Higgs boson. This particle is predicted by the theory of Englert, Brout and Higgs, in which particles acquire mass via spontaneous symmetry breaking in the electroweak segment of the standard model. Previous particle accelerators have been able to put a lower limit on the mass of this particle: $114.1 GeV/c^2$ [11].

Unfortunately, no experiment has been able to observe the Higgs boson. Therefore, new accelerators, able to reach energies in the TeV range, have to be built. One such accelerator, the Large Hadron Collider (LHC), will be built in CERN, Geneva.

1.2 The Large Hadron Collider

The LHC [3] is a proton-proton accelerator presently being built at CERN, the laboratory of the European Organization for Nuclear Research, near Geneva. The accelerator will be built in the 27km long tunnel that was used before by the Large Electron Positron Collider (LEP).

The LHC will accelerate the protons to an energy of 7TeV, thus collisions with an energy of 14TeV in the center of mass are attainable. The constituents of the protons (quarks and gluons) will interact at energies up to 1TeV.

Before being injected into the LHC, the protons will be accelerated through the injection chain shown in figure 1.1. First the protons will be accelerated in a small linear accelerator to an energy of 1.4GeV. The Proton Synchrotron (PS) will increase their energy to 25GeV before injecting them into the Super Proton Synchrotron (SPS). Here their energy will be raised to 450GeV. The final acceleration up to 7TeV will be done in the LHC itself using superconducting acceleration cavities and bending magnets.

The production cross sections of physics channels of interest are very small compared to the total cross section which is around 100mb[1]. For instance the Higgs production cross section at the LHC is of the order of 1pb for a Higgs with a mass of $500 GeV/c^2$. Therefore the luminosity of the collider has to be high enough in order to attain a measurable rate of occurrence. The rate of occurrence r is related to the luminosity L and the cross section σ by: $r = L\sigma$.

The luminosity of the accelerator depends on the number of particles per bunch in the two beams, N_1 and N_2, on the bunch crossing frequency f, and on the cross sectional area of each particle bunch. If the spatial distribution of the particles inside the bunches is Gaussian, the luminosity can be written as:

$$L = \frac{1}{4\pi} \frac{N_1 N_2 f}{\sigma_x \sigma_y} \tag{1.1}$$

[1] 1b=1 barn=$10^{-24} cm^2$

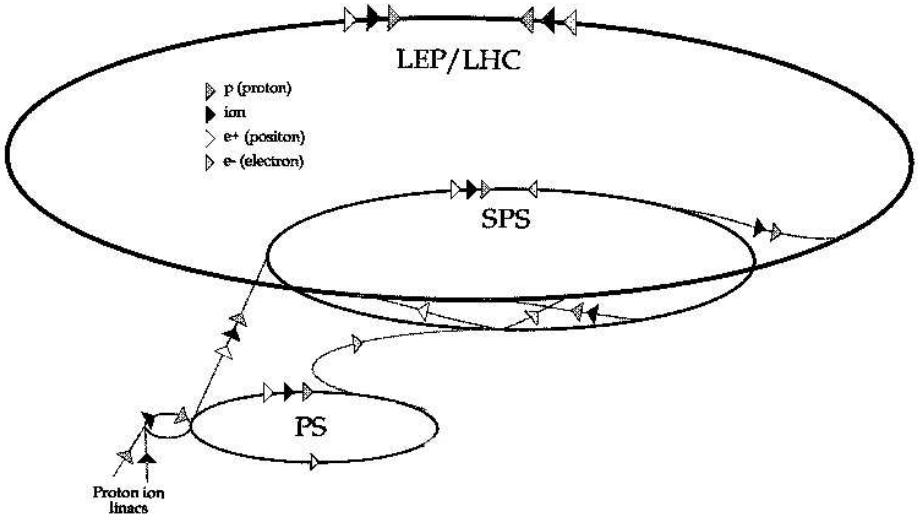

Figure 1.1: Layout of the CERN injection chain used to accelerate the protons.

where σ_x and σ_y are the R.M.S. of the spatial distribution of the protons in the directions transverse to the movement of the beam. The design luminosity for the LHC is $10^{34} cm^{-2} s^{-2}$. This is called high luminosity and corresponds to a rate of occurrence for Higgs production of $10^{-2} Hz$ (for a Higgs with a mass of $500 GeV/c^2$). However, the observable decay modes usually have a branching ratio of the order of 10^{-3}, leading to a rate of occurrence of $10^{-5} Hz$. This rate has to be compared to the total rate of interactions of $10^{9} Hz$ (for the maximum luminosity and the total p-p cross-section which is 60mb).

The design luminosity will be achieved with a bunch crossing frequency of $40 MHz$, a particle density of 10^{11} per bunch and a transverse beam dimension of $15 \mu m$ R.M.S. at the interaction points. An integrated luminosity of $5.10^5 pb^{-1}$ is expected over ten years of operation. This corresponds to $5.10^7 s$ running at high luminosity. In the first years of operation, the LHC will run at a lower luminosity. In the first year of operation, it will run at 10% of its nominal value. In the second and third year this will be increased to 33% and 67% respectively. An integrated luminosity of $3.10^4 pb^{-1}$ will be accumulated during this low luminosity start. In the remaining 7 years the LHC will run at the the maximum possible luminosity.

Inside the LHC, the proton beams will move inside two separated vacuum tubes. The beams will move in opposite directions and will be kept on their quasi circular paths via a magnetic field of $8.4 Tesla$. To produce these high fields, superconducting coils, cooled at 1.9K, will be used. The beams will intersect in four experimental interaction regions. In these regions the transverse dimensions of the bunches will be reduced by focusing magnets in order to obtain the requested luminosity.

Around each of these interaction regions, detectors will be built. Two of them, ATLAS and CMS, are general purpose detectors and will be used for physics studies at the highest LHC luminosities. Around the two remaining points, ALICE and LHC-B will be build. LHC-B is designed for the study of B-physics and ALICE will study heavy ion physics. The emplacement of the detectors can be seen in figure 1.2.

1.3 Physics goals of the LHC

1.3.1 High luminosity

The cross-sections of various processes as a function of the proton collision center of mass energy $\sqrt{s}$ is shown in figure 1.3. The values expected at a center of mass energy of $14 TeV$ are standard

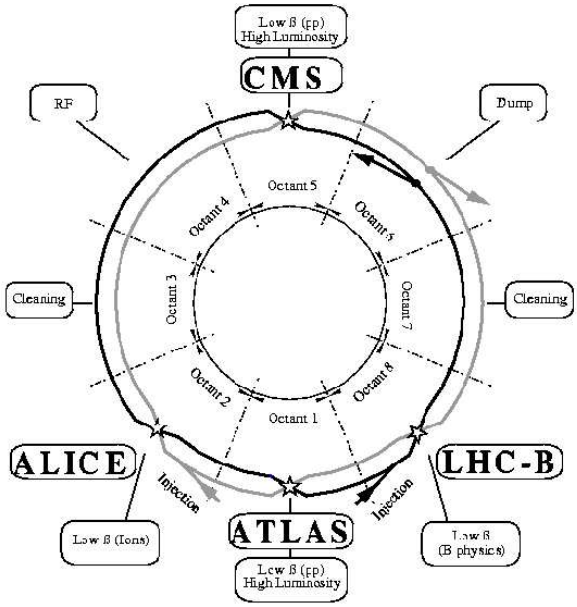

Figure 1.2: Schematic layout of the LHC. The figure shows the location of the four experiments as well as the emplacement of the acceleration cavities (RF) and the locations where the beam will be injected, cleaned or dumped.

model extrapolations from data obtained in previous experiments. The event rates for some interesting channels are $10^{-2}Hz$ for Higgs production for a Higgs with a mass of $500GeV/c^2$, $10Hz$ for $t\bar{t}$ creation and more than 10^6Hz for $b\bar{b}$ production. The total event rate will be one gigahertz.

It is convenient to introduce a new variable called the pseudorapidity η, defined as:

$$\eta = \frac{1}{2}\ln\left(\frac{p+p_z}{p-p_z}\right) = -\ln(\frac{\theta}{2}) \tag{1.2}$$

where θ is the angle of emission of the particle with respect to the beam axis and $p_z = p*cos\theta$ is the z-component of the particle momentum. The distribution of the number of particles $dN/d\eta$ is roughly constant with the pseudorapidity in the range $|\eta| < 5$, corresponding to angles from 1^O to 179^O. On average, 1000 particles will be emitted in this pseudorapidity interval per bunch crossing. The transverse momentum distribution dN/dp_T^2 approximates an exponential in p_t with an average value of 0.5GeV/c [4].

1.3.1.1 Searching for the Higgs.

The present understanding of elementary particle physics is entirely based on the standard model. This theory combines the Glashow-Salam-Weinberg model of electroweak interactions, the quark model and quantum chromo dynamics (QCD). This model has been extensively tested during the past decades and until now, no deviations have been found.

However, this model does not include massive particles. The masses of the particles are introduced via a breaking of the gauge symmetry in the electroweak sector of the theory. This is done by the introduction of a new field, the 'Higgs' field, to which the massive particles couple to acquire mass. This solution was independently proposed by F. Englert and R. Brout [6] and P. Higgs [7]. The characteristic property of the Higgs field is that it's state of minimal energy (vacuum) is attained at a non zero expectation value of the field. In breaking the gauge symmetry in this way, one preserves the renormalizability of the theory, ensuring that the divergences encountered in the calculations of physical quantities can be absorbed into a finite number of free parameters.

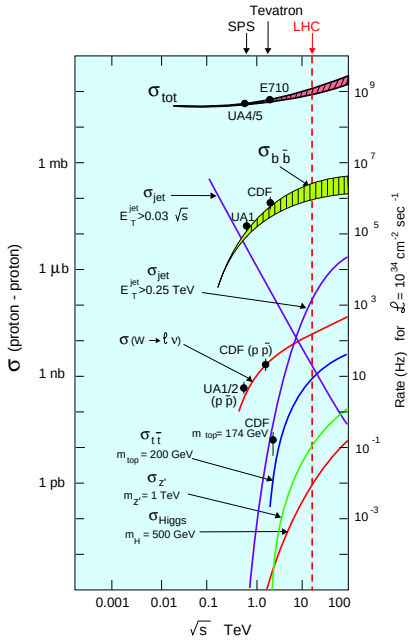

Figure 1.3: Cross- section and event rate of various processes at a luminosity of $10^{34} cm^{-2} s^{-1}$ as a function of the proton center of mass energy. [4]

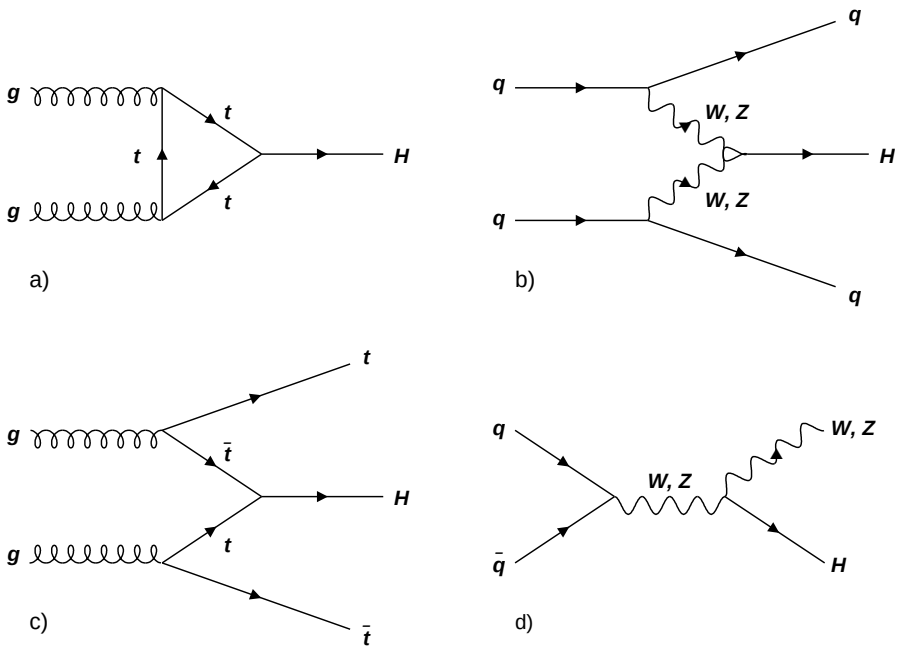

Figure 1.4: Dominant Higgs production mechanisms at hadron colliders. a) gluon-gluon fusion, b)WW or ZZ fusion, c)$t\bar{t}fusion$, d)W or Z bremsstrahlung

As the Higgs field couples to the other particles with a strength proportional to their mass, the dominant Higgs production mechanisms will involve weak exchange bosons and top quarks, which are much heavier than the other leptons and quarks. The dominant diagrams are shown in figure 1.4. The expected Higgs production rates at the LHC range between 10^4 and 10^6 events per year at the maximum luminosity for Higgs masses varying from 0.1 to $1TeV/c^2$[12]. Unfortunately, the decay channels which provide the best experimental signature have small branching ratios (of the order of 10^{-3}). The branching ratios of the dominant decay modes of the standard model Higgs can be seen in figure 1.5.

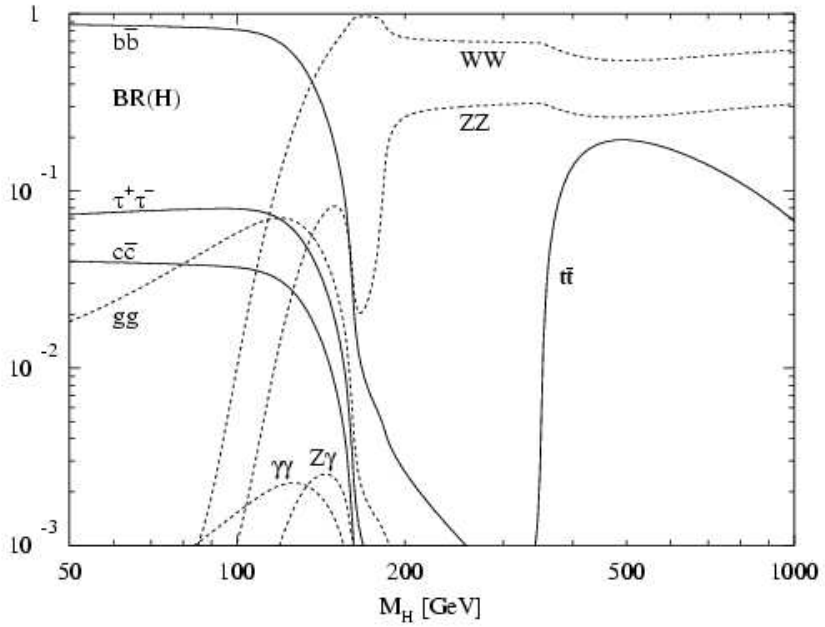

Figure 1.5: The dominant decay modes of the standard model Higgs. [23]

The most promising decay channels (from the point of view of detection) are summarized in table 1.1. For a Higgs mass between 80GeV and 150GeV, the preferred decay mode for detection will be the decay into two photons. This will be detected as two isolated electromagnetic showers pointing to the vertex. The predominant decay mode ($H \rightarrow b\bar{b}$) in this mass region cannot be exploited experimentally since it is overwhelmed by the direct $b\bar{b}$ pair production. For $120GeV \leq m_H \leq 2m_Z$ the decay mode will primordially be $H \rightarrow ZZ^* \rightarrow 4l^{\pm}$, with l being a lepton (electron or muon) and Z^* a virtual Z boson. When the mass of the Higgs is larger than $2M_Z$ it can decay into two real Z bosons. As the cross section for Higgs productions decreases rapidly at high m_H, other decay modes will have to be considered above $m_H > 500GeV$. The Higgs will then decay following $H \rightarrow ZZ \rightarrow 2l^{\pm}2\nu$, where ν is a neutrino. A good measurement of the missing energy will thus be required.

Final state	Mass interval
$H \rightarrow \gamma\gamma$	80 GeV/$c^2 \leq m_H \leq$ 150 GeV/c^2
$H \rightarrow ZZ^* \rightarrow 4l^{\pm}$	120 GeV/$c^2 \leq m_H \leq$ 180 GeV/c^2
$H \rightarrow ZZ \rightarrow 4l^{\pm}$	180 GeV/$c^2 \leq m_H \leq$ 650 GeV/c^2
$H \rightarrow ZZ \rightarrow 2l^{\pm}2\nu$	500 GeV/$c^2 \leq m_H \leq$ 1 TeV/c^2
$H \rightarrow W^+W^- \rightarrow l\nu jj$	$m_H \sim$ 1 TeV/c^2
$H \rightarrow ZZ \rightarrow 2l^{\pm}2\nu$	

Table 1.1: Most favorable discovery channels of the Standard Model Higgs and corresponding mass intervals.

1.3.1.2 The Minimal SuperSymmetric Model

Up to now, no experimental evidence is found for any deviation from the standard model. However, major unsolved (theoretical) problems remain. The most important of them are the hierarchy problem and the incorporation of gravity into the theory.

The fundamental energy scale of the theory, at $10^{15}GeV$, is so much different than the other two scales of the theory: a scale of 10^2GeV at which weak interactions breaks itself and a scale of $1GeV$ at which strong interaction breaks chiral symmetry. To obtain a reasonable mass for the Higgs boson, the parameters in the electroweak part of the Lagrangian have to be adjusted by a factor $(10^{13})^2 = 10^{26}$[8]. This 'unnatural' adjustment is called the hierarchy problem. Furthermore, no way was found to incorporate gravity into the standard model, as gravity is thought to be mediated by the graviton, which is a spin 2 particle.

The Minimal SuperSymmetric Model (MSSM) offers a solution to this problem. It introduces new couplings between fermions and boson. By doing so new particles are created. Each particle now has his supersymmetric partner, which differs from this first one in its spin by 1/2. The model also predicts the existence of five physical Higgs bosons, two charged scalars ($H^{\pm}$), two neutral scalars (h,H^0) and one neutral pseudo scalar (A).The model predicts that the lightest one (h) will have a mass below 130GeV. This puts an experimentally verifiable limit on the theory. If no light Higgs boson is detected, the theory will be flawed.

1.3.2 Low luminosity

The LHC will permit a detailed study of the heavy quarks (beauty and top). A large amount of them will be produced, even at low intensity. The mass of the top will be measured via different decay channels. Recent measurements indicate a top mass of $(176.8 \pm 6.5)GeV/c^2$[13].

The second matter to be addressed in the low intensity start-up phase is the CP violation in the $B^0 - \overline{B^0}$ system. C and P are transformations of the particle wave function corresponding to the exchange of the particles by their anti-particles (Charge conjugation) and to the reversal of space coordinates (Parity). CP violation was first observed through a difference in the decay rates of the K_0 and $\overline{K_0}$ mesons, both containing the strange (s) quark. It is believed that this is possible because the weak interaction can distinguish between particles and anti-particles. Therefore this decay asymmetry is also present in the decay of mesons made out of heavier quarks. CMS will study the decay asymmetry of B_0 and $\overline{B_0} \rightarrow J/\psi K_0^S$ in further detail.

1.4 CMS

The Compact Muon Solenoid (CMS) detector is designed to run at the highest LHC luminosities. The design of the detector was made following the stringent requirements that it should be able to operate for at least 10 years in the LHC experimental environment and that it should be able to discriminate between known and new physics.

To this end, a few design rules were followed. A very good muon identification and momentum resolution, a high resolution for the energy measurement of photons and electrons, and the capability of measuring high transverse momenta (p_T) with very good resolution are the most important of them. Furthermore, a large detector acceptance is mandatory. Due to the collision frequency and the radiation environment present, fast and radiation hard detectors and read-out electronics are required.

As most detectors in high energy physics today, CMS is a modular detector. As its name already reveals, the basis of the detector are the muon system and the solenoid. The solenoid will produce the uniform $4T$ magnetic field needed for a good momentum measurement for muons of high momentum (1TeV) up to a rapidity of 2.5. The muon chambers will identify the muons as such and measure their momentum with a precision better than $\frac{\Delta p}{p} \approx 15\%$.

The tracker and both the electromagnetic and hadronic calorimeters will be placed inside the solenoid. The tracker will further improve the momentum resolution to the level of 1% for charged particle tracks with a $1GeV < p_T < 100GeV$. For tracks with $p_T > 100GeV$, the precision on

the p_T will be $\frac{\Delta p_T}{p_T} \simeq 0.1 p_T$ (p_T in TeV). The calorimeters will determine the energy of electrons and photons (electromagnetic) and hadrons (hadronic). The combined information of tracker and calorimeter will be used for particle identification.

A 3D picture representing the CMS detector can be seen in figure 1.6. The overall dimensions of the detector are: 21m in length and 15m in diameter. The total mass of the detector will be 14500Tons. The detector is subdivided into 3 space regions: a central 'barrel' region and two identical 'endcaps', placed at both ends of the barrel.

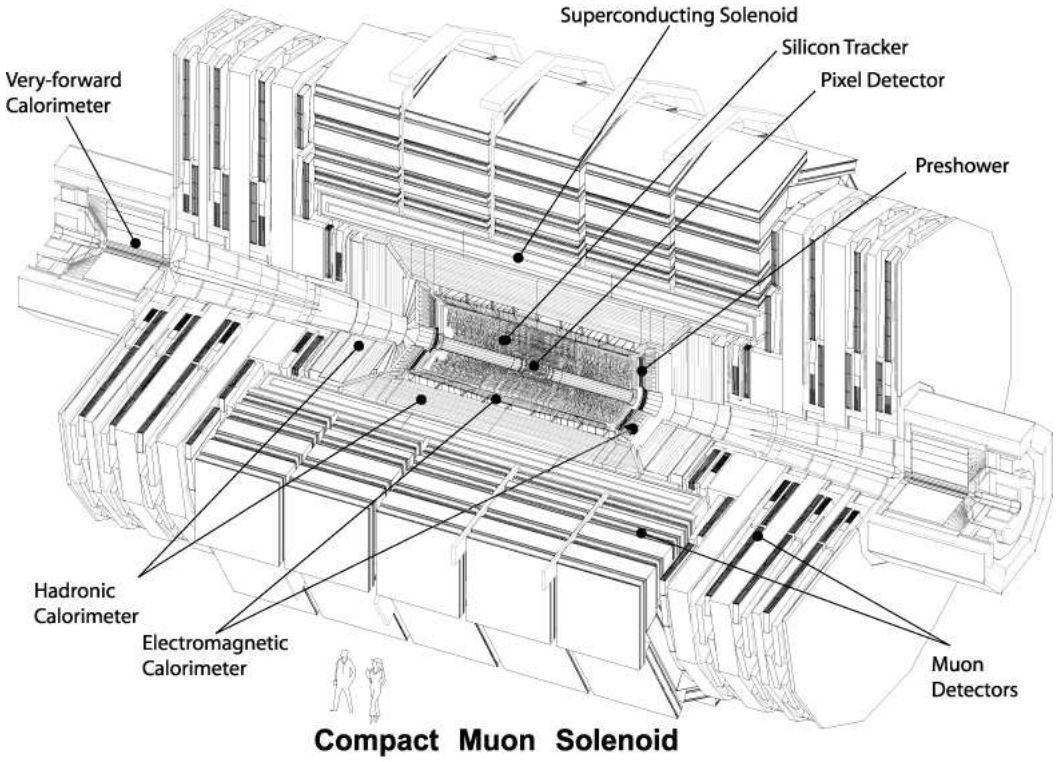

Figure 1.6: Schematic view of the CMS detector

The high event rate ($10^9 Hz$) and large amount of data per event (1Mb) makes it impossible to store all data coming out of CMS. An online selection called 'triggering' is needed to reduce the data to the maximal rate at which data can be stored on tape: $100 Hz$. In CMS, this will be done with a multilevel trigger system selecting candidate events with a clear signature for new physics (high p_T leptons and photons, missing energy, etc).

1.4.1 Trigger strategy

Some of the most important selection criteria that will be used for the Higgs searches are: the identification of a high energy photon in the ECAL ($p_T(\gamma) > 40 GeV/c$) identifying the channel $H \rightarrow \gamma\gamma$, the observation of a high energetic muon and electron ($p_T(e) > 20 GeV/c$; $p_T(\mu) > 20 GeV/c$) to identify a Higgs from the channel $H \rightarrow ZZ \rightarrow 4l$ (where l denotes a lepton). Another major selection criterion is a cut on the missing energy ($E_T^{miss} > 100 GeV/c$) in order to designate a candidate Higgs coming from $H \rightarrow ZZ \rightarrow ll\nu\nu$ where ν is a neutrino. The last important channel comes from the contribution $H \rightarrow ZZ \rightarrow lljj$, where two hadron jets(j) are produced, the applied cuts are $p_T(l) > 50 GeV/c$; $p_T(Z \rightarrow jj) > 150 GeV/c$.

A multilevel trigger strategy is followed in order to reduce the event rate from $10^9 Hz$ down to less than $100 Hz$, rate at which data can be stored on tape.

The level 1 trigger is a fully hardware based trigger using only coarsely segmented data from the muon stations and the calorimeters. It will be performed by custom electronics. The level 1 decision will be taken in $3.2 \mu s$, equivalent to 128 25-ns beam crossings. 128 is the length

of the pipeline memory in the front-end electronics. These $3.2\mu s$ include the latencies for the transmission of all data and control signals.

The rate of events at the output of the level 1 (L1) trigger will be $75kHz$. The needed reduction of three orders of magnitude down to $100Hz$ will be performed by the high level trigger (HLT). This is a software based trigger that will be performed on a dedicated CPU farm using the ORCA (Object-oriented Reconstruction for CMS Analysis) program. The HLT is subdivided into 3 distinct levels (L2, L3 and L4). Each level will reduce the rate by one order of magnitude. Current expectations are that the mean processing time per event will be $50ms$ with some events taking up to 1s. This implicates that the CMS Data Acquisition system must provide significant buffering capability.

The L2 is mainly a refinement of the L1 algorithm. It will determine the quantities used at L1 with a greater precision allowing a better rejection of low p_T, $E(\gamma)$, $E(e)$ and E_T^{miss} events. At L3 the tracker data will be used for the first time. Full track reconstruction is envisaged at this stage. The p_T of the tracks can now be measured with a precision of 1.5%. The L4 stage will investigate the topology of the event in order to select events coming from new physics.

1.4.2 Particle identification: basic principles

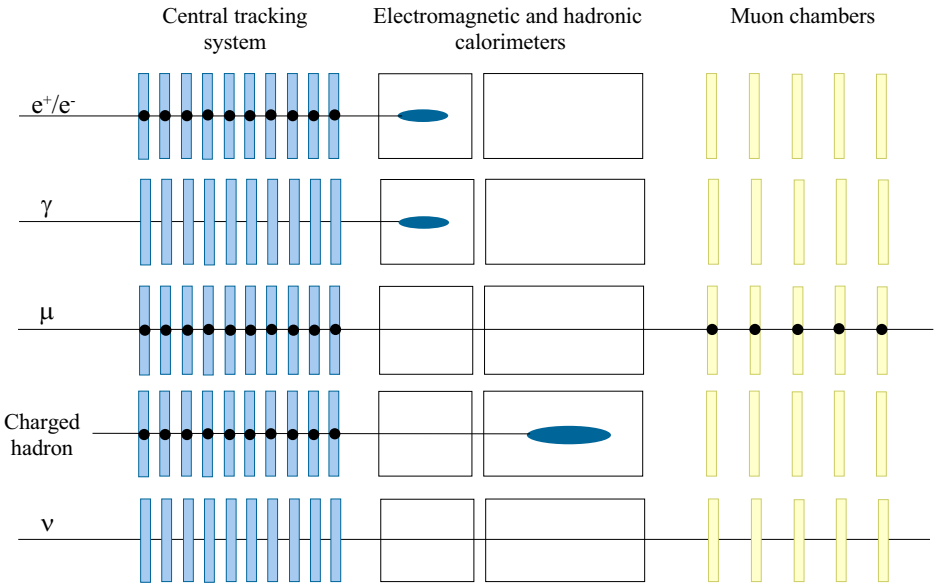

Figure 1.7: Signatures of different types of particles upon their traversal of a detection system like CMS.

The identification of particles relies on the specific signature left by its traversal through the different sub-detectors. A summary is given in figure 1.7.

All charged particles (e^{+-}, μ^{+-}, charged hadrons) will leave a track in the central tracking system. The magnetic field will curve the paths of the charged particles. This allows the determination of their momentum and the sign of their charge. The particles that interact electromagnetically (e^{+-},γ) will loose all of their energy in the electromagnetic calorimeter and should not give rise to a signal in the hadronic calorimeters. Hadrons will lose most of their energy in the hadronic calorimeters.

Two special particles remain: The muon and the neutrino. The muon interacts via the weak and the electromagnetic force. However, due to its high mass (compared to the electron), it will lose only a small fraction of its energy in the detector and will escape the detector. It is the only particle that creates a track in both the central tracking system and the muon stations (all other particles are stopped before they can reach the muon chambers). As the neutrino only interacts via the weak force, it escapes the detector without leaving any signal. Its presence in

the event must be deduced from the momentum and energy conservation laws. It is therefore very important that the detector is hermetic over a 4π angle and has a good energy resolution.

The identification of photons can be problematic due to a conversion into an e^+e^- pair. Therefore the amount of material in front of the electromagnetic calorimeter must be as little as possible. This has a direct effect on the reconstruction of $H \rightarrow \gamma\gamma$ channel. A lightweight tracker is also needed in order to reduce the electron and positron absorption probability.

1.4.3 The magnet

The magnet [16] used in CMS is a superconducting solenoid, 13m long and with an inner radius of 2.95m. The design magnetic field is 4T. The superconducting cable is made out of 40NbTi strands enveloped in 2 layers containing Al. These layers stabilize the magnetic field and protect the coil in case of a quench. This is an important issue since the energy stored in the magnet will be $2.52GJ$. The cooling of the magnet will be done using a liquid helium circuit.

The magnetic flux will be returned via a 1.5m thick saturated iron yoke that is instrumented with the muon chambers.

1.4.4 The muon system

The muon system [17] is composed of four muon stations interleaved with the magnetic flux return yoke. The muon system is required to identify the muons and measure their momentum with an accuracy of 8 to 40% for muons having a p_T between 10 and $1000GeV/c$. As part of the new physics will manifest itself through high p_T muons, the muon system shall take part in the trigger. Levels 1 and 2 of the trigger rely heavily on the information coming from the muon system. It must therefore be composed of fast detectors, delivering a signal that can be associated with one bunch crossing, and be able to deliver a fast estimate of the p_T of the muon.

To fulfill these requirements, 3 different detector technologies have been chosen for the muon system.

1. Drift tubes (DT): DT are drift chambers build up with tubular cells that have a $4 \times 1.1cm^2$ section. The baseline cell has a pitch of 40mm by 13mm with at its center a $50\mu m$ diameter stainless steel anode wire. The tubes are filled with an Ar/CO_2 gas mixture. The DT will only be used in the barrel part of the muon system. Each Barrel muon station will be composed of twelve layers of drift tubes, grouped four by four. Two groups will measure the (R, ϕ) coordinate of the muon and the third group will measure the coordinate along the beam (z). The spatial resolution of each group is better than $250\mu m$ for particles with an angle of incidence up to 40^O. The time resolution of the drift tube is about $5ns$ when averaging the drift time measured in the four layers of the group.

2. Cathode strip chambers (CSC): CSC will only be found in the forward muon spectrometer. These trapezoidal detectors will be filled with an $Ar - CO_2 - CF_4$ gas mixture. Their width will range from 487mm to 1270mm at the top of the trapezoid and from 201mm to 665mm at the bottom. Their length will vary between 1505mm and 3215mm. The cathode strips are radial whereas the wires are parallel to the basis of the trapezoid. Spatial resolutions of $75\mu m$ in the (R, ϕ) coordinate have been obtained with this system. Each forward muon station will be equipped with six CSC layers.

3. Resistive plate chambers (RPCs): The RPCs will be used to identify the LHC bunch crossing to which the muon belongs. Therefore the response time of the RPCs have to be better than $25ns$. The RPCs have proved to be able to achieve a time resolution of $3ns$, largely satisfying the requested time resolution. The read-out electrode is segmented to provide a coarse measurement of the p_T of the muons.

1.4.5 The electromagnetic calorimeter

The main task of the electromagnetic calorimeter (ECAL) is to measure the energy of electrons and photons. It does this by absorbing their energy and by giving a signal proportional to the deposited energy.

The CMS ECAL will be build up with lead tungstate ($PbWO_4$) crystals. $PbWO_4$ crystals have a short radiation length (0.89cm) and a small Moliere radius (2.2cm). The short radiation length allows for a compact calorimeter, allowing it to be placed inside the magnet. The small Moliere radius reduces the spread of the lateral electromagnetic shower thus improving the shower isolation efficiency, reducing the pile-up and leading to a spatial resolution that can be parametrised by $\sqrt{(2.02/\sqrt{E})^2 + (0.29)^2} mm$[22]. This corresponds to a spatial resolution of $400\mu m$ at $50GeV$. Moreover, more than 60% of the light is collected within 15ns, allowing the ECAL to be part of the Level 1 trigger.

The barrel ECAL crystals will have a $22x22mm^2$ section and a height of $230mm$. The barrel will be equipped with 61200 such crystals. Each endcap will be composed of 10764 $24.7x24.7x220mm^3$ crystals.

A very good energy resolution is needed in order to observe the Higgs decay channel $H \rightarrow \gamma\gamma$. The energy resolution of a homogeneous calorimeter like the ECAL can be parametrized as follows:

$$(\frac{\sigma_E}{E})^2 = (\frac{a}{\sqrt{E}})^2 + (\frac{\sigma_n}{E})^2 + c^2 \tag{1.3}$$

where a, σ_n and c are constants. $a/\sqrt{E}$ is a stochastic term corresponding to statistical fluctuations in the number of primary processes that generate the signal, σ_n/E takes the electronic noise and pile-up into account an c takes care of all the other contributions like non uniformities inside the crystals. The best energy resolution is obtained with a homogeneous calorimeter, in contrast with a sampling calorimeter. For the case of CMS, the stochastic term is of the order of $2\%/\sqrt{E}$, σ_n is estimated to be $210MeV$ and c is 0.55%. The mass resolution obtained for a Higgs of $130GeV/c^2$ in the two photon channel after an integrated luminosity of $10^5 pb^{-1}$ will then be $650Mev/c^2$ with a signal significance above 12.

To improve π^0/γ separation in the endcaps ($1.65 < |\eta| < 2.6$) a preshower composed of two silicon strip planes alternating with lead converters will be installed in front of the crystals. A π^0 rejection factor of 2-3 can be achieved with this setup.

1.4.6 The hadron calorimeter

The task of the hadron calorimeter (HCAL) [19] is to measure the energy of hadron jets. Some decay channels for the Higgs ($H \rightarrow W^+W^- \rightarrow l\nu + 2jets$ for instance) include jets and missing energy. Missing energy is also a signature for supersymmetry. It is therefore important to have a good measurement of the total energy contained in one event. The sum of the energy deposited in the ECAL and the HCAL is subtracted from the center of mass energy to determine the missing energy. This implies an angular coverage of almost 4π and a complete hermeticity.

The HCAL is an interlacement of Cu plates and plastic scintillator tiles. Since it is a sampling calorimeter its energy resolution is worse than the ECAL: $\sqrt{(100\%/\sqrt{E})^2 + (4.3\%)^2}$. It was proved via simulations that this energy resolution is adequate to discover the MSSM in the b-jet + missing energy channel.

The HCAL is divided into 2 parts: the barrel part ($|\eta| < 3$) is contained within the magnet. The forward part of the HCAL will partly be outside the magnet as the amount of material inside the magnet is not enough to collect all the energy. This part of the calorimeter will cover the area in η between 3 and 5.

1.4.7 The central tracking system

The central tracking system will measure the momentum of charged particles and will contribute to the identification of these particles. Its main problem is the harsh radiation environment

in which is has to operate. As the main subject of this thesis is the development of tracking detectors, this subsystem of the CMS detector will be described in some more details.

1.4.7.1 Radiation environment

The main problem to be addressed in the tracker is the ability of the detection elements and their readout electronics to survive the radiation environment that will be present. The tracking system must remain operative even after ten years of operation at the highest LHC luminosities. The irradiation has mainly two sources: a direct particle flux coming from the interaction region and neutrons produced in nuclear interactions in the surrounding material.

Figure 1.8 shows the expected radiation dose, neutron and charged hadron fluxes as a function of z, the distance from the interaction point along the beam, for different distances from the beam pipe (R). The charged particle flux roughly decreases as $1/R^2$ and is nearly independent of z. In the endcap regions the neutron fluence rises with z due to an increased contribution coming from neutrons that are backscattered from the ECAL endcap.

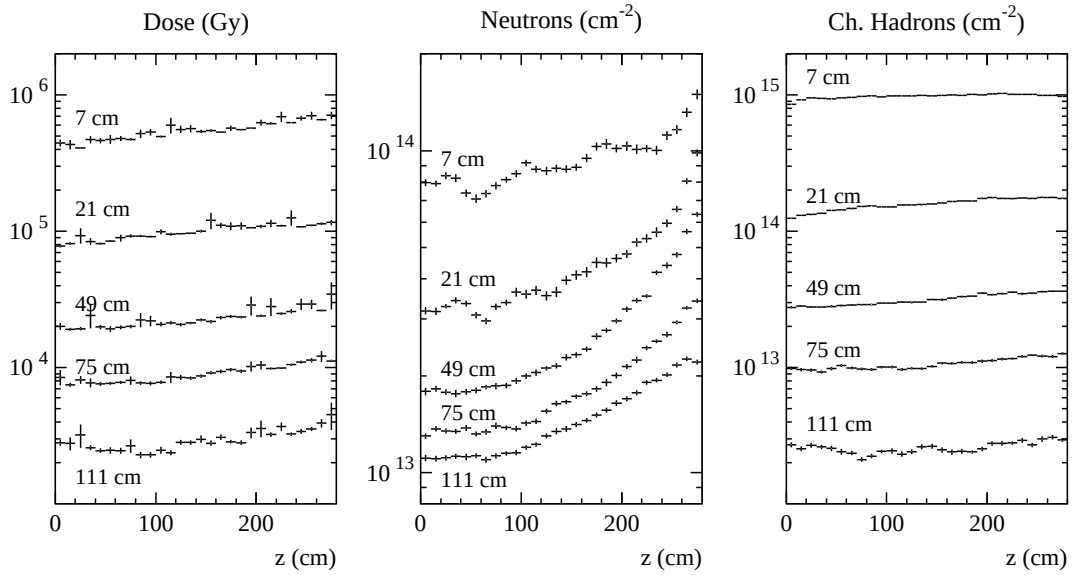

Figure 1.8: Radiation dose, neutron and charged hadron flux in the CMS tracker as a function of z for different R values. The numbers are given for an integrated luminosity of $5 \times 10^5 pb^{-1}$ or tens years of operation of the LHC.

1.4.7.2 Objectives and requirements

The CMS tracker is designed in such a way that it is able to reconstruct most of the tracks produced by charged particles. In addition the tracker will measure the momentum of these charged particles down to very low transverse momenta ($1GeV/c$ at high luminosity). In order to reach the physics goals set for the CMS detector, the tracker must comply to the following requirements:

- an intrinsic momentum resolution of $\Delta p_T/p_T \simeq 0.1 p_T$ (p_T in TeV) for high p_T particles. This condition implies for the present tracker an average $R\phi$-resolution of $25\mu m$
- a reconstruction efficiency of 95% for isolated tracks and 90% for tracks in jets
- a response time below 50ns, corresponding to two LHC bunch crossings
- radiation hard detectors to survive the high level of radiation in the tracker

- the smallest amount of material as possible. This is needed to reduce photon conversions in the tracker and the energy loss of electrons due to bremsstrahlung, spoiling the energy determination in the ECAL. Furthermore, multiple coulomb scattering will affect the momentum resolution for low momentum charged particles.

1.4.7.3 Tracker technology

Initially, three types of detectors were chosen to equip the central tracking system of CMS: silicon pixel detectors, silicon strip detectors and micro strip gas chambers (MSGCs).

Silicon pixel detectors are intrinsically two-dimensional read-out devices with $150\mu m \times 150\mu m$ unit detection cells. Their spatial resolution in both coordinates is $15\mu m$. The pixel tracker will provide three hits per track, allowing to detect displaced vertexes from particles such as decaying b and c quarks. The silicon strip detectors will be able to measure the $R\phi$ coordinate with a precision of $20\mu m$. Here, the size of one detection cell will be $\approx 100\mu m \times 70mm$. To obtain the second coordinate, some layers will be equipped with double sided counters. The strips of these counters will make a stereo angle of 100mrad with respect to the $R\phi$ strips. This will allow the measurement of the second coordinate with an accuracy of 1mm. The MSGC detectors would have larger detection cells ($200\mu m \times 100mm$) but with a spatial resolution better than $40\mu m$. Some layers will also be equipped with counters whose strips are tilted by a small angle with respect to the $R\phi$ strips in order to measure the second coordinate with an accuracy of 1mm.

Both Si-strip and MSGC detectors with a stereo angle will have an increased detection cell size (by a factor 2) in order to reduce the number of readout channels. The targeted spatial resolution will nevertheless be reached.

In the barrel part of the detector, the counters will be tilted over an angle of 9^O (Si-strip) and 14^O (MSGC) with respect to the radial direction thereby compensating the effect of the magnetic field on the drift direction of the charge carriers.

1.4.7.4 Tracker layout

Two competitive tracker layouts have been considered by the CMS community: a design including both Si-strip and MSGC detectors (MST=MSGC Silicon Tracker) and an all silicon tracker (AST). A brief description of both layouts and a performance comparison will be given in the next section [20, 21].

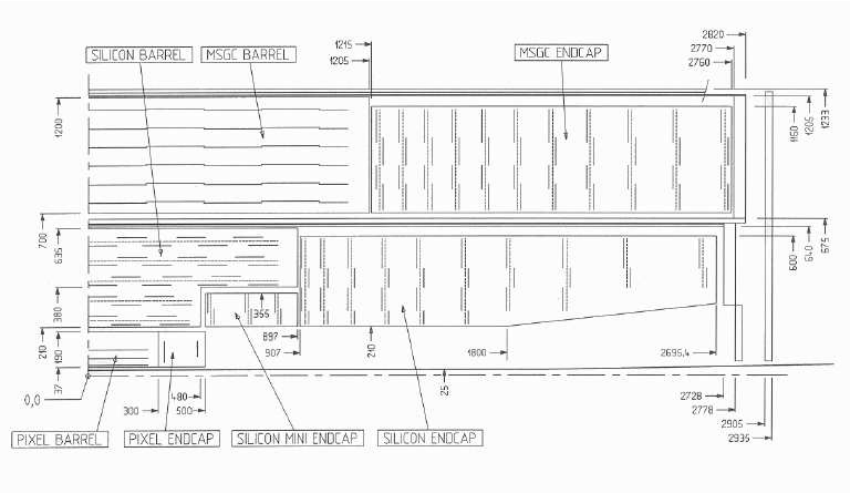

Figure 1.9: Longitudinal view of one quarter of the CMS MST tracker layout.[20]

A longitudinal section of the MST, as proposed in the tracker TDR (Technical Design Report), can be seen in figure 1.9. The pixel detectors are located close to the beam pipe (between radii of 7.5 and 15cm). The silicon strip detectors occupy the space at radii between 20 and 60cm and

finally the MSGCs are located between 70 and 120cm from the beam pipe. The barrel part of the tracker is equipped with 3 pixel layers, 5 Si-strip layers, from which layer 1, 2 and 5 are double sided, and 6 layers of MSGCs. The forward-backward part of the detector is arranged in disks that present themselves in the form of two end-caps.

In the end-cap two pixel layers will be installed. Further on, a mini end-cap composed of 3 Si-strip layers, fully double sided will be installed. The Si-strip endcap will comprise 10 disks, where the inner and outer radii will be stereo detectors. The last part of the end-caps will be composed of 11 disks filled with MSGCs. Here also the inner and outer radii will be composed of stereo detectors. A thermal shield separating the MSGCs from the silicon detectors placed at a radius of 65mm divides the tracker into an inner and an outer part. The shield thermally isolates the Si detectors operated at $-10^{O}C$ from the MSGCs operated at room temperature.

The AST layout is very similar to the MST except for the fact that all MSGC layers are replaced with Si-strip detectors. Due to the higher cost the number of layers has also been reduced: there will be 10 rather than 11 barrel layers and 9 rather than 11 disks in each end-cap. Furthermore all stereo layers are now concentrated below a radius of 90cm, whereas the MST provided one additional layer at a radius of 120cm. The thermal shield is moved outside and placed beyond the last Si-strip detector. This layout can be seen in figure 1.10.

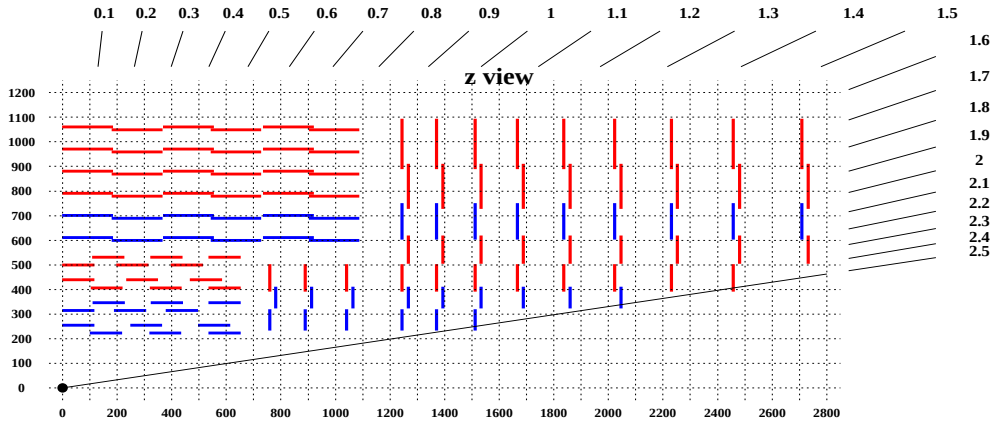

Figure 1.10: Full silicon tracker layout[21]

The amount of material present in the MST tracker, expressed in fractions of radiation length, is shown in figure 1.11a. Electrons emitted at $\eta = 2$ will loose on average 45% of their energy by bremsstrahlung before reaching the electromagnetic calorimeter. Moreover the probability of photon conversion before the calorimeter, at this same pseudorapidity, is as high as 37%. On average 20% of the hadrons will experience strong interactions in the tracker material.

The ratio of the radiation lengths of the AST and MST layouts is shown in figure 1.11b. Fluctuations in this histogram are mainly dominated by the the different position of material such as hybrids, cooling pipes and disks in the two layouts. In the Barrel region, the two layouts show a comparable material budget. The AST end-caps are lighter than the MST ones, due to the reduced number of stations and rings.

An other important parameter to be compared is the occupancy of the tracker. The occupancy is defined as follows:

$$Occupancy = \frac{Total\ number\ of\ strips\ in\ reconstructed\ clusters}{Total\ number\ of\ strips}$$

Due to the faster response time of the Si-strip detectors, the occupancy is a factor 2 higher in the MST than in the AST. This because the impact of 'early' and 'late' events is much larger in MSGCs than in Si-strips.

The transverse momentum resolution is very comparable in the two layouts. Figure 1.12a

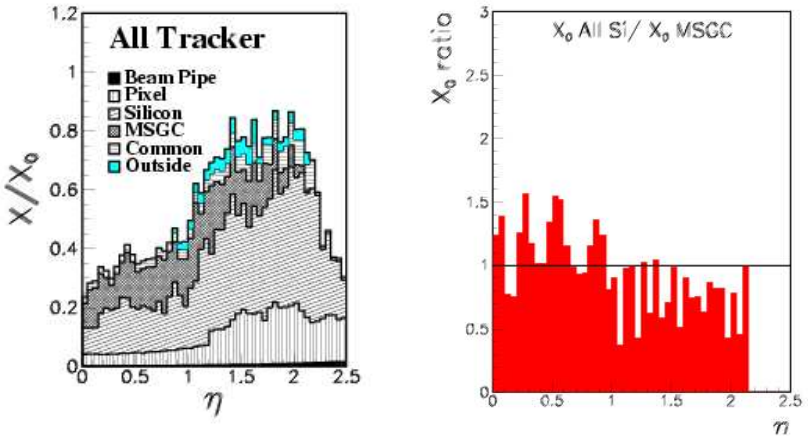

Figure 1.11: Thickness of the MST tracker as a function of the pseudorapidity in radiation lengths (a) and ratio of the fractional radiation lengths contributed by the outer detectors of the AST and MST layouts as a function of η (b).

shows the transverse momentum resolution as a function of the pseudorapidity for muons of different p_T in the AST layout. Figure 1.12b shows the ratio of the performance AST/MST.

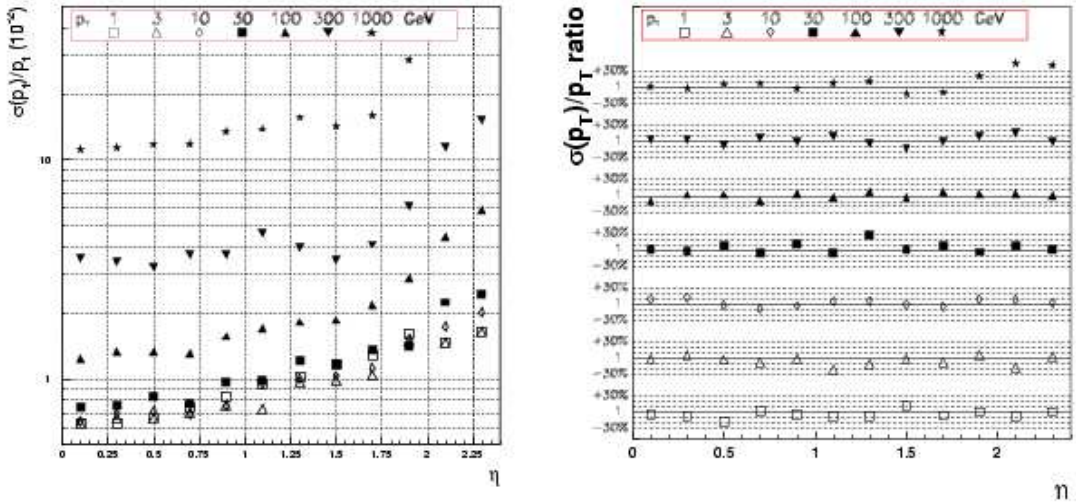

Figure 1.12: a) Transverse momentum resolution as a function of the pseudorapidity. Isolated muons of different p_T have been reconstructed using the AST layout. b) The ratio of the performance AST/MST.

Track finding efficiencies for different topologies where also studied in both layouts. The analysis revealed equivalent track finding efficiencies for tracks within jets, the reconstruction of $B \rightarrow J/\psi K_S^0$ and converted photons. However, the track parameters that measure the track in the r-z plane are better estimated for tracks crossing the AST layout. This improvement is due to the better hit resolution in the z-coordinate measured by the silicon sensors.

Eventually, the CMS management adopted the AST design. Although the MSGCs had proven their value and ability to fulfill all requirements posed by the tracker, a few decisive arguments made the management choose for the AST design:

- Moving from two 'parallel' technologies to a single one was a unique opportunity to concentrate all available effort onto a reduced set of problems.
- The maturity of the APV25 readout chip and its excellent properties that was only ready

in its Si version.

- The excellent quality of sensors manufactured on high volume industrial 6' production lines, as well as the possibility of streamlining module assembly through automation.

Chapter 2

Micro Patterned Gas Counters

2.1 Working principle of gaseous detectors

2.1.1 Particle interactions with matter

Two main types of particle interactions must be considered in particle detection: the electromagnetic and nuclear interactions. The electromagnetic interactions will be used to generate a measurable signal in the detector, whereas the nuclear interactions will put limits on the operation of the gaseous detectors.

Three types of electromagnetic interactions are possible for charged particles:

- collisions with atomic electrons, creating exited atoms or electron-ion pairs. This is the main process responsible for signal formation.
- emission of Bremsstrahlung in the Coulomb field of the nuclei and the electrons.
- elastic scattering on the nuclei and on the atomic electrons. This effect deviates the charged particle from its previously followed trajectory.

Photons can interact electromagnetically with matter via the following phenomena:

- the photoelectric effect, in which the energy of the photon is absorbed by an atomic electron.
- the Compton effect, which corresponds to the diffusion of the photon by an atomic electron.
- the conversion of a photon into an electron-positron pair in the Coulomb field of a nucleus or atomic electron.

2.1.1.1 Electromagnetic energy loss of charged relativistic particles in matter

A relativistic charged particle heavier than the electron looses its energy primarily via collisions with the electrons from the traversed medium thereby ionizing or exiting these atoms or molecules [27].

The average energy loss per unit path length $-dE/ds$, experienced by a particle traversing a material which consists of separate molecules is related to the cross section for all possible individual collisions by:

$$-\frac{dE}{ds} = \sum_i N_i \sum_n E_{ni}\sigma_{ni}$$

where σ_i is the cross section for the inelastic collision which raises a molecule of type i to an energy level E_{ni} above its ground state, and where N_i is the density of molecules of type i.

The differential cross section in the lowest-order (Born) approximation is then given by:

$$d\sigma_n = \frac{1}{4\pi^2\hbar^4 v v'}|(p', n|V|p, 0)|^2 p'^2 d(cos\theta)d\varphi \tag{2.1}$$

in which p and p' are the initial and final momenta, v,v' are the initial and final velocities and V is the electromagnetic interaction between the incident particle and the atomic electrons.

The momentum transfer ($q = p - p'$) relates to the kinetic energy transfered to the electron in the following way: $Q(1 + Q/2mc^2) = q^2/2m$ in the relativistic case and by $Q = q^2/2m$ in the non relativistic case. When the momentum transfer is large, the electron can be seen as initially at rest and then Q and E_n coincide.

The electromagnetic interaction V between the charge and spin of the incident particle and the atomic electrons can be subdivided into two term. The first one is the unretarded static Coulomb interaction and the other is the interaction through the emission and reabsorption of virtual photons:

$$(p', n|V|p, 0) = \frac{ze^2}{2\pi} \int dk \{ \frac{(p'|e^{-ikr}|p)(n|\sum_j e^{ikr_j}|0)}{k^2} + \sum_s \frac{(p'|\alpha.\hat{A}_s e^{-ikr}|p)(n|\sum_j \alpha_j \hat{A}_s e^{ikr_j}|0)}{k^2 - (E_n/\hbar c)^2} \} \tag{2.2}$$

It is clear from momentum conservation that the matrix elements between momentum eigenstates of the incident particle will vanish except if $k = (p - p')/\hbar = q/\hbar$.

Equation 2.2 is calculated in three Q ranges. In the low Q range, the exponentials in 2.2 are expanded in powers of q. Only the the lowest order terms (q^0 and q^1) are retained. When Q becomes much larger than the mean kinetic energy of the atomic electron, the atomic electron can be considered at rest. Therefore: $p_0 = 0$ and $p_n = q$. Between these two regimes, an intermediate Q exchange regime is identified. In this regime, the contributions from transverse excitations is assumed to be negligible, yielding a simplification of 2.2.

An integration over dQ of the obtained formulas then yields the mean energy loss normalized to the density of the traversed medium of a particle with charge ze and velocity $\beta = v/c$, also known as the Bethe-Bloch formula:

$$-\frac{dE}{\rho dx} = \frac{Kz^2 Z}{A\beta^2} [\frac{1}{2} ln \frac{2m_e c^2 \beta^2 \gamma^2 T_{max}}{I^2} - \beta^2 - \frac{\delta}{2}] \tag{2.3}$$

herein A and Z are the atomic weight and the atomic number of the medium, $m_e c^2$ is the rest energy of the electron and $\gamma = (1 - \beta^2)^{-1/2}$ is the Lorentz factor. The constant K is equal to $0.307 MeV g^{-1} cm^2$ and I is the mean excitation energy of the atom. T_{max} is the maximum kinetic energy that can be transferred to the electron in a single collision. It is given by the following formula:

$$T_{max} = \frac{2m_e c^2 \beta^2 \gamma^2}{1 + 2\gamma m_e/M + (m_e/M)^2} \tag{2.4}$$

where M denotes the mass of the incident particle. T_{max} amounts to about $100 MeV$ for $1 GeV$ muons. The term $\delta/2$ is a correction due to the polarization of the medium.

Function 2.3 is shown in figure 2.1 for various materials and various particles. As can be seen, the ionization loss in a given medium is mainly dependent on the velocity β and only slightly on the mass of the particle.

At low energies, the ionizations falls steeply (as $1/\beta^2$) and then goes through a minimum at $\beta\gamma = 3 - 4$. Particles having energies close to this energy are called Minimum Ionizing Particles (MIPs). Slow particles deposit large amounts of energy and are subsequently called Highly Ionizing Particles (HIPs). Most of the particles produced in todays high energy physics experiments are MIPs.

At relativistic energies ($\beta \approx 1; \gamma \rightarrow$ inf) a slow logarithmic increase of the energy loss occurs. At even higher energies, the energy loss reaches a plateau, the Fermi plateau. The plateau is reached due to the fact that the particle is now polarizing the traversed medium leading to a shielding effect. This gives rise to the term $\delta/2$ in equation 2.3[25].

In practice however, the amount of energy transferred is not equal to the mean value given by equation 2.3. Landau was the first to derive the distribution $F(x, \Delta)$ of the energy loss Δ

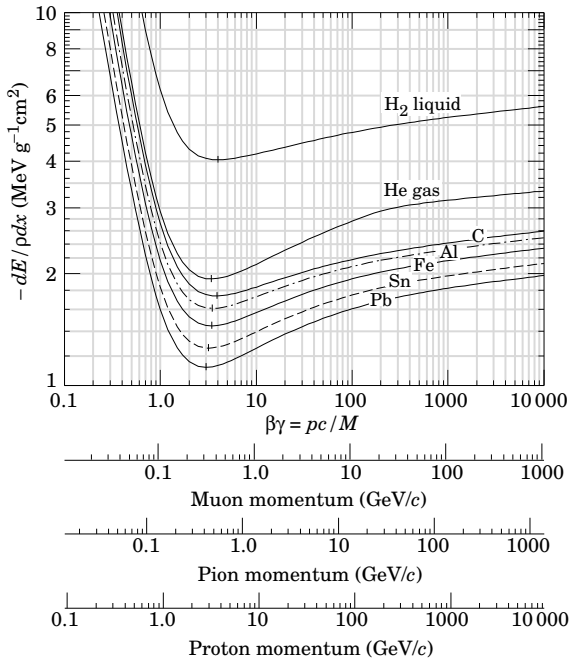

Figure 2.1: Average energy loss as a function of the particle momentum, for muons, pions and protons in various mediums.

in a layer with thickness x[26]. He considered the atomic electrons as free and used Rutherford scattering to describe the interaction between the incident particle and the atomic electrons. He obtained a universal function ϕ of only one reduced variable λ:

$$F(x,\Delta)d\Delta = \phi(\lambda)d(\lambda) \tag{2.5}$$

with

$$\lambda = (\frac{\Delta - \Delta_0}{\epsilon})$$

The parameters Δ_0 and ϵ are respectively the most probable energy loss and a scaling factor. ϵ takes the following form as a function of x:

$$\epsilon = \frac{K}{2}\frac{Z}{A}\frac{\rho x}{\beta^2} \tag{2.6}$$

K is the same constant as in expression 2.3.

The Landau theory only holds for those energy transfers in which the atomic electrons can be considered as free, i.e. in which the energy transferred to the electron is large compared to its binding energy. This can be expressed by the condition that $\epsilon >> I$, which is only satisfied in gasses at atmospheric pressure for $x >> 10cm$. In the seventies, theories including the contribution from low energy transfer to the energy loss distribution were worked out [28, 29, 30]. Figure 2.2 shows the energy loss distribution for 3GeV π^- in 1.5cm of argon at atmospheric pressure and compares it to two models. The Landau distribution has a smaller width than the experimentally observed distribution. The model of Cobb et al. [28] describes the data in a better way.

2.1.1.2 Primary and secondary ionizations

When the amount of energy transferred to the struck electron exceeds it binding energy, the electron will be emitted. Such electrons are called primary electrons or δ-rays. The average energy needed to create an electron-ion pair (W_I) is defined as follows:

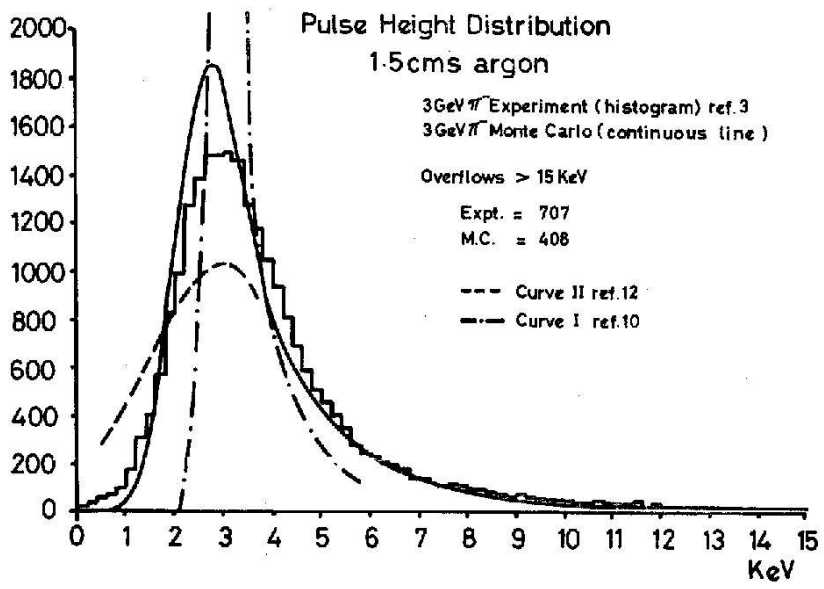

Figure 2.2: Comparison of the experimental energy loss distribution of 3GeV π^- in a 1.5cm thick Ar layer at standard temperature and pressure (histogram) with the Landau function (dash-dotted line)[26] and the model of J.H. Cobb et al. (full line)[28].

$$-\frac{dE}{dx} = n_P * W_I \tag{2.7}$$

Herein n_P is the average number of primary electrons released by the incident particle per unit length. Values for W_I for different gasses can be seen in table 2.1.

Gas	n_p (cm^{-1})	n_t (cm^{-1})	W_I (eV)	F
He	3.3	7.6	42.3	-
Ne	10.9	40	36.4	0.17
Ar	24.8	97	26.3	0.4
Ne+0.5%Ar	-	57	25.3	0.05
CO_2	33.6	100	32.8	-
CH_4	24.8	59	27.1	-
DME $(CH_3 - O - CH_3)$	55	160	23.9	-
CF_4	51	100	54	-

Table 2.1: Ionisation potential (W_I), primary (n_p) and total (n_t) ionisation densities and Fano factor (F) for some detection gases. Values hold at 20^0C and $1013hPa$. Fano factors according to [31].

In case of gas mixtures, W_I is usually a weighted average of the W_I of the components. However, in some cases this approach fails, as excitations from a molecule of one of the components can be transferred to the molecules of the other gas, resulting in ionization of the latter. This effectively lowers the W_I of the mixture. This phenomenon is called the "Penning effect" and gasses in which this occurs are called "Penning Mixtures". It occurs under the condition that the first excitation level of one gas lies above the ionization potential of the other gas. Ar+Ne and Ar+DME (Di Methyl Ether) are known to be Penning Mixtures.

The total number (k) of primary electrons released in a path of length x is Poisson distributed with an average number equal to $n_P x$. The probability of having k primary electrons in a distance x traversed by the incident particle is given by:

$$P(k) = \frac{(n_P x)^k}{k!} exp(-n_P x) \tag{2.8}$$

For a large number k, one expects the distribution to be a Gaussian with variance $\sigma^2 = k$ around the mean value k. When the energy of a particle is completely absorbed in the sensitive volume of a detector, as is the case for X-rays or low energy charged particles, the distribution around the mean energy deposit is much more peaked and the variance is reduced by a factor F, the Fano-factor[27]. The effect arises because, when a particle looses all of its energy, the fluctuations in the energy loss will be correlated. Thus:

$$\sigma^2 = Fk \tag{2.9}$$

It is usually too difficult to calculate the Fano factor in individual cases, so mostly it is determined experimentally. It ranges between 0.05 and 0.20 for most detection gases (see table 2.1).

A primary electron traveling through the medium can loose its kinetic energy and thus create new electron-ion pairs by itself. The electrons freed by this mechanism are called secondary electrons.

The total of primary and secondary electrons released per unit of length into a medium (n_T) is an important quantity as these electrons will give rise to the signal induced on the electrodes.

2.1.1.3 Bremsstrahlung

High energy electrons lose their kinetic energy essentially by the emission of photons (Bremsstrahlung) in the Coulomb field of the nuclei and electrons of the traversed medium. When a high energy electron travels over a distance of one radiation length (X_0) in a certain material, it will lose all but a fraction $1/e$ of its energy by Bremsstrahlung. Therefore the thickness of a detector is often measured in radiation lengths.

An empirical formula for X_0 is given by [33]:

$$X_0 = \frac{716.4A}{Z(Z+1)\ln(287/\sqrt{Z})} gcm^{-2} \tag{2.10}$$

where A and Z are respectively the atomic weight and the atomic number of the medium. In CMS, Bremsstrahlung affects the detector performance in two ways. First, it will increase the photon background in the electromagnetic calorimeter, and second, it will degrade the momentum resolution of electrons because of discontinuities of curvature in the photon emission points[18, 20].

Although muons are also subject to Bremsstrahlung, the problem is not so pronounced as in the electron case since the cross section for the process is inversely proportional to the mass squared. Therefore the energy loss for muons is about 40.000 times smaller than for electrons of the same energy.

2.1.1.4 Multiple Coulomb scattering

A charged particle passing through a medium is deflected by many small angle scatters. This is mainly due to Coulomb scattering by the nuclei and electrons of the medium. However, hadrons can be deflected due to the strong interaction. The standard deviation of the total deflection angle due to multiple Coulomb scattering, projected onto a plane parallel tot the direction of the incident particle, can be expressed as [33]:

$$\theta_0 = \frac{13.6MeV}{\beta cp} z\sqrt{x/X_0}[1 + 0.038ln(x/X_0)] \tag{2.11}$$

herein p is the momentum of the incident particle and z its charge. The distribution of the multiple Coulomb scattering (MCS) is Gaussian for small angles, i.e. the central 98% of the distribution. At large angles, the scattering behaves like Rutherford scattering, resulting in larger tails than Gaussian ones.

MCS will play an important role in the track reconstruction at CMS. Particles with a momentum of $10GeV/c$ will have a deflection of 0.3mrad R.M.S. in each layer. In the next detection layer, 10cm further, the particle impact point will differ by $30\mu m$ R.M.S. from its unperturbed measurement, which is comparable to the spatial resolution of the detection elements.

2.1.1.5 Interactions of photons with matter

Photons are generally divided into 3 groups: UV-photons, X-rays and gammas. UV-photons are the lowest in energy: between 4 and 100eV, created by the decay of an outer shell electron of an atom or molecule from an exited state to the ground state. X-rays have energies ranging between 0.1and 100keV. They are produced when an outer shell electron falls back to an empty position on one of the inner (K or L) shells. Gammas originate from nuclear decays, e^+e^--annihilation, or other processes involving high energy transfers. Their energy is generally above 100keV, and can be up to more than $10^{20}eV$ as observed in ultra-high energy cosmic rays[34]. A summary of the photon classification can be seen in figure 2.3.

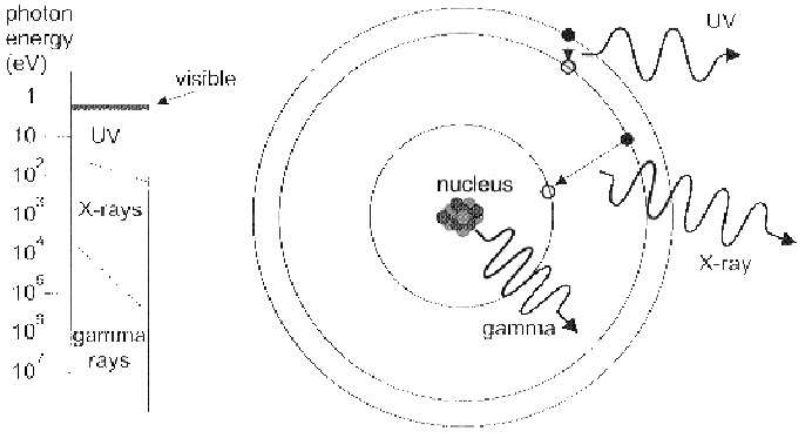

Figure 2.3: Classification of photons according to their origin and energy.

The interaction of photons with matter is described by three fundamental processes:

1. the photoelectric effect
2. the Compton effect
3. pair creation

The photoelectric effect is the absorption of a photon by a bound electron. This electron receives enough energy to escape from the atomic shell structure. To liberate the atomic electron, the photon energy (E_γ) should exceed the electrons binding energy (E_b), which is typically in the keV range. The freed electron then has a kinetic energy given by $E_{kin} = E_\gamma - |E_b|$.

In the Compton effect, the photon is scattered of a quasi free electron. The energy transfer is governed by the conservation laws of mass-energy and linear momentum. It depends therefore on the scattering angle θ, the energy E_γ of the incident photon and the effective mass m_0 of the particle at which the photon is scattered:

$$\Delta\lambda = \lambda_{scattered} - \lambda_{incoming} = \frac{h}{m_0 x}(1 - \cos\theta) \tag{2.12}$$

at $\theta = 180^o$, $\Delta\lambda$ is maximal. For a free electron $\Delta\lambda_{max} = 2.4\,10^{-12}m$. This is called the Compton wavelength of an electron.

Pair production involves the creation of a particle-antiparticle pair, in practice an electron-positron pair. Since the sum of the rest masses of e^+ and e^- is 1022keV, this is the threshold energy

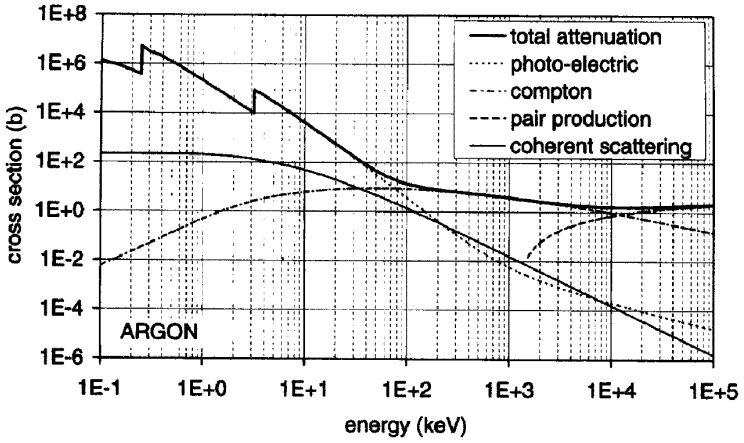

Figure 2.4: Cross section for photon conversion processes, and their sum (total attenuation) in argon.

above which pair production can occur. For reasons of energy and momentum conservation, pair production will only occur in a high electric field, i.e. in the vicinity of a (heavy) nucleus. The cross-section is proportional to Z^2.

A summary of the different contributions of the photon attenuation in Ar as a function of the photon energy can be seen in figure 2.4. Photons with an energy below $100keV$ are mainly absorbed into the gas by the photo-electric effect. At photon energies between $100keV$ and $5000keV$, the dominant process becomes the Compton scattering, at energies above $10000keV$ pair production will become the most important process.

2.1.1.6 Interactions of neutrons with matter

Since neutrons are neutral particles, they can only interact electro-magnetically via their magnetic momentum. This interaction is however small and short-ranged, and usually does not create enough ionisation to be detected. Their detection is done indirectly when the neutron is captured by a nucleus. This is then immediately followed by the emission of one or more charged particles, which then produce ionizations.

Neutrons can also have elastic collisions. A commonly used detection technique is to allow the neutron to strike a thin foil of hydrogenous material that is put in front of the counter. Protons will then emerge from the foil and can subsequently be detected.

2.1.2 Drift and diffusion of electrons in gases

2.1.2.1 Macroscopic model of the electron motion

The motion of charged particles in an electric and magnetic field $\vec{E}$ and $\vec{B}$, is described by the equation of motion: $m\frac{d\vec{u}}{dt} = q\vec{E} + q\vec{u}X\vec{B} - K\vec{u}$, where m and q are the mass and charge of the particle, $\vec{u}$ its velocity and $K\vec{u}$ the frictional force caused by collisions with the gas molecules. The drift velocity is then defined as the solution of the steady state equation ($\frac{d\vec{u}}{dt} = 0$):

$$\frac{\vec{u}}{\tau} = \frac{q}{m}[\vec{E} + \vec{u}X\vec{B}] \tag{2.13}$$

where $\tau = m/K$ has the dimensions of time and depends on the gas properties through the parameter K. τ can be seen as the average time interval between two collisions, since the right hand side of equation 2.13 is the acceleration of the charged particle between two collisions due to the electromagnetic force.

For the special case where $\vec{E}$ is perpendicular to $\vec{B}$, (choose for instance $\vec{E} = (E, 0, 0)$ and $\vec{B} = (0, 0, B)$) the solution is as follows:

$$\vec{u} = \sqrt{u_x^2 + u_y^2} = \frac{\frac{q}{m}E\tau}{\sqrt{1 + (\frac{q}{m}B)^2\tau^2}} \tag{2.14}$$

Thus, the drift velocity is reduced by a factor $\sqrt{1 + (\frac{q}{m}B)^2\tau^2}$ by the presence of a magnetic field. The drift velocity makes an angle α_L with the electric field:

$$\alpha_L = \frac{u_y}{u_x} = -\frac{q}{m}B\tau \tag{2.15}$$

This angle is called the Lorentz angle. In the 4T magnetic field of CMS, in MSGCs filled with DME based mixtures, α_L is around 14^o and the the reduction of the drift velocity is only of the order of 3%.

In the case where both fields are parallel to each other, neither the drift speed nor the direction are affected. The transverse diffusion, however, will be (see section 2.1.2.3).

2.1.2.2 Microscopic model of the electron motion

The classical microscopic model described below will relate the microscopic parameters from the gas and the electron to the macroscopic quantities derived in the previous section.

In the absence of any external field, the electron would be in thermal equilibrium with the gas and would posses an average kinetic energy $\epsilon_v = \frac{3}{2}kT$, where k is the Boltzmann constant and T the absolute gas temperature (at room temperature, $kT \approx 1/40eV$). In the presence of an electric field, the average kinetic energy will increase to become $\epsilon_v = \frac{1}{2}mv^2 = \epsilon_E + \frac{3}{2}kT$. ϵ_E is the contribution of the electric field to the average kinetic energy. At drift fields used in gaseous detectors and in most gases, ϵ_E amounts to a few eV, so the thermal energy can be neglected. In a time interval τ between two collisions with the gas molecules, the drift speed induced by the electric field E can be written as:

$$u = \frac{eE}{m}\tau = \mu_e E \tag{2.16}$$

where μ_e is the electron mobility.

In every collision with a gas molecule, the electron loses on average a fraction δ of the energy ϵ_E that it had gained by being in the electric field, so that there is a balance between the losses in collisions and the acceleration due to the field. The electric field will thus cause a net drift speed $u << v$. When the electron travels over a distance dx in the direction of the field, the number of collisions is equal to $\frac{dx}{u\tau}$, so the energy balance reads:

$$\frac{dx}{u\tau}\delta\epsilon_E = eEdx$$

The average time interval between two collisions can be expressed as a function of the non-motive velocity v, the collision cross-section σ and the molecular density N:

$$\frac{1}{\tau} = N\sigma v \tag{2.17}$$

Neglecting the thermal motion, the expression of the equilibrium velocities can thus be written as:

$$u^2 = \frac{eE}{mN\sigma}\sqrt{\frac{\delta}{2}} \tag{2.18}$$

$$v^2 = \frac{eE}{mN\sigma}\sqrt{\frac{2}{\delta}} \tag{2.19}$$

The total collision cross section as expressed in equation 2.17 can be divided into several distinct contributions:

$$\sigma = \sigma_{tot} = \sigma_{el} + \sigma_{inel} = \sigma_{el} + \sigma_{exc} + \sigma_{ion} \tag{2.20}$$

where σ_{el}, σ_{inel}, σ_{exc} and σ_{ion} are the cross-sections for electron-molecule collisions that are respectively elastic, inelastic and leading to excitations or ionizations. The cross-sections are dependent on the velocity of the electron relative to the gas molecules, or equivalent, to the electric field. Figure 2.5 shows the distribution of the different collision types as function of E/p for Ne, Ne+0.1%Ar and H_2. Note the strong ionisation increase due to the penning effect in the second plot via the addition of only 0.1% of Ar. The bottom plot illustrates the possibility of inelastic collisions at low electric fields in a molecular gas (here H_2), due to the presence of vibrational excitation levels.

Normal drift fields in gaseous detectors are between 5 and $10kV/cm$, so that the probability for ionisational collisions in pure Ne is very low. The addition of a Penning gas drastically improves the situation.

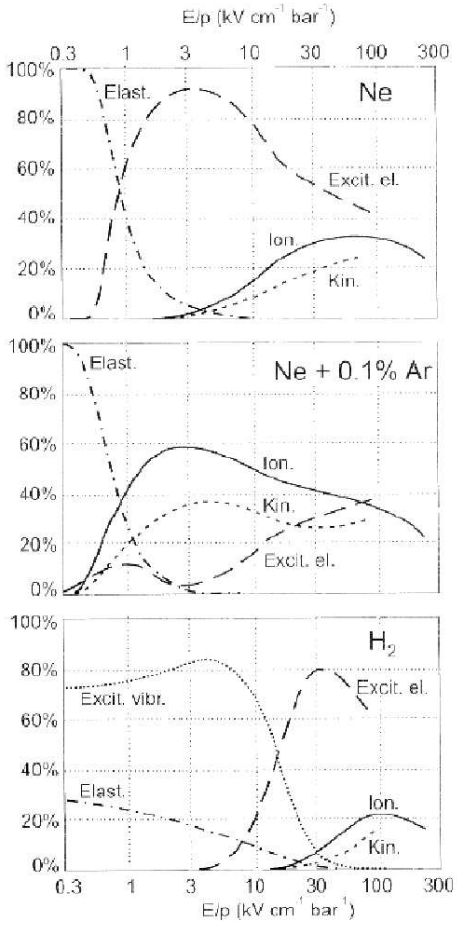

Figure 2.5: Distribution of elastic (Elast.), excitational (Excit.) and ionisational (Ion.) collisions in Ne, Ne+0.1%Ar and H_2 as percentage of the total cross section. Also shown is the increase in the kinetic energy of the electrons. (E_{kin} in arbitrary units) [41]

2.1.2.3 Diffusion

The diffusion of electrons is expressed through the diffusion coefficient D. It is related to the velocity v or the kinetic energy. The mean squared displacement in a given direction $\vec{y}$ after a large number of collisions (n) can be computed as:

$$\sigma_y^2 = \sum_{i=1}^{n} y_i^2 = n < y^2 >$$

where $< y^2 >$ is the mean squared displacement in the direction $\vec{y}$ between two collisions. The free path l between two collisions is distributed as a decreasing exponential, and because $u << v$, the direction of motion can be considered as isotropic in first approximation. Therefore

$$< y^2 >= \int_0^{+\inf} \frac{dl}{L} \int_{-1}^{+1} \frac{d\cos\theta}{2} (l\cos\theta)^2 e^{-l/L} = \frac{2}{3} L^2$$

where $L = v\tau$, the mean free path between two collisions. The expression of the diffusion coefficient then becomes:

$$D = \frac{\sigma_y^2}{2t} = \frac{2}{3}\frac{\epsilon_v}{m} \tag{2.21}$$

obtained by replacing the drift time t by $n\tau$.

The empirical quantity ϵ_K, called the characteristic energy, is defined as: $\epsilon_K = \frac{eD}{\mu_e}$. Combining this with 2.16 yields that $\epsilon_K = \frac{2}{3}\epsilon_v$.

The diffusion is very often expressed in centimeters per unit of drift distance:

$$D' = \frac{\sigma_y}{\sqrt{x}} \tag{2.22}$$

Therefore $D' = \sqrt{2D/u} = \sqrt{2\epsilon_K/eE}$. Thus the size of the electron cloud is proportional to the square root of the drift distance.

The key to understand the drift and diffusion of electrons in gases thus resides in the parameters ϵ_K, σ an δ as a function of the electric field or the electron energy. These curves are shown in figure 2.6. Values of the drift velocities for various $Ar + CH_4$ mixtures as a function of the electric field can be seen in figure 2.7.

2.1.2.4 Thermal limit

In some gases, among which CO_2, CH_4 and DME (Di-Methyl-Ether), the electron kinetic energy remains constant at $\frac{3}{2}kT$ in a large range of electric fields. Even up to $\approx 1000V/cm$. This is explained by the presence of rotational and vibrational excitation levels. The first excitation level for CH_4 for instance is as low as $0.03eV$, whereas it is $11.5eV$ for Ar. The energy loss per collision will thus be much larger in CH_4 than in Ar. Hence v and τ are no longer dependent on E, resulting in a constant diffusion coefficient and electron mobility. The drift velocity then rises linearly with E. Often these gases are added into the mixture in order to decrease the diffusion thus permitting to obtain a better spatial resolution.

2.1.2.5 Transverse and longitudinal diffusion.

Wagner et al. [35] showed that the diffusion is not isotropic in the presence of an electric field. It was explained theoretically by a difference in electron mobility in the leading and trailing edge of the electron cloud [37], which then results in a longitudinal diffusion coefficient D_L that is different from the transverse diffusion coefficient D_T.

In the presence of a magnetic field, the diffusion coefficient is reduced in the direction perpendicular to $\vec{B}$, due to the incurved trajectory of the electrons. The diffusion in the direction parallel to the magnetic field is not affected.

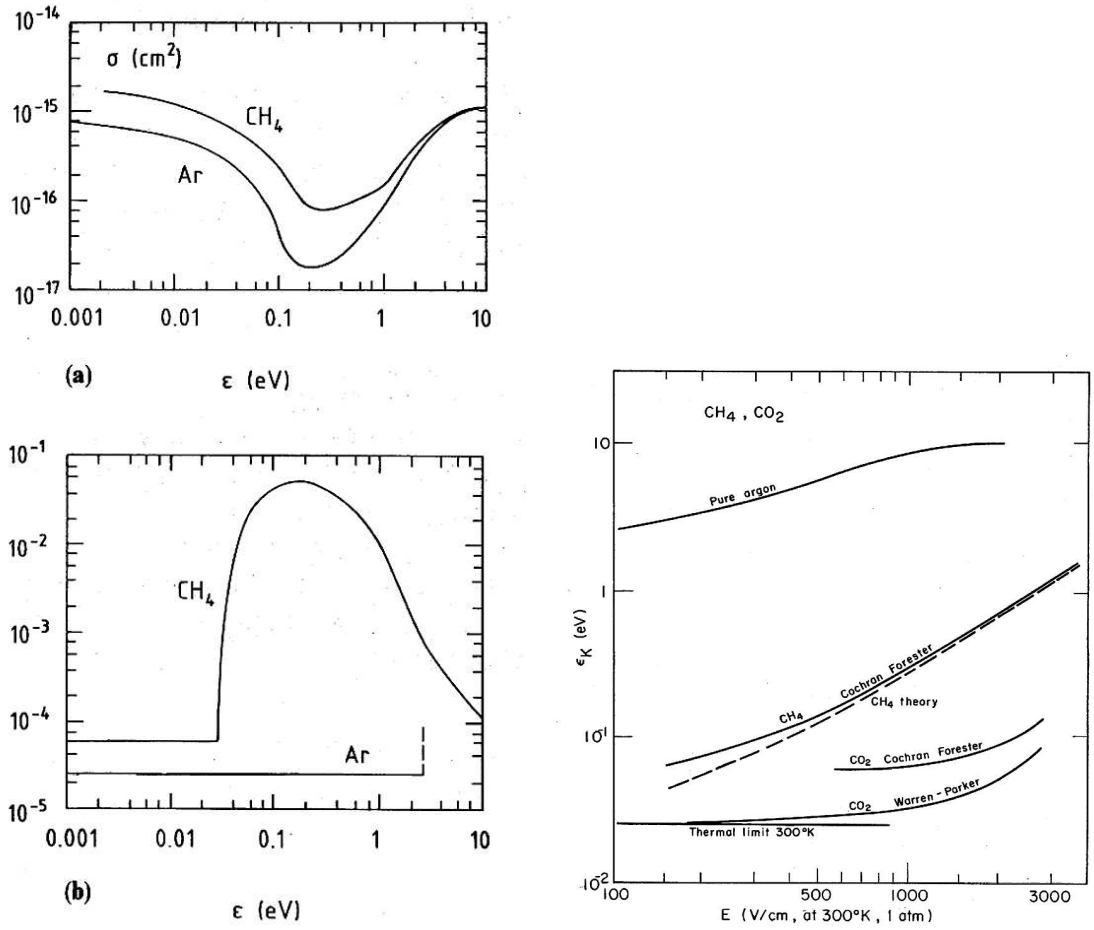

Figure 2.6: Collision cross-section (a) and fractional energy loss (b) in Ar and CH_4[25]. Characteristic energy as a function of the drift field intensity in various gases (c)[14].

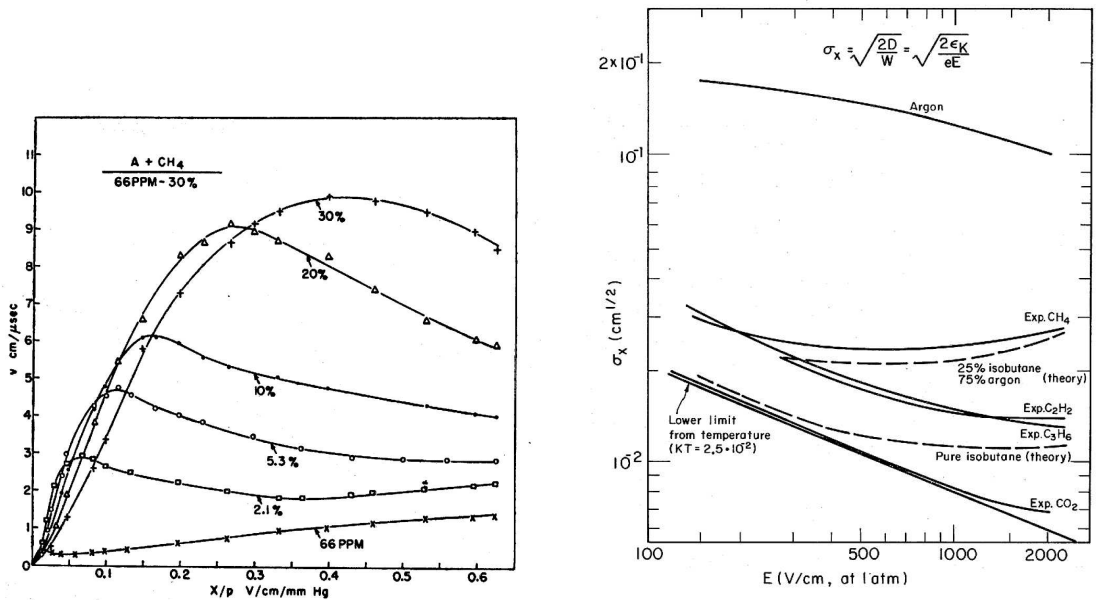

Figure 2.7: Left) Drift velocity in Ar based mixtures as a function of the reduced electric field E/p, for various contents of CH_4. Right) Diffusion as a function of the electric field intensity, in various gases at atmospheric pressure.[14]

2.1.3 Ion movement

Not only the electrons, but also the ions start moving under the influence of the electric field.As will be shown later (section 2.1.5), the movement of the ions essentially determines the signal generation in a gaseous detection counters.

Similar laws as those derived for electrons in section 2.1.2 apply for the ions. However, since their mass is 2.000 to 100.000 times larger, an important fraction of their gained kinetic energy is lost in every collision. And since the collision cross-section is 4 times higher than that for electrons, the mean energy is almost thermal and the ion drift velocity is roughly 10^4 lower than the electron drift velocity.

The mobility of the ions, defined in analogy with 2.16, is constant up to about $E/p = 10kVcm^{-1}bar^{-1}$, with typical values between 0.2-2cm/s per V/cm. Exceptions are light elements like He, H_2, and Ne with $\mu_{ion} = 10.4, 6.7$ and $4.1cm^2V^{-1}s^{-1}$ respectively.

Since the ion energy is mostly thermal, the diffusion coefficient and Lorentz angle are also reduced by a factor 10^4. The high mass of the ions thus implies that the distortions from their paths are small, so that they can be assumed to follow the electric field lines with a drift velocity proportional to the field strength.

As a consequence of their low mobility, the ions can pile up in the gas at high rate operation of the detector, in particular in the avalanche region (see section 2.1.4) where the ion density is high. This space charge can then locally reduce the electric field, further reducing the ion drift velocity, which leads to slower an lower signals. Also the electrons coming from a next event might recombine with the ions, causing signal attenuation.

2.1.4 Gas amplification

Ionisation starts to occur around $E/p \approx 10 - 20kVcm^{-1}bar^{-1}$. These high fields are normally met only in the vicinity ($100\mu m$) of the anodes. The freed electrons will then acquire enough energy in the high electric field to produce new ionisations, which in turn will produce further ionisations, leading to an avalanche like formation as can be seen in figure 2.8.

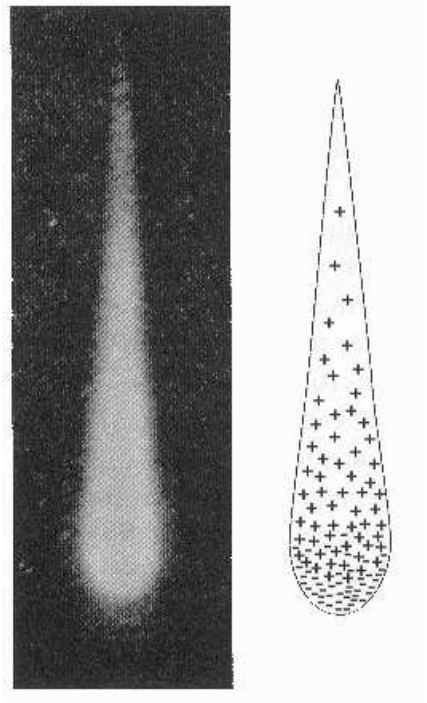

Figure 2.8: Photograph of a single electron avalanche (left) and a sketch of the internal charge distribution (right). The picture was taken by H. Reather in 1937. The avalanche was allowed to grow for several μs to the present length of about $2.5cm$[14].

2.1.4.1 Gas gain

The first Townsend coefficient α is the macroscopic quantity used to describe ionsations provoked by electrons drifting in a gas. It represents the average number of liberated electrons over a path of length ds:

$$\frac{dN}{N} = \alpha ds \tag{2.23}$$

α must be a function of the electron speed an thus dependent on E/p. Korff suggested the following form [42]:

$$\alpha = \frac{a}{l_0} \exp(-\frac{aV_{ion}}{l_0 E}) \tag{2.24}$$

Here, a is a fit parameter an V_{ion} is the ionisation potential. Noticing that the mean free path l_0 is proportional to E/p, one arrives at:

$$\frac{\alpha}{p} = a' \exp(-\frac{a' p V_{ion}}{E}) \tag{2.25}$$

Figure 2.9 shows α for several inert gases in terms of $\nu = \alpha/E$, which is the number of ionisations that occur per traversed Volt in the potential field. Note again the big importance of the Penning effect upon addition of only small amounts of Ar to the Ne gas.

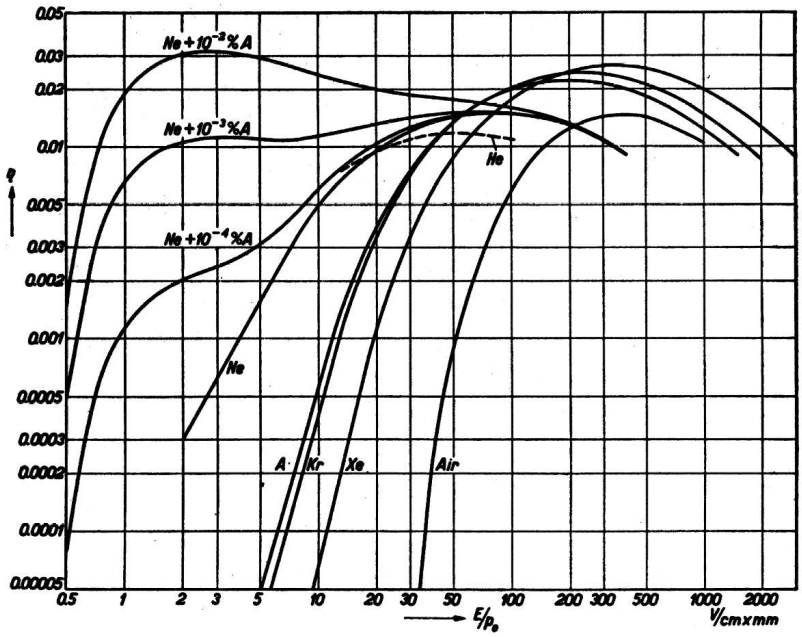

Figure 2.9: The ionisation coefficient $\nu = \alpha/E$ as a function of the reduced electric field for the inert gases, air, and some Penning mixtures

To determine the gas gain, one has to evaluate the following integral:

$$G = \frac{N}{N_0} = \exp[\int_{\gamma_s} \alpha(s) ds] = \exp[\int_{E_a}^{E_b} \frac{\alpha(E)}{dE/ds} dE] \tag{2.26}$$

Where γ_s is the path followed by the electron. In all practical cases, the gain is computed using experimentally measured curves of α as the ones shown in figure 2.9.

2.1.4.2 Gain fluctuations

Gas multiplication is a stochastic process. The gain distribution in a uniform electric field can be described by Yule-Fury statistics, which states that, if $\overline{G}$ is the average gain, the probability of having a gain G in a single avalanche is:

$$P(G) = \frac{1}{\overline{G}}(1 - \frac{1}{\overline{G}})^{G-1} \rightarrow^{\overline{G}>>1} \frac{1}{\overline{G}} exp(-G/\overline{G}) \tag{2.27}$$

This expression only holds if the probability of ionisation is independent of the amount of energy that the electron has acquired since its last ionisation. This is only true for low α. However, this assumption is invalid in proportional counters since the gain distribution shows a clear maximum instead of the exponential decrease.

Byrne [38] and Lansiart and Morucci [39] took the history of the electrons into account by the introduction of a dependence of the already created electrons in the expression for the probability for ionisations:

$$a(G) = \alpha(1 + \mu/G)$$

where μ is an empirically defined parameter. This leads to a Polya distribution for the gas gain:

$$p(z) = \frac{m^m}{\Gamma(m)} z^{m-1} e^{-mz} \tag{2.28}$$

with $m = 1 + \mu$ and $z = G/\overline{G}$. The variance σ_z^2 of the Polya distribution is equal to 1/m. In the particular case that $m = 3/2$, this distribution is equal to the experimentally observed distribution in proportional counters. For an MSGC (see section 2.2.2) it was found[64] that m=2, in agreement with Alkhazov[65, 66] who found less gain fluctuations for higher values of $\nu = \alpha/E$. Hence the width of the distribution is mainly determined by the weaker field at the beginning of the avalanche.

2.1.4.3 Photon feedback, ion feedback and the role of quencher gases

The gas multiplication process yields not only electrons, but also excited gas atoms. These loose their energy upon a collision or return to their ground state by a radiative transition. Accordingly, a large number of photons is produced in the visible and UV region. If not absorbed properly, some of these photons can ionise gas molecules outside the avalanche region or reach the cathode where they can release new electrons via the photoelectric effect, occurring at photon energies above the work function of the metal (typically 4-5eV)

These "secondary electrons" generated from photo-ionisations in the gas, or at the cathode, are multiplied again and can add to the existing pulse. This process, known as photon feedback, degrades the energy resolution, or worse, can be self-sustaining, resulting in dark currents or even in electrical breakdown. To avoid the nuisance of photon feedback, a so-called quencher is added to the gas, which is mostly an organic, poly-atomic gas having a large photon absorption cross section in the visible and UV regime as a consequence of rotational and vibrational energy levels from which the molecules can de-excite radiationless (i.e. via collisions or dissociation). Common quencher additives are CH_4, CO_2, isobutane and DME.

Quenchers play a second important role for the stability of the counter, namely by the prevention of ion-feedback. Ion-feedback is the production of secondary electrons at the cathode, upon neutralisation of the positive ions emanating from the avalanche. At this neutralisation process, there is a small chance that the excitation energy of the ion is released by extraction of an electron from the cathode surface. This way of secondary electron generation can affect the detector in a similar manner as photon-feedback, with the annotation that ion-feedback gives rise to delayed pulses (or "after pulses") due to the small drift velocity of the ions.

In case of ions of a quencher, the energy liberated on neutralisation at the cathode results in dissociation of the gas molecule, rather than secondary electron emission. Since most quencher

molecules have a lower ionisation potential than inert gases, an inert gas ion is likely to exchange its charge when it collides with a quencher molecule. This phenomenon of charge transfer as well as the Penning effect are the reason that generally, only ions of the quencher constituent reach the cathode; hence the problem of ion-feedback is averted. The break-up of molecules provokes however polymer formation on the electrodes, which degrades the detector performance after long term operation. This phenomenon is termed "aging".

2.1.4.4 Breakdown: streamers and sparks

As the avalanche progresses, the space-charge fields of the clouds of electrons and ions can become important. When the number of electrons in the head approaches 10^6, the avalanche begins to slow down owing to the attraction of the positive ions; when it is 10^8, the electrons are much restrained[40].

At 10^8, the space-charge field in the middle of the avalanche is so increased as to practically negate the applied field, and the neighboring field is modified as by a dipole. As a consequence, recombination occurs within the avalanche and ultra-violet photons are emitted isotropically (see figure 2.10). These photons can then ionise molecules in the region surrounding the primary avalanche. The electron-ion pairs created in front of the head and behind the tail of the initial avalanche will find themselves in an enhanced electric field, while those to the side will experience a reduced field. As a result, those electrons freed before and after will accelerate quickly to form new avalanches. These will grow until they too become large enough to repeat the process. The old and new merge into each other to form a "streamer" whose extremities advance toward the anode and cathode at a speed of about $10^8 cm\, s^{-1}$. On arrival, the electrodes are connected by what is essentially a low resistance conducting plasma.

This limit on the electron density has since been known as the Reather condition. This condition has some implications on the requirements for spark formation. Using equation 2.23 to compute the number of electrons when the primary electron has traveled a distance d, one gets:

$$n = n_0 exp[\int_0^d \alpha ds]$$

When combined with the Reather criterion ($n \geq 10^8$), this results in:

$$ln\, n_0 + \int_0^d \alpha ds \geq 20$$

Assuming n_0 to be small and α to be constant over the integration path of interest, the Reather condition becomes:

$$d > \frac{20}{\alpha} \tag{2.29}$$

This means that a spark can develop if its formation length (d) is larger than $20/\alpha$, where the formation length is defined as the length over which amplification occurs. Although being a rough approximation, this criterion has proven to be a good rule of thumb.

A second mechanism for spark formation relies on the ejection of secondary electrons from the cathode which feed the normal avalanche. Two secondary processes are at the basis of the process:

1. The positive ions that strike the cathode are likely to eject secondary electrons.

2. Photons emanating from the discharge may also release electrons through the photoelectric effect.

3. Field emission of electrons at defects in the MSGC artwork. This effect is due the high local electric fields existing around spikes in the metalisation.

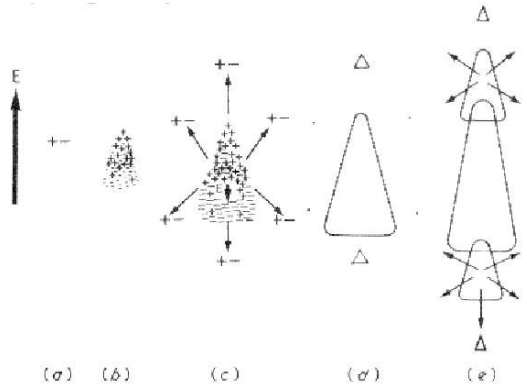

Figure 2.10: Stages in the growth of a streamer: a) creation of initial seed electron and positive ion, b) rapid acceleration of the electrons results in the formation of an avalanche, c) growth of the avalanche until the internal field negates the applied field, and recombination causes photons to be emitted, d) the electrons released at head and tail of the initial avalanche grow themselves into avalanches e) continuation of the process with merging of avalanches and growth of streamer. [41]

This second mechanism does not need the prior development of a streamer and is much slower to propagate compared to the streamer case. The time for breakdown can be very long ($> 10\mu s$) because of the cyclic nature of the process: electrons release ions, which at the cathode release electrons, which release ions, etc., and can amount to hundreds of cycles. This type of sparking can be self sustained, meaning that they subsist in the counter even though the irradiation source has been removed. A breakdown sparking potential can be determined [41]:

$$V = \frac{-\ln \gamma}{\nu} \tag{2.30}$$

In this γ is the number of electrons liberated from the cathode per single ionizing collision in the gas. $\nu = \alpha/E$ as defined in section 2.1.4.1. The logarithm is negative since γ is much smaller than 1.

2.1.5 Signal development

Although the avalanche development takes less than a nanosecond, the rise time of the signal in a gaseous detector is much longer (a few nanoseconds in an MSGC for instance). The reason for this is twofold.

- First, the signal on the anode is only partially determined by the movement of the electrons in the avalanche. The main signal contribution comes from the current induced by the motion from the ions.
- Secondly, the detector capacitance and anode resistance causes an RC-time.

This second effect, however, is rarely the main source for the signal elongation. It is essentially the low mobility of the positive ions left behind that sets an intrinsic limit on the signal rise time.

An intuitive picture of the signal formation is the following: suppose all the electron pairs are created at a distance d from the anode. Shortly ($1ns$) after that all the electrons have reached the anode. As the ions are still in the vicinity of the anode, they will exert a Coulomb force on the electrons. Therefore, these will not be free to move. Only a few electrons will be able to escape the influence of the ions and will be collected immediately. As the ions continue to move from the anode, more and more electrons will escape and be collected by the front-end electronics. However, this timescale of this release is governed by the movement of the ions and hence will be the formation of the signal.

A straightforward mathematical way to study the development of the signal is through Ramo's theorem[43]. A thorough discussion can be found in [25]. Ramo's theorem describes the charge and current induced by a moving test charge q on electrodes at arbitrary position and potential, under the condition that the electrodes are connected to an infinite reservoir of charge. The current I_i that is induced in electrode i by the test charge q at position $\vec{r}(t)$ that moves with a velocity $\vec{v}(t)$ can be obtained with equation 2.31, provided that the potential $V_i(\vec{r})$ and the electric field $\vec{E}(\vec{r})$ are calculated for a fictitious situation where all electrodes are on ground potential, except for electrode i, which is set at U_i. The charge ΔQ_i induced on electrode i in a time interval $[t_1, t_2]$ is obtained via the integration of the current as in equation 2.32.

$$I_i(t) = -\frac{q}{U_i}\frac{dV_i(\vec{r}(t))}{dt} = -\frac{q}{U_i}\frac{d\vec{r}(t)}{dt}\nabla V_i(\vec{r}(t)) = q\frac{\vec{v}.\vec{E}(\vec{r})}{U_i} \tag{2.31}$$

$$\Delta Q_i = \int_{t_1}^{t_2} I dt = -\frac{q}{U_i}\int_{t_1}^{t_2}\frac{dV_i(\vec{r}(t))}{dt} = -q\frac{\Delta V_i}{U_i} \tag{2.32}$$

In the case of a charge cloud, the total induced charge or current is the superposition of the contributions of the individual charges. The factors $\frac{\vec{E}(\vec{r})}{U_i}$ and $\frac{V_i(\vec{r})}{U_i}$ are called the weighting field and weighting potential of electrode i.

The electrons are generated within a few microns from the anode and travel quickly to the anode. Hence the velocity and the weighting field for the electrons are high and so is their current contribution. However, since they are collected very quickly, the integrated induced current, i.e. the induced charge, is small.

The remaining part of the charge signal is induced by the movement of the ions from the avalanche region to the cathodes, traveling over a relatively large ΔV_i. Since the electric field intensity drops at increasing distance from the anodes, the ions slow down on their way to the cathodes, causing a long tail in the charge collection diagram.

An estimation of the relative contribution of electrons and ions to the signal will for different detectors will be discussed in section 2.2.2.

The movement of the charges also induces opposite signals on the other electrodes. This is what is known as cross-talk.

2.1.6 Signal read-out

Although the amplitude of the signal profits from the gas multiplication, electronic amplification is needed before further processing is possible. This task is performed by dedicated pre-amplifiers.

Gaseous detectors are usually equipped with charge amplifiers as the one shown in figure 2.11. If the gain of the operational amplifier is very high (usual values are $10^4 - 10^6$), it is easy to show that the output voltage V_o is proportional to the input charge Q as:

$$V_o = -\frac{Q}{C_f}$$

Where C_f is the value of the feedback capacitance as depicted in figure 2.11. The feedback circuit also contains a resistor R_f which serves to reset the amplifier and to shape the signal with a time constant $\tau_f = R_f C_f$. One speaks of pile-up when a new signal arrives before the pre-amplifier output is back on its baseline. Together with the charge collection time and the RC-time of the detector, the rise-time and fall-time of the pre-amplifier determine the shaping of the signal.

Since most pre-amplifiers used for MSGCs have an integration time of about $30 - 50ns$ and a fall time $\tau_f \approx 100ns$, not all charge is collected in the front-end, as shown schematically in figure 2.12. This phenomenon of unbalance between total signal and the signal used for read-out is known as ballistic deficit. When operating the read-out electronics in peak mode[1] a not to long

[1]In peak-mode, a sample is taken 50ns after the trigger was given. A second sample is taken a long time after the signal has disappeared to determine the baseline of the channel. The difference of the two measurements yields the pulse height.

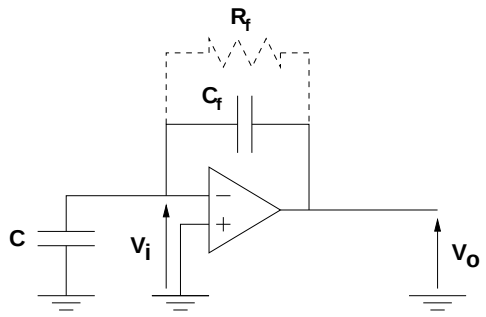

Figure 2.11: Principle of the charge amplifier. V_i and V_o are the voltages at the input and output of the amplifier, C is the capacitance of the electrode connected to it, C_f and R_f are the feedback capacitance and resistance.

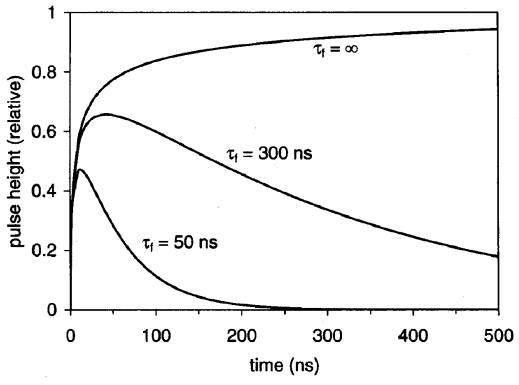

Figure 2.12: Schematic diagram of the integrated charge signal, for different fall times of the pre-amplifier.

τ_f is needed to avoid that a second pulse developing whereas the first one is not yet completely extinct, thus causing pile-up. A balance must thus be found between pile-up an ballistic deficit.

An elegant solution is found in the double correlated sampling method. In this, a sample is taken at the trigger time and 50ns after the trigger signal. The difference between the two samples again yields the pulse height. If the τ_f is taken to be long enough (of the order of ms), the ballistic deficit will be strongly reduced. Also pile-up is no longer an issue since the two samples are taken $50ns$ apart. Due to the much increased value of τ_f, the tail of the previous signal will not change much during this time interval.

An other important number for the characteristics of electronics is the noise. The noise is the random fluctuations of the amplifier output voltage in the absence of any signal. In charge sensitive pre-amplifiers the noise is usually expressed in term of the 'Equivalent Noise Charge' (ENC), which is the hypothetical charge at the entry of the pre-amplifier that would cause the observed R.M.S noise level at the output.

An unavoidable noise source is the thermal motion of the electrons inside the resistor constituted by the electrode connected to the amplifier. This noise contribution can be expressed as:

$$V_{noise} = \sqrt{4kTRB} \tag{2.33}$$

Where V_{noise} is the noise voltage R.M.S, R is the input resistance and B is the pre-amplifier bandwidth. The thermal noise thus increases with the input resistance and with the amplifiers response speed. At room temperature, it amounts already to $25\mu V$ for an amplifier of $40MHz$ bandwidth connected to an electrode of $1k\Omega$ resistance. For a typical electrode capacitance of $10pF$, this amounts to 1500 electrons ENC.

2.1.7 Efficiency and position resolution

For sake of completeness, the efficiency and position resolution of the detector will be defined here although they depend strongly on the detector geometry, the used gas and the flight direction of the particle with respect to the detector.

The efficiency is defined as the number of registered events, divided by the number of radiation particles that entered the sensitive volume of the detector. The position resolution σ_{pos} is the root mean square of the deviations Δx of the reconstructed position from the measured one.

It can be shown that in the case that only one detection element is hit, the position resolution is given by:

$$\sigma_{pos} = \frac{p}{\sqrt{12}} \tag{2.34}$$

where p is the pitch with which the detection elements are spaced. In the case that multiple, neighboring channels are hit in the same event, interpolation techniques allow to enhance σ_{pos}. The efficiency and position resolution will be treated for various cases in the next section.

2.2 The Micro-Strip Gas Counter and the Gas Electron multiplier

2.2.1 The Multi-Wire Proportional Chamber

The Multi-Wire Proportional Chamber (MWPC) was developed by G. Charpak [36]. The outline of the MWPC is shown in figure 2.13. Thin wires of $20 - 70\mu m$ diameter are strung parallel in a gas volume that is closed by two conducting planes. The anodic wires are put to a potential of a few thousand volts. The cathodic planes are put on a negative potential. When a charged particle crosses the active volume of the MWPC, it will ionise gas molecules on its way. The electrostatic force will make the electrons move towards the anodes, and the positive ions to the cathodic planes. As there exists a very high field in the vicinity of the anodes, the electrons will experience avalanche multiplication there.

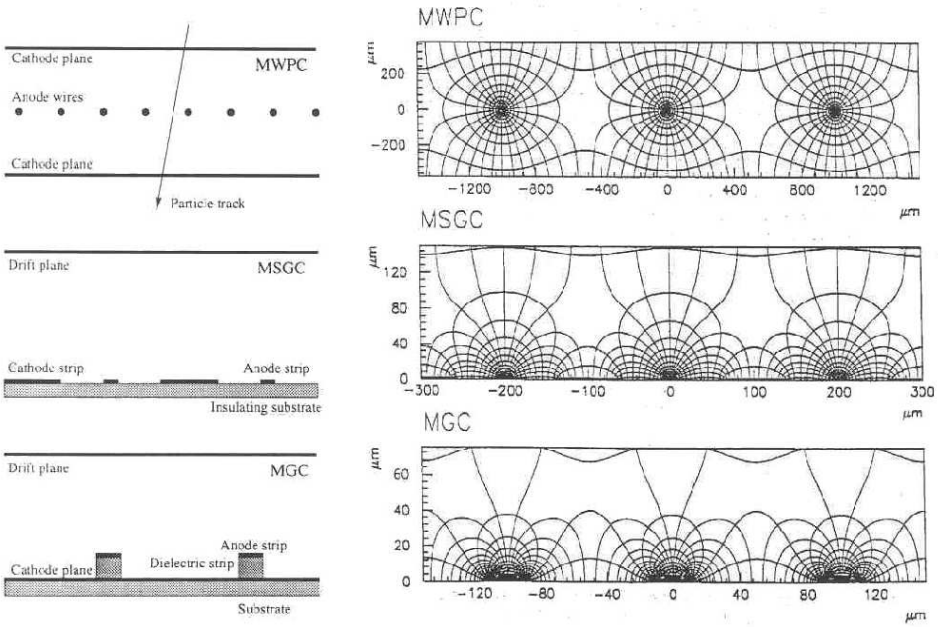

Figure 2.13: Outline of the MWPC, the MSGC and the MGC and the corresponding field configurations. [64] The drawings on the left are not to scale.

2.2.2 The Micro-Strip Gas Chamber

The main limitation of the MWPC lies in the spacing of the wires. As they are sustained mechanically and they exert strong repelling electrostatic forces upon each-other, their inter distance cannot be made much smaller than 1mm. A second limitation is its response time of a few hundred nanoseconds. Therefore the counting rate of the MWPC cannot exceed 10^4 charged particles per cm^2 per second.

To overcome these limitations, A. Oed proposed a detector where the wires are replaced by strips, printed on an insulating surface by photolythographic processes [15]. This detector, the Micro-Strip Gas Counter, is schematically drawn in figure 2.14. It is made up of a thin $(300-500\mu m)$ insulating plate upon which narrow $(7-10\mu m)$ anodes are interleaved with wider $(80-100\mu m)$ cathodes. A few millimeters above the substrate, a drift plane is positioned. This defines the active volume that is filled with the detection gas. The anodes are usually put to ground potential, whereas the cathodes are put to $-500V$ typically. The drift plane is put to a potential around $-3500V$.

When a charged particle enters the active volume it will, as in the MWPC case, ionize some gas molecules. The electrons will drift towards the substrate whereas the positive ions will move towards the drift plane. Close to the substrate ($< 50\mu m$) a strong dipolar field ($> 100kV/cm$) exists and will cause avalanche multiplication. Gas gains of the order of $10^3 - 10^4$were achieved with this type of detectors.

The MSGC detector shows a number of advantages over classical wire chambers:

- Due to the lithographic techniques used, an inter anode distance (pitch) of $200\mu m$ can easily be achieved. A spatial resolution as good as $30\mu m$ was obtained for normal incident particles.

- As the cathodes are very close to the anodes (typically $45\mu m$) the space charge is removed very quickly. The electric field configuration is such that the signal induction is faster in MSGC than in MWPCs. This is demonstrated in figure 2.15 where the fraction of charge collected by the strips is shown for an MWPC and an MSGC as a function of time. It is seen that after $50ns$, 70% of the charge is collected in an MSGC whereas only 25% of the charge is collected in the MWPC case for the same time interval.

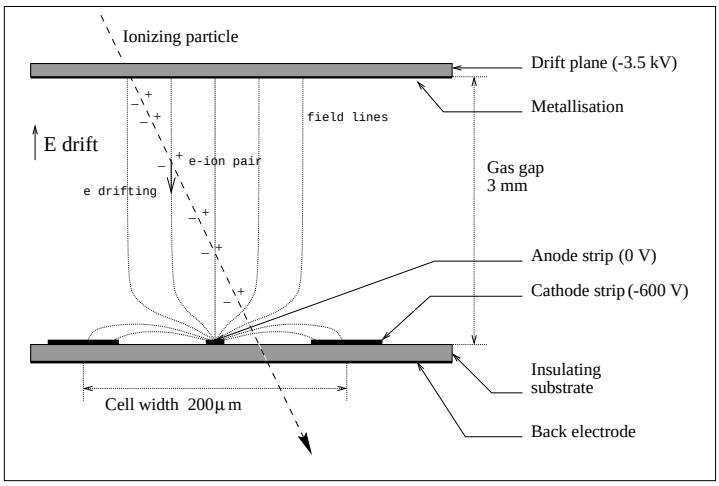

Figure 2.14: Section of the MSGC. Typical dimensions and voltages are indicated on the figure.

- Owing to the high granularity of the MSGC, it can operate up to fluxes of $10^6 Hz/mm^2$.
- Smaller gain fluctuations are achieved with the MSGC compared to the MWPC. This is a consequence of the highly concentrated amplification field.
- When mounted in an experiment, as the position of the anodes is fixed with respect of his neighbors on one substrate, alignment becomes easier.

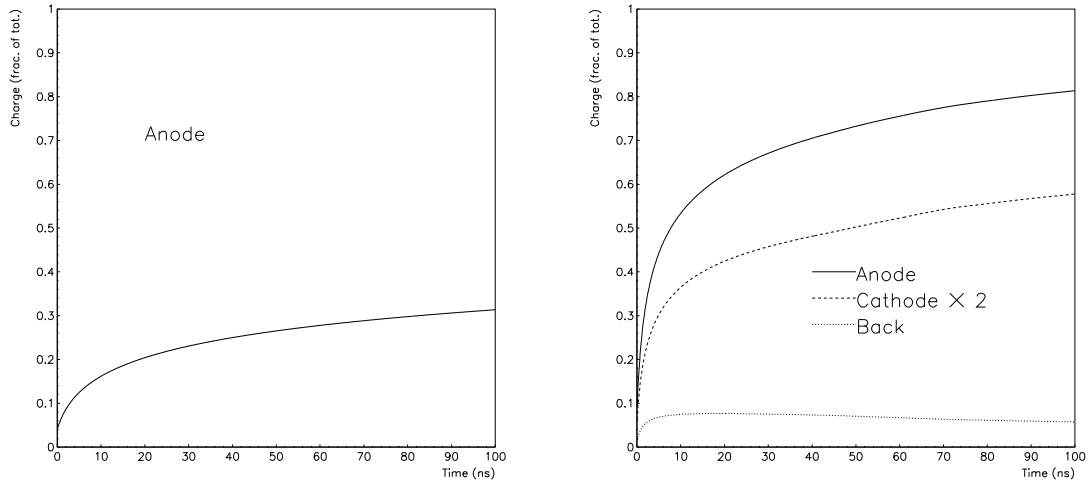

Figure 2.15: Time development of the induced charge on the electrodes of a MWPC (left) and a MSGC (right).

2.2.3 Factors that influence the behavior of the MSGC

Since their introduction in 1988, various factors that influence the behavior of the MSGC have been studied. Since then they have shown promising results as to their ability to operate in a wide range of experiments.

However, due to their sparking behavior under a flux of highly ionizing particles (HIPs) some experiments reconsidered their position towards MSGCs.

2.2.3.1 Substrate

Almost any high resistivity substrate that is flat enough to allow the use of photolythographic techniques can be used to manufacture MSGCs. MSGCs have been shown to work on substrates made of plastic[63], Si plates [60] and glass. However, most MSGCs are made on DESAG D-263 glass that has a resistivity of $10^{15}\Omega cm$. It was chosen for its good surface quality and the availability in different sizes and thicknesses which makes it suitable for high energy experiments. Unfortunately, two problems remain with this kind of substrate: after an accumulated charge of $100mC/cm$ of strip, the gain drops by 40% and more.

A second problem concerns the behavior of the counter under high particle fluences. It was demonstrates for several types of high resistivity substrates that the initial gain of the counter drops when the counting rates exceed $10^4 Hz/mm^2$ (see figure 2.16). This effect is attributed to the charging up of the substrate. Ions can remain trapped on the surface of the highly resistive substrates and under high enough particle fluxes ions can accumulate between anode and cathode in order to alter the local field configuration, hence making the gain drop.

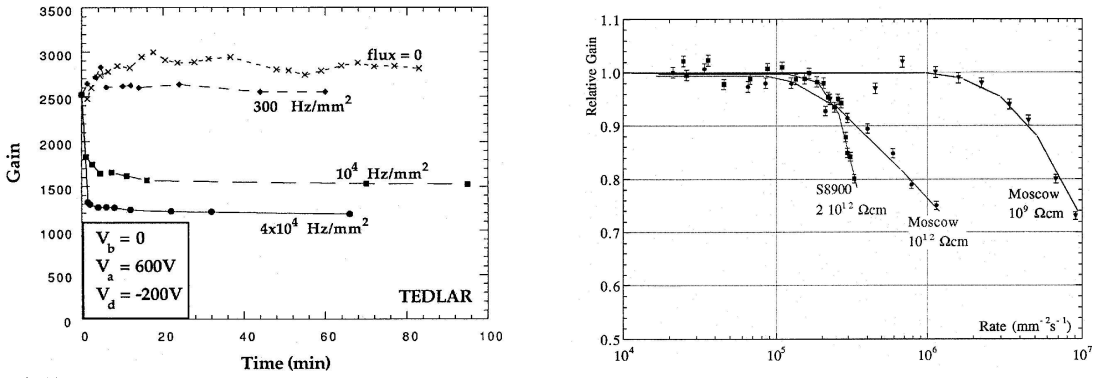

Figure 2.16: Rate behavior of MSGCs a) Gain as a function of time, at various irradiation rates with 5.9keV X-rays, for an MSGC made with a Tedlar plastic substrate of resistivity $10^{14}\Omega cm$. b) Rate dependence of the gain for MSGCs manufactured on several semi-conducting glass plates , having a bulk resistivity between 10^9 and $10^{12}\Omega cm$.

The charging up of the substrate can be reduced by the use of substrates with a lower resistivity. Studies have shown that the rate capability increases as the resistivity decreases. Substrates with a bulk resistivity of $10^{14} - 10^{16}\Omega/\Box$ have shown to be able to cope with particle fluxes up to $10^6 Hz/mm^2$ without a significant gain drop. Low resistivity not only solves the rate problem, it also appears to solve the aging problem as is shown in figure 2.17.

Reducing the resistivity of the glass can be done in several ways. The two main techniques used in MSGC technology are:

- Chemical vapor deposition of thin ($\approx 1500\,Angstrom$) diamond like layers. Several plates with different dimensions have been given a surface resistivity in the range $10^{14} - 10^{15}\Omega/\Box$ in this way. They have shown stable operation up to irradiation doses of $80mC/cm$ of strip and no gain drop until rates in excess of $10^6 Hz/mm^2$.

- Sputtering of electronic conductive glass (f.i. Pestov glass) on normal glass. A layer of $\approx 1\mu m$ is typically sputtered. Equally good results were obtained with this type of coating.

However, the use of low resistivity glass presents some drawbacks:

1. They often contain heavy metals, which increase the multiple Coulomb scattering and thus worsens the tracking capabilities of a detector like CMS.

2. The gain of the detector for a given potential difference is reduced due to the altered field configuration as seen in figure 2.18a). In the right plot of the same figure the electric field

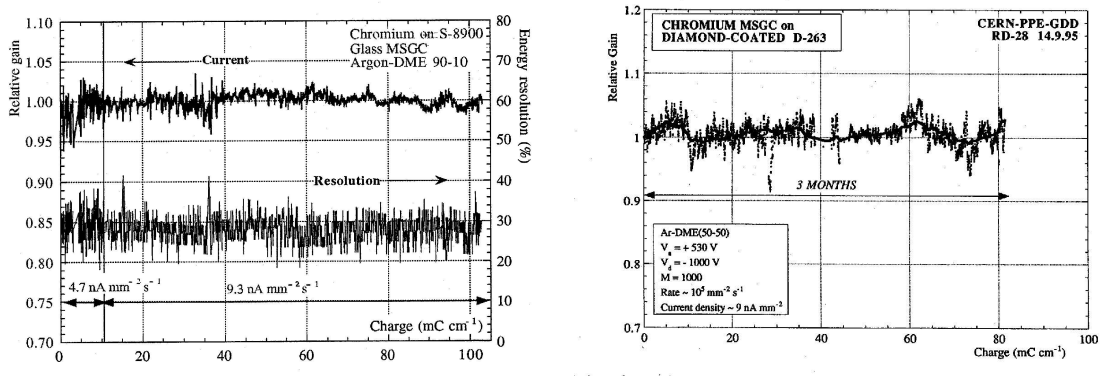

Figure 2.17: a) Relative gain and energy resolution as a function of the accumulated charge per cm of strip, for an MSGC made with S-8900 glass and chromium strips. b) Relative gain as a function of the cumulative charge for an MSGC made on diamond-coated DESAG D-263 glass.

is shown as a function of the distance to the anode. It is clearly seen that the electric field is much reduced in the coated case, thus reducing the gain. For a given gas gain this will increase the energy released when breakdown occurs, hence increasing the probability for breaking the fragile anodes.

3. It is technologically far more challenging to make good quality MSGC on substrates that have been overcoated. Very often the flatness of these coating is worse than the original substrate or the coating may not be able to withstand the chemicals used during the manufacturing procedure.

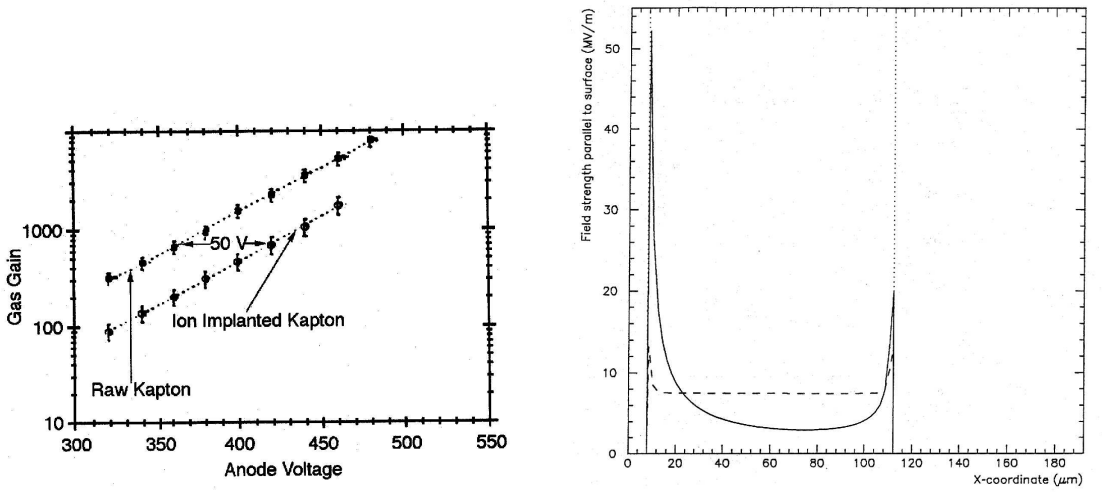

Figure 2.18: a) Gas gain as a function of the voltage difference between the anode and the cathode strips in MSGC made with substrates of surface resistivity $10^{17}\Omega/\Box$ (raw Kapton) and $10^{13}\Omega/\Box$. b) Electric field strength parallel to the substrate a a function of the distance to the anode, for a chamber with a surface resistivity of $10^{14}\Omega/\Box$ (solid line) and for a chamber having a $4\mu m$ thick $10^{13}\Omega/\Box$ resistivity layer on top.

2.2.3.2 Electrodes

Electrodes material, dimensions and shape all play an important role in the short or long term behavior of the MSGC.

The material from which the strips are made has to be chosen with great care. Strips made of Al are known to be subject to fast aging even for low irradiation doses. In [67] a drop of the

gain by 10% is seen after an irradiation dose of 1mC/cm. On the other hand, detectors made with gold strips could sustain irradiation doses up to 50mC/cm strip.

Both electrode width and thickness influence the gas gain. Figure 2.19a) shows the gain as a function of the anode voltage, for different cathode widths. The pitch and the anode width are constant at values of respectively $200\mu m$ and $7\mu m$. Figure 2.19b) shows the dependence of the gain on the anode width. Here the pitch and the cathode width are kept constant at $200\mu m$ and $90\mu m$ respectively. It is seen that the gain is steeply dependent on the anode width. At a cathode voltage of $-500V$, a difference of $5\mu m$ of the anode width changes the gain by a factor 2. The dependence on the cathode width is far less pronounced. To obtain a difference of a factor 2 in gain at $-500V$, a difference in cathode width of $\approx 40\mu m$ is needed.

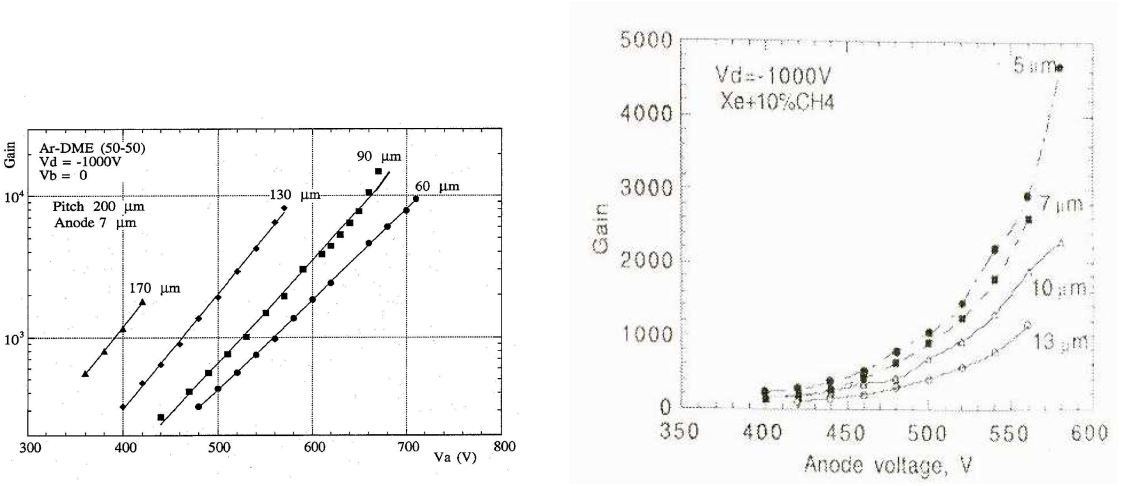

Figure 2.19: a)Gas gain as a function of the anode voltage for different cathode widths and a fixed pitch and anode width. b) Gas gain a a function of the anode voltage for different anode widths an a fixed pith and cathode with.

In figure 2.20, the dependence of the gain on the anode voltage is shown for two different strip thicknesses. The anode width was $13\mu m$, the pitch $200\mu m$ and the cathode width $80\mu m$.

The end of the curves in figures 2.19 and 2.20 was determined by an overcurrent that was measured by an electrometer. Meaning that the detector becomes unstable. The end of the curves thus determines the highest attainable gain for the given electrode configuration.

This means that although a cathode width of $130\mu m$ gives a higher gain for a given anode voltage, the highest attainable gain is a factor 2 lower than for $90\mu m$ wide cathodes. In the case of the anode width, a $7\mu m$ anode is preferred since $5\mu m$ wide anode are too fragile. The strip thickness, however, is often dependent on the photolythographic process used and can therefore not always be changed.

The gas gain is also affected by the pitch. This can be seen in figure 2.21. Fixing the anode width and the gap between anode and cathode leads to an increase of the gain with increasing pitch. This is explained by the increasing number of field lines collected per anode if one increases the pitch, resulting in a higher total amplification. Fixing the anode and cathode widths leads to a decrease of the field in the gap between the anodes and cathodes and thus to a gain drop when the pitch increases. The two effects can be compensated by varying the pitch and the cathode width at the same time following the semi-empirical law developed at the NIKHEF[2] institute[44]:

$$g = p/8 + 20\mu m \tag{2.35}$$

which has since been known as the NIKHEF rule. Herein g is the anode-cathode gap and p the pitch. Both quantities have to be expressed in microns.

[2]NIKHEF: Nederlands Instituut voor Kern- en Hoge Energie Fysica.

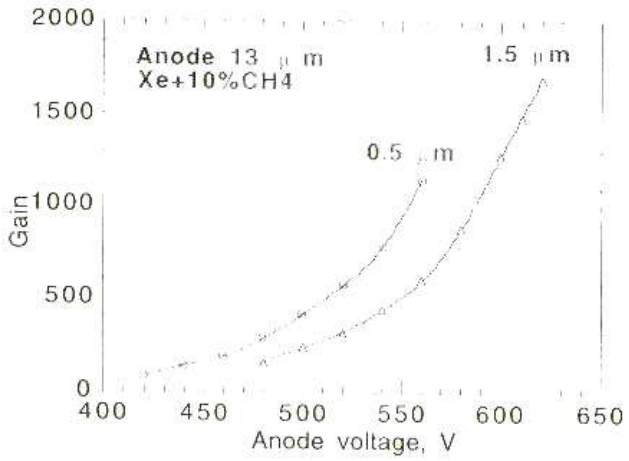

Figure 2.20: Dependence of the gas gain on anode voltage for different strip thicknesses.[?]

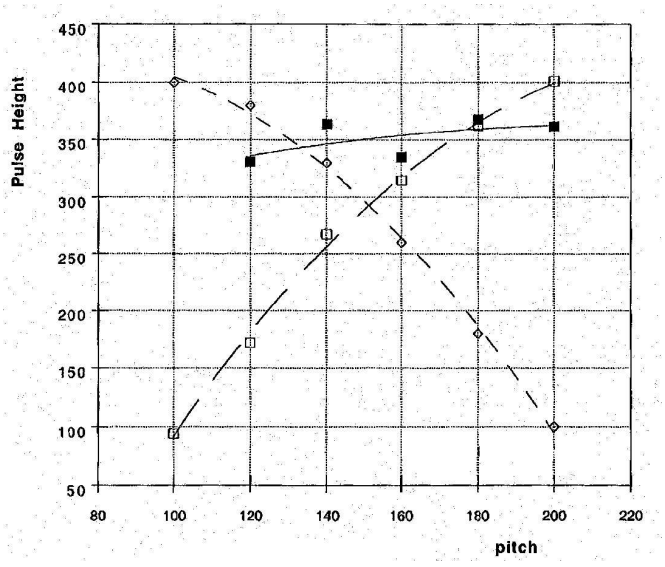

Figure 2.21: Pulse height as a function of the anode strip pitch for different electrodes configurations. Open squares: fixed anode width and anode cathode gap. Open diamonds: fixed anode and cathode widths. Closed squares: fixed width, cathode width varied according to NIKHEF rule (2.35)[44].

2.2.3.3 Gas filling

The choice of the active gas is dictated by several requirements that can change according to the use that will be made of the detector. We will focus on the demands put on the MSGC in a high energy experiment like CMS at the LHC. The detector will have to be able to detect MIPs with a spatial resolution of less than $40\mu m$ in less than $50ns$ as to reduce the pile-up to two bunch crossings. It will also have to cope with the high radiation environment present in CMS for at least 10years. Furthermore, as the MSGC will operate in the 4T magnetic field, a small Lorentz angle is required. These requirements lead to the following requirements on the gas used:

A high primary (n_p) and total (n_T) ionization density. For a 3mm gas layer, an ionization density of 30 electrons per cm gives rise to a theoretical detection efficiency of 99.9%. This restricts the choice of the gas to CO_2, DME, CF_4, organic or heavy noble gases.

The heavy noble gases cannot be used because of photon feedback that will make the detector unstable. A good quenching gas like DME or CF_4 can overcome this problem. However, organic compounds like methane or isobutane lead to fast degradation due to polymer deposition on the strips [67], while long term tests have successfully been performed with DME based mixtures. Therefore, DME was chosen as the main component of the gas mixtures used in the MSGCs for CMS.

Unfortunately, pure DME is not a good choice for a detection gas. It has a relatively low drift speed of $50\mu m/ns$ that is only reached above drift fields of $10kV/cm$. A high field is also needed to get enough gas amplification to detect MIPs (600V). This enhances the probability for destructive sparks. On the other hand, the transverse diffusion is low ($120\mu m/\sqrt{cm}$), leading to a good position accuracy.

Therefore DME based mixtures were investigated. Adding CO_2 to the mixture provides a high drift velocity ($70\mu m/ns$ for DME-CO_2 60/40 at $E_{drift} = 10kV/cm$) and low diffusion ($100\mu m/\sqrt{cm}$) but still needs a high field to achieve sufficient amplification since they are both good quenching gases. Finally, the choice was made for a Ne/DME gas mixture in a 40/60 proportion. This choice was made because the mixture has a drift velocity of $5.5cm/\mu s$ which leads to a charge collection time of 53ns, matching reasonably well with a bunch crossing pile-up of two. The Lorentz angle at $B = 4T$ and $E_{drift} = 10kV/cm$ is 14^o. Furthermore, Ne/DME (40/60) is 98% efficient at a cathode voltage of 530V, i.e. 40V below the pure DME case.

The chosen gas affects the spatial resolution. If one is to obtain a better spatial resolution than $p/\sqrt{12}$ the electron cloud has to be spread over more than one anode. J. Schmitz [45] evaluated the distribution of the ionisation reaching the strip. The R.M.S of the electron distribution reaching the substrate could be modeled according to:

$$\Delta x \approx \frac{1}{2}\sigma_T\sqrt{L}$$

where σ_T is the transverse diffusion coefficient and L is the thickness of the gas volume. Measuring the the position of every electron that reaches the substrate would allow to localize the incident particle with accuracy:

$$\Delta x_N \approx \frac{1}{2\sqrt{N}}\sigma_T\sqrt{L} \approx \frac{\sigma_T}{2\sqrt{n_T}} \tag{2.36}$$

Herein N is the number of electrons and n_T the total ionization density. It shows that the position accuracy is related to the diffusion coefficient and the ionization density. It is not affected by the gas gap in first approximation since the increase in the electron spread for larger L is compensated by the larger electron statistics.

In practice N fluctuates statistically from event to event and the ionization is not spread uniformly along the track leading to a spatial resolution worse than predicted from equation 2.36.

2.2.4 The Gas Electron Multiplier

The main disadvantage of the MSGC is its brittle strips. When operated under normal conditions, the energy released in a spark is often enough to melt part of the anode. A part of the strip is

now detached from the read-out electronics and can therefore not be used any more to detect particles.

Several solutions to overcome these limitations were investigated. They usually consist in dividing the gas gain over two or more amplification stages via the introduction of an amplifying device.

One of these is the Gas Electron Multiplier (GEM) that was developed at CERN by the group of F. Sauli [46]. It consist of a thin ($50\mu m$) polymer foil, metal clad on both sides. The used polymer is often Kapton and the metalisation chosen is a $5\mu m$ thick Cu layer. The foil is then perforated by a regular pattern of holes.

A voltage difference of typically $350V$ is then applied over the Kapton, resulting in fields up to $100kV/cm$ in the holes. The resulting field configuration can be seen in figure 2.22.

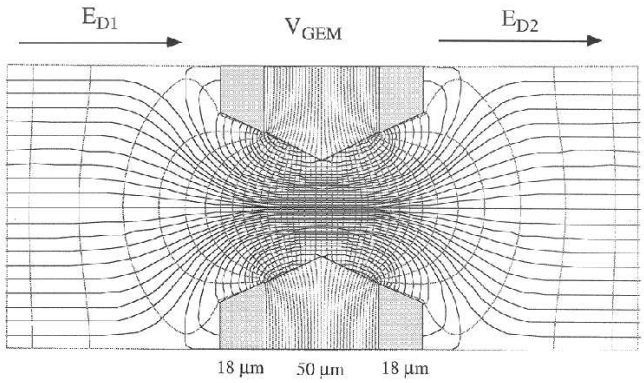

Figure 2.22: Electric field and equipotential lines in a GEM hole.[82]

The GEM foil is inserted into the gas volume as depicted in figure 2.23. Here the GEM is inserted in the middle of the drift volume of an MSGC. It creates two gas volumes: one between the GEM and the drift plane, called the drift volume, and one between the GEM and the MSGC, called the transfer field.

Electrons liberated in the drift field will move toward the GEM foil. Due to the high field inside the holes, a first amplification will occur. The created electrons will drift further toward the MSGC substrate where a second amplification will take place.

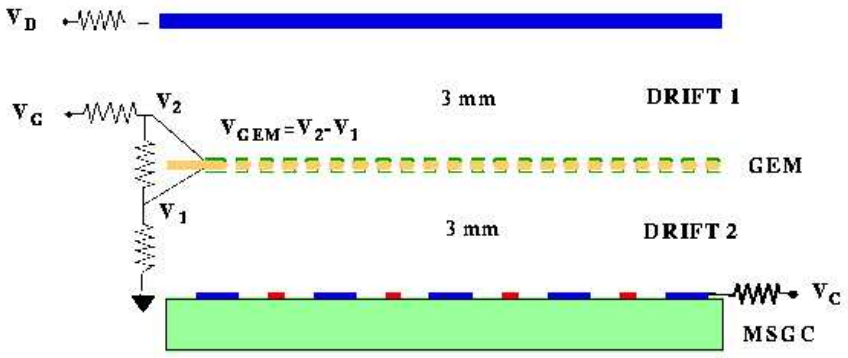

Figure 2.23: GEM foil placed in the middle of the drift volume of an MSGC.

The gain is now shared by the two amplification stages. The voltage on the cathodes can be decreased by more than $100V$, reducing the probability for damaging sparks. In [ref1] it is shown that for a gem potential difference (ΔV_{gem}) of 400V, a cathode voltage of 400V is sufficient to reach 98% detection efficiency. Several authors also report [ref2,ref3] that the spatial resolution attainable with an MSGC+GEM detector is comparable to that of a plain MSGC. Figure 2.24

shows the dependence of the spatial resolution to the angle of incidence of the particle. The MSGC+GEM detectors show spatial resolutions comparable to the ones of the MSGC.

The excellent rate capability of the MSGC are conserved in the MSGC+GEM setup. Particle rates up to $10^5 Hz/mm^2$ have been achieved in Ar/DME mixtures with no loss gain [ref2]. The same authors report an increased maximum attainable gain of the MSGC+GEM compared to the MSGC when exposed to X-rays and α-particles. An increase of a factor 10 in the maximal attainable gain was demonstrated.

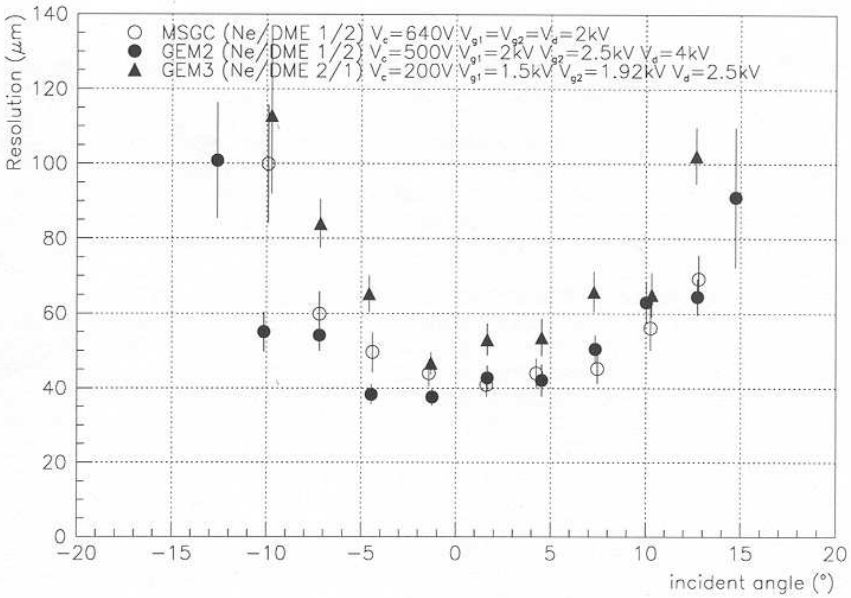

Figure 2.24: Angular dependence of the spatial resolution for 3 detectors, comparing MSGC+GEM detectors to plain MSGC detectors.

Chapter 3

Processing of MSGC substrates

3.1 Introduction

The basis of the MSGC detector is its substrate. It is nearby the substrate that gas amplification will occur. It is its structure of cathodes that are close to the anodes which allows a fast charge collection (70 % of the total charge in $100ns$). This same structure also allows a very good spatial resolution ($40\mu m$).
To obtain these properties, one must put thin metal layers on glass which must have a width of $7\mu m \pm 1\mu m$. It is important that the width of the anodes does not vary too much, as the gas gain is strongly dependent on this parameter as can be seen in fig 3.1.[61] The width of the cathodes is a less critical parameter, as a difference of $30\mu m$ results in only a 10% change in gain in the range of cathode width that we use ($80 - 100\mu m$)[62]. The dependence of the gain on voltage for different cathode widths can be seen in figure 3.2. The pitch was $200\mu m$ and the anode width was $7\mu m$.

These are all fairly standard feature sizes in MCM (multi chip module) technology. Still, it poses a great problem when one tries to have a good quality artwork over large surfaces ($100cm^2$). This is needed to guarantee 98% detection efficiency over the whole surface. It was shown [57] that one missing strip results in only a reduction of 1.5% in detection efficiency and deteriorates the local spatial resolution up to 50% for normal incident particles [97]. The design goal of the MSGC substrates was therefore chosen to be the following: more than 98% of the anodes have to be operational.

Research in optimizing such a process flow was performed at IMEC (Interuniversitair instituut voor Micro EleCtronica) which is located in Leuven, Belgium. The technique used consisted in sputtering a layer of $0.8\mu m$ Cu, then etching the pattern and covering the obtained strips with a gold layer using electroless plating. In this way the desired feature size was obtained.

Moreover, it was possible to make 98% of the total surface defect free as required.

3.2 Processes

3.2.1 Sputtering

Sputtering is a process whereby material is freed and ejected from the surface of a solid or liquid by momentum exchange associated with surface bombardment by energetic particles. A target made out of the coating material is placed into a vacuum chamber together with the substrates. The pressure in the vacuum chamber is typically in the range of 5.10^{-4} to 5.10^{-7} Torr. The bombarding particles are usually Ar ions but could in principle be any particle. The substrates are placed in front of the target so that they can intercept the flux of sputtered atoms.
The most commonly used method for providing the ion bombardment is to fill the evacuated chamber with the working gas and then ignite an electric discharge with the target serving as the cathode. The schematical view of a sputtering device can be seen in fig 3.3.

The fundamental events in sputtering are atomic collisions. It can be seen that a simple

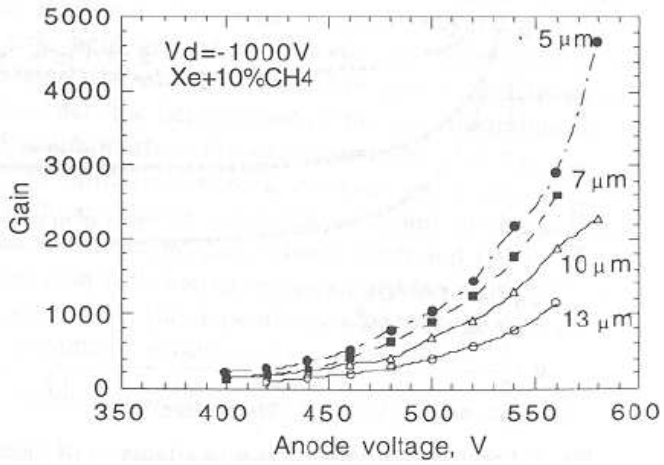

Figure 3.1: Dependence of the gain on the voltage difference between the anode and cathode strips, for various anode widths. The pitch is $200\mu m$.

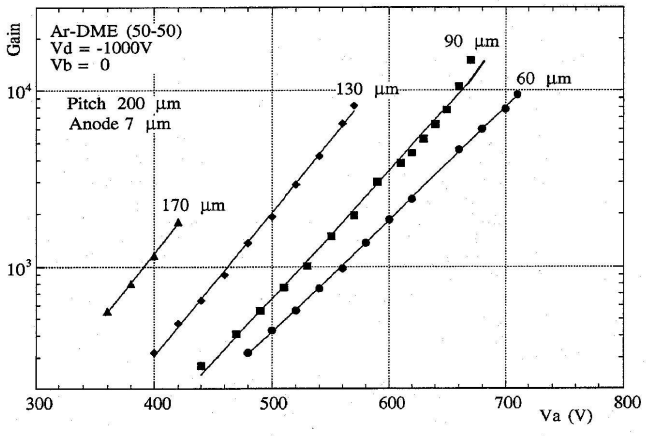

Figure 3.2: Dependence of the gain on the voltage difference between the anode and cathode strips, for various cathode widths. The anode pitch is 200 μm and the anode width is 7 μm.

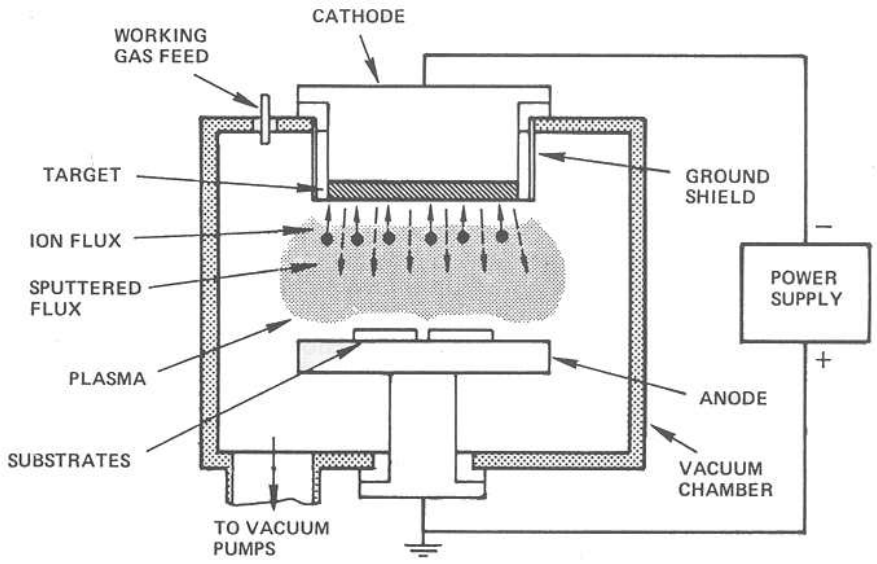

Figure 3.3: Schematical view of a sputtering device.

head on collision, from a particle that comes in normal to the target surface, will not cause the target molecule to be sputtered as this will only drive the atom further into the lattice. At the bombarding energies usually used, sputtering ejection is believed to result from the scooping action as a low energy knock-on passes underneath an adjacent atom, or from a primary knock-on or reflected ion which approaches the surface from within the target and dislodges a surface atom by striking it from below. Both cases are shown in fig 3.4.

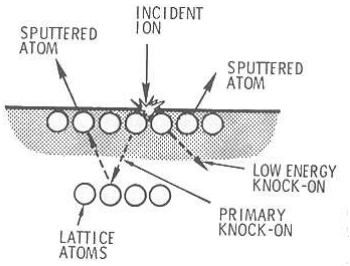

Figure 3.4: Schematical view of the sputtering processes.

3.2.2 Pattern generation

The pattern generation in thin film technology is usually accomplished by either masking during deposition to permit only selected substrate areas to be covered by the film or by uniformly covering the substrate with the film and then selectively removing it to obtain the desired pattern. Other means such as direct photochemical etching or laser-beam shaping also exist, but were not used in this work.

3.2.2.1 Masks

Masks are usually glass plates on which the pattern (or its negative) is scribed upon with chromium. Depending on the photoresist used (see section 3.2.2.2) the pattern that has to be formed on the substrate will be either opaque or transparent on the mask.

3.2.2.2 Photoresists

Photoresist are film-forming materials which undergo marked changes in solubility under the influence of ultraviolet light. Two sorts of photoresists exist: negative and positive resists. A negative resist undergoes, on exposure to UV-light, cross-linking reactions which decreases their solubility in certain solvents. Positive photoresists undergo photochemical decomposition reactions which affects their dipole moments, increasing their solubility in aqueous solvents.

As the resists used were from the positive family, the discussion will only be focused on this. Positive photoresists come in mainly 2 families: the novolak resin based resists and the chain scission polymers based resists (such as polymethylmethacrylate PMMA)

When a hydrophobic Dyazoquinon (DQ) is added to an alkali-soluble resin (for instance phenolic-formaldehyde, better known as novolak (N)), the resin dissolution is inhibited. The photochemical destruction (see figure 3.5) of the inhibitor and the release of uncomplexed resin induces, upon development, the dissolution of the exposed resist. Upon photolysis, the DQ generates a carbene (C) which rearranges into a ketene (K). The ketene reacts with adsorbed moisture present in the resin to form a soluble acid (A).

In polyesters (as for instance PMMA) and polyketones the direct absorption of energy results in Norrish type I and II cleavage of the main chain (figure 3.6) or side chain scission (figure 3.7).

3.2.2.3 Pre-bake

After having spin coated the substrate, a short pre-bake step is needed to partially remove the solvent from the photoresist. This will prevent that illuminated parts of the resist will mix too

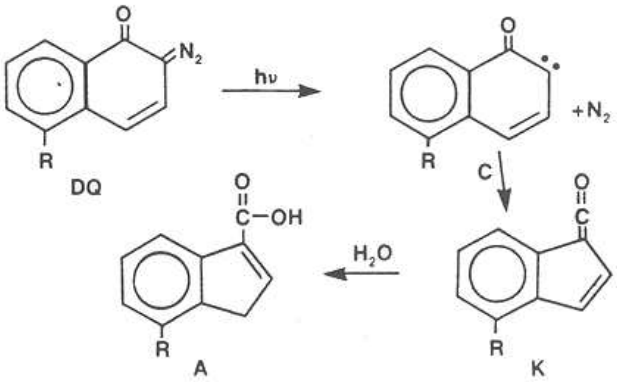

Figure 3.5: Reaction chain that renders the DQN resist soluble by illumination.

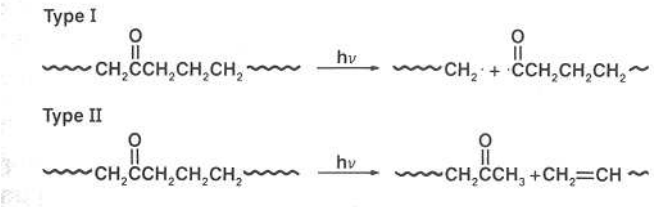

Figure 3.6: Cleavage of the main chain by addition of energy to a polyester or polyketone.

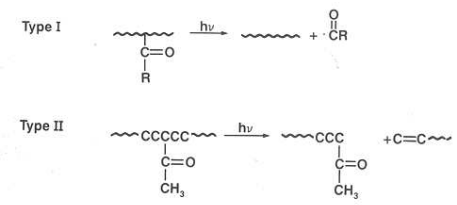

Figure 3.7: Chain scission by addition of energy to a polyester or polyketone.

much with non-illuminated parts due to diffusion. Baking should be done at a temperature between T_g (the glass transition temperature, which is 105^oC for PMMA and between 70^oC and 120^oC for novolak) and the T_d (the decomposition temperature, being 100^oC for diazoquinone, $150 - 300^oC$ for novolak and 200^oC for PMMA). The glass transition (T_g) marks the disruption of intermolecular bonds and is characterized by a change from a brittle glass to a flexible plastic. Baking a polymer such as PMMA above its T_g causes a shrinkage of its free volume, excluding solvent from its intermolecular voids. Above the T_g, the solvent diffuses rapidly out of the film.

Since the used resist was a diazoquinone novolak resin, a pre-bake temperature of 80^oC was chosen. The heating was applied for $5min$ and was carried out immediately after spinning.

3.2.2.4 Exposure

The profile of the resist after development is affected by scattering of the light in the resist. The effect can be seen in figure 3.8. Indeed, scattering will occur outward, resulting in over-development in positive resists and in underdevelopment in negative resists.

The exposure of the resist was done with a strong H_g lamp as DQN strongly absorbs the 365-, 405- and 435nm lines emitted by these lamps.

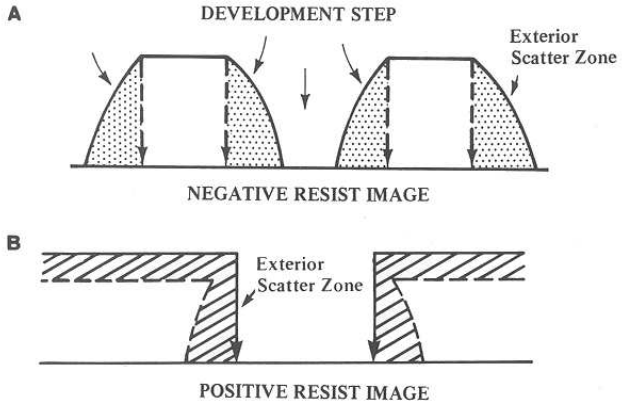

Figure 3.8: (A) Negative image developing inwardly from the outer light scatter zone to the heavily exposed region; (B) positive resist image developing outwardly from the heavily exposed zone into the light scatter zone.

3.2.2.5 Post-bake

After development the film is further hard baked to improve its resistance to the chemicals it will be exposed to. This is again done at a temperature between T_g and T_d but for a longer period. The temperature at which our wafers were hard-baked was chosen to be 120^o and the duration was 2.5h.

3.2.3 Subtractive etching

Subtractive etching involves the selective patterning whereby the region to be etched is chemically transformed into a volatile or soluble species.
These processes can be isotropic or anisotropic. Isotropic etching refers to an etching process which proceeds randomly at a uniform rate in all spatial dimensions. Anisotropic etching results from some deviation from isotropic etching. (see figure 3.9)

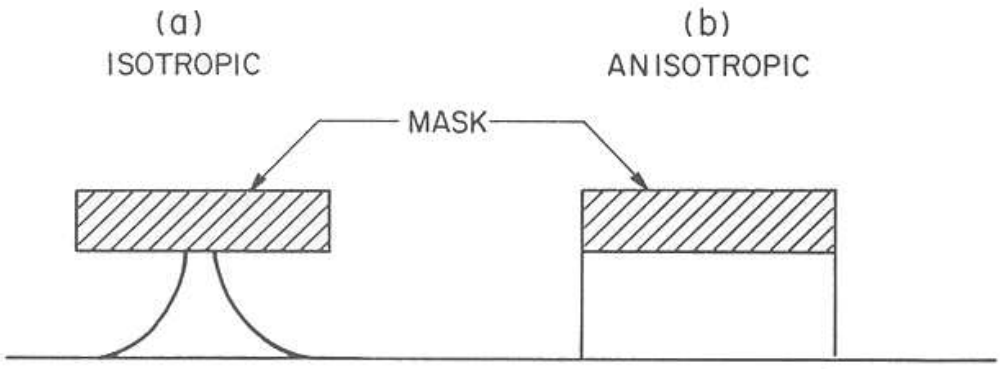

Figure 3.9: (a) Schematic cross section of a layer isotropically etched with a mask over a portion of the layer. (b) Cross section of an anisotropically etched layer.

3.2.3.1 Wet etching

Liquid etching involves oxidation-reduction reactions for metals and displacement (acid-base) reactions for inorganic oxides.

In the liquid state, metal etching involves many electro-chemical principles. The metal acts as its own anode, a chemical effect which induces passage of current: $M- > M^{n+} + ne^-$

Since most metals are covered by an oxide, a secondary etchant has to be added to etch the passivating layer.

Many oxidizing agents of the inorganic type are known. The most common agent is H^+. The most commonly used etchant for Cu are: Hydrochloric acid (HCl), Ferric chloride ($FeCl_3$) or nitric acid (HNO_3). For Ti wet etching a dilute hydrofluoric (HF) acid is mostly used.

3.2.3.2 Dry etching

As in the sputtering process (see section 3.2.1), dry etching is performed using ions which are accelerated in an RF field and thus produce a plasma. The main difference, however, is that the etching process is in many cases chemical. Ions reaching the species to be etched react with this last to form a volatile species, which is then evacuated through the vacuum system. Commonly used etchants are O_2 and CF_6.

Physical etching also exists and here the ions are merely knocking the target molecules away, which are then also evacuated via the vacuum system.

Both chemical and physical dry etching require a positive mask.

3.2.4 Electroless plating

Electroless plating is an autocatalytic process characterized by the selective reduction of metal-ions only at the surface of a catalytic species. Therefore the species is immersed into an aqueous solution of solid metal ions.

3.2.4.1 Ni plating

The plating of the Ni is done by the following redox reaction:

- Oxidation of the reducing agent: $H_2PO_2^{2-} + H_2O- > H_3PO_3^- + 2H^+ + 2e^-$
- reduction of the Ni: $Ni^{2+} + 2e^- - > Ni$

The overall reaction then reads: $Ni^{2+} + 4H_2PO_2^- + H_2O- > Ni + 3HPO_3^- + H^+ + P + \frac{3}{2}H_2$ as the electroless plating of Ni is accompanied by hydrogen evolution. The reaction also involves

the creation of phosphorus which is also plated. After plating we will have a Ni-P alloy in which the P is present for about 8-10% by weight.

A Ni plating bath should thus contain the following constituents:

1. A source of Ni ions: $NiSO_4$.
2. A reducing agent: $NaH_2PO_2 : H_2O$ (sodiumhypophosfite).
3. Stabilizers.
4. Energy given in the form of heat: the solution is kept at a temperature of 90^0.

Unfortunately, Cu is one of the metals that will not catalytically initiate the hypophosphite electroless Ni reaction. To render the Cu surface catalytic it is first immersed into a dilute palladiumchloride solution.

3.2.4.2 Au plating

Gold plating happens via a galvanic displacement reaction which is often called immersion process. The redox reaction reads as follows:

- oxidation of the Ni: $Ni- > Ni^{2+} + 2e^-$.
- reduction of the Au: $Au^{2+} + 2e^- - > Au$.

As soon as the Ni surface is immersed into the Au bath, the Ni atoms are dissolved and are spontaneously replaced by Au atoms from the solution. As soon as the reaction starts, the surface of the Ni substrate becomes a mosaic of Ni and Au atoms. The process continues until the entire Ni surface is covered with gold. Due to the nature of the process the thickness of the deposited layer is limited to $\approx 0.2\mu m$ of Au. The source for Au ions was $KAu(CN)_2$ (potasiumgoldcyanide).

The growth of both Ni and Au in electroless plating as a function of time are represented in figure 3.10.

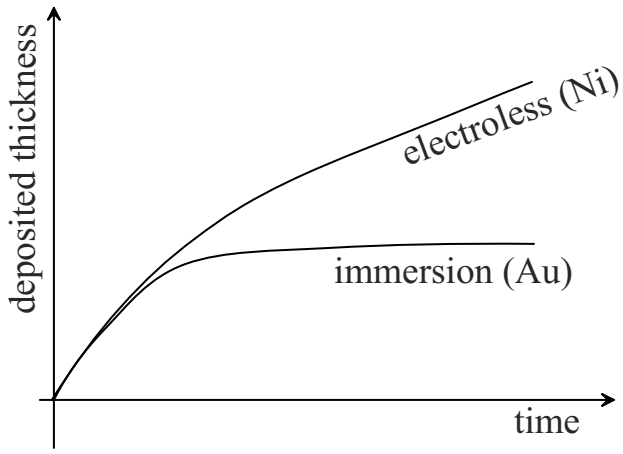

Figure 3.10: Thickness of electroless plated Ni and Au layers as function of immersion time.

3.3 Optimization of the process flow

3.3.1 Feature size

In order to obtain the correct feature sizes on the wafer after completion of the whole process, one has to take into account the underetch from the etching procedures (both from the development of the mask as from the etching of Cu and Ti layers) as well as the side growth due to the

electroless plating in the design of the mask that will be used.
To ensure this, preliminary measurements were performed on a mask containing test structures. These test structures contained meanders and strip like formations of different widths and distance between the structures. This was done to make sure that the measured parameters are not feature size dependent. The feature sizes ranged from $10\mu m$ to $60\mu m$. The different structures were repeated over the whole surface of the $6\,inch$ wafer in order to test the uniformity of the used process.
Figure 3.11 shows the difference between the feature size on the wafer after the complete processing of the wafer compared to the one on the digital file used to create the mask. This value represents twice the underetch. The measurement was performed using a laser probe which uses the refraction of light on the surface to measure height differences on the wafer. An example of this is given in figure 3.14. This machine has a precision of $0.05\mu m$ in the z-direction and $0.5\mu m$ in the x and y directions as the movement in these directions is mechanical. The width of the features was taken to be the width at half height.

As can be seen in figure 3.11, slight differences in underetching can appear from wafer to wafer. The underetch does not seem to depend too much on the feature size on the mask (see figure 3.12).

As seen in figure 3.13 the spread occurring in the line width can be explained by the consecutive errors introduced during the entire process. We can see that the resulting etched product (E) contains the image distortion of the mask ($\pm 0.1\mu m$), the resist bias ($\pm 0.5\mu m$) and the final etched bias of $\pm 1.0\mu m$ with a tolerance of $\pm 1.0\mu m$ meaning that differences up to $1.6\mu m$ in line width are to be expected. Including the measurement error of $0.5\mu m$, a spread in the measurement of the underetch of $1.6\mu m$ can be expected.

Finally, a mean feature size deviation of $2.09\mu m$ with a standard deviation of $0.91\mu m$ was ascertained. This converts to an underetch of $1.04\mu m$. The smaller measurement error compared to the computed one probably originates from an overestimate of the error of the etch bias.

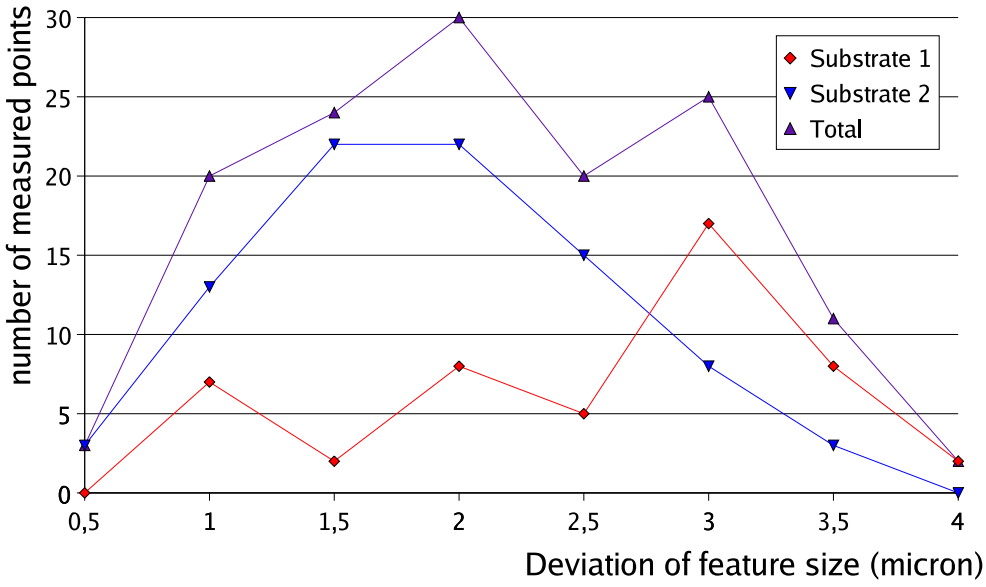

Figure 3.11: Difference of the feature size on the wafer compared to the feature size on the mask for 2 different substrates.

3.3.2 Cleaning of the glass substrate [91]

It is of common use in Si technology to clean the wafers in the first processing step. As the Si wafers arrive pre-cleaned and are shipped and packed in a clean-room compatible way, spraying the wafer with acetone is enough to remove any dust or handprints that might be on the wafer.

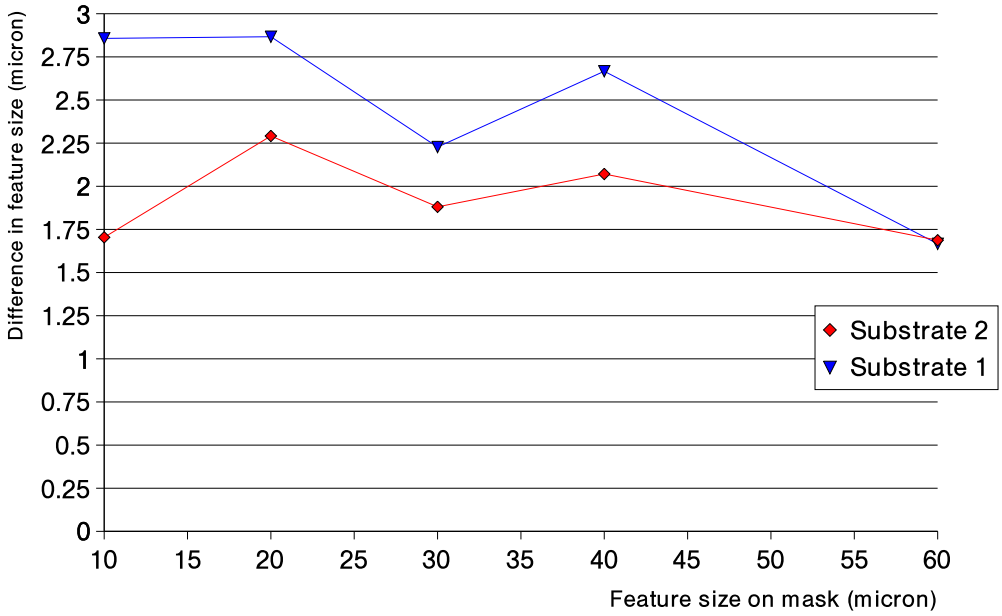

Figure 3.12: Difference of the feature size on the wafer compared to the feature size on the mask for different feature sizes present on the mask.

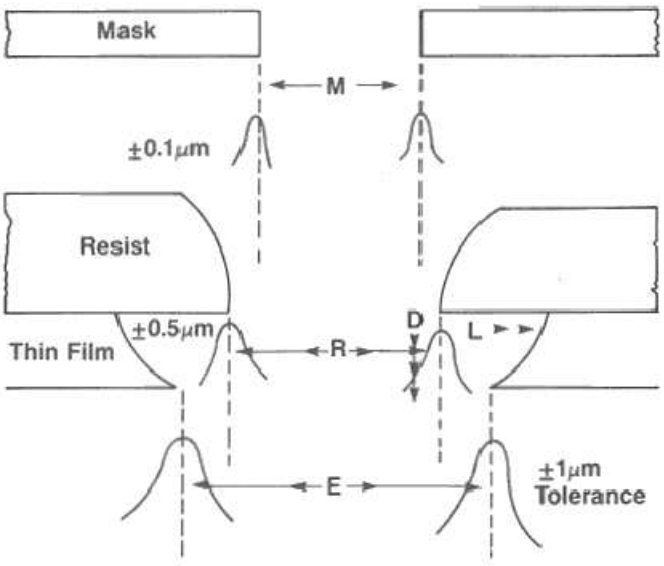

Figure 3.13: Etch bias in transfer of the image from the resist into the substrate by isotropic etching.

This is not true for glass plates. The standard glass production does not include extensive cleaning of the substrates nor the shipping in materials that do not leave residues onto the glass. Therefore a more sophisticated procedure had to be developed.
The proposed method consists of three steps:

1. First the glass plates are immersed into a bath composed of tridistilled water and a neutral soap (Extran MA02). They are left in this bath for at least 12 hours after which ultra sound energy is put on for 30 min.
   Big, loose particles, coming from the material in which the wafers were packed, are removed in this way. However, eye inspection shows that after this step particles remain on the surface of the wafer.
   This step was performed in a non clean-room environment. But during further processing no indication was found that this was a problem.

2. The next step was performed in a class 1000 clean-room. The wafers are put in a bath composed of H_2SO_4 and H_2O_2 in a 4:1 proportion. The wafers are left herein for about 5 min. and are then extensively rinsed with water in order to make sure that no trace of the solvent is left on the surface. This step removes grease and some oxides.
   Caution is however needed in this cleaning step as the acid solution used is known to etch the glass.

3. The last cleaning step consists of the immersion of the substrates into an alkaline bath consisting of H_2O, H_2O_2 and NH_4OH in a 10:3:1 proportion.
   This step removes any left traces of fat. Again, the wafers are rinsed extensively with water and then dried with a flow of N_2 gas. A last dehydratation step is applied to remove traces of water that cannot be removed with N_2 alone. For this the wafers are placed in an oven at 100^0C for 45 minutes.

After these steps the wafers are clean. Only indirect prove of this is available. A first check is optical: no visible traces are left on the substrate. The second one is of more importance: if a good adhesion is to be guaranteed between wafer and the thin film metalization that will be put onto it, the wafer has to be very clean. Never have we experienced any adhesion problems between the wafer and the metalization put onto them with wafers cleaned as described above. This indirectly justifies the method.

3.3.3 Sputtering

Cu sputtering was first performed in an Alcatel 810 machine which is a magnetron sputtering device. A gas flow of 100sscm Ar^+ ions is accelerated in a RF field.
A first RF step is performed to remove the possible oxide layer onto the targets surface. This is performed at a pressure of $2.10^{-2}mbar$ and a power of $400W$.
As Cu does not adhere to well to silicides, a first layer of Ti is sputtered onto the substrate. This is done at a pressure of $1.10^{-2}mbar$ and a power of $400W$ for $45s$. This deposits a layer of approximately$300nm$.
Upon this layer the Cu layer is then sputtered. This is done at a pressure of $8.10^{-3}mbar$ and a power of $3000W$ for a duration of $1min\,35s$. As can be seen on fig 3.14, a Cu layer with a thickness of $0.8\mu m$ is sputtered in this way (dashed line).

However, this device has some flaws. By eye inspection, it could clearly be seen that after sputtering, a lot of 'particles' were present on the surface. This resulted in defects after etching. Figure 3.16.a shows a general view of the substrate after plating. The picture is taken with the SEM (scanning electron microscope) technique. The dimensions of what can be seen in picture 3.16a is $4.5cm$ x $3cm$. A lot of these particles are present on the substrate. A more detailed view of one such 'particle' is given in figure 3.16.b. A distance of $0.5cm$ on the picture corresponds to

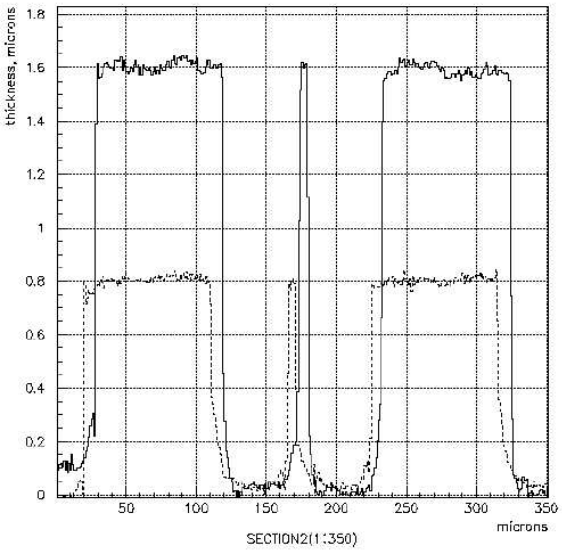

Figure 3.14: Thickness of the layers. The lowest profile (dashed line) is taken after Cu sputtering and wet etching, the highest one (full line) after plating.

$10\mu m$. As can be seen, the typical dimensions of the particles is of the order of tens of microns. X-ray analysis of these particles revealed a high Si content (see figure 3.15). This can be explained in two ways. Prior to the appearance of the particles the vacuum chamber of the machine had been cleaned with a sand beam under high pressure. This is a standard cleaning procedure. The small size particles could thus be sand. However, as the size of the e^- in the SEM machine is of the order of $1\mu m^2$, it is easy to miss the particle and to include part of the glass in the analysis. As was found later on, what is seen in figure 3.15 is most probably coming from the substrate. A, much later performed, cleaning of the palettes on which the substrates are fastened made the problem disappear almost completely. Flakes of Cu present on these plates by deposition due to the extensive use of these plates were being ripped off by sputtered Cu particles.

An additional difficulty in the operation of the Alcatel sputtering machine comes from the securing and fastening of the substrates. As the Ar plasma reaches high temperatures, the heat must be removed from the substrate. This is done by mechanically pressing the substrates against a heat conducting pad. The substrates are secured by 3 metal pieces that are screwed tight. This action is very delicate. In the process an average of 10% of the wafers was lost during this step.

While the Alcatel was being cleaned and re-cleaned, a new solution was found in the LLS sputtering machine. On this machine, 24 wafers are sputtered at the same time and no screwing is needed since the wafers are vacuum sucked to a plate that is inserted into the machine. The properties of the sputtered layer are exactly the same as the ones obtained with the Alcatel. Therefore it was decided to do the further processing with this machine.

3.3.4 Spinning of the photoresist

Spinning of the photoresist is a crucial step in the processing. Any dirt particle remaining on the substrate can have its consequence.

But new errors can be introduced at the spinning stage and are called pinholes. Their origin can be very different in nature: physical contact of the resist surface with another surface, particles being dislodged during development or even air bubbles in the resist can be the cause [92].

Reduction of the number of pinholes is mostly a matter of preventing the pinholes to appear, as removing them is not possible. Several things can be done. Among them are:

1. Use the thickest resist as possible. (see figure 3.17)

2. Thoroughly clean surface, chemically and physically.

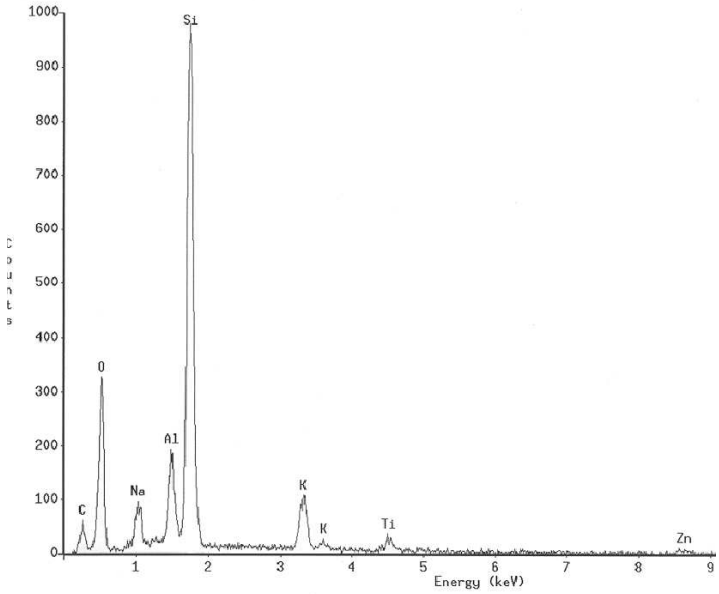

Figure 3.15: X-ray analysis of the particles present on the substrate after sputtering with the Alcatel 810.

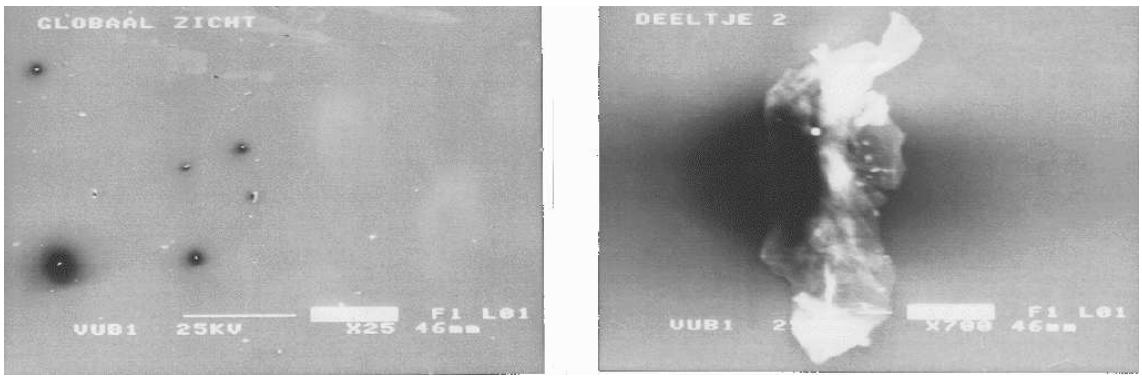

Figure 3.16: Left: SEM picture taken of the surface of the substrate after sputtering in the Alcatel 810. Lots of particles are visible. Right: zoom of the left picture on one of the particles.

3. Reduce particles and contaminants in coat area. (see figure 3.17)

4. Use highest prebake to melt resist.[94]

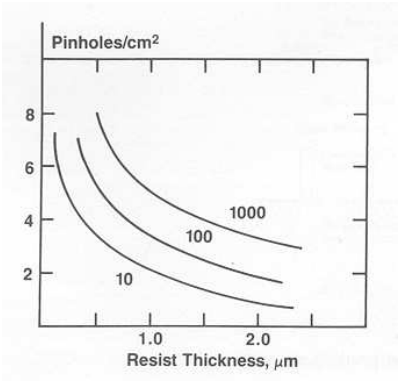

Figure 3.17: Pinhole density as a function of resist thickness for different classes of clean-rooms.

Some of these solution were tried. A thorough cleaning of the glass substrate was discussed in 3.3.2. The spinning of the photoresist was carried out in a class 10 clean-room, which is the best one available at IMEC. During the optimization, the choice was made to go from a $1\mu m$ photoresist to a $2\mu m$ photoresist.

Standard photoresist processing simply pours the photoresist on the wafer, which is then spun. This technique however introduces defects in several ways. First, the sides of the bottle from which the photoresist is poured have to be cleaned. In this way, fibers from the cleaning tissue can remain on the sides of the bottle, ready to be introduced on the wafer the next time photoresist is poured onto a wafer. Second, due to the pouring, air bubbles can get trapped underneath the photoresist, which will not be spun off the wafer, nor get baked out at the pre-baking step.

To counter these effect, a pouring device was made. A flexible tube was mounted on a bottle with a hole at the bottom. The photoresist was thus guided through the hole in the bottle, via the tube onto the substrate. This did not decrease the number of pinholes dramatically, however, in this way the amount of photoresist poured on the substrate could be controlled and thus less photoresist was lost, as the thickness of the layer of photoresist that will be left on the substrate is only a function of the rotation speed and the viscosity of the photoresist[96].

A longer prebake is not advised as problems to remove the photoresist completely were already encountered at normal prebake lengths (5min at 100^0) (see section 3.3.5)

3.3.5 Removal of the photoresist

The removal of the photoresist is done in 2 fazes. First the wafers are immersed into an acetone bath and next into an IPA (iso propyl alcohol). These baths dissolve most of the photoresist. The wafer is then rinsed with water. To remove some very sticky parts of photoresist, the wafer is placed for 20s into a RIE (Reactive Ion Etching) machine with an O_2 plasma.

Figure 3.18 shows part of the strips after plating. A halo next to the strips is seen. This halo is formed after the removal of the photoresist with RIE. Although it is less clearly visible at that moment. As the electroless plating is growing on any trace of Cu, the halo is enhanced in this step.

The halo comes from resputtering of Cu due to the O_2 plasma. Different approaches were tested: removing the RIE step, diminishing the power of the RF field or changing the gas used for the plasma. An optimal was sought between resputtering and total removal of the photoresist. This last condition is mandatory as parts covered by photoresist will not be plated.

Attempts were also made to reduce the baking of the developed photoresist. This gave rise to a substantial increase of the underetch. Making a new mask and including the new factors could

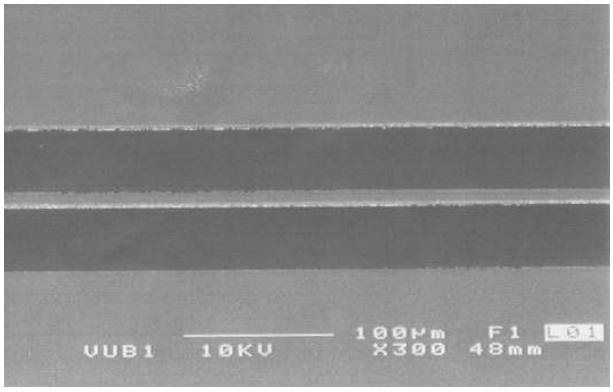

Figure 3.18: SEM picture of a strip taken after Au plating. The halo is clearly visible on the side of the strips.

be a solution.
It was found that removing the photoresist in an acetone and IPA bath while applying Ultra Sound energy is able to remove all traces of photoresist without any unwanted side effect. Using this method gave remarkably good results. No more traces of photoresist were present

3.3.6 Etching of the metal

Etching is mainly a timing problem. An optimum has to be found between a complete etching and underetching. As in some parts of the wafer the Cu is still being etched, in other parts underetching can already start.

3.3.6.1 Cu etching

The Cu etching was performed in an acid bath. The etching time is strongly dependent of the acid concentration in the bath. Due to this, the etching time is dependent on the history of the bath. As it is a rather slow etching (duration is 8 to 10 minutes), the optimal etching time must be tuned during the etching of the substrates. It was found that the only way to achieve a good etching with the correct underetch factor is to closely monitor the etching of the first substrate under a microscope. This is done until no more traces of Cu are left on the substrate. The moment to perform the first check can easily be timed as Ti and Cu have very different colors. This first check should thus be performed when the gray metallic color of the Ti starts to emerge from under the brown Cu color in the areas to be etched.

Also the orientation of the substrates deserves special attention. When the substrates are inserted horizontally into the etching solution, the etched Cu moves down due to gravitation and re-attaches itself to the substrate in lower positions. This effectively thickens the Cu layer as one moves down the substrate and can be seen visually. This effect happens independently of the orientation of the strips relative to the gravitational field. The substrate should thus be inserted vertically into the solution. To avoid local (uniform) redeposition, the wafers have to be agitated while immersed in the solution, in this way evacuation of the etched Cu is guaranteed. Wafers etched in this way were etched uniformly over the entire surface.

3.3.6.2 Ti etching

Ti etching was performed in a buffered HF solution. As the Ti layer was very thin, the immersion time was only $30s$. Due to this, underetch was starting even though the whole surface to be etched was not stripped of Ti. This is a very important point since Ni plating will start on any traces of Ti left on the substrate and so increasing the probability for defects. But as underetching starts rather rapidly, anodes could come loose.

Furthermore, some processing tests were done on glass that had been coated in different ways. This coating reduces the surface resistivity of the glass from $10^{17}\Omega/square$ to $10^{14}\Omega/square$.

Wafers coated with Aluminum nitride were not able to withstand the HF bath as 'pearls' of coating were visible after this step. On the contrary, wafers with a 'Diamond Like Coating' (DLC) did not show any sign of degradation.

To overcome these problems, a dry etching of the Ti layer was tried. The photoresist is first removed and thus the Cu acts as a mask for the Ti etching. After this a quick (2-3s) immersion in the buffered HF solution is done to remove the last traces of Ti. This method gave good results and was then adopted in the standard procedure.

3.3.7 Plating

Cu in contact with air oxidizes. Wafers processed a few hours before plating already show signs of this (mainly visible through a change in color). This oxide layer has to be removed. This is done in a 10%HCl solution. The wafers are left in this bath for $10 - 20s$. Then they are rinsed with water.

As Ni does not autocataliticly plate on Cu, the substrate is immersed in an SMT Pd solution, which is an industrial standard, for $15 - 20s$ and are then rinsed with water.

Next the wafers are plated with Ni. The composition of the bath was as follows:

- Ni: 6g/l
- Natriumhypophospite: 30g/l

This bath is kept at a temperature of 88^0C and has a pH of 4.8. The bath is continuously agitated both via a mechanical movement of the wafer and air inlet via the bottom of the container. In this bath, Ni is deposited at a rate of $5\mu m$ in $15 - 20min$. As our aim was to grow $1\mu m$ of Ni, the wafers are left in the bath for $3 - 4min$.

At some occasions wild-growth of Ni over the entire surface was observed. When changing the rinsing of the substrate from quick dump rinse (QDR)[1] to water spraying, the problem disappeared. This effect is due to traces of Pd remaining on the glass surface even after a QDR but who are apparently removed when one sprays the water directly on the substrate.

Au plating is done in a next bath containing a Au concentration of $4g/l$ provided by potassiumgoldcyanide ($KAu(CN)_2$). The pH of the bath is 5.8 and it is kept at a temperature of 90^0C. Again, agitation is performed. This time via mechanical movement and N_2 inlet. The thickness of the Au layer as function of immersion time for this particular bath can be seen in figure 3.19[95].

Usually the first two or three wafers in a batch were plated in a satisfactory way. On the third or fourth wafer gold droplets started to appear on the sides of the anodes and cathodes. Adhesion of the Au to the Ni layer started to become worse. The Au layer was literally falling off the Ni layer as it was taken out of the plating bath. This effect was visible through the change in color of the substrate (from yellow gold to metallic gray).

The effect turned out to be a Au concentration problem which was detectable via a pH measurement. As the first wafers were being plated, the Au concentration was decreasing as was the pH. This resulted in the formation of Au lumps that adhered to the side of the strips and a change in the adherence properties of the Au. A careful monitoring of the pH of the solution and addition of new $KAu(CN)_2$ if needed proved to be the key to successful plating. In this way batches up to 8 wafers could be processed faultlessly[2].

An advantage of using electroless plating compared to other ways of processing like lift-off comes from the fact that electroless plating naturally rounds of edges. This can be seen on figure 3.20 which is a SEM image taken from the end of one anode after gold plating. This is an interesting feature for an MSGC since discharges between anodes and cathodes are believed (ref) to be started in the high electric field that exists near the edges of the anodes. By rounding them off, the electric field should be lowered.

[1]The quick dump rinse consist in immersing the substrate in water and then emptying the recipient from the bottom. Hereby all the impurities that were dissolved in the water are removed an a faster cleaning is attained.

[2]This method can surely be applied to a larger amount of batches, it was however not tried by us.

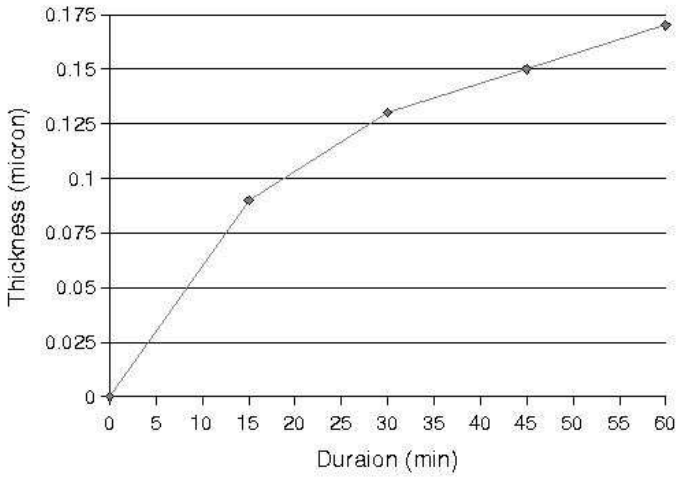

Figure 3.19: Au layer thickness as a function of immersion time in the gold plating bath used at IMEC.[95]

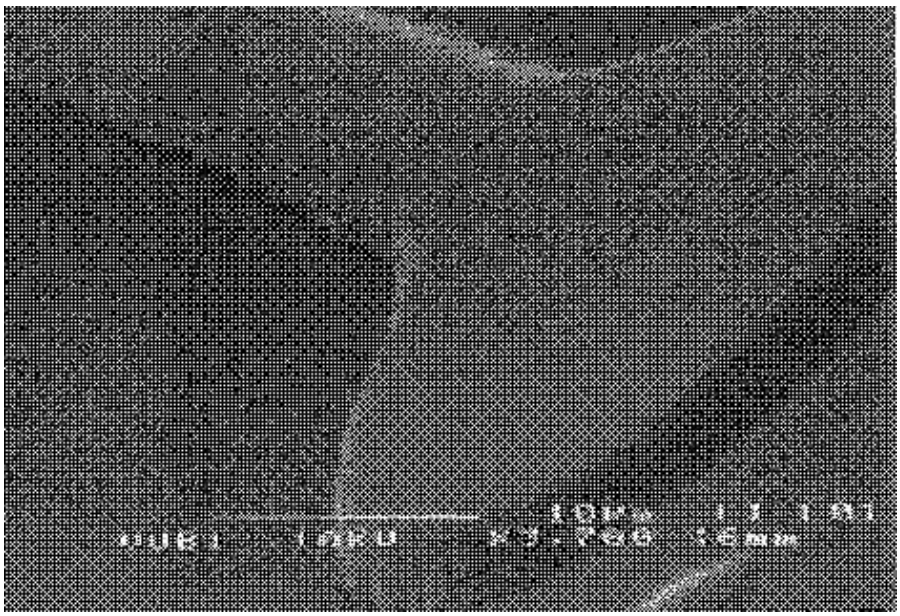

Figure 3.20: Round of edges due to electroless plating.

3.3.8 Dark current

After completion of the procedure, the wafers were tested on their HV behavior. These tests were done in the 'aquarium'. This is a glass box which is filled with dry N_2. The cathodes are then connected to the HV supply and the anodes are grounded (see figure 4.8). The dark current is defined as the current that flows between anode and cathode in the absence of any irradiation. This dark current for a substrate of 512 anodes with a length of $10cm$ should be of the order of a few nA.

This current was measured and was found to be of the order of mA. However, applying the HV for a longer period of time made the dark current decrease. Also wafers that went to an extra processing step to passivate the edges of the cathodes with BCB (Benzo Cyclo Butheen) did not seem to suffer from this defect.

The explanation resides in the chemicals used in the plating bath which are not easily removed from the substrate and thus form a high Ohmic short circuit.

Repeated cleaning of the wafers with water, IPA and acetone was also able to reduce the dark current. This is a time consuming (1day), dangerous (wafers are easily broken in this way) and not totally satisfactory procedure as the dark current was still of the order of $10nA$. As the passivated wafers were unaffected, a treatment of the substrate with chemicals used during this step was tried, unfortunately without success.

The solution to this problem revealed to be an additional post baking step in an oven with a N_2 atmosphere. The substrates were placed into the oven, which was heated to a temperature of 230^0C, for a period of $8\frac{1}{2}h$. This method reduced the dark current to normal levels without the risk of breaking the substrates.

3.4 Optimized process flow

3.4.1 General considerations

First of all care should be taken to have a conscious, clean and rigorous working method. This manifests itself in different ways as described in this section.

Since the glass plates are only $300\mu m$ thick, they are easily broken. Plates that thin, even bend due to gravitation when taken at one side and held horizontally. Special attention is thus required when handling them. When moving them (for instance to be inserted into a machine) the wafers are easily broken due to strain put on them by the tweezers used for this purpose. Putting less strain however makes them slide out of the tweezers. A delicate balance had thus to be found. Wafer handling is the main source of broken wafers. Fortunately, growing expertise was able to reduce the percentage of broken wafers from $10-15\%$ to 1%.

Great care should also be taken to remove all dust (or other) particles on the wafer that were introduced between 2 processing steps. Any such particle bigger than $1\mu m$ can give rise to a defect on the MSGC. Therefore one should blow over the substrate with an N_2 flow before every step in order to remove them. If evidence is found of remaining particles (by eye inspection) this step has to be repeated. The N_2 should also be kept almost parallel to the wafer. Normal incident flow represents a strain that can cause the wafer to break.

A last point of attention is to avoid that the top side of the plates touches anything unwanted during the whole processing. The first wafers processed were awful due to scratches affecting several anodes. These scratches were introduced by inadvertently rubbing with our sleeves over the photoresist. An attempt made to scratch a number in the Cu to identify the wafer later on, lead to a disaster because the removed Cu flew all over the wafer. All deposited Cu was plated later on leading to shorts and islands (pieces of metalization in the open space between anodes and cathodes).

Not only the wafers but the mask itself must remain impeccable. At the illumination stage, the mask is brought at a distance of $50\mu m$ of the substrate. It is brought this close to reduce the effect of diffraction. The lines obtained by illuminating the photoresist from different distances between mask and photoresist are shown in figure 3.21. Unfortunately, some parts of the photoresist can

get attached to the mask in this way. These kind of errors are easily detected as they show up on every wafer processed after the moment the dirt got attached to the mask. A regular cleaning of the mask (if possible after every exposure) avoids these kind of problems. The best cleaning results were obtained by immersing the mask in the acid solution described in section 3.3.2. This method was not pursued since the bath also attacks the Cr on the mask that defines the pattern. Cleaning of the mask in an IPA bath after every exposure and cleaning in the acid bath after every 20 exposures gave equally good results and was then adopted. Cleaning of the mask after every illumination is a lengthy but necessary operation. It extends the illumination faze from 4minutes per substrate to at least 10 to 12 minutes per substrate.

Although contact illumination gives the best defined lines, it was quickly abandoned since it introduced too much dirt on the mask.

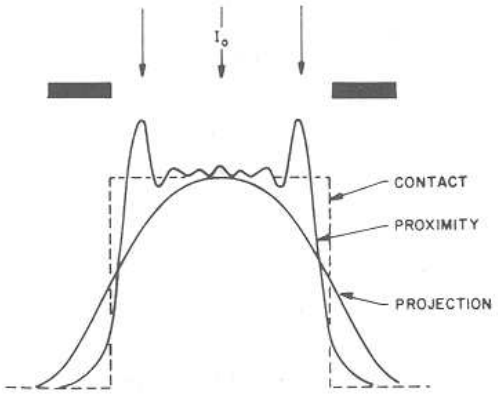

Figure 3.21: Incident profiles of masked pattern defined by contact printing, proximity printing and projection (through a system of lenses).

3.4.2 Cleaning

As mentioned in section 3.3.2 the cleaning procedure first adopted gave excellent results. No visible particles were left on the substrates and Ti adhesion was always satisfactory. It is however a very time consuming step. The first batches took on average 2.5h for a batch of 6 wafers. As expertise grew, this could be reduced to 2h for 9 wafers. Of course a non negligible time is spent in the preparation of the baths, which should be done with great care. Not only must one work without spilling a single drop of these strong acids or bases, but from chemistry we know that the order in which to mix the products is important. Water should not be added to an acid as the water will start to boil violently from the heat of reaction and spatter the acid [99]. Instead the acid should be added to the water very carefully as several hundred kJ of heat are released for every mole of acid added to the water.

3.4.3 Sputtering

Sputtering was performed in two different machines: the Alcatel and the LLS.

The Alcatel sputters the wafers in series. The wafers are screwed tight on a pallet, that is grabbed inside the vacuum chamber by a mechanical arm. This arm puts the wafers on a disk which rotates the wafers one by one before the target of the metal to be sputtered. Therefore, this is also a time consuming operation and the duration is increasing linearly with the number of wafers to be sputtered. As already described in section 3.2.1 the screwing of the substrates on the palettes is a very delicate operation. The glass plates used at first had a thickness of $500\mu m$. When screwing them tight, sometimes a crack was heard but no visible damage could be observed. Unfortunately this always meant to throw away the wafer as upon heating the plate,

with the plasma inside the machine, the glass always broke. This problem became even more pronounced when processing $300\mu m$ thick plates.

It is no wonder that it was in this step that most of the wafers were broken. At first, one out of 5 wafers were broken during this step. Later on, this could be reduced to 1 out of 10.

The LLS machine on the other hand processes the wafers in parallel. A total of 24 wafers can processed together. The time needed to do this is 1.5h.

The wafers are placed on a plate and are fastened by vacuum adherence. The plate is then inserted in the sputtering machine and all wafers are then sputtered. Due to cost optimizing arguments, the machine must always be fully loaded.

3.4.4 Etching

Etching is probably the bottle neck in the overall procedure. First because of the preparation and control of the baths and second because wafers could only be processed one at the time. This takes 12-13 minutes for every substrate. Unfortunately inspection under the microscope to ensure perfect etching was necessary after every wafer to optimize the timing for the next wafer.

Problems arose also when changing the design of the MSGC from square to trapezoidal. Due to the large area to etch at the side of the MSGC, underetching was setting in at the time that the edges were far from being completely etched. This could be resolved by a home made trapezoidal cache which was covering the edges of the substrate to about 2cm from the MSGC. As these parts were no longer exposed to the UV light, the photoresist remained and the Cu was not etched.

This solution gave satisfactory results but is not advised since introducing foreign parts to the exposing machine can add scratches or dust particles in the resist. It should be taken in consideration in the design of the mask. One should make sure that there are no big empty spaces present that are not required by the design.

3.4.5 Plating

The plating procedure was the most difficult to optimize. As the products used in these bath are highly toxic and aggressive they must be operated by a qualified chemist by the Belgian law. It was thus necessary to have the help of someone working at IMEC who performed most of the tests. Unfortunately this person was only working half-time and had a lot of other activities. Once all the baths are heated, the total procedure takes $2 hours$ per batch of 6 wafers.

3.4.6 Overall procedures

Taking the bare received substrate through all the steps needed to become a gold plated MSGC took on average a week time for a batch of 8 to 12 wafers. This is in fact longer than the sum of the all the time needed to complete the overall procedure. This effect is due to the time sharing of the equipment at IMEC. People working there had priority to the use of the machines. This lead us to working early in the morning when the machines were still free and late at night when they were free again.

Plating had to be timed also since the person doing the plating for us had to be available.

Lots of time was also lost in using pre-made baths. Procedures that gave good results in one batch could be disastrous in the next. This effect was no longer observed when the switch to self-made, fully controlled baths was made. Since no record was kept as to where the baths were used for, nor any measurement of pollution was done, the contents of the baths was always a mystery.

Control of the pH of the plating bath has now been made a standard procedure of the plating as the wild-growth occasionally occurred with Si wafers also. However it seems less critical on Si than on glass.

Due to this it took 25 batches processed over the period of a year and a half to optimize the procedure and to have a good (less than 2% defects) and reproducible result. Many of the problems result from a difference in dimension of the components. As the size of the MSGC is a complete substrate, 2% defects on one substrate means to throw it away. This same 2% of defects

in chip technology will result in the loss of 10% of the chips present on the wafer. Procedures can become less strict as the component dimensions decrease.

3.5 Conclusions

In the previous study it was shown that it is possible to fabricate large area MSGCs ($10cmx10cm$) via the standard procedure used at IMEC (Leuven). This procedure consists in first sputtering of an adhesion layer of Ti, followed by a layer of $0.8\mu m$ Cu. The pattern is then wet etched in the Cu. The Ti is removed by reactive ion etching (RIE). The pattern is then covered with Ni and next with AU via electroless plating.

It was possible to make the substrates so as that more than 98% of the surface was defect free. Successful tests were performed with these substrates, mounted into a detector, in several test beams. Results will be presented in chapter 4.

To achieve such a good quality art-work, the procedure had to be optimized. First a learning faze was needed to be able to work as clean as possible since every particle bigger than $1\mu m$ can give rise to defects. Second, a more thorough cleaning of the glass plates compared to Si processing was needed since the plates are neither manufactured nor shipped in a clean-room compatible way. Last, every step has to be fully under control. A controlled etching bath was introduced followed by a visual inspection of every wafer under a microscope. The Ph of the Ni plating bath turned out to be a critical parameter. As the Ph was rising, wild-growth or bad adhesion properties of the Ni were observed. Regular checks of the Ph and consequent adding of chemicals were able to solve the problem. Chemicals remaining on the glass plate after plating, giving rise to a high ohmic short-circuit between anode and cathode, could be removed by a last baking step of more than $7h$ in an oven filled with N_2.

Chapter 4

Testing of imec MSGCs

4.1 Introduction

The validity of the substrate manufacturing procedure as described in chapter 3 needs to be validated. Therefore, after the substrates were produced, they were assembled into a particle detector.

Two main goals needed to be achieved:

1. Proof the validity of the imec technology; i.e. can detectors equipped with substrates made in IMEC efficiently detect Minimum Ionising Particles (MIPs)?

2. Are these same detectors able to cope with a radiation environment comparable to what is expected at the LHC?

To answer these questions, the detectors were irradiated in particle beams. The properties of the IMEC substrates were investigated in an $8GeV/c$ pion beam, which contains only MIPs. The LHC conditions were reproduced by a $300MeV/c$ pion beam. Here the detectors are subjected to a high flux of MIPs, superposed to a rate of Highly ionising Particles (HIPs).

Furthermore, a comparison was made between detectors equipped with imec made substrates and detectors equipped with substrates made in ALENIA (Italy) using the lift-off technique. In this technology, a layer of photoresist is spun upon the bare, cleaned, glass substrate. The resist is illuminated through a mask and then developed. After this step, the negative image of the MSGC substrate remains on the glass. Next, a thin ($0.4\mu m$) Au is deposited on the substrate via e-beam evaporation. In a last step the photoresist is removed from the substrate, removing the superfluous gold and leaving the MSGC pattern. A comparison of both techniques is shown in figure

4.2 Description of the particle beams used

4.2.1 T9 pion beam at CERN

The T9 beam is dedicated to the CMS and ATLAS experiments. It is a secondary beam derived from a $24GeV/c$ proton beam, extracted from the PS. The extracted protons interact in a Cu target. The reaction products are then used to produce the T9 beam. This secondary beam is composed of pions and protons up to a momentum of $10GeV/c$ with an energy resolution of 0.24%. The content of the beam as a function of the particle momentum can be seen in figure 4.2.

The beam was tuned to a momentum of $8GeV/c$ during the tests. The beam follows the PS extraction bunches, yielding 2 periods of 300ms with full intensity (i.e. $10kHz/mm^2$) per spill. Each cycle has a duration of $12s$, resulting in a duty cycle of 5%. The surface irradiated by the the beam was $2 \times 4cm^2$.

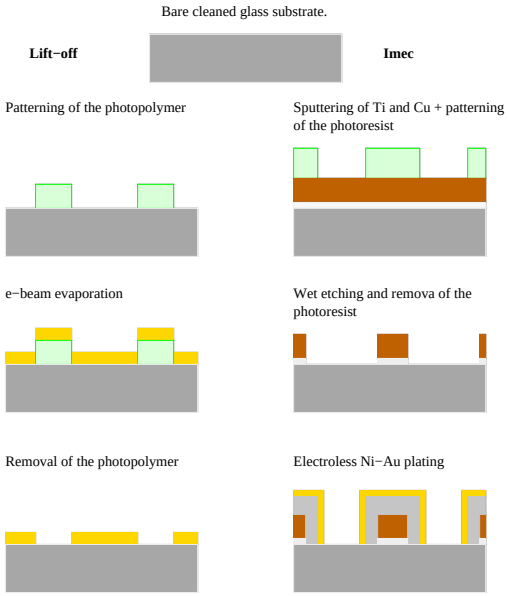

Figure 4.1: schematical view of lift-off (left) and electroless plating (right) process flows.

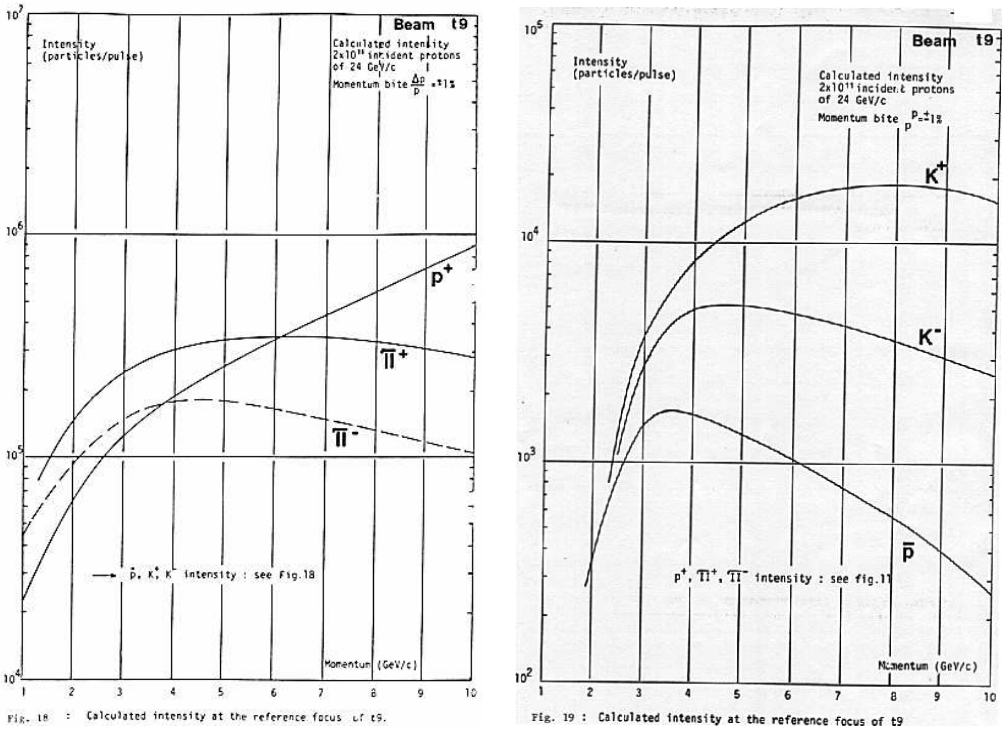

Figure 4.2: Pion, proton and kaon content of the T9 as a function of the mean beam energy.

4.2.2 πM1 pion beam at PSI

The πM1 beam at the Paul Sherrer Institute (PSI) in Villigen (Switzerland) is a secondary beam generated by collisions of protons produced by the PSI cyclotron. The proton energy is 590 MeV. The cyclotron is bunched at a frequency of 50MHz. The protons collide against a 5mm thick graphite plate.

The momentum spectrum of the resulting pion beam can be seen in figure 4.3. The average pion momentum is $350 MeV/c$. Pions in this momentum range have a high cross section for inelastic π-p scattering (see figure 4.4)[105]. When the pions interact strongly with the detector material, the resulting nuclear fragments can enter the gas volume. The energy loss of these fragments in the gas volume can be up to 100 times larger than for minimal ionizing particles [106]. The intensity of the pion beam can be varied from $10 - 20 Hz/mm^2$, called low intensity (LI), up to $5 kHz/mm^2$, called high intensity (HI). At high intensity the particle rate can reach $9 kHz/mm^2$ in the center of the beam.

Simulations have shown that the PSI πM1 high intensity beam reproduces the experimental conditions to which the MSGCs would have been subjected inside CMS[106].

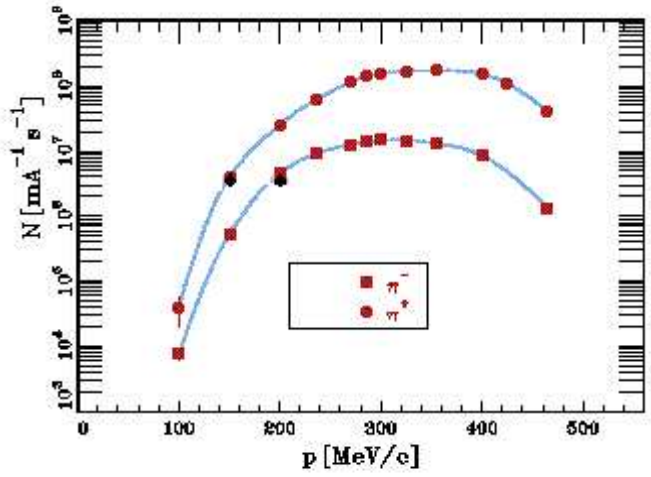

Figure 4.3: Momentum spectrum of the pions in the πM1 beam.

4.3 General detector description

4.3.1 Substrate layout

A general view of an MSGC substrate is given in figure 4.5. This figure is merely illustrative as the details of the design can vary. For instance the location of anodes and cathodes, and the actual dimensions of the substrate can differ according to the design.

We will thus concentrate on the features that are common to most designs. On one side of the substrate (at the bottom in figure 4.5), the cathodes are grouped together. Usually a group is composed of 16 cathodes. The HV supply can be done via this metal connection.

At the opposite side of the substrate, the anode starting points are located: the anode bond-pads. These pads typically have a width of $20 \mu m$ for wire bonding them to the read-out electronics. The cathodes ends just behind the point where the anode bond-pads are narrowed down to $7 \mu m$ to become the actual anodes. The anodes then stretch to the other side of the substrate

To avoid high local electric fields due to the point effect, both cathode and anode endings are round off as seen in figure 4.6. High local fields lead to an increased sparking probability.

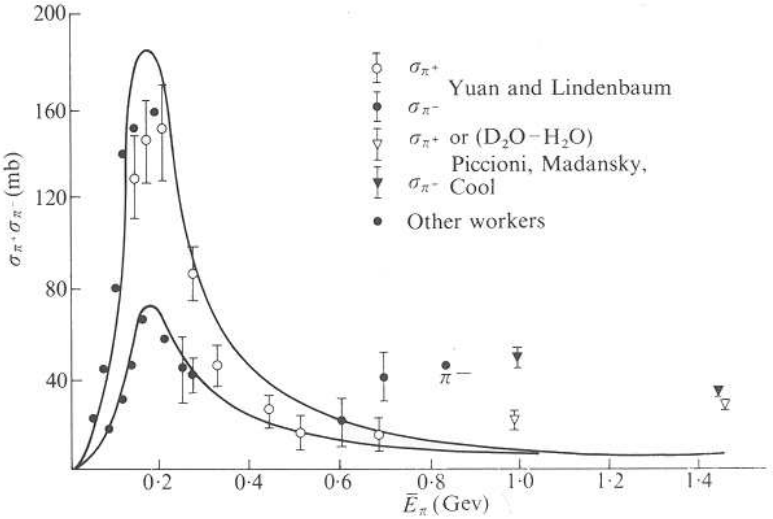

Figure 4.4: $\pi^{\pm} - p$ total cross section as a function of the π energy. [105]

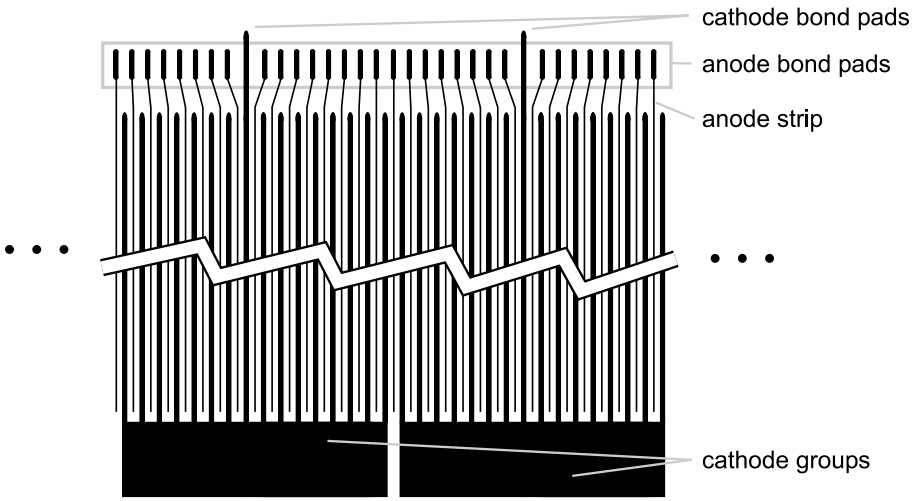

Figure 4.5: General layout of an MSGC.

Therefore these areas are usually passivated by a polyimide layer. The passivated areas are hatched in the figure, the dark areas represent the metalised surface and the white space is the uncovered glass surface.

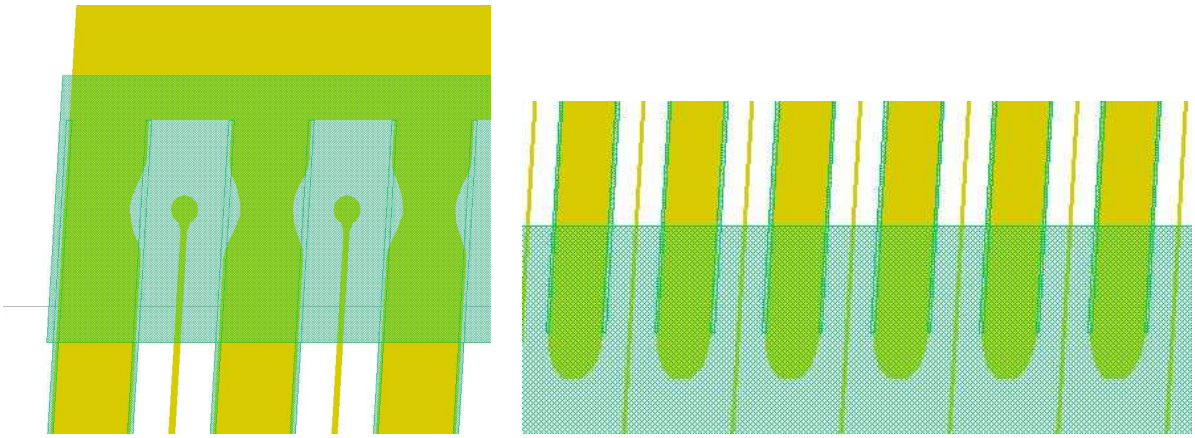

Figure 4.6: Left: round off anode ends; Right: round off cathode ends.

4.3.1.1 Square geometry

The square geometry MSGC layout is an adaptation of a design made by the INFN Pisa [110]. The pitch of the anode cathode structure is $200\mu m$, the width of the cathodes $90\mu m$, and the anode width $7\mu m$. Both cathode and anode bond-pads have a length of $7mm$. This length is needed to be long enough to pass under the $3mm$ broad frame that is to be glued upon them. It also comprises a gluing imprecision of $\pm 1mm$. The remaining $3mm$ is needed for wire-bonding purposes. The wire-bonding is done at an angle of 45^o, looking over the frame. The height of the frame being $3mm$, an additional $3mm$ bond-pad is needed. As the design had to fit into a $6inch$ wafer, as used at IMEC, the strip length was shortened to $9.3cm$.

The cathodes are grouped together in groups of 16 by their bond-pad, via which they are connected to the high voltage. On the opposite side of the substrates the anodes are connected to the read-out chip via their bond-pads.

To be able to locate the anodes that have been marked as unusable by a visual scan, a number had been put at the start of each 16^{th} anode thereby identifying the start of a new cathode group. This concept was further elaborated to facilitate the work of the scanning person by introducing numbers inside the first cathode of each group. This number, placed every cm, allows to map the recorded errors. The number seen in figure 4.7 (i.e. 4-0) identifies the seen position as being the 4^{th} cathode group at the top of the substrate (cathode bonding side). This allows to identify the anodes that should not be bonded without always having to go and look at the bottom of the substrate. Furthermore, it eases the finding of the error in case it is small enough to be corrected with ablation laser.

4.3.2 Testing prior to assembly

Prior to the mounting of the substrate into a detector, a first test is performed in dry atmosphere, usually nitrogen. Figure 4.8 shows the scheme of the test setup used.

The substrates are fixed to a support by vacuum adherence inside a glass tank. Next, the tank is filled with nitrogen.

The anodes are all connected to ground[1] and the cathodes are coupled to a HV system. The current flowing from the cathodes to the anodes is monitored.

[1]The anodes are bonded to a big metal residual in the form of a half moon at the side of uncut substrates, which is then put to ground potential. The metal residual remained on the substrate due to a mismatch in the shape of mask and substrates as used in the production of the MSGC substrates.

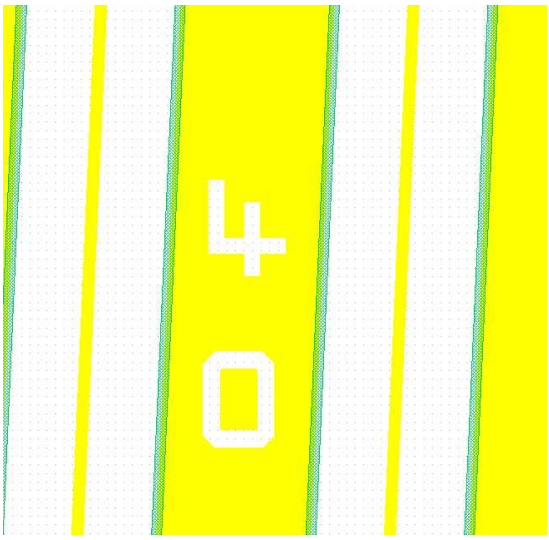

Figure 4.7: Numbers introduced to map the errors present on the MSGC substrate. Picture taken from the wedge layout.

A typical "dark current" (defined as the current flowing from anode to cathode in the absence of any irradiation) is a few nA. A current substantially higher than a few nA indicates a short circuit. The exact location of the short circuit is identified by first disconnecting cathode group by cathode group until the current drops. Once the cathode group is identified, it is reconnected to the HV. The same procedure is performed again for the anodes. The anode giving rise to the over-current will not be bonded to the read-out electronics and will be left floating.

When all short circuits have been identified, the cathodes are brought to a potential of 500V and left there for a few hours, ensuring that the substrate will be able to withstand high voltage for a longer time period.

4.3.3 Mounting

4.3.3.1 Open design

The MSGC substrates are assembled into detectors in a way that eases interventions, called the 'open design'[107] and that is schematically depicted in figure 4.9. Its main characteristic is to build and test complete MSGC counters, including their electronics, before mounting and aligning them inside a module. During the entire assembly and test procedure of the individual counter, all parts remain accessible for intervention and even replacement.

The gas box bottom plate consists of an aluminum carbon fiber honeycomb composite. The curved edges are made out of aluminum tubes with a rectangular section of $3 \times 10mm^2$ and a wall thickness of $200\mu m$. These tubes are used as integrated gas distribution manifolds, as the gas is being delivered via laser-drilled holes facing every MSGC inside the box.

4.3.4 Readout

Readout of the MSGC signals was done using the Premux128[48] chip. Figure 4.10 shows one readout channel of this chip. It consists of a low impedance signal input, two protection diodes, a charge sensitive preamplifier, a CR-RC shaper with a shaping constant of 50ns and a Double Correlated Sampling (DCS) circuit.

Via an analogue multiplexer, build in the chip, the 128 channels can be read out in series. Several chips may also be daisy chained and read out by a single flash ADC (FADC).

The premux has two readout modes: the DCS and the peak mode. In the DCS mode, two $2pF$ capacitors per channel are connected to the CR-RC shaper through the switches S_1 and S_2. When the switch is closed, the corresponding capacitor stores the signal voltage. In this way, two

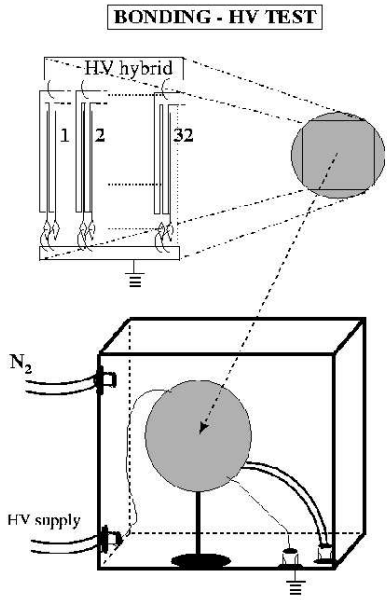

Figure 4.8: Test setup to determine the channels not to be connected to the readout electronics.

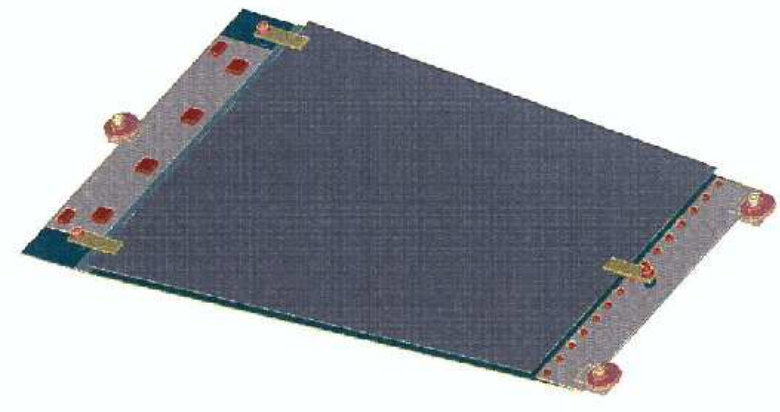

Figure 4.9: Schematical view of an open design detector.

samples of the signal can be stored. S_1 is closed at the maximum of the signal and S_2 is closed sufficiently long before or after the maximum to provide a measurement of the baseline of the channel.

In peak mode an additional 129^{th} channel, that is grounded, furnishes the information S_1 for all the channels.

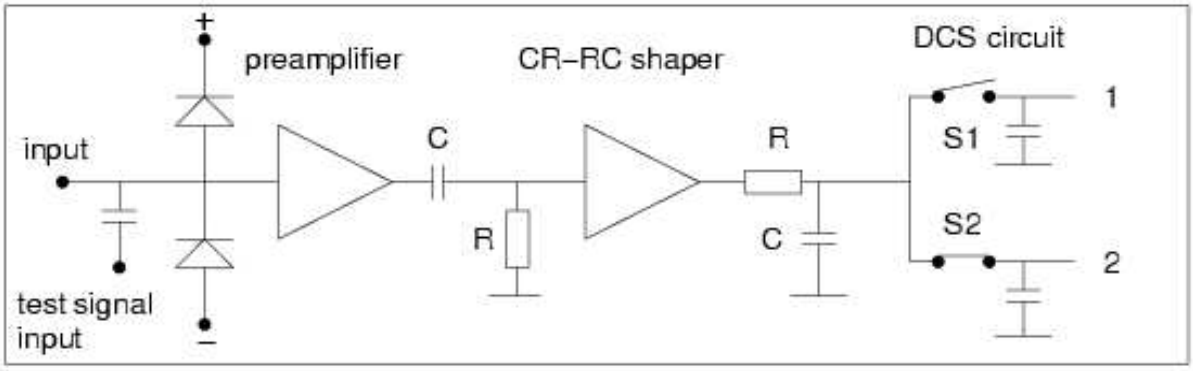

Figure 4.10: Schematic layout of one Premux128 channel.

When using fast electronics (compared to the signal formation), part of the signal charge may be lost (see §2.1.6). A quantification of this loss is given by the ballistic deficit:

$$ballistic\ \ deficit = \frac{S}{S_{delta}} \tag{4.1}$$

Where S is the signal seen by the readout electronics and S_{delta} is the signal that would have been seen if the input charge had arrived in the form of a delta pulse. The ballistic deficit depends on the electron and ion collection time, the evolution of the signal with time, the signal shaping and the sampling method. The deficit is below 1 for all gas detectors. For instance, for an MSGC operated in a Ne/DME (40/60) gas mixture, operated with a drift field of 4kV/cm, and read-out by premux electronics, the ballistic deficit is 0.7. This means that 30% of the signal is lost.

4.3.5 Data analysis

The raw ADC data as seen at the output of the Sirocco ADC can be seen as composed of 3 parts:

$$Signal_i^k = S_i^k + P_i + C_i^k \tag{4.2}$$

in this equation, S_i^k is the real signal induced by the charged particle. P_i is the pedestal of the strip. It is the channel pulse height in the absence of a particle signal. This pulse height varies and is Gaussian distributed. The mean of this distribution is called the pedestal of the channel. The RMS of the distribution is called the noise of the channel. C_i^k is a common mode contribution which takes into account a possible baseline shift in a group of channels in the same readout chip. The pedestal and noise are computed on dedicated runs. These runs have been taken in the absence of any irradiation. To take into account the drifting or slow changes in the average, these runs are repeated every $12\,hours$. Even though the particle beam is stopped, one cannot avoid particles passing through the detector. For this reason, in a second iteration, the signals differing by more than 3 times the noise from the previously computed average are no longer taken into account in the pedestal calculation. The pedestals and noise are calculated on 500 events on average.

A pedestal and noise distribution can be seen in figure 4.11. The noise amounts to 10 ADC channels on average, corresponding to $1700\,e^-$ENC.

To take into account the diffusion of the electrons in the gas, which can cause the signal to be spread over more than one channel, channels with a real signal are grouped into clusters. The 'seed' cluster has a signal (S_i^k) which is at least 4 times the strip noise. Strips neighboring the

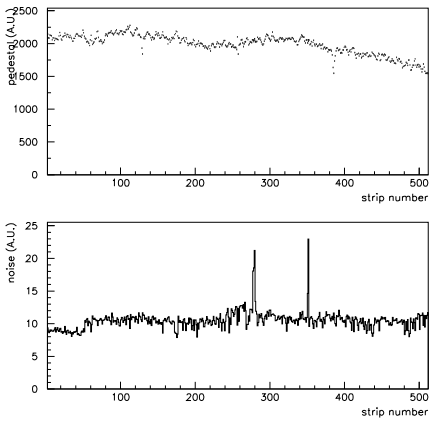

Figure 4.11: Typical pedestal and noise distribution.

seed cluster are added to the cluster if their signal exceeds 2 times the strip noise.
A channel is marked as dead if the noise of the channel is less than 0.66 the average noise in the detector. A channel is marked as noisy if the noise is more than 50 times the average noise in the detector. The clustering algorithm is built in such a way that it allows one dead or noisy channel in the cluster.
Once the clustering is performed, the impact position of the charged particle can be computed via the barycenter of the cluster:

$$y_{clus} = \frac{\sum_{i=1}^{N} n_i S_i}{\sum_{i=1}^{N} S_i} \tag{4.3}$$

n_i is the number of the strip that has a signal S_i.

Once the strips are grouped into clusters, the collected charge of the cluster (S) divided by the squared mean of the individual strips noise (N), corresponds to the cluster S/N. The histogram composed of all the cluster S/N registered in one run can be approximated by a Landau distribution. The S/N of the detector in the particular run is defined as the maximum probability of this distribution and determined via a fit to a Landau distribution (see §2.1.1.1).

4.4 Test in an 8 GeV/c pion beam (T9)

For the first time detectors equipped with substrates manufactured with the IMEC technology were tested in a particle beam. The tests performed inside the T9 beam needed to achieve a number of important goals:

- prove that detectors equipped with IMEC substrates were able to detect Minimum Ionising Particles
- prove that the substrates can survive the experimental conditions (i.e. not lose detection elements during irradiation)
- determine the maximal attainable S/N under the given experimental conditions.

Two detectors were tested in this beam. Both were equipped with substrates produced at IMEC. The first substrate was made on D263 glass and had no passivation (called NON). The second had a glass substrate with a $AlNO_3$ coating on top. On this substrate the edges of the cathodes were protected by the advanced passivation. This detector was called CAP.

Both detectors had the square geometry and were mounted using the open design. Read-out was performed by premux as will be described in the next section. No 'slow control' was present.

This means that the currents on the different electrodes were not monitored in order to detect discharges between some of the electrodes. The gas mixture used was Ne/DME (Di-Methyl-Ether) in a 1/2 proportion.

4.4.1 Experimental set-up

4.4.1.1 Test-bench set-up

The test bench consisted of a number of detectors that are placed behind each other in the direction of the beam. The number of detectors in front of our detectors was not constant. This does not affect the beam characteristics as it was a beam of high energetic (8GeV) pions, whose interaction with the detector material is low.

In front of the detectors, a $6x6cm^2$ scintillator was placed, in the middle of the test bench, a $12x12cm^2$ scintillator was found, and behind all the detectors, a $2.5x5cm^2$ scintillator plate was mounted.

Two detectors with different substrates were tested in this beam: a coated and advanced passivated one (CAP) and an MSGC without coating or passivation (NON)

4.4.1.2 Data acquisition

The Data acquisition (DAQ) system was a distributed system divided in a front-end and an event builder part. For scalability, the front end-crates could be segmented into several front end-crates.

A sequencer synchronizes the VME FADC that sends the read-out signals necessary for the front-end chips. The trigger was given by a coincidence between a $2.5x5cm^2$ and a $6x6cm^2$ scintillator read-out by fast photomultipliers. The multiplexed analog output of the front-end electronics are then transmitted by means of the Fast Intelligent crate Controller (FIC) to the FADCs where they are digitized, demultiplexed and stored. The data is then transferred to the event builder via a daisy chained fast data link.

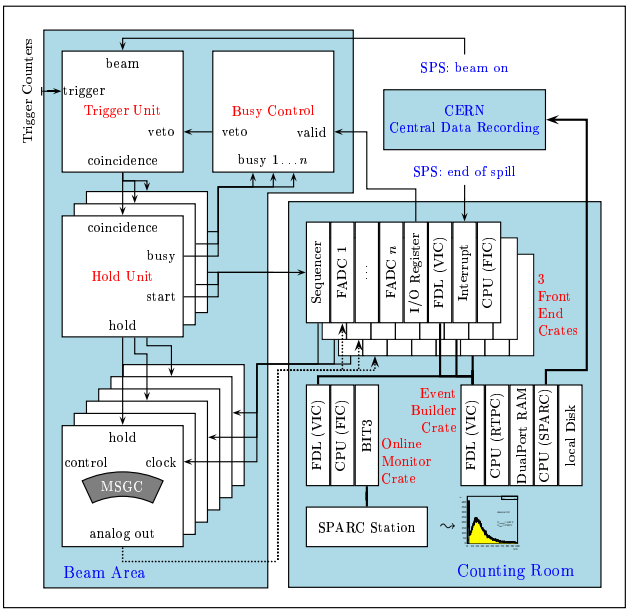

Figure 4.12: The DAQ system used at the T9 beam.

The event builder takes care of the synchronization between the front-end crates, creates ZEBRA format data banks [115] and transfers them to a dual port memory. Data are then written to disk to be stored on tapes later on.

Data Quality is checked on-line with a PAW [116] display, via a monitoring program developed at INP Lyon.

A more detailed description of the DAQ system used at T9 can be found in [113] and [112].

4.4.2 General operation conditions

As this beam test was the first one in which the IMEC technology was used, an important property to investigate is the capability to detect particles. This can be demonstrated by the beam profile. This histogram represents the number of times a particular strip was hit during one run. It is an integration of the beam over the length of the strip of the detector.

Figure 4.13 shows the beam profile for the CAP (a) and NON (b) detectors. As can be seen, both detectors are able to detect particles. The two profiles are each others mirror image as the detectors were mounted back to back. The hole in the beam profile of the NON detector occurring between strip 267 and 277 is due to electrodes that were found unsuitable for detection at the scanning stage and were therefore never bonded to the read-out electronics. Also a number dips and spikes are noticed. The dips correspond to interrupted strips. As at the time of the beam test, the production scheme for substrate production was not optimised, the number of dead strips in the detectors was more than 50 (i.e. 10% of the strips were affected). But due to the electric field configuration in the neighborhood of these strips (see figure 4.14) the neighboring strips will collect the primary charge. Therefore, a missing strip does not imply any loss of detection efficiency, but only a local degradation of spatial resolution and a modest increase of the electric field and the gas gain (25%) on the neighboring anodes. The primary charges are thus derived to the neighboring strips which resulting in an increased counting rate, hence the appearance of spikes in the beam profile.

In this run, 8939 particles were detected by the CAP detector and 8956 by the CAP detector. One run is delimited by memory requirements as the data files should not exceed 40Mb. Therefore most runs contain 9.000 events on average.

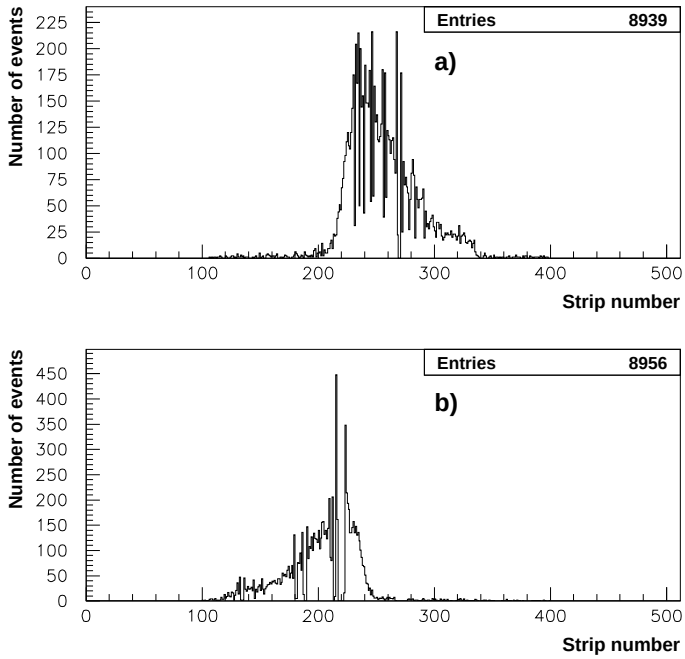

Figure 4.13: Beam profile as seen by the CAP (a) and NON (b) detectors in the T9 beam. Th holes in the beam profiles correspond to unbonded anodes.

Figure 4.15 shows the cluster charge distribution (a), strip noise versus strip number (b), cluster size distribution (c) and event multiplicity (d) for the CAP counter. The cluster size corresponds to the number of strips contained in a cluster. The event multiplicity is the number of clusters identified within a single event. The drift voltage was -3700V and the cathode voltage -560V. The strip noise is 7.5 units on average, which amounts to $1500e^-$ ENC.

It is noticed that the average number of clusters in the detector per event is not 1 but 1.8. In the analysis, only the cluster with the highest S/N is taken into account. As a result of this an

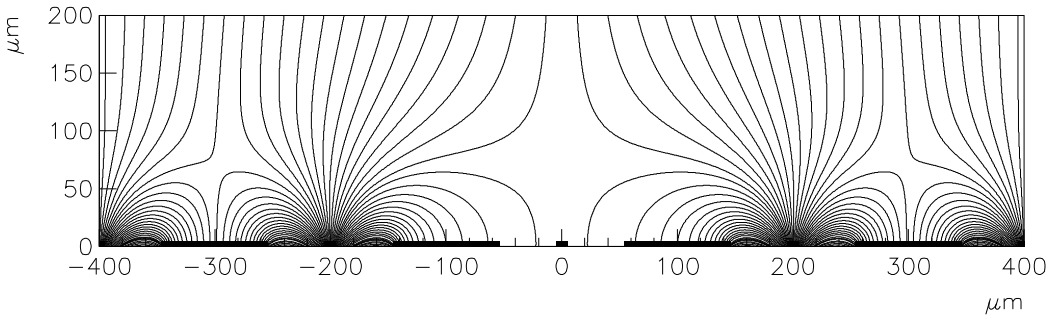

Figure 4.14: Electric field lines near a missing or disconnected anode.

apparent S/N enhancement is anticipated as will be explained in section 5.6. Since many events only contain one cluster, this enhancement could be estimated directly by considering only those events in the determination of the S/N. For the observed cluster multiplicity distribution, the signal enhancement was below 3%.

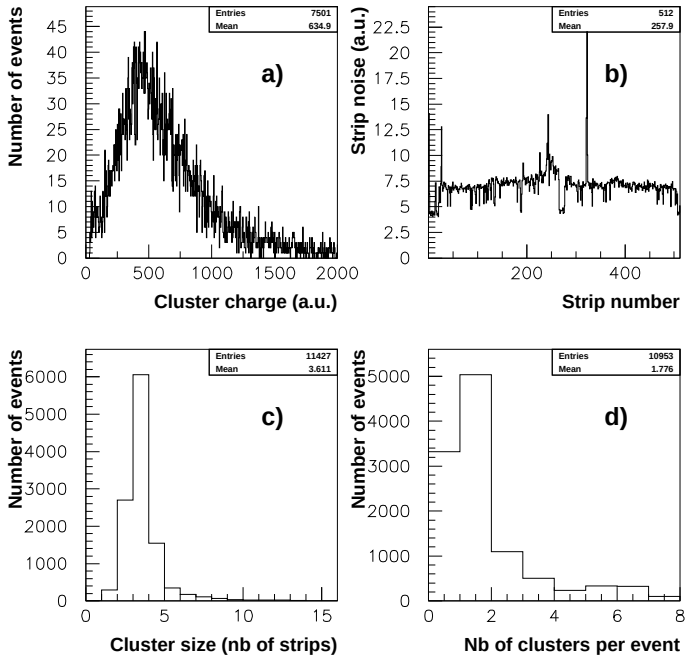

Figure 4.15: Cluster charge distribution (a), strip noise versus strip number (b), cluster size distribution (c) and event multiplicity for the IMEC counter in the T9 beam.

Typical Landau curves obtained with these detectors are shown in figure 4.16. The curves are obtained by retaining only the cluster with the highest S/N in each event. Figure 4.16a) shows this for the CAP detector and 4.16b) for the NON detector. The setting in for this particular run were: for the CAP: $V_d = -3000V$, $V_c = -580V$; for the NON: $V_d = -3500V$, $V_c = -600V$.

The large difference in S/N between the two detectors is mainly due to the presence or absence of the low resistivity surface coating. The difference in behaviour was investigated via electric field calculations [64, 68]. These calculations have shown that the electric field near the edge of the electrodes is reduced when a low resistivity coating is present. Hence the gain should be lower for a given voltage setting. This was confirmed experimentally by several authors [88, 89].

Reference [89] also demonstrates that there is no clear correlation between the nominal value of the surface resistivity and the gain if the coatings are different in nature. This is explained as an altering of the surface resistivity by chemicals used in the cleaning and etching procedure.

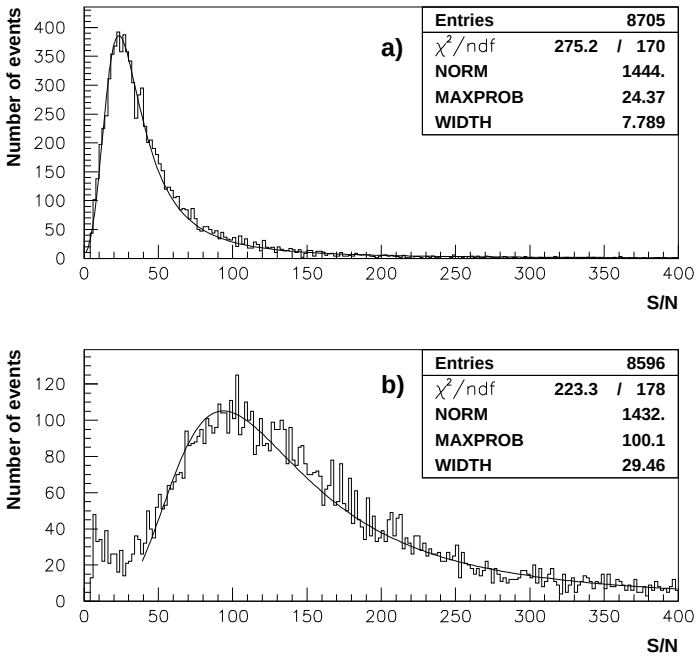

Figure 4.16: Landau distributions for the CAP (a) and NON (b) detectors. The S/N values found were 24,4 and 100,1 respectively.

4.4.3 Counter behaviour

Several voltage scans were performed on the non coated, non passivated IMEC detector (NON). A summary can be seen in figure 4.17a). As expected an exponential dependence of the S/N as a function of the voltage applied to the cathodes is observed. At a S/N of 90, the exponential dependence is lost and a slower rise is observed. This is due to a saturation of the read-out channels.

The S/N can also be improved by rising the drift voltage. It can be seen from the figure that a raise of 100V volts on the drift cathode is roughly equivalent to a raise of 10V on the cathodes. This can be important in order to reduce the energy released in case of a discharge between anodes and cathodes, thus limiting the risk for strip damages. It has also been shown [83] that increasing the drift voltage can reduce the number of noise hits, which is, in the view of the authors, a criterion for the onset of sparking.

As the limit for 98% detection efficiency for MIPs has been found to be 13[20], our detector shows a margin of a factor 6 in gas gain.

When reaching such high S/N values one has to be careful that the cluster size does not grow to large. The cluster size should be larger than 1 to obtain a better spatial resolution than $p/\sqrt{12}$, but it should remain close to 2 to keep the occupancy as low as possible. Figure 4.17b) shows the average cluster size as a function of the S/N for the NON detector. An increase from 2.8 to 3.4 can be seen when going from a S/N of 25 to a S/N of 100. This increase in the cluster size can be countered by using different selection procedures for the strips to be contained in a cluster. If the neighbouring strip is required to have a certain fraction of the signal of the seed strip, a constant cluster size is obtained[72].

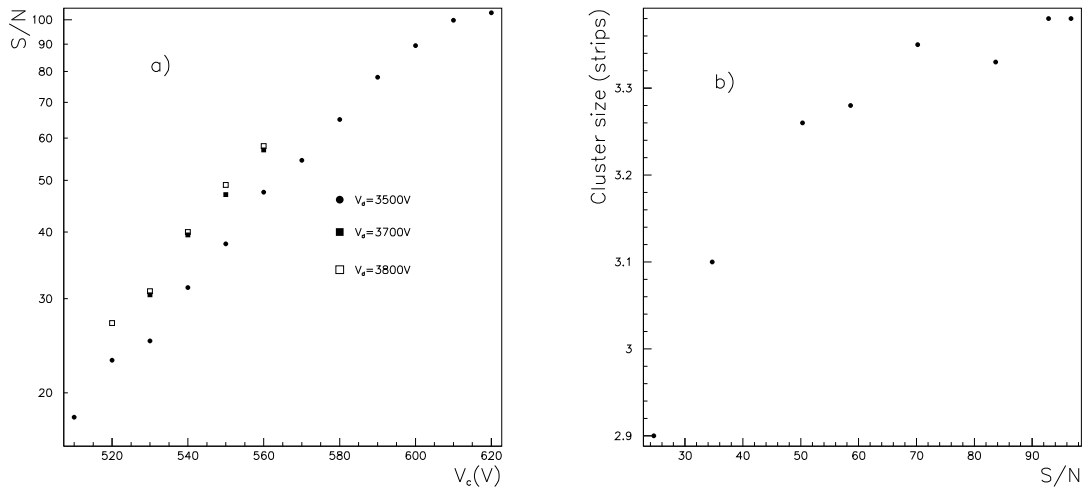

Figure 4.17: a)S/N versus cathode voltage for different drift voltages for the NON detector as measured in the T9 beam. b) Cluster size as a function of the S/N as observed during the voltage scans represented in a)

4.4.4 Counter stability

4.4.4.1 Gain

Counter stability has several components. The first one is connected to the gain. Figure 4.18 presents the S/N as a function of time for the two detectors. The voltage settings on the electrodes were: for NON:$V_d = 3500V$, $V_c = 600V$; for CAP: $V_d = 3000$, $V_c = 580$. As each run lasts ± 0.75 hour, the time interval represented by the x-axis is 6 hours. Both detectors show a stable gain over this time period.

The stability of the S/N over a longer period of time (1day) for the CAP detector is shown in figure 4.19a). The voltages applied were:$V_d = 3000V$ and $V_c = 580V$. The starting time was 16:00. Variations up to 30% can be observed. When looking at a still longer period of time (5days) in figure 4.19b), taken at the following voltage settings:$V_d = 3000V$, $V_c = 570V$, S/N differences up to 50% can be observed.

These differences might partially be due to temperature and pressure variations. The lowest values in figure 4.19b) were obtained after a gas problem had arisen. However, these big variations seem in contradiction with a report of a large scale test of coated and passivated MSGC in the PSI beam by Bellazzini et al. [71]. They report S/N fluctuations below 10% over a period of 3 weeks. In the same beam, fluctuations up to 25% in S/N were reported for a system of MSGC+GEM detectors [74, 75].

After a period of 1 week, the NON detector developed a short when conducting a new voltage scan and no further operation of the counter was possible. At that time, the counter operated at a S/N of 113.

4.4.4.2 Strip loss

The second quantity that is associated to the stability of operation is the robustness of the strips. It is therefore important to determine the number of strips lost during irradiation.

Identifying broken strips can be done in two ways. The first one uses the noise spectrum of the detector. When a strip is interrupted, its contribution to the noise is also lost, resulting in a lowering of the noise. A convenient way to detect these strips is to divide the noise spectrum taken in one of the last runs by the noise spectrum coming from one of the first runs. In this way, the lost strips appear as dips in the spectrum.

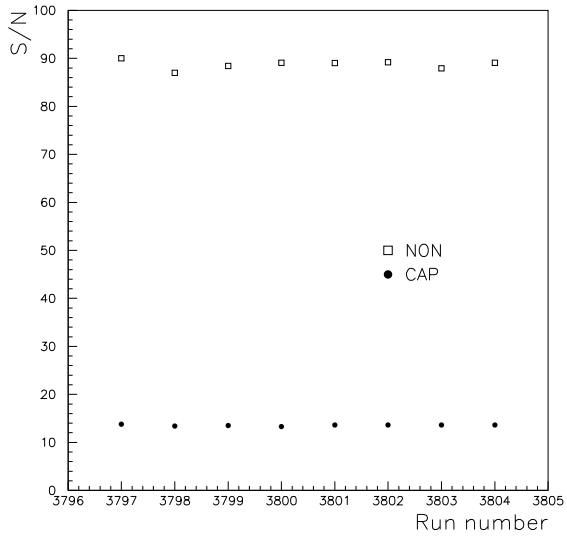

Figure 4.18: S/N as a function of run number (1 run corresponds to roughly 45min.) for the NON and CAP detectors. The detection gas is Ne/DME (1/2)

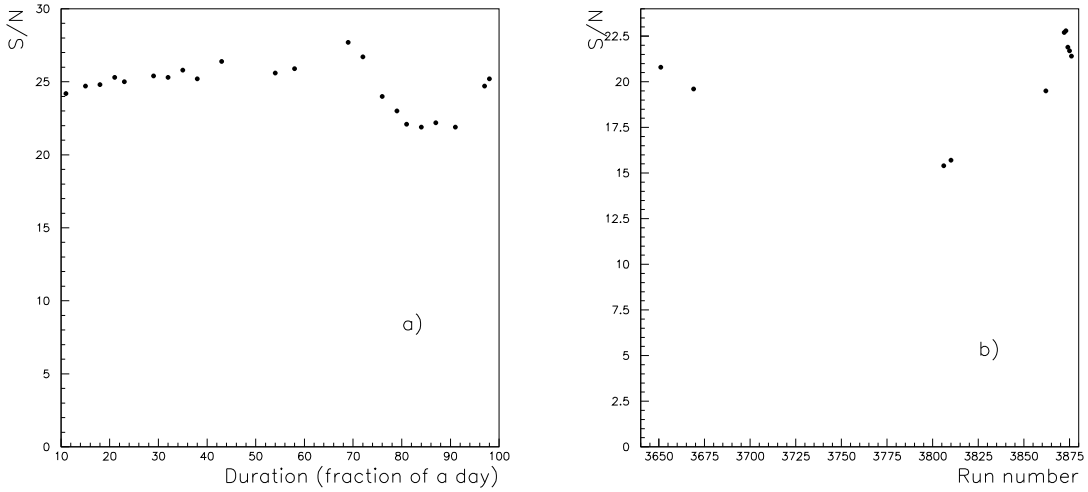

Figure 4.19: Long term stability of the NON detector. a) Over a period of 1 day. b) Over a period of 1 week. The voltage settings were a) $V_d = 3500V$ and $V_c = 580V$ and b) $V_d = 3500V$ and $V_c = 560V$.

The second method uses the beam profile. Indeed, when the strip does not collect charge anymore, a hole should be found in the beam profile in that location. However, the software used (TBeam [111]) allows for one dead strip to be part of the cluster. This is needed since the charge from a broken strip will be collected by neighboring strips (see section 4.4.2). The software does allow, however, for the seed strip (see section 4.3.5) to be displayed. If the strip does not appear in the seed strip profile, chances become real that it is broken. However, it can not be excluded that part of the the strip is still intact, but is collecting the primary charges less frequently and is thus rarely designated as being the seed strip.

The result of the noise analysis can be seen in figure 4.20. As will be explained in the next paragraphs, the NON detector became instable. So the reference noise spectra were taken before this occurrence.

Two dips are noticed in ratio of the spectra: one at strip 176 for the CAP detector and one at strip 188 for the NON detector. The hole in the NON detector could be correlated to a hole in the beam profile, identifying this strip as broken. However, in the case of the CAP detector, there was no beam activity in the neighborhood of the dip in the ratio of the noise profiles. The dip is also less pronounced than in the NON case. It is likely that a portion of the strip was detached, leading to a reduced noise.

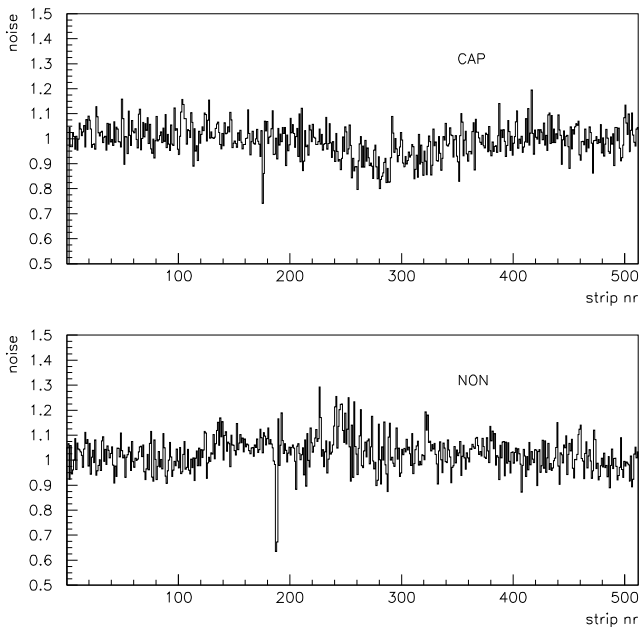

Figure 4.20: Ratio of the noise spectra of the 2 detectors under test. The used spectra are taken before the NON detector instabilities occur.

In figure 4.21 the number of times a strip is designated as being the seed strip in 4 different runs is shown for strips with numbers between 210 and 270. The spectra shown are for the NON detector. As can be seen, dead strips seem to appear and disappear. Shortly after this, the NON detector developed a short circuit and it was not possible to operate it afterwards. It is most probable that the strange behaviour shown in figure 4.21 are instabilities leading to the short circuit. At the time of the instabilities, a voltage scan was performed and the detector was operating at a S/N above 90. The last S/N recorded was 112.

4.5 Tests in a 350 MeV/c pion beam ($\pi M1$)

Micro-pattern detectors have been considered since ten years for use in high energy experiments and have shown very promising results since. Several groups have nevertheless reported problems

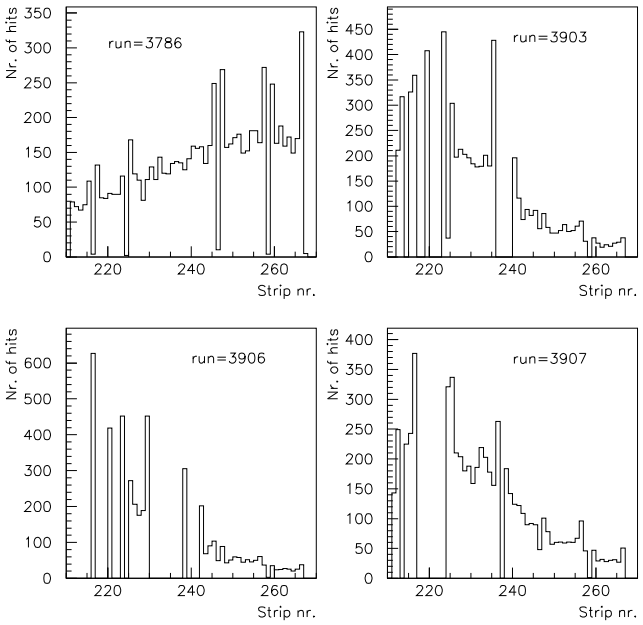

Figure 4.21: Seed strip profile for different runs for the NON detector.

with these devices when subjected to a flux of highly ionising particles. The group of F.Sauli noticed that the operation of an MSGC became unstable when irradiated with $5MeV$ α particles[62]. The maximum attainable gain dropped with a factor 2, thus putting a severe constraint on the operation of these devices.

The HERA-B group observed a considerable amount of damaging discharges between anodes and cathodes when exposing their detectors to the PSI 350 MeV/c pion beam.

Furthermore, simulations have shown that this beam reproduces the condition under which the MSGC will have to operate[106] inside CMS. An important test of any tracking detector that will be operated at the LHC is thus to withstand this beam. An account of tests performed at PSI is given in the following sections.

4.5.1 Experimental set-up

4.5.1.1 Readout and slow-control

As in the tests performed at T9, readout was performed using the premux chip. A scheme of the data acquisition can be seen in figure 4.22. The detectors were read out by service board modules (SBM)[53]. These modules can read out 2 Premux128 hybrids, each containing up to 4 PreMux128 chips.

The trigger was provided by a coincidence of 2 scintillators, placed in front and behind the test setup. A sequencer controls the readout of the multiplexed Premux128 channels via FADCs.

Currents on the different electrodes were monitored via current monitors in the HV supply line and were read out every 2ms by an ADC card.

4.5.1.2 Used detectors

A wide variety of counters have been tested in PSI. Different technologies were tested. The counters were tested during two beam periods: the first one in November '98, the second one in April '99.

Different types of MSGC substrates produced at IMEC were tested. Some substrates only had the metalized structure on them (Called NON), others where coated before being processed

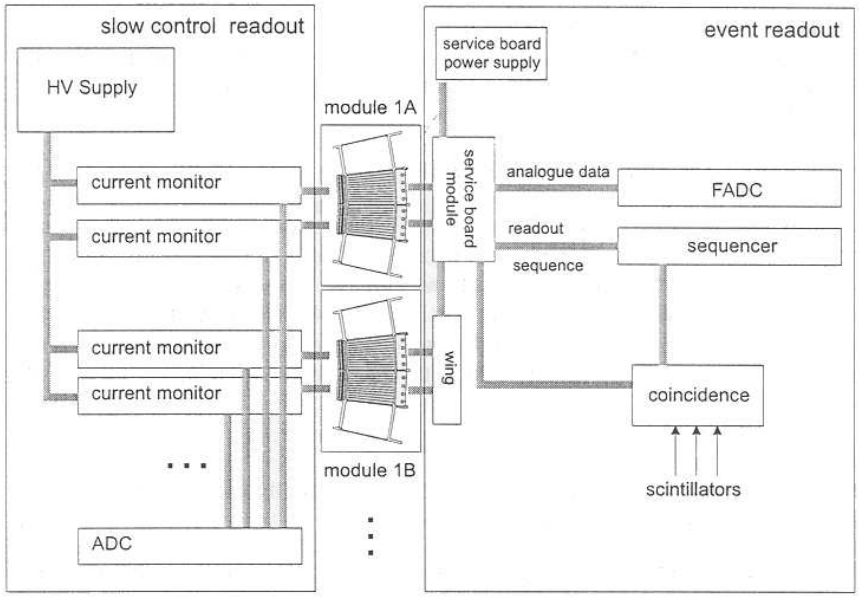

Figure 4.22: Scheme of the data acquisition system used at the PSI test facility.

(C) and some others were advanced passivated (AP). The naming scheme for the used detectors is summarized in table 4.1.

Detector type	Coating	Passivation
NON	no	no
UAP	no	yes
CAP	yes	yes

Table 4.1: Naming scheme for the substrates tested in PSI.

Furthermore, substrates coming from different batches were tested. The number behind their names indicates the batch.

A summary of the exposure periods and exposed detectors can be found in table 4.2.

Period	Detector	Exposure time
November '98	UAP2,NON2,CAP2	205h
April '99	UAP3, ALENIA	155h

Table 4.2: Detector exposures periods and duration in the PSI beam.

4.5.2 Counter behaviour

4.5.2.1 S/N

Figure 4.23 shows the S/N as a function of the applied cathode voltage for different substrates. The drift voltage was around 3600V in all the cases. For comparison of different substrate made by different manufacturers, a detector produced in ALENIA, using the lift-off technique, was also put in the beam. This detector had advanced passivated strips and a coating with a surface resistivity of $10^6\Omega/square$.

The different behaviour of coated and non coated substrates can again be explained by reduction of the electric field near the anodes due to this coating.

The two UAP detectors behave quit different. Two differences are observed: a much higher voltage must be applied to the UAP2 detector to achieve the same S/N and the UAP3 is able to

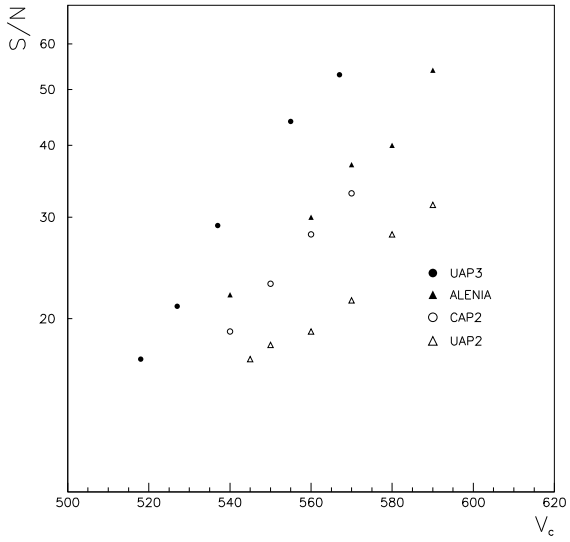

Figure 4.23: S/N as a function of the applied cathode voltage for four different detectors. The applied drift voltage was 3600V.

achieve higher S/N values than the UAP2. Both can be explained by the etching process. The UAP2 was one of the first attempts to make an advanced passivated substrate. At that time the procedure was not optimised, leading to a lower quality substrate. Most probably the etching was not fully completed resulting in both a broader anode and metal residuals on the substrate. The first effect leads to a lower gain and the second to an increased sparking rate.

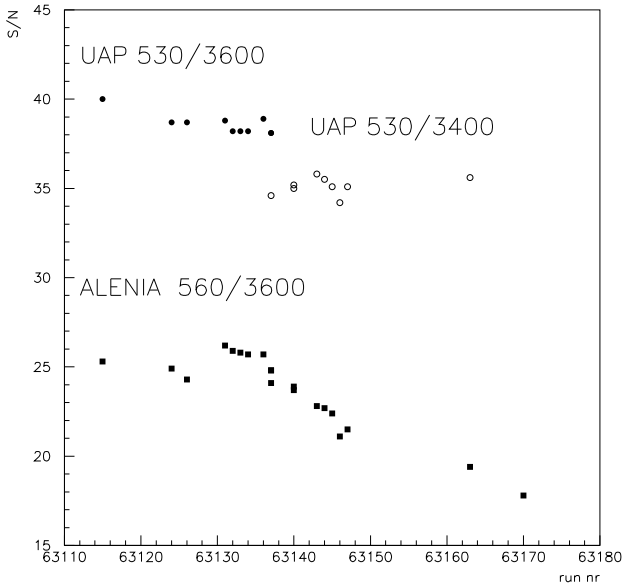

Figure 4.24: S/N versus run number. One run roughly takes 45minutes.

As can be seen in figure 4.24 the S/N for the UAP3 detector is stable over a period of two days (one run corresponds to 45 minutes). Variations up to 10% are noticed. These variations are, however, much less than those noticed in the T9 beam (see section 4.4.4.1).

After having had a stable operation for several days, the ALENIA detector showed a decrease of its S/N value with a factor 2 over a period of one day. This decrease manifested itself after an

intervention was done in the experimental area. After a careful check of the gas system, it was noticed that a gas leak of $2ml/hour$ had been established. The normal gas flow was $20ml/hour$. The leak introduced a rapid aging of the detector.

4.5.2.2 Sparks

Sparks are detected by the picoamperometers as an over-current on one of the electrodes. A spark is identified if an over-current exceeding a threshold of 3 standard deviations above the average irradiation current is noticed.

Two types of sparks were identified: substrate and drift sparks. An example of both is seen in figure 4.25. The time development of the observed current spikes is due to the recharging of the electrodes with a time constant fixed by the picoamperometer.

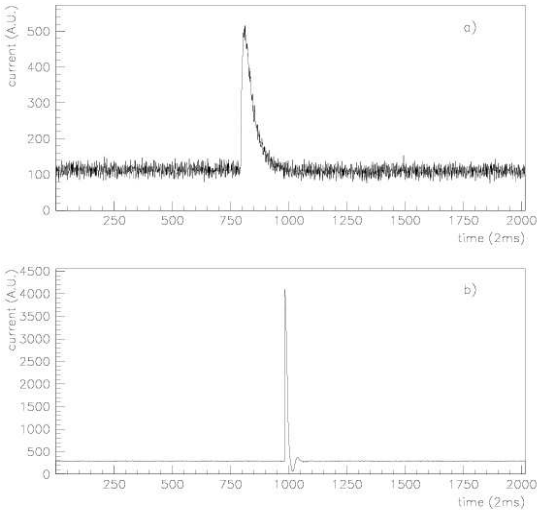

Figure 4.25: Cathode (a) and drift (b) sparks as a function of time when a spark occurs. The two event are not correlated.

The cathode sparks are the discharge of the charge located on one cathode group onto an anode. The spark charge distribution for this kind of sparks is shown in figure 4.26. Several peaks are observed. Discharges with a charge less than 2nC are considered as quenched streamers. The peak around 40nC is attributed to the partial discharge of one cathode group. As the total capacitance of 1 cathode group is $100pF$, the charge stored onto them is $53nC$ at $V_c = 530V$. The lower value observed can also be due to calibration errors.

The second type of sparks are drift sparks. These drift sparks are usually correlated with sparks on the cathodes. The UAP2 and CAP2 accumulated a large number of this type of sparks. They were attributed to the mechanics of the drift plane. Indeed, when changing the drift plane from glass to Ferrozell and protecting the detectors edges by a frame in the UAP3 detector, nearly no more drift sparks were detected.

Figure 4.27 shows the spark rate as a function of the cathode voltage for the ALENIA (top) and UAP3(bottom) detectors. The onset of sparking happens at $V_c = 550V$ for the ALENIA detector, whereas the UAP3 already starts sparking at $V_c = 500V$. This behaviour is also seen in figure 4.23 where the highest attainable S/N in the high intensity PSI beam is seen to be higher for the ALENIA detector than for the UAP detectors. The increased sparking rate was not at all anticipated from the features of the electroless plated electrodes that are naturally rounded off.

Two possible reasons are at the basis of this. First, the ALENIA detector issued from a long development program and was thus of excellent quality whereas the IMEC procedure was understood rather well at the time, but was not perfected yet.

An other possible explanations is given by the manufacturing procedure. Due to the lift off procedure, the edges are straight in the ALENIA case. However, the IMEC shows a more ribbled

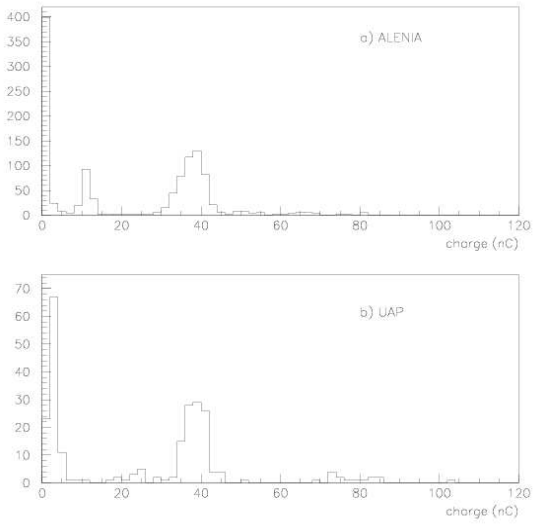

Figure 4.26: Charge distribution of cathode sparks for a) ALENIA and b) UAP3 MSGCs. The counters were operated at the following settings: $V_d = -3400V$ and $V_c = -530V$.

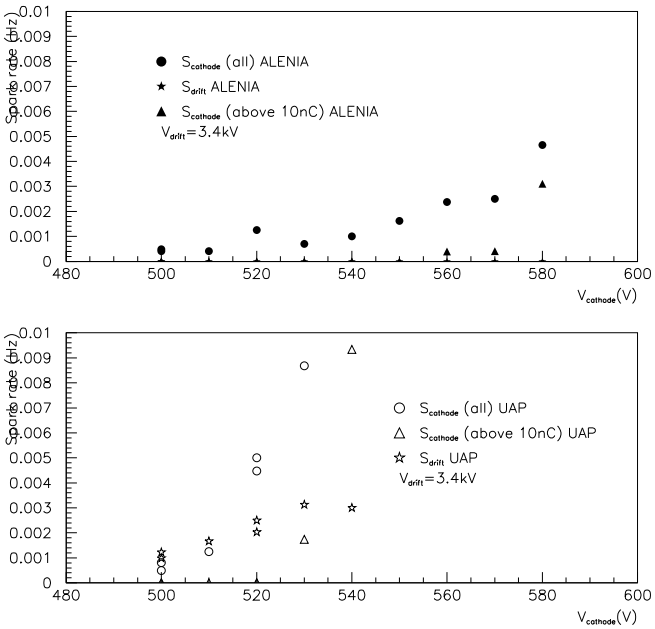

Figure 4.27: Spark rate as a function of the applied cathode voltage for the ALENIA (top) and UAP(bottom) detectors.

structure, probable inherent to the wet etching procedure. This might explain the slightly better performance of the ALENIA detector.

However, in spite of their higher sparking rate, the IMEC detectors do not lose more strips. The number of sparks, lost strips, and the exposure time at high intensity are shown in table 4.3. As seen, the IMEC detectors can sustain an impressive amount of sparks without losing channels. The NON detector developed a short after 4h of operation in the HI beam and accumulated more dead strips in this amount of time than any other detector. This demonstrates the need for advanced passivated strips when using plain MSGC detectors.

In [56] an estimation of the dead time introduced by sparking is given. They estimate that a dead time of $10\mu s$ for 80% of the detector and 4ms for the remaining 20%. At the maximal allowable sparking rate of $0.03Hz$ and a particle rate of $10kHz/mm^2$ this would lead to a particle detection inefficiency of $2.4\,10^{-5}$.

Detector	Time at HI	# sparks	# lost channels
CAP2	205h	2800	1
UAP2	135h	5000	3
NON2	4h	220	8
UAP3	137h	737	3
ALENIA	24h	6	2

Table 4.3: Time at high intensity, number of sparks and lost strips for different detectors.

4.5.2.3 Margins

The highest S/N values measured with these detectors in the PSI high intensity beam were 54 for the UAP3 and 46.4 for the CAP2. This is 3 times the S/N needed for full efficiency.

4.6 Conclusions

For the first time detectors equipped with substrates produced at IMEC were tested in particle beams. The detectors showed to be very promising. S/N ratios up to 100 could be reached in an $8GeV/c$ pion beam, whereas the minimum required for 98% detection efficiency was determined to be 14.

The S/N was proven to be stable within 8% over several hours. However, over longer periods of time, unexplained fluctuations in the S/N of up to 30% were observed.

To the best of our knowledge, only two strips were lost during the irradiation of the detectors in the T9 beam, where no highly ionising particles were present. Also a short circuit developed. However at that time, the detector was operating at 8 times the minimum required S/N for operation in CMS, or 16 times the minimum S/N needed for 98% detection efficiency for MIPs.

When subjecting our detectors to the $350MeV/c$ pion beam at PSI, a reduction in the maximum attainable S/N of more than a factor 2 was observed. This factor is even larger when the quality of the substrates is worse.

The IMEC detectors have a sparking rate that is 5 to 10 times higher than similar detectors where the substrates have been made using the lift-off procedure. The sparking rate is strongly dependent on the quality of the artwork. Nevertheless, the IMEC detectors do not lose more strips due to the increased thickness of their strips. Even at sparking rates of $0.03Hz$, the particle detection inefficiency due to the dead time is only $2.4\,10^{-5}$.

Chapter 5

Large scale test of MSGC+GEM detectors

5.1 Introduction

In the winter of 1999, a large number of MSGC+GEM detectors were assembled and tested together in the PSI high intensity beam.

This test revealed to be a great opportunity to evaluate some tracking capabilities of the technology. Furthermore, another unresolved questions could be tackled: is the minimum S/N required for 98% detection efficiency for MIPs in a high intensity environment the same as in a low intensity environment?

The decision to use MSGC+GEM detectors was driven by the results obtained by the HERA-B collaboration. They observed massive sparking when they operated their MSGC detectors in the PSI high intensity beam. A fast aging of these detectors was also observed. On the other hand, they were able to operate their MSGC+GEMs at gains above 10.000, needed for participation in the HERA-B trigger. Here no aging and only a limited amount of strips lost were observed.

Furthermore, at that time, only one manufacturer of advanced passivated substrates was able to produce substrates of a sufficient quality in order to comply to the strong criteria imposed by the CMS collaboration. It was not sure that this producer could deliver all of the needed substrates within time.

The large scale test was set up as a milestone test for CMS. The milestone and its results are the subject of the first half of this chapter. The second half is devoted to the determination of some important properties of the operation of MSGC+GEM detectors in a high intensity environment.

5.2 Definitions

5.2.1 Detectors

Substrates

The forward and backward parts of CMS will have wheel structures. For easy pattern recognition, the strips are therefore pointing towards the center of the beam pipe. As a consequence, the anode cathode pitch is not a constant and the form of the substrate becomes a trapezoid.

When a non constant anode-cathode pitch is used, care must be taken to have a constant gas gain along the strips. This is guaranteed by the semi-empirical formula found by the NIKHEF (Nederlands Instituut Voor Kern- en Hoge Energie Fysica) institute in which a relation between the anode-cathode gap (g) and the anode-cathode pitch (p) is given (see §2.2.3.2):

$$g = \frac{p}{8} + 20\mu m \tag{5.1}$$

where all the quantities are to be given in microns. The pitch is also equal to the width of the cathode (W_c) plus the width of the anode (W_a) plus twice the gap: $p = W_c + W_a + 2g$. substituting this into 5.1 gives us:

$$W_c = \frac{3}{4}p - W_a - 40\mu m \tag{5.2}$$

Substituting in equation 5.2 the pitch used in the square layout ($200\mu m$) would result in a cathode width of $103\mu m$. This is $13\mu m$ wider than what is used in the square design for the same value of the pitch and consequently in an anode-cathode gap that is reduced by $6.5\mu m$. As a result the gain for a given cathode voltage will be higher in the wedge configuration.

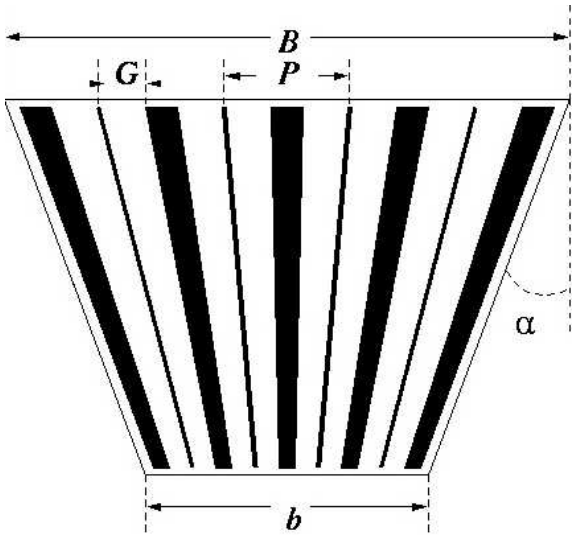

Figure 5.1: Wedge geometry layout.

When the final dimensions of the glass substrate and the total number of anodes per substrate are known, the pitch at a given position along the strips can be computed. The design used had 512 anodes. The total width of the substrate at a given point along the strips (W_t) can be written as: $W_t = 512p + W_c + 40$. The 513^{th} cathode is needed since every anode must be surrounded by 2 cathodes. As the cutting is done at $20\mu m$ from the border of the last (first) cathode in order to minimize the risk of damaging them, an extra $40\mu m$ has to be added to the total width. Therefore, the pitch at a given position along the strips can then be calculated in the following way:

$$p = (W_t + W_a)/512.75 \tag{5.3}$$

W_a is the width of the anode and is usually $7\mu m$. It is thus negligible in comparison with W_t which is of the order of $10cm$.

The dimensions of the wedge substrate were the following: the small basis of the trapeze has a length of 94.79mm, the large basis of the trapeze has a length of 107.85mm. The height amounts to 110mm, resulting i a length of 97.5mm for the central anode. The detectors foreseen to be placed on ring 2 inside the CMS MSGC tracker would have been equipped with substrates having these dimensions. When, throughout the rest of this work, wedge shape detectors are used, they will have these dimensions.

The shown dimensions result in the following set of parameters: the minimal pitch amounts to $181\mu m$ and the maximal to $203\mu m$. This leads to a minimal gap of $43\mu m$ and a maximal one of $45.5\mu m$.

O. Bouhali[57] has simulated the gas gain for a wide range of anode widths, pitches and cathode width. He proposes an extension of the NIKHEF rule:

$$0.8a + 38\mu m \leq g = \frac{p}{8} + 20\mu m \leq 1.4a + 45\mu m \tag{5.4}$$

in which a is the anode width. In fact, the extension comprises two boundary conditions for the validity of the NIKHEF rule. Applying the boundaries to our substrate yields the interval $[43.6\mu m, 54.8\mu m]$ for the width of the gap. As noticed, the smallest gap is not contained in the interval. However, using the data in [57], the gain drop is estimated to be less than 5% in this region.

For this design the read-out and the high voltage supply were done at the same side of the substrate. This option was taken to reduce the size of the detectors to be put into CMS. Therefore every first cathode of a group of 16 was elongated in order to reach the border of the substrate after cutting. As read-out is performed at the small basis of the trapeze, the anodes had to fan in, making room for the cathodes coming trough. In order to be compatible with the design from INFN Pisa, the following positions were attributed to the anodes and cathodes bond pads: $P_c = 200 * i$ and $P_a = 200 * i + 175 * k + 516$. In this $i = \{0, 16, ..., 496\}$ and $k = \{0, 1, 2, ..., 15\}$. The positions given define the most left side of the bond-pad. Counting is done from left to right when looking from the read-out side (small basis of the trapeze) up to the anode ends (large basis of the trapeze). A picture of the result can be seen in figure 5.2. The lower part of this picture is the HV and electronics side; at the top, the starting of anodes ans cathodes can be seen.

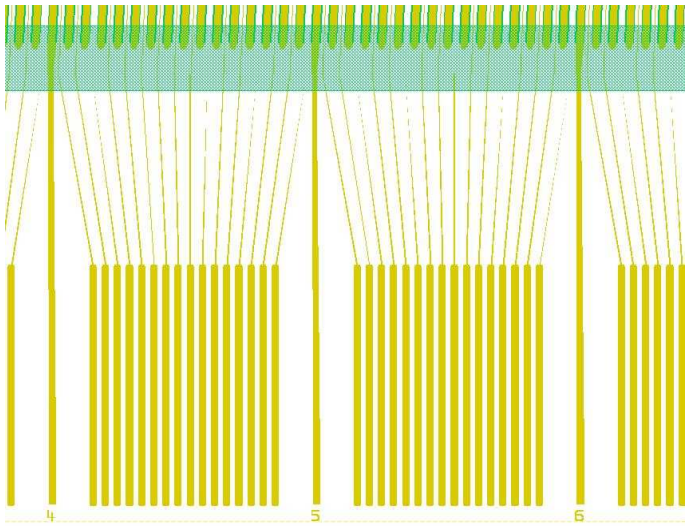

Figure 5.2: Fan in of the anodes and feed-through of the first cathode of each group.

Modules

The detectors consist of four wedge shaped MSGC substrates glued side by side on a common Peek[1] frame. As a result the detector has the shape of the sector of an annulus and a single gas volume[108]. Neighbouring substrates are aligned in such a way that the anode pitch across the boundary is twice the pitch elsewhere on the substrate. It was shown that with such an assembly, no detection efficiency loss occurs at the boundaries of the substrates[58]. Each trapezoidal MSGC substrate had 512 anodes, having a width of $7\mu m$ and a length of $10cm$.

Different substrate and GEM manufacturers were asked to produce the equipment for the detectors. A total of 91 MSGC substrates have been delivered by three different producers: IMT[2] that uses the lift-off technique, OPTIMASK[3] that uses direct gold etching and IMEC that uses electroless plating. Out of these, the substrate with more than 98% good anodes were

[1]Peek from Vitrex Europa GmbH, Zanggasse 6, D-65719, Hofheim (Germany)
[2]IMT Masken und Teilungen AG, Im Langacker,CH-8606 Greifensee (Switzerland)
[3]OPTIMASK Av. Ferdinant-de-Lesseps F-91420 Morangis (France)

selected, resulting in the following quantities: IMT: 60 good substrates out of 66; OPTIMASK: 8 good substrates out of 12; imec: 4 good substrates out of 13. The low yield in the imec substrates was due to problems with the Au bath for the plating. Due to the very stringent timescale, the solution could not be found before the deadline. The detectors made with imec substrates were put in the beam 'as such' but we were unfortunately not able to operate them. Therefore no reference will be made to them in the rest of the chapter.

All plates were made of uncoated DESAG D263 glass of $300\mu m$ thickness. Seventeen modules have been equipped with a GEM foil produced at CERN's printed circuit workshop. These GEMs had their copper electrodes segmented in four sections, matching the MSGC substrates. One detector module was equipped with a GEM foil produced by Würth Elektronic GmbH[4] without segmentation.

Prior to assembly, every substrate was cut to the required shape and dimensions using a diamond scriber. The cut was performed parallel to the edge of the cathode strips at a distance of only $20\mu m$. Before gluing, the substrates are rinsed in isopropyl alcohol and later on in deionised water in an ultrasound bath. The module assembly continues with the use of precision jigs for substrate alignment under a 3D measuring device or using an optical fiber system allowing to reach a positioning accuracy better than $5\mu m$.

Capacitance measurements of each anode revealed 1% of dead strips. The GEM foils were tested in a dry atmosphere at a potential difference of 500V prior to assembly.

The assembly then proceeds with the stretching and gluing together of the GEM foil with the gold plated Ferozell[5] drift plane and two frames of $3mm$ (defining the drift region) and $2mm$ (defining the transfer gap). This assembled cover is then aligned and glued over the substrates already glued to the support frame. A more detailed description of the assembly procedures can be found in [81].

Out of the 91 substrates delivered, 72 were mounted in 18 detector modules. A picture of an assembled detector module can be seen in figure 5.3. One can see a detector module mounted on its aluminum support plate. The two central detectors are read out by premux electronics. The round structures are a mechanical support for the drift plane.

Figure 5.3: Multi substrate MSGC+GEM detector module mounted on a support plate with electronic readout and power supply boards.

[4]Würth Elektronic, Rudolf Dieselstr. 11, Rot am See (Germany)
[5]Ferozell from Helmut Zeder Elektronik Kuchengrund 20, D-71522 Backnang (Germany)

5.2.2 Milestone

The exercise was performed as a milestone test for the CMS tracker. The requirements for the milestone to be met were the following:

- Twelve fully functional GEM+MSGC detector modules had to be operated for 360 hours in the PSI $\pi M1$ high intensity beam. This means that at least 48 good quality substrates[6] had to be mounted into detector modules.
- Only the two central substrates were to be exposed to the beam. However, their operation should be done at a S/N that guarantees 98% detection efficiency in CMS with the final electronics. This value of the S/N ratio is defined as the 'working point'.
- During the 360 hours of operation, less than 0.27% of the anode strips could be lost. So out of the 12288 strips exposed, only 33 were allowed to become inoperative. When extrapolated to 10 years ($5.10^7 s$) of operation at the LHC at full luminosity, this would lead to the loss of 10% of the strips. Due to this amount of strip loss, 5% of the MSGC detector area would have a reduced spatial resolution (from $35\mu m$ to $60\mu m$) [58].

The working point was determined to be a S/N of 17 with premux electronics. This result was obtained independently in the PSI high intensity beam[75] and in the X5 beam[79] (this beam contains muons with momenta between 75 and $120 GeV/c$). However, to ensure 98% detection efficiency with the faster electronics foreseen to be used in CMS, a factor 2.2 has to be taken into account[20]. This electronics uses an algorithm that adjusts the rise time of the MSGC signal to the 25ns between each bunch crossing at the LHC. The increased S/N value needed mainly comes from the increased ballistic deficit and noise when using faster electronics[51]. It has been shown that it is very difficult to accommodate both good time tagging and S/N properties[52] when using this kind of electronics with a slow[7] detector like an MSGC.

To accommodate for this reduction of the S/N when switching to the final electronics, all detectors were operated at a S/N of ≈ 37.

The detectors were mounted on support plates two by two. The gas mixture used was Ne/DME (2/3) and was fed in parallel to the nine pairs of modules with a flush rate of 1l/h or two gas renewals per hour.

At the same time as our milestone, a milestone for barrel MSGC detectors took place. Our detectors were sandwiched between two boxes, each containing 16 of these detectors. More information about these detectors can be found in [71]. A picture of the complete setup can be seen in the left panel of figure 5.4. In the right panel the scheme of the set-up is shown.

The emplacement of the different scintillators is revealed in the right panel of the same figure. The scintillators labeled LIF and LIB were used for the trigger in low intensity, whereas the scintillators labeled HIF and HIB were used for the trigger in high intensity.

The total exposure time was divided into four distinct parts.

1. Set up: Delays[8] are optimized and the detectors were gradually brought to a S/N of 37. Voltage adjustments were done only at high intensity to avoid excessive sparking when going from low to high intensity. After a stable configuration of the electrode potentials was found, a low intensity run was performed to check the S/N value. This part of the test was performed in the PSI low intensity beam ($10 Hz/mm^2$)
2. Hardening: The modules were operated for one week at nominal S/N values in the high intensity (HI) PSI beam ($5 kHz/mm^2$) to allow infant mortality of weak strips or electronic channels.

[6] A substrate is labeled as good if less than 2% of its anodes are found unsuited for bonding. An anode is considered as bad if it is interrupted or if, in the anode-cathode gap, a metal residual is present that covers more than 1/3 of this gap.

[7] Slow as compared to the CR-RC shape function peaking time.

[8] A delay is set on the read-out sequence with respect to the trigger. In this way S1 (see section 4.3.4) can be optimised in order to collect as much charge as possible.

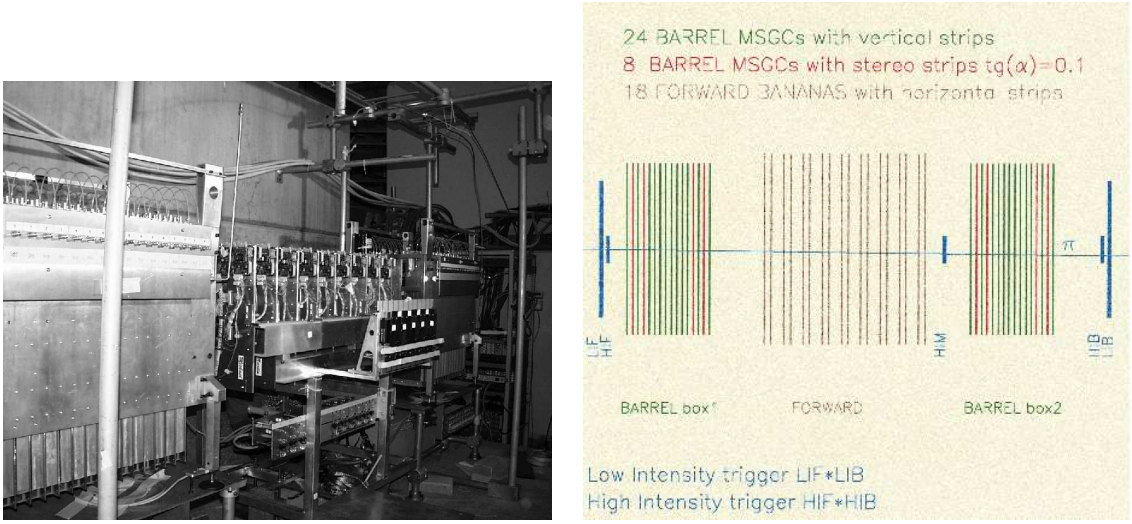

Figure 5.4: Left: Picture of the entire set-up at PSI seen in the direction of the beam. The central detectors are the MSGC+GEM detectors used for the milestone test. In front and behind our detectors a group of 18 MSGCs was placed. Right: Schematical view of the set-up revealing the emplacement of the scintillators used.

3. Milestone: The detectors were operated for 376 hours at nominal S/N values in the HI beam.

4. Safety margin scan: The S/N of six modules was increased in order to investigate the operation margins. Again, this was performed with the HI beam on.

5.3 Detector uniformity

Figure 5.5 shows the delays as set for the different detector modules in the milestone test. A substantial spread in the values is noticed. The delay ranges from 5 to 80ns. This can be explained by a sagging of some of the GEM foils towards the drift cathode. Indeed, the delay is mainly determined by the time the secondary electrons need to drift from the GEM foil to the MSGC substrate. Opening of several modules with a big delay confirmed this hypothesis. Sags up to $0.5mm$ were observed. The sagging of the GEMs can also be demonstrated using a plot of the average S/N as a function of the strip number as shown in figure 5.6. A normal detector has a constant average S/N between strips 200 and 800. In the edges the count rate is lower because this area is not covered by the scintillator and so no particles should be detected there at LI. The large non uniformities observed clearly demonstrate the need for a good stretching and gluing procedure in the mounting scheme of the MSGC+GEM detectors[81].

In figure 5.7 the voltages applied to the cathodes and the voltage difference over the GEM foils are shown for all the detectors used for the milestone test. Also here a spread in the settings is noticed. However, all detectors were able to reach the required S/N value. On some detectors, minor adjustments of the potentials were applied. The maximum and minimum potentials applied to the detectors are depicted by the error bars.

These large differences can be a drawback of the technology as this would require a monitoring and adjustment of the voltage settings when used in a big experiment like CMS. It could be a major problem to keep track of 4 voltage setting for more than 8000 modules.

5.4 Detector stability

The detectors have been kept at the same voltages for 376 hours. Only minor adjustments of $\pm 5V$ on V_c and $\pm 15V$ on ΔV_{gem} were performed to reduce the spark rate or to increase the S/N.

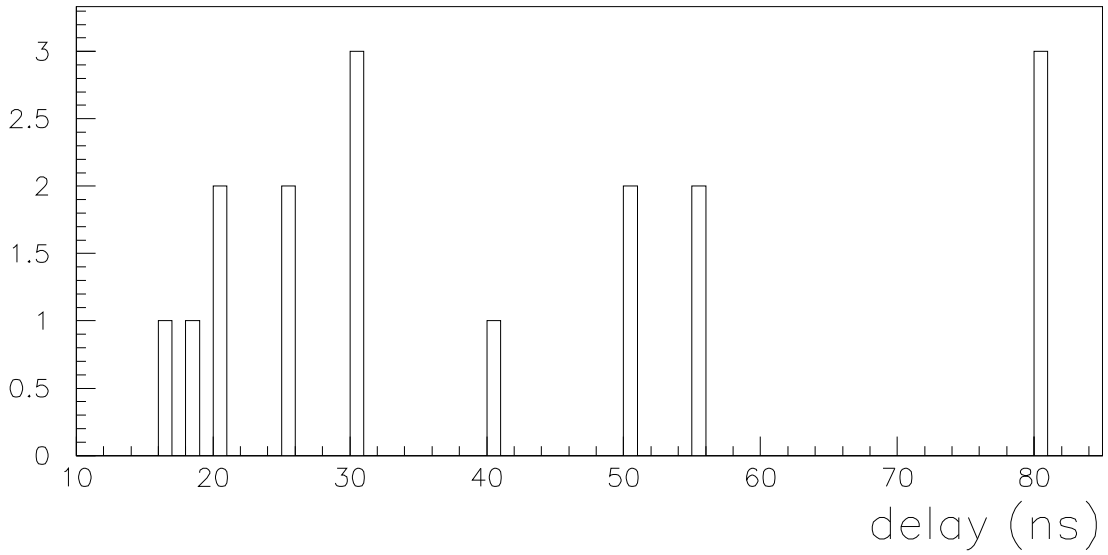

Figure 5.5: Delays as used for the different detectors in PSI.

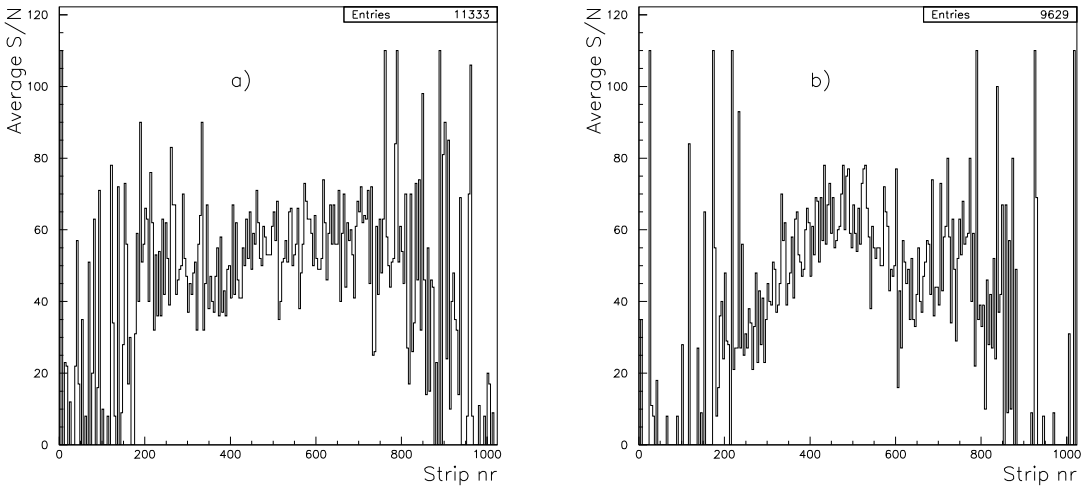

Figure 5.6: Average S/N as a function of the position on the substrate for a) a normal detector and b) a detector with a sagging GEM.

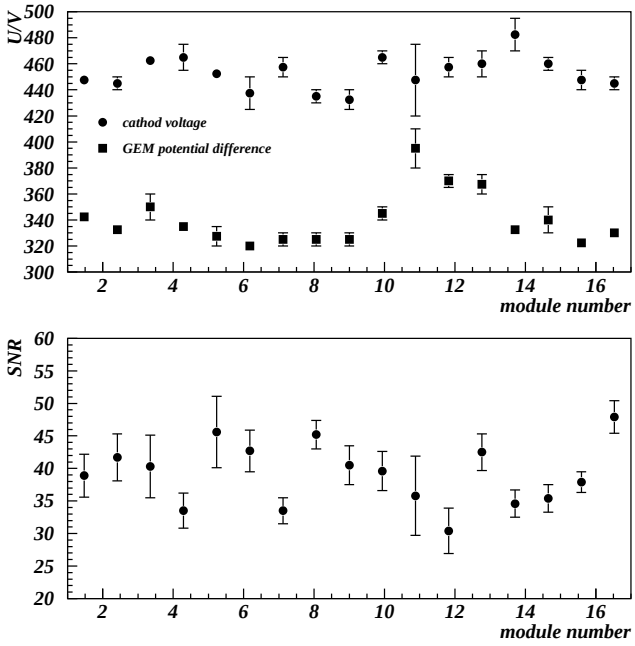

Figure 5.7: Top: Applied cathode voltage and GEM voltage difference for the different modules tested in the MF2 test. Bottom: Corresponding S/N value for the voltage settings shown in top plot.

It was made certain that the sparking rate did not exceed a few (3-5) sparks per hour. Figure 5.8 shows the evolution of the S/N(left) and average noise (right) as a function of time for low and high beam intensity. It is shown for a typical detector with no GEM sag. Some features of this evolution are readily noticed: there is a factor 2 difference between the S/N observed when the detector is irradiated with a low intensity beam compared to when its irradiated with a high intensity beam. In section 5.6, it will be proven that this effect is purely statistical in nature and is an artefact of the cluster selection algorithm.

Secondly the shape of the curves self. A big bump in the beginning of the irradiation period it noticed for the S/N. Also a decrease of the signal at the end of the milestone period is seen as well as a linear increase of the noise with time. Furthermore, variations up to 25% in the signal are noticed. Extensive study of environmental variables like the beam intensity, pressure variations and day night temperature variations yielded no clear explanation of the observed signal fluctuations[75].

A slow aging of the detectors was discarded since all detectors have the same qualitative gain behavior irrespective of their position in the bench. As the difference in irradiation dose between the first and the last module is roughly 50%, aging is not a valid explanation.

The increase in the noise might be partially due to the use of non radiation hard read-out electronics as here a small dependence on the irradiation is observed.

The strips lost versus time are depicted in figure 5.9. The accumulated number of lost anodes for 33 substrates as a function of time is shown. The milestone limit is given by the full line. The slope of the strip loss is clearly below this upper limit. During the whole milestone period, only 24 out of 13321 channels were lost. No clear correlation was found between the sparking rate of the detector and its strip loss as demonstrated in figure 5.10. Note the high number of sparks in detector 45 which lost, on it own, 35 strips. After careful checking of the production history of the substrate, it was found that this substrate was badly cut and that, probably, remnants of the cutting were present on the substrate. This substrate should have been discarded at the substrate selection stage. It is therefore not counted in the accumulated strip loss in figure 5.9.

An other point concerning dead strips is the weakening of the strips due to the presence of a nearby interrupted anode. Indeed, the anodes neighbouring an interrupted anode will collect more charge since the field lines are deviated towards them. Figure 5.11 shows the distance

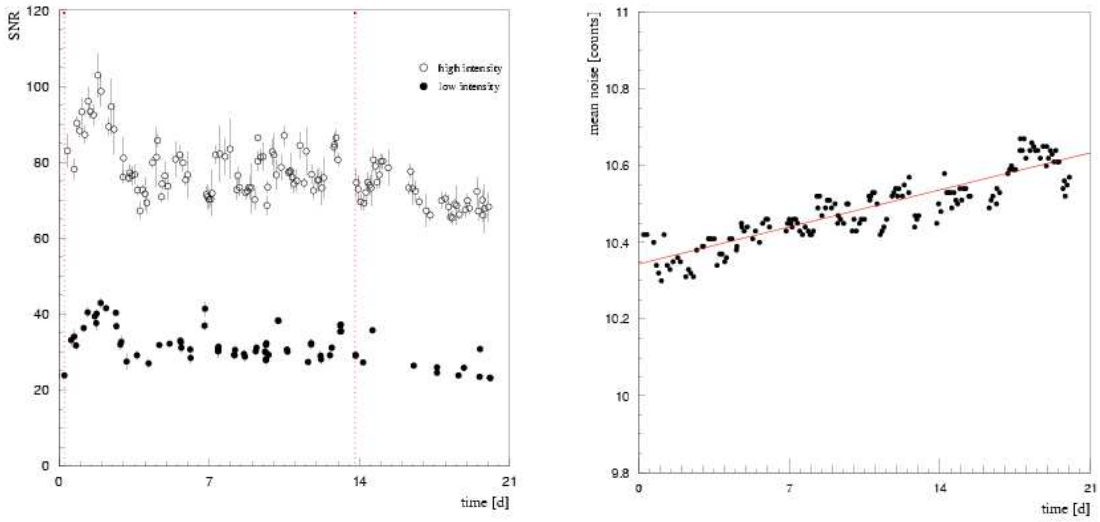

Figure 5.8: Left: S/N as a function of time for both HI and LI for detector 47. The dotted line indicates a change of -10V on ΔV_{GEM} Right: Average noise as a function of time for the same detector.

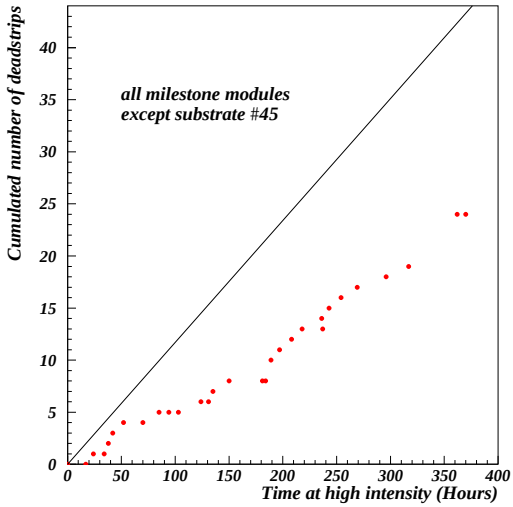

Figure 5.9: Number of anodes lost versus time during the milestone period. The full line corresponds to the milestone ceiling.

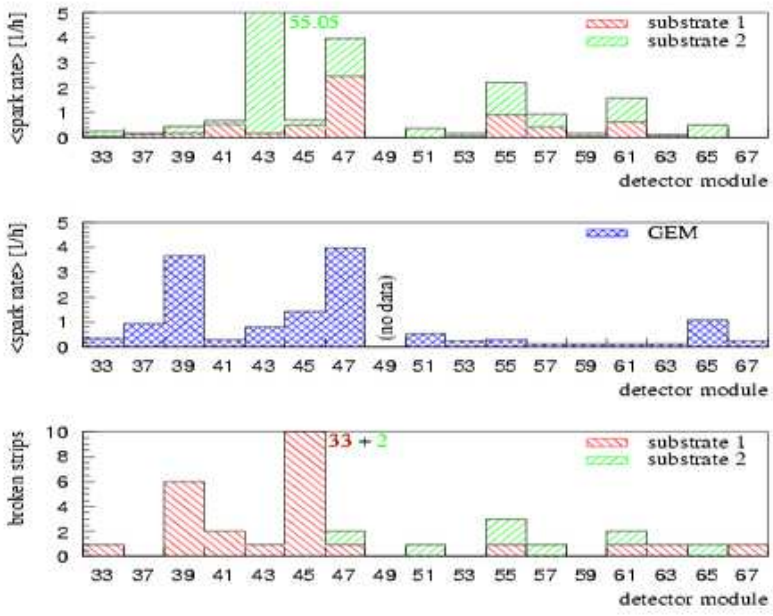

Figure 5.10: Average spark rates (for both the substrates and the GEM) and number of broken strips during the milestone phase.

between the broken strips created during the milestone phase and the nearest broken strip that was already present at that time. No pronounced accumulation at $\Delta strip = 1$ is observed. This picture is even enhanced when taking into account that 3 out of the 4 entries with $\Delta strip = 1$ originate from detector 39 which had a sagging GEM.

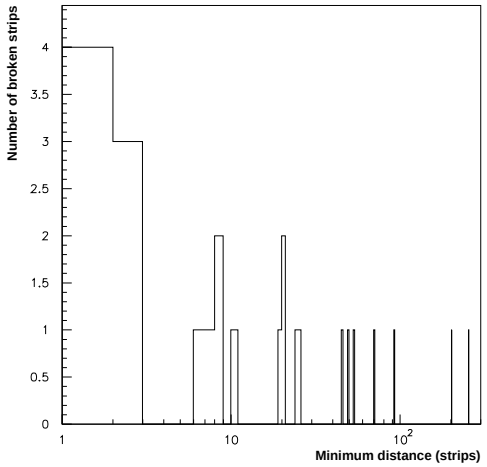

Figure 5.11: Distance between a newly emerging broken strip and the nearest broken strip.

5.5 Operation margins

In the last week of the exposure, some detectors were operated at a higher S/N value than needed for a detection efficiency of 98% in order to reveal the operation margins of this type of detectors. Figure 5.12 illustrates the behavior of a detector module during this period.

Initially, the voltages were raised as to obtain a S/N value that is a factor 1.5-2 higher than the working point. The detectors were left at these settings for 2 days. By increasing the voltages

again, it was possible to attain a S/N of 100 for four of the detector modules. The other detectors were left at a S/N around 60.

It was found that raising the voltages on the GEM electrodes was a safe way to increase the total gain in the detector. In this way sparking rate and strip damages remained low. This was already observed by Fonte et al. [87]. They attribute the effect to the spreading of the electron cloud. As the electron cloud becomes larger, the charge density will reach the critical limit for streamers at a higher value of the total gain (see section 2.1.4.4). They found that the maximal reachable S/N before breakdown (defined as the regime where more than one spark every few minutes occurs) is inversely proportional to the spread of the electron cloud generated by the device used.

The increase of the GEM potential difference widens the electron cloud and therefore higher gains can be attained before sparking sets in.

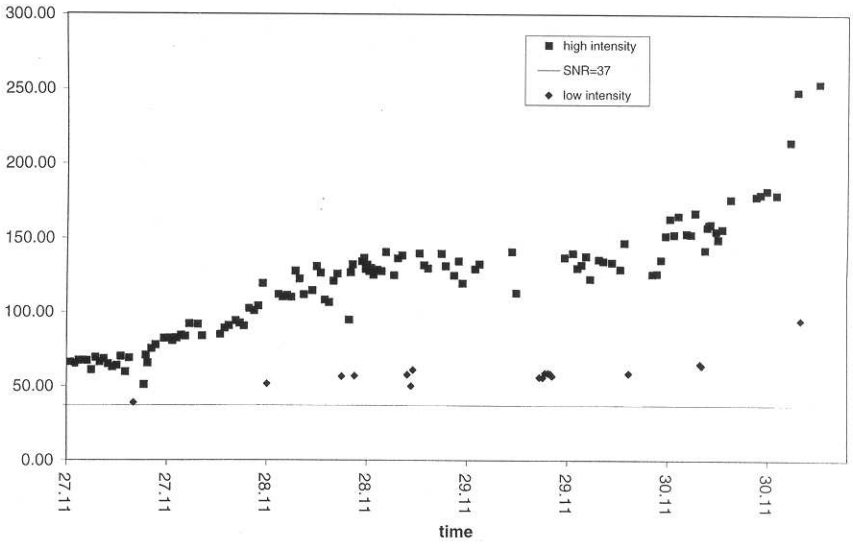

Figure 5.12: S/N of a detector module as a function of time during the margins period.

5.6 S/N determination at high intensity

As observed in figure 5.8 and 5.12, a different value for the S/N is determined at low intensity (LI) and at high intensity (HI). No changes were made to the applied potentials when changing the intensity. The effect was first attributed to pile-up, or the passage of 2 or more particles over the same anode in a time laps that cannot be resolved by the read-out electronics. However, the probability for this to happen is roughly 2% (for an intensity of $9kHz/mm^2$, $200\mu m$ anode pitch, and $10cm$ long strips). S/N enhancements up to a factor 3 have nevertheless been observed, excluding pile-up as a possible cause. The next sections will investigate the nature of the effect by simulations at the detector level.

5.6.1 Out of time particles

When the particle rate crossing the detector exceeds $1kHz/mm^2$ (for $10x10cm^2$ plates and a total preamplifier integration time of 100ns), so called 'out of time particles' can sneak into the S/N distributions. These particles are called out of time because their peaking time in the preamplifier is not synchronized with the read-out of the event. A lower S/N than its nominal value will be recorded.

The resulting S/N distribution will no longer be a Landau distribution. In fact, the distribution looks like figure 5.13a). This distribution was obtained for a detector with a cluster multiplicity distribution as shown in figure 5.13b). It can be seen that the S/N distribution has

no longer a clear maximum that is different from zero. It becomes therefore impossible to define a S/N value only by the use of this curve.

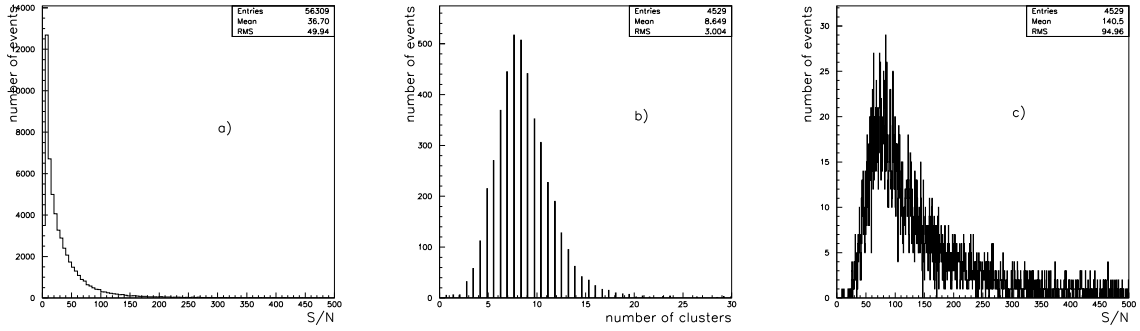

Figure 5.13: a): S/N distribution for a detector whose cluster multiplicity is depicted in b). c) represents the S/N distribution when in each event the cluster with the highest S/N value is selected.

When selecting the cluster with the highest S/N in each event, the Landau distribution is again seen and the S/N is attributed to the maximum probability of the distribution. This is demonstrated in figure 5.13c). It is constructed by taking the cluster with the highest S/N in each event out of distribution 5.13a). It is however not clear that this should be the case. Moreover, the so obtained S/N is enhanced compared to the value obtained at LI by a factor that is detector and intensity dependent.

Choosing the cluster with the highest S/N is mainly motivated by restrictions set by the online monitoring program: this program needs to be fast, so no elaborate tracking algorithm can be used. Furthermore, this criterion allows to recover a landau shape and thus to define a S/N value.

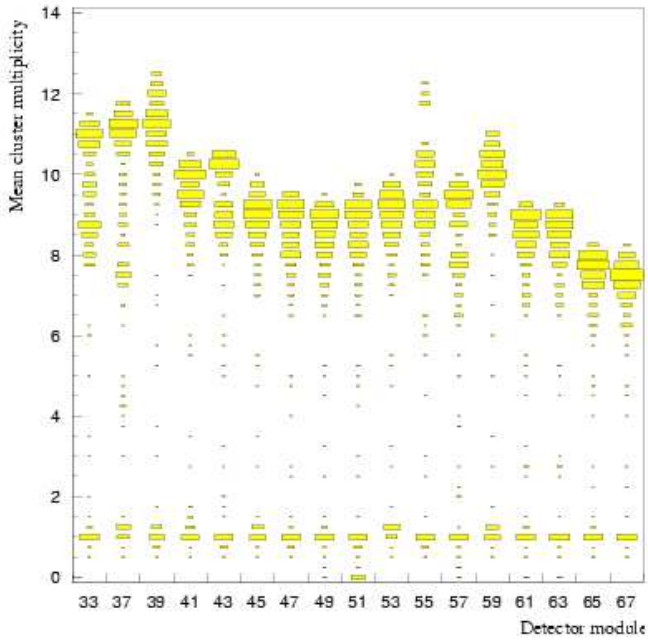

Figure 5.14: Frequency of the mean cluster multiplicity for all detectors over the whole milestone period. The size of the boxes is proportional to the frequency. The broad band with values above 6 represents the HI runs, the band around a value of 1 the LI and the intermediate region represents a few runs taken at MI.

A graph of the average number of clusters in each detector over the whole milestone period

can be seen in figure 5.14. The intensity drops with the detector position in the bench. This is mainly due to the divergence of the beam and the multiple scattering. Nevertheless, some detectors depart from this trend. For instance detector 59. This can partly be explained by an increased number of noise clusters and partly by the increased sensitivity of some detectors with a sagging GEM to out of time particles.

5.6.2 Delay curve

To be able to detect particles with an MSGC+GEM using the premux chip, use is made of a trigger system, usually consisting of a number of scintillators. If a particle traverses all the scintillators, a trigger is given to read out the premux electronics.

As the signal formation is slow with respect to the trigger decision, the read-out sequence is delayed in order to maximize the collected amount of charge.

When there is a mismatch between the peaking time of the preamplifier and the read-out sequence, the signal will be attenuated. This is demonstrated in figure 5.15. The measured S/N value is shown as a function of the delay with respect to the trigger. This curve is usually referred to as the 'delay curve'.

The curve shown in figure 5.15 was taken under irradiation of the substrate with a ^{90}Sr source[80][9]. The delay curve reflects the shaping function of the pre-amplifier which is theoretically represented by:

$$f(t) = \frac{t}{J} e^{-\frac{t}{J}} \tag{5.5}$$

In this, t is the time from the beginning of the signal and J is the CR-RC shaping time. For the Premux, the shaping time should be $50ns$ according to specifications[48]. Nevertheless, the fit returns a value of $41ns$, an under estimate of 20%. However, the χ^2/ndf is as large as 52. The main reason for this is that the error on the points with a low S/N value are underestimated. Furthermore, the point at t=0 still has a S/N over 20 where it should be 0. It can therefore be concluded that the performed fit is compatible with a 50ns shaping time.

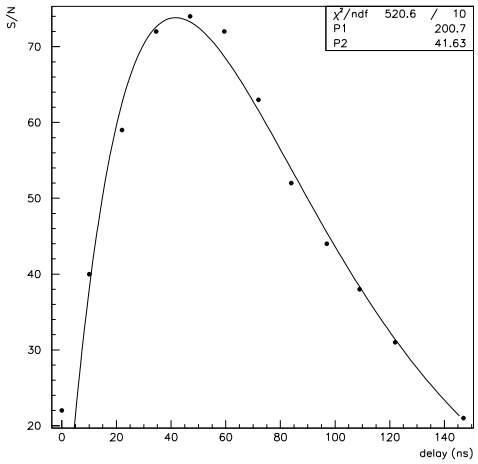

Figure 5.15: Delay curve: measured points and fit to equation 5.5.

5.6.3 Monte-Carlo program

To better understand the determination of the S/N in high intensity beams, a Monte-Carlo program was written.

The program takes a Landau curve, a delay curve and a cluster multiplicity distribution as arguments. For each event, the number of clusters to be generated is randomly selected according

[9]The trigger was given by a coincidence measurement of 2 scintillators.

to the given cluster multiplicity distribution. Once the number of clusters for the event is chosen, the program will select that number of clusters and attribute them a S/N according to a random selection out of the given Landau distribution. The particles are then distributed uniformly over time. However, one 'in time' particle, the alleged triggering particle, is retained. This is an important point. The delay curves were measured during LI runs where only one particle crosses the detector during the read-out sequence. The delays of the detectors were then adjusted as to collect the most charge. In this way the read-out sequence is synchronised with the passage of the triggering particle through the detector. It is therefore assumed that there is always one in time particle. It is the properties of the detector with respect to this particle that we are interested in.

Next, a reduction of the signal according to their position in time is applied using the delay curve. The clusters are then regrouped into a histogram. The cluster with the highest S/N is then selected in each event to regain the Landau shape.

5.6.4 Results

5.6.4.1 Histograms appearance

Two types of histogram have to be reproduced by the Monte-Carlo. The histogram containing the S/N of all the clusters and the resulting Landau curve obtained by selecting the cluster with the highest S/N in each event. The time interval over which the particles were distributed was varied to determine the approximate time distribution from particles that contribute to the observed S/N distributions.

The cluster multiplicity distribution was initially chosen to be a Poisson distribution with a mean value of 8. For each histogram, 20.000 events were generated.

The time interval over which the particles were distributed was equal to 10ns*i, were i was ranging from 1 to 18 (i.e. $\Delta t = 10ns$ to $180ns$). The interval is chosen around the maximum of the delay curve.

When i is small the 'all clusters' histogram looks like a Landau distribution. A clear maximum, different from zero, can be observed. This is due to the small attenuation of the signal as the particles are distributed near the maximum of the Landau distribution. The resulting 'all clusters' histogram will therefore be the sum of a number of Landau curves.

Upon increasing i, more and more particles will see their signal reduced considerably as they arrive more and more out off time. The maximum of the 'all clusters' histogram moves towards zero as the number of low S/N particles starts to become larger. From i=9 onward, the simulated 'all cluster' histogram has the same shape as the experimentally observed one.

However, as in the real experiment, a cutoff S/N value of 4 is maintained to reject noise hits. When i becomes bigger than 11, some particles that are generated are no longer taken into account since their S/N value becomes too small. This is reflected in the simulated cluster multiplicity. Slowly its mean value starts to become smaller than 8, reaching 6.6 at i=18.

An appropriate value for i can althus be found: $i \in \{9, 10, 11\}$, corresponding to $\Delta t \in [90ns, 110ns]$, as expected from the premux shaping function where (fig. 5.15) one can see that the signal is attenuated by 45% when the particle is 50ns out of time.

When this time distribution of the particles is used, the resulting S/N histogram (obtained by selecting the cluster with the highest S/N in each event) has a clear peak that can be fit with a Landau distribution, confirming the observations made in high intensity beams.

5.6.4.2 S/N enhancement

The signal enhancement was experimentally found to be detector dependent and S/N independent.

To prove that the signal enhancement is S/N independent, we will use data from the T9 beam (see section 4.2.1). The intensity of this beam corresponds to the intensity of the low intensity PSI beam, and no intensity variations are performed. However, an estimate of the S/N enhancement can be given by separating the events containing only one cluster form the ones containing more than one cluster.

The reference S/N is then the maximum probability of the distribution of all the cluster found in events containing only one cluster. The enhanced S/N is then the maximum probability of the distribution containing all the clusters obtained by selecting the cluster with the highest S/N value in the events which contain more than one cluster. In the T9 beam the cluster multiplicity of the events with more than one cluster is 3 on average.

The results obtained with the T9 data and a simulation performed with the Monte Carlo program as described in §5.6.3 can be seen in figure 5.16. the figure shows the procentual signal enhancement $=[S/N(more\,than\,one\,cluser) - S/N(one\,cluster)]/S/N(one\,cluster)$

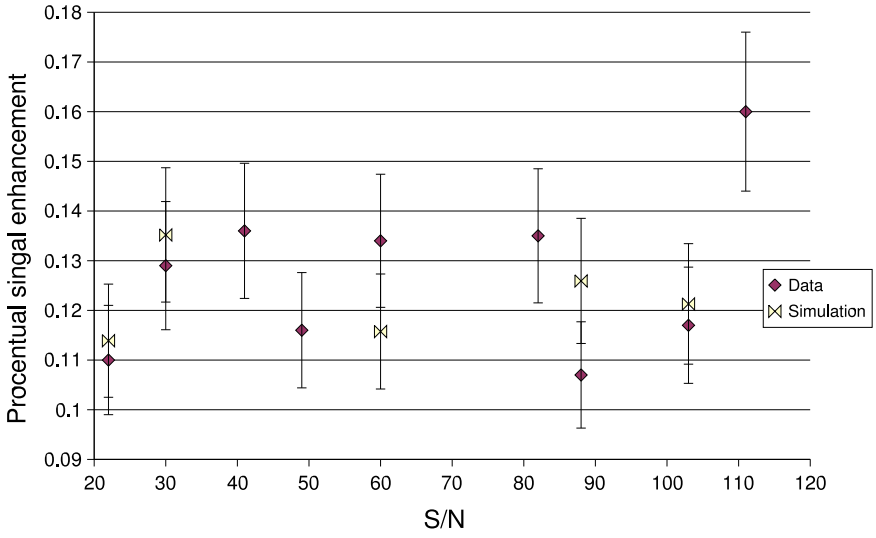

Figure 5.16: Procentual signal enhancement as a function of the S/N. The cluster multiplicity amounted to 3 on average.

In figure 5.17 the S/N enhancement as a function of the average cluster multiplicity can be seen. These results are obtained in the PSI beam. Also here, both simulated and experimentally observed enhancements are shown. As can be seen, the simulated dependence of the signal enhancement on the average cluster multiplicity is in good qualitative agreement with the experimentally observed one.

The data points represented in the figure are actually a straight line fit to the observed average signal enhancements coming from 18 different detectors subjected to 2 different beam intensities. This approach was followed since the experimentally observed signal enhancements can differ by 50% for comparable average cluster multiplicities. This is understood by the influence of the experimentally observed cluster multiplicity distributions and delay curves. The delay curves and the cluster multiplicity distributions are detector dependent. For instance, the peak of the delay curve shifts with respect to the incident particles arrival when the transfer field is changed. Moreover, the delay curve broadens with a decreasing drift field[80].

The cluster multiplicity distribution has its own influence. Cluster multiplicity distributions coming from two different detectors are shown in figure 5.18. The average number of clusters is very comparable (8.5 for the left one and 8.9 for the right one) . It is observed that none of the two distributions fit well to the theoretically expected Poisson distribution ($\chi^2/ndf = 8.5$ (left) and $\chi^2/ndf = 18.5$ (right) probably due to the presence of noise clusters in the distributions. However, qualitatively, the two distributions look different: the right one has more high multiplicity events for instance.

This leads to the conclusion that although the simulation correctly describes an 'average detector', to have a better data-Monte Carlo agreement, each detector should be treated individually. And thus the appropriate delay curve and cluster multiplicity distributions should be fed to the simulation. The result of such a simulation is summarised in table 5.1. In this table the experimentally observe S/N and the simulated one are given. Furthermore, as an indication of the intensity, the average number of clusters is also added.

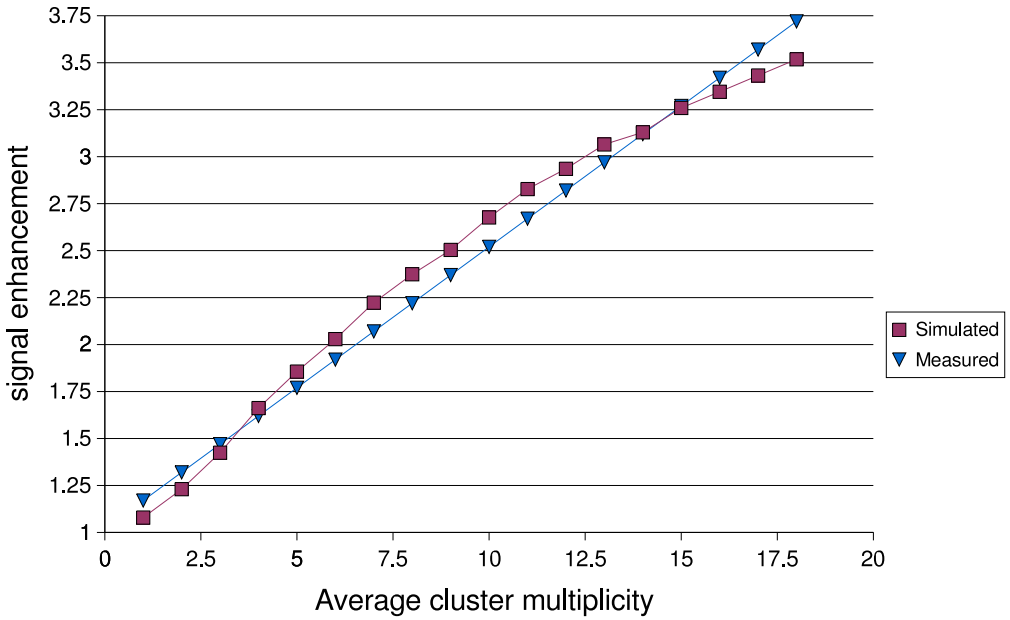

Figure 5.17: S/N enhancement as a function of the average cluster multiplicity.

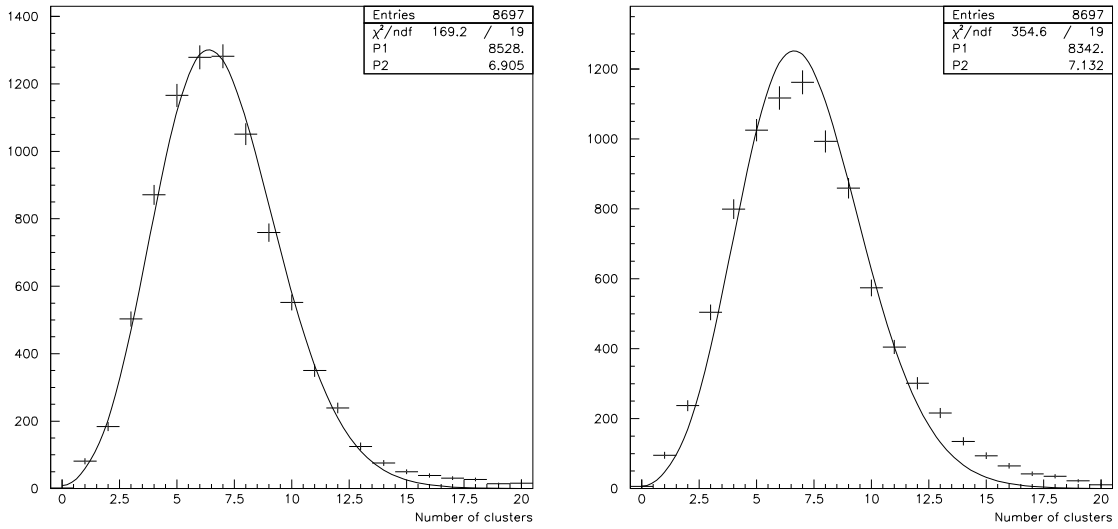

Figure 5.18: Fit of a Poisson distribution to two experimentally observed cluster multiplicity distributions in the PSI beam.

The simulated S/N value reproduces the experimental one, but it is systematically overestimated. The most probable reason for this is the the presence of noise clusters in the cluster multiplicity distribution. These clusters increase the number of generated particles per event in the simulation whereas they don't contribute to the signal enhancement in the experimental case.

detector	av. #clusters	S/N	S/N (sim)	av. #clusters	S/N	S/N (sim)
1	5.2	72	71	8.6	98	100
2	5.6	65	73	9.1	95	109
3	5.2	80	82	8.5	91	102
4	5.6	62	64	8.1	73	79
5	4.6	49	52	8.3	96	105

Table 5.1: Comparison of the measured and simulated signal to noise ratio as a function of the number of particles crossing the detector per trigger.

5.6.5 Conclusions

In this section we showed that the experimentally observed S/N enhancement in high intensity beams is an artefact of the selection procedure used in the algorithm that determines the S/N value. The selection of the cluster with the highest S/N among all present clusters leads to an apparent S/N enhancements even if the signal of a number of them is reduced because the read-out sequence is not synchronised with the peaking time of their signal.

It was possible to qualitatively reproduce the dependence of the enhancement on the cluster multiplicity via the simulation. Unfortunately as a number of parameters, like the delay curve and the arrival time of the out of time particle with respect to the trigger, are known with too little accuracy, differences in the simulated and observed S/N could be as large as 10%.

In section 5.7 an attempt will be made to overcome this problem by a tracking approach. Also a more complete discussion of the problems involved will be given.

5.7 Tracking in a high intensity beam

5.7.1 Introduction

Since a large number of MSGC+GEM detectors were assembled together, one can try to evaluate the tracking capabilities of the technology. Figure 5.19 graphically demonstrates the ability to 'see' tracks with a system of MSGC+GEMs. At low intensity, only one track is seen, whereas at high intensity, a multitude (up to 7 or 8) can be observed.

It is also a great opportunity to determine an important quantity of the MSGC+GEM in LHC like conditions as this has never been done before: we will try to determine the S/N needed for 98% detection efficiency in this environment. But first we will attempt to reconstruct the S/N determined at LI in the HI environment.

In order to be able to correctly reconstruct tracks, the detectors need to be aligned with respect to each other. Also here the Coulomb scattering will be the limiting factor.

5.7.1.1 Multiple Coulomb scattering

A more quantitative tracking was attempted. However, the measurements are severely affected by multiple Coulomb scattering (MCS). Table 5.2 shows the different materials used to fabricate the detector modules and their thicknesses both in μm and in radiation lengths. The total amount of material gives rise to an average MCS angle of $0.00249\,rad$[10]. The maximal distance between two detectors is $10cm$, resulting in a mean deviation of the position of $229\,\mu m$ for a 350MeV/c pion. Therefore the spatial resolution will be completely dominated by MCS. In this beam, it

[10]Equation 2.11 was used to compute the MCS angle

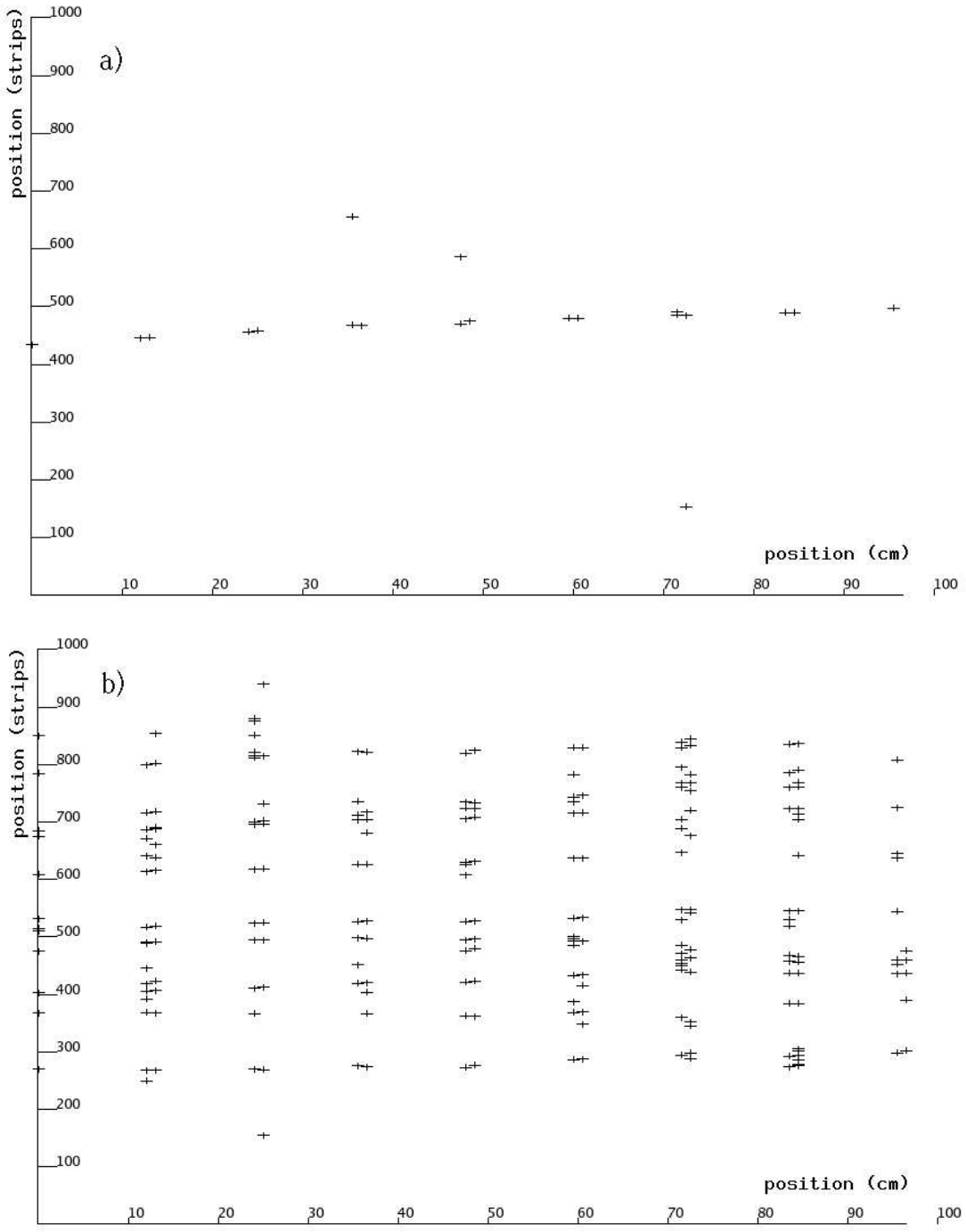

Figure 5.19: Tracks as seen by a setup of 17 MSGC+GEM detectors in low (a) and high (b) intensity. The x-axis represents the beam position of the detectors (in cm) whereas the y-axis represents the position of the reconstructed cluster (in strip numbers).

will thus be impossible to determine the intrinsic spatial resolution of the MSGC+GEM, which is of the order of $40\mu m$.

Material	thickness (μm)	x/X_0
SiO_2	300	$2.5\,10^{-3}$
capton	100	$3.4\,10^{-3}$
Cu	10	$7\,10^{-4}$
polyimide	300	$1\,10^{-3}$
Au	0.02	$2\,10^{-6}$

Table 5.2: Material used in our detector modules, with their respective thickness in μm and radiation length.

5.7.2 Tracking procedure

All the clusters found in the first detector are identified as being a possible starting point for a track. These possible starting points will be called 'seeds'.

In the next detector, a cluster is sought in a space window of 50 strips around the predicted position. This prediction assumes perpendicular tracks and a perfect alignment of the detectors.

When such a cluster is found, a new prediction is done by extrapolating the straight line going through the first two points to the next detector. In a window around this prediction, one again looks for a cluster. If it is found, it is added to the track. The procedure is repeated until the last detector is reached.

Tracks are accepted when they contain clusters belonging to 8 or more different detector modules.

In first order approximation, the particles move in a straight line through our detectors. One can then fit the experimental points to a straight line via the minimization of the χ^2:

$$\chi^2 = \sum \frac{(y_i - az_i - b)^2}{\sigma_i^2} \tag{5.6}$$

In this, z_i are the positions of the detectors in the bench, y_i are the positions of the clusters as determined by the clustering algorithm and σ_i are the experimental errors on the i^{th} measurement. As all the detectors are made following the same technology and mounting procedure, it is assumed that all the measurement errors are the same. This is only valid if the incident angle of the particles with respect to the detector are the same (see §2.2.4).

After having performed a fit on the tracks, the points are compared to the prediction made by the straight line approximation. The difference between the position predicted by the fit and the actual measurement is called the 'residual'. If the detectors are perfectly aligned, the residuals distribution should be Gaussian and centered around zero.

Figure 5.20 shows the standard deviation of the residuals distribution for the different detectors used in the test. The tracking was performed on a LI run in which 1500 tracks were analysed. The differences in the obtained resolutions point to the fact that the fit to a straight line is not the appropriate tool to treat the data. Indeed, as all the detectors were manufactured in the same way, only variations of the level of a few percent are expected.

To investigate this effect further, a Monte Carlo simulation was written. It generates points in the detectors that lie along a track of a particle moving perpendicular to the detector planes when it encounters the first detector. The same tracking and fitting algorithm as described above is then applied to the simulated data.

Several simulation conditions were tried. First tracking was performed on simulated tracks with no MCS present. Only an uncertainty with a standard deviation of $40\mu m$ was added to the simulated points. A second sample was generated with MCS and was treated in two distinct ways: first all the errors on the positions are treated as constant and second an error that is function of the position of the bench is taken into account.

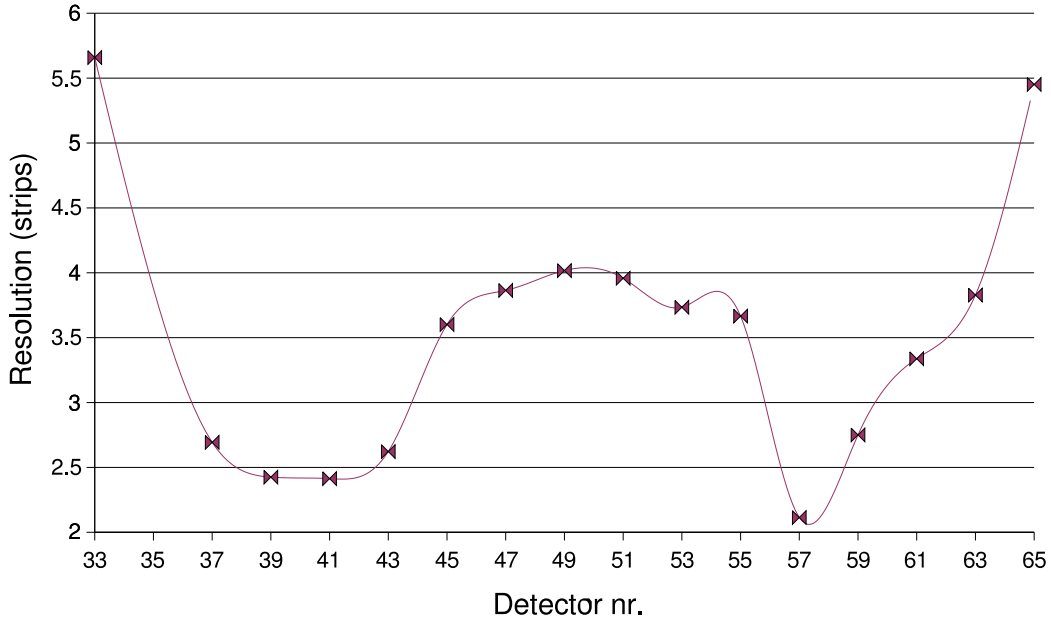

Figure 5.20: Standard deviation of the residual distribution for the different detectors used.

This error on the position in the bench reflects the mean deviation that a particle will have from its position if its trajectory had not been changed by MCS.

Equation 5.6 then becomes:

$$\chi^2 = (Y - HA_x)^T V^{-1} (Y - HA_x) \tag{5.7}$$

where

$$Y = \begin{pmatrix} y_1 \\ y_2 \\ \dots \\ y_n \end{pmatrix}; H = \begin{pmatrix} 1 & z_1 \\ 1 & z_2 \\ \dots & \\ 1 & z_n \end{pmatrix}; A_x = \begin{pmatrix} b \\ a \end{pmatrix} \tag{5.8}$$

V is the error matrix and is given by

$$\begin{aligned} V_{ij} &\equiv < \delta y_i \delta y_j > = \\ &\theta_0^2[(z_i - z_1)(z_j - z_1) + (z_i - z_2)(z_j - z_2) + \dots + (z_i - z_{i-1})(z_j - z_{i-1})] \end{aligned} \tag{5.9}$$

in this, θ_0 is the multiple Coulomb scattering angle as defined by equation 2.11. For the calculation of the error matrix see reference [76].

The spread of the particles in the i^{th} layer can then be calculated as:

$$\sigma_i^2 \equiv < y_i^2 > = \theta_0^2[\sum_{j=1}^{i-1}(z_i - z_j)^2] \tag{5.10}$$

The validity of formula 5.10 for our particular geometry is verified by the same simulation. The result is shown in figure 5.21. A good agreement between Monte Carlo and calculation is observed for an MCS angle of 0.00250. However, when the simulation is compared to the data obtained in a LI run, it is seen that the data has a systematically larger spread. A better data-simulation agreement is reached when an MCS angle of 0.00333 is used. This can be explained by the limited precision with which the average pion momentum is known and the the spread on the momenta of the pions in the beam.

The effect of the different methods on the residual distributions can be seen in figure 5.22. As expected, the standard deviation for residuals obtained with no MCS present is roughly the

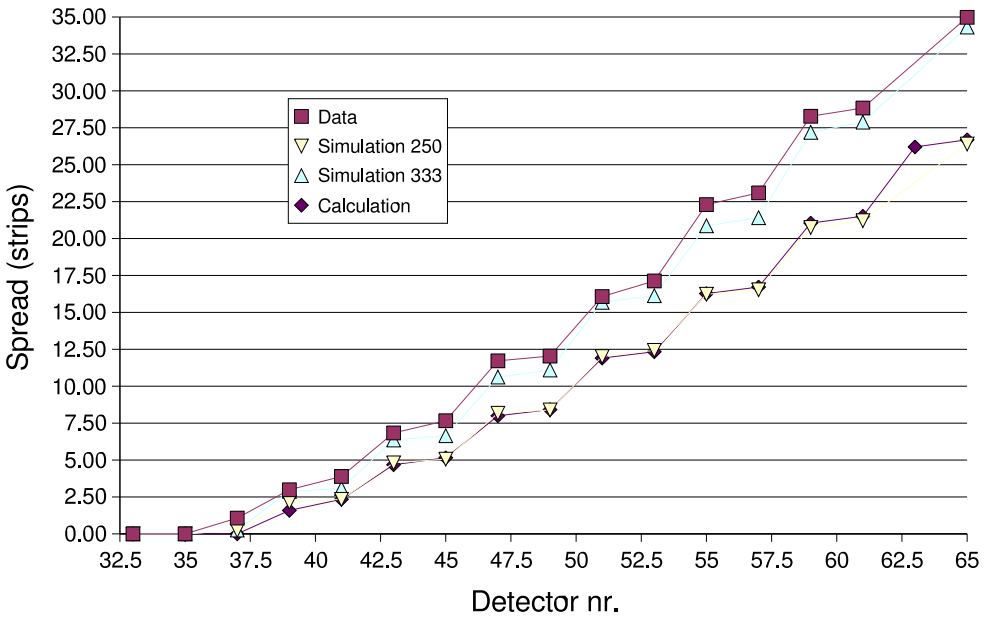

Figure 5.21: Comparison between simulated, calculated and experimentally observed mean spread of the particles due to MCS as a function of the encountered detector. Simulations have been performed for mean MCS angles of 0.00250 and 0.00333.

same for each detector and varies around $40\mu m$. When MCS is turned on, a structure like the one observed in the real data (added for comparison) is also noticed.

This can be understood by the path the particle follows due to MCS. It is no longer a straight line, but has, in general, some bending points. If one tries to fit a straight line through such a path, the line will be drawn in such a way as to minimize the sum of the squares of the distances between all the points and the fitted line, resulting in the observed residual distributions.

Considering the spread of the particles as an error on the measurements, it is seen that the first two detectors are treated as if no MCS was present, the next 7-8 detectors have errors of the order of the MCS error ($\approx 250\mu m$) and the following detectors almost don't contribute to the fit as here the error on the position becomes too large.

It is unfortunately impossible to treat the data with MCS in such a way that al detectors are treated on the same footing when using the hypothesis that the particle travels in a straight line. Therefore an alternative description of the particle track was tried.

Linear splines

The path of the particles moving through the detectors can be described by a succession of linear line segments, whose direction can change in a given number of points (for instance at the detector plane). The mathematical tool to describe such a movement are piecewise linear splines[98].

First, a set of $N+1$ knots is defined on the interval $[a,b]$ on which the interpolation will be performed: $K = \{z_0, z_1, ..., z_n\}$. The knots are a set of points in which the straight line can change its direction. Then, the spline l_j is defined as:

$$l_j(z) = \begin{cases} 0 & a \leq z \leq z_{j-1} \\ \frac{z-z_{j-1}}{z_j-z_{j-1}} & z_{j-1} \leq z \leq z_j \\ \frac{z-z_{j+1}}{z_j-z_{j+1}} & z_j \leq z \leq z_{j+1} \\ 0 & z_{j+1} \leq z \leq b \end{cases} \tag{5.11}$$

Interpolation of $f(z)$ then becomes:

$$f(x) = c_0 l_0(x) + ... + c_N l_N(x)$$

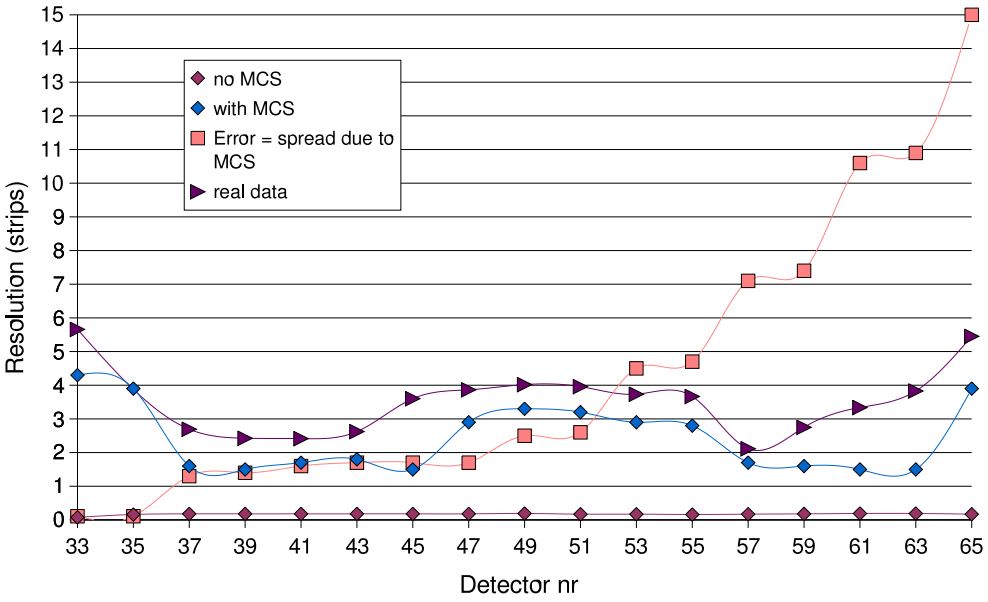

Figure 5.22: Resolution as a function of detection plane for four different methods used.

The parameters are again found via the minimization of the χ^2 function, which this time takes the following form:

$$\chi^2 = \sum_{j=0}^{M} \frac{1}{\sigma_i^2} \{ \sum_{i=0}^{N} c_i l_i(z_j) - f_j \} \tag{5.12}$$

Where f_j are the experimental data points (in our case, the positions of the clusters in the detectors).

As expected from the particular setup, a set of 9 knots is sufficient to recover the correct resolution. Indeed, the set-up can be viewed as composed of 9 scattering planes, 10 cm apart. Each scattering plane is composed of 2 detectors, $1cm$ apart. These sets of 2 detectors will now be called 'detection plane'.

5.7.3 Detector alignment

The preceding studies were performed on simulated events in order to find a proper way of aligning the detectors. In order to correctly align the detectors, they all should be treated in the same way. This is clearly not the case with the fit to a straight line as the obtained resolutions differ from one detector to another. If we use splines with 9 knots, we can obtain the same resolution for every detector.

Due to the large MCS and the absence of 2 dimensional information about the path of the particles, only an alignment of the detectors in the direction perpendicular to the strips will be performed. No adjustments in the direction along the strips or angle corrections will be performed.

Problems arise however when one tries to align the detectors using splines. These are set-up related problems. For clarity, we consider two kinds of misalignment: misalignment of the two detectors within a detection plane and the misalignment of the detection planes with respect to each other.

If the two detectors within a detection plane are mis-aligned, the spline will interpolate between the two of them. However, if one does not take into account the detector under study, interpolation will be at the position of the second detector. If we now compute the difference between the interpolation and the measured value, we get the misalignment between the two detectors in a detection plane. A cross check is made by verifying that the misalignment of the second detector (computed in the same way) should only differ by their sign.

When one tries to use the same method for alignment between detection planes, none of the two detectors in the detection plane being aligned can be used. The matrix inversion involved becomes a problem due to the many zero elements. In many cases the matrix becomes singular and thus inversion cannot be performed.

Another method was then adopted. A least-square fit was performed using only the information coming from the detection planes right in front and directly behind the detection plane under study. Combining these two methods, it was possible to align the detectors. The results of the alignment are given in table 5.3. This table is constructed as follows: in the first column, the detector under test is noted. The numbering scheme follows the numbering as was used during the milestone test. A few detectors are not represented in the table: the first one: all detectors are aligned with respect to this detector; the second one: this was the detector equipped with IMEC substrates. Detectors 55 and 57 have a non typical behavior, therefore, only one of them was included. Due to technical problem with the clustering software, the last detector, 67, could not be included in the analysis. This naming scheme will be used throughout the rest of the chapter.

The second and third columns give the mean residual and standard deviation to this mean when calculated using the spline method. The forth column displays the number of events used. Columns 5 to 7 are analogue to 2 to 4, only here the linear interpolation method is used. Detector 65 could not be analysed using this method due to the absence of a detector behind it. As can be seen, most average values agree with 0.

det. nr	mean (strips)	stdv (strips)	#	mean (strips)	stdv (strips)	#
37	-0.0150592	1.95156	1342	0.0044242	2.50051	1339
39	0.013812	1.78891	1342	-0.0018298	2.66958	1339
41	0.135833	3.64988	1461	0.148037	2.08335	1458
43	-0.0151884	2.69348	1368	0.152937	2.15244	1365
45	0.09636	2.58761	1470	0.0701945	2.01899	1424
47	-0.096578	2.60027	1477	-0.023285	2.47636	1443
49	0.10787	2.7285	1477	0.0992313	1.989	1474
51	-0.092451	2.3552	1477	-0.195221	2.53268	14474
53	0.0425291	2.10516	1318	0.0561715	2.51369	1207
55	-0.0425211	2.10518	1318	0.045298	2.24899	1207
57						
59	-0.904362	19.80246	1366	0.159864	2.05261	1366
61	0.0646506	1.88933	1389	0.0252245	1.89786	1246
63	-0.0690364	1.99734	1302	-0.0057511	1.94267	1218
65	-0.458381	12.7351	1302			

Table 5.3: Alignment of the detectors: The 2^{nd} column gives the average residual when using spline. Column 3 gives the standard deviation of this distribution and column 4 the number of tracks used. Column 5, 6 and 7 are the analogue of 2,3,4 but now using the linear interpolation as described in more detail in the text.

5.7.4 S/N at HI

As discussed in section 5.6 the S/N determined at high intensity is enhanced by a factor 2 to 3. It was argumented that this effect is purely statistical in nature and is due to the inaptitude of the algorithm used to identify the triggering particle.

The question arises if one can determine which has been the triggering particle when using the information coming from the entire set-up and thus being able to directly determine some important properties of the detector, such as the S/N and the efficiency, in a HI run. The tracking algorithm described in the previous section was used in an attempt to do so. The algorithm was

tried on runs taken in two different intensities: an intermediate intensity ($2.5kHz/mm^2$) that will be referred to as MI in the rest of the text and high intensity ($5kHz/mm^2$) .

As expected, the number of tracks found in an event by the algorithm scales with the intensity. At MI this amounts to 3.5 and at HI, this amounts to 7.5 as can be seen in figure 5.23b) and c). Also shown (figure 5.23a) is the number of tracks in LI, with a mean value of 1.1, as expected from the particle flux.

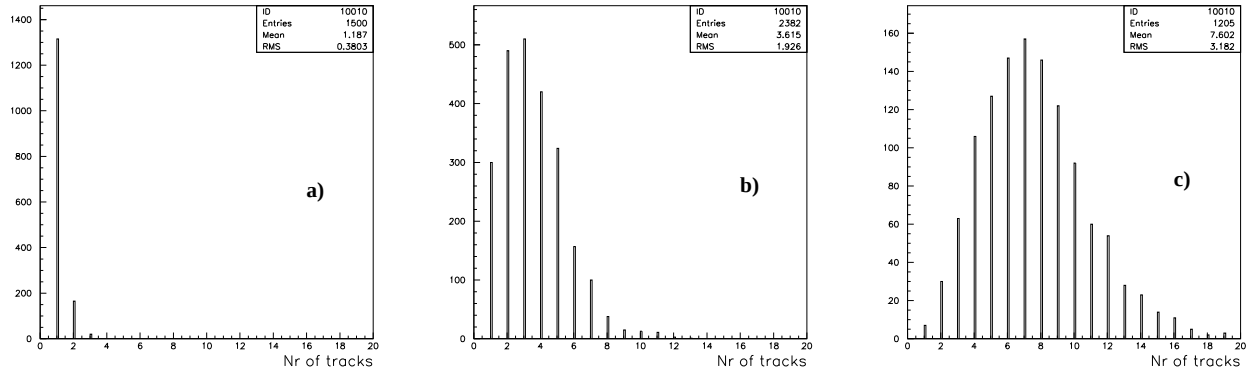

Figure 5.23: Number of tracks identified in a)LI, b)MI and c)HI.

We now have a number of tracks but still aren't able to determine which one belongs to the triggering particle. A way to differentiate between them is based on the mean S/N value of the track. This value is defined as:

$$\overline{S/N} = \sum_i (S/N)_i / \sum_i 1 \tag{5.13}$$

where i runs over all distinct detectors in the track. The track with the highest mean S/N value is associated to the triggering particle. No additional quality conditions can be set on the track since almost all the tracks have bending points due to MCS. The effect of this choice can be seen in figure 5.24. The average S/N value for the track with the highest average S/N value is given for LI, MI and HI. The average values for these distributions are: 63.4 for LI, 65.6 for MI, and 69.7 for HI. This means that we have effectively reduced the average S/N enhancement from 1.7 (MI) and 2.5 (HI) to 0.03 and 0.10 respectively by introducing the tracking algorithm.

Figure 5.25 shows the average S/N for the track with the highest average S/N, the one but highest S/N and the two but highest S/N in a) LI, b) MI and c) HI. It is observed that both for MI and HI the three distribution overlap quit a lot. It is therefore not obvious that our choice of the track with the highest average S/N value is a good one. In the next section we look at this problem both with simulations and data.

5.7.4.1 Monte Carlo

A first step is to investigate the methods used in a simulation of the set-up. We will investigate the effect of choosing the track with the highest mean S/N and determine if this track really identifies the triggering particle.

For each simulation, a number of detectors and a number of tracks are specified. The program will then, for each event, generate a number of tracks that is Poisson distributed with a mean value given at the start. For all detectors in the track, a cluster will be generated with a S/N value that is distributed as a Landau with a maximum probability value of 46. The tracks are then uniformly distributed over time and an attenuation coefficient, based upon an idealised premux CR-RC shaping function with a rise time of $50ns$, is then applied to the whole track. This procedure is the same as used for clusters in the determination of the S/N enhancement factor (§ 5.6). Next, the tracks are classified according to their mean S/N value as defined in formula 5.13.

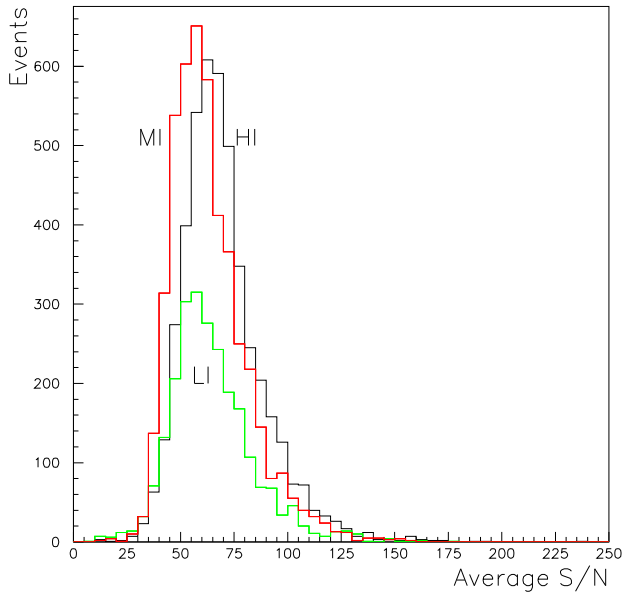

Figure 5.24: Average S/N value of the track with the highest average S/N in HI (black), MI (red) and LI (green).

To reconstruct the LI value from a HI run, the following procedure is followed: first, the track with the highest mean S/N is determined. For all clusters in this track, the S/N is added to a histogram representing the detector to which the cluster belongs. This histogram is then fitted to a landau as usual. The result is shown in figure 5.26. The full line is set at a S/N of 46, representing the LI S/N value of each of the detectors. It is seen that, even though the reconstructed S/N is decreasing very rapidly with the number of detectors, there still is an overestimate of this value by about 5%, even with 15 detectors per track and only an average of 3 tracks per event. This enhancement is a consequence of the selection performed. Note that if only 1 detector is present in the track, the signal enhancement as described in section 5.6.4.2 is found.

As the S/N value is reconstructed rather well, one can hope that the track with the highest mean S/N value will correctly identify the triggering particle. Figure 5.27a) shows that this is not the case. The probability to correctly identify the triggering particle[11] is shown as a function of the number of detectors contributing to the track. It is depicted for different intensities, here represented by the mean number of tracks per event. For 8 tracks, on average, per event (roughly corresponding to HI), and 18 detectors per track, the probability to identify the in time particle is 45%. When the mean number of tracks is reduced to 4 (roughly corresponding to MI) this probability increases to 75%. The selection of the tracks with the highest average S/N thus increases the probability to identify the in time particle from 12.5% to 45% at HI and from 25% to 75% at MI[12].

Figure 5.27b) shows that the reconstructed S/N value is not correlated with the correctness of the identification of the triggering particle. Indeed, it shows the reconstructed S/N value as a function of the probability to correctly identify the triggering particle. One can see that for the same identification probability, a wide variety of reconstructed S/N values are possible. For instance, for a correct identification probability of 50%, the reconstructed S/N is off by 50 to 170% from the real (LI) value, depending on the number of detectors contributing to the track (when using 18 and 1 detectors respectively).

So, if enough detectors are present, a good estimate of the LI can be given, irrespective of

[11] The probability to correctly identify the triggering particle was calculated as the number of times the algorithm correctly identified the in time particle divided by the number of events generated.

[12] The comparison is made with a random selection of the tracks.

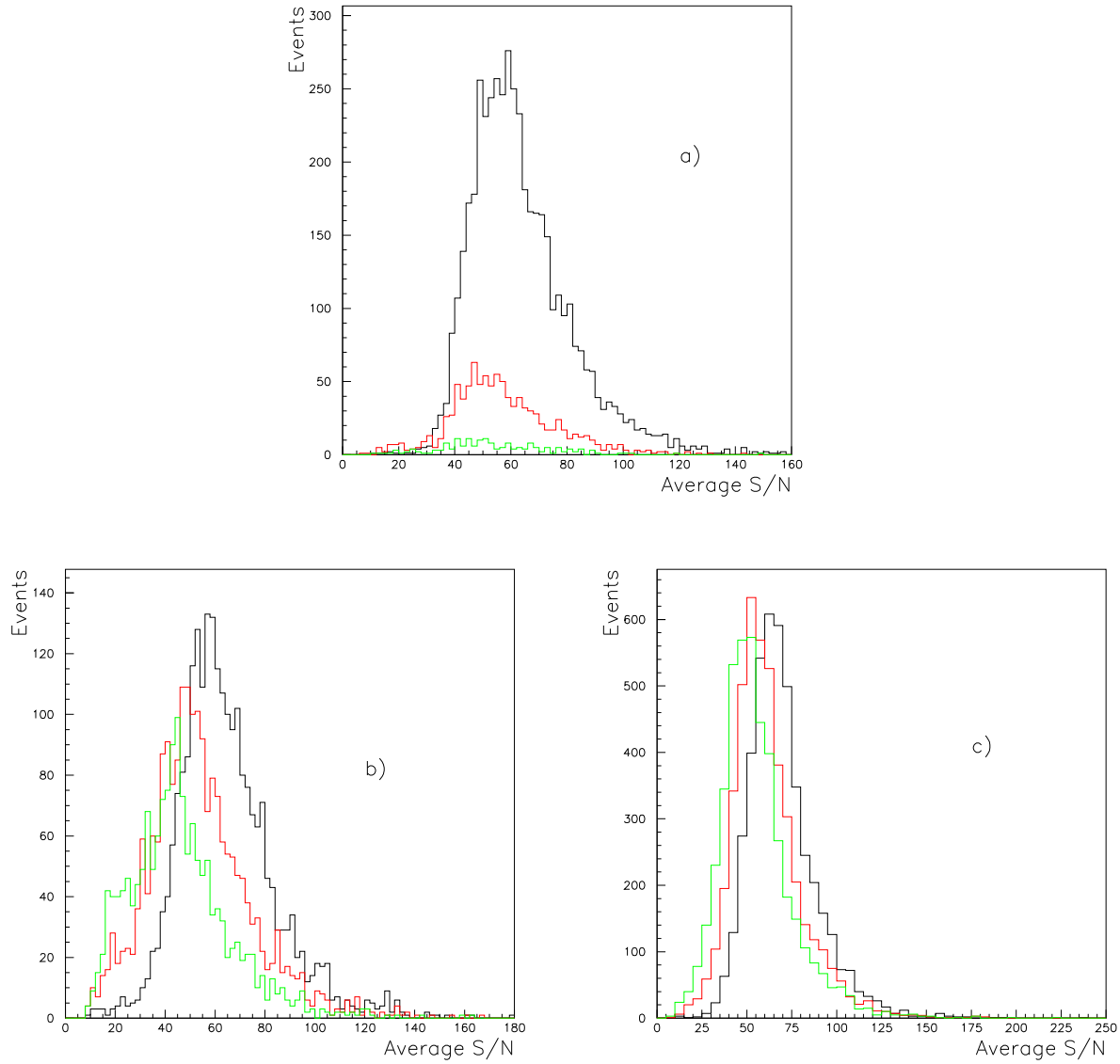

Figure 5.25: Average S/N for the track with the highest average S/N (black), the one but highest S/N (red) and the two but highest S/N (green) in a) LI, b) MI and c) HI.

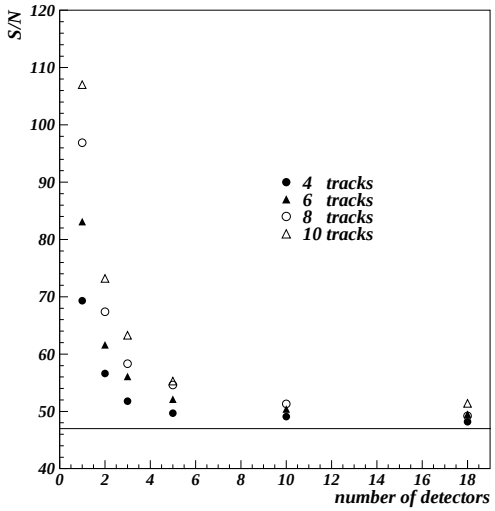

Figure 5.26: Reconstructed S/N value of the test detector as a function of the number of detectors contributing to the track, for different beam intensities. The beam intensity is represented by the average number of tracks.

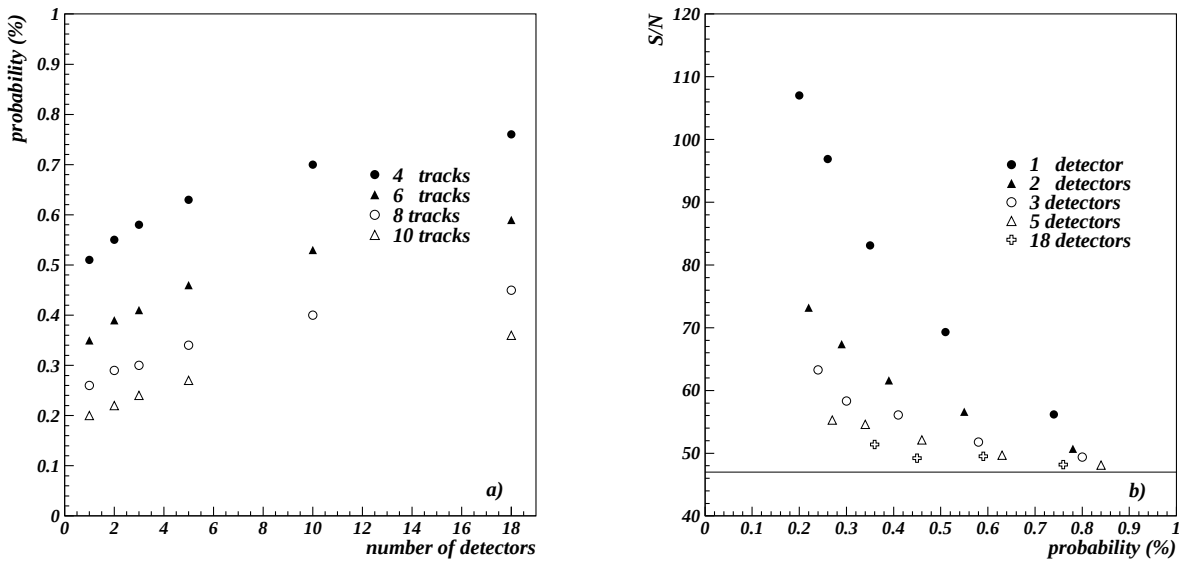

Figure 5.27: a) Probability to find the triggering particle as a function of the number of detectors in a track and b) S/N as a function of the probability to find the triggering particle, both for different beam intensities (represented by the mean number of tracks per event).

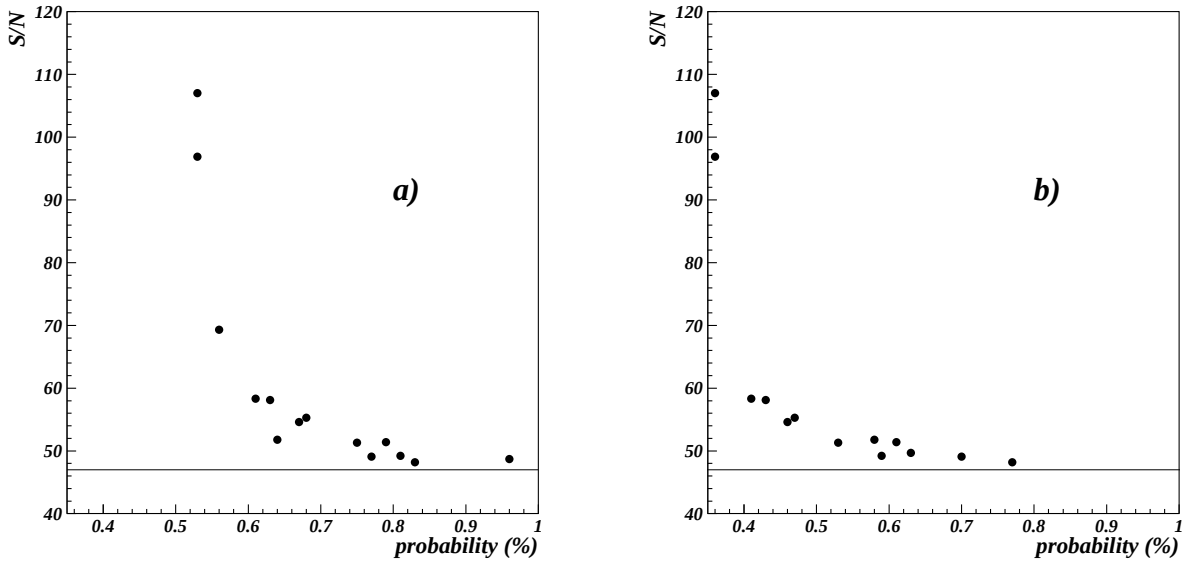

Figure 5.28: S/N as a function of the probability that the cluster with the highest mean S/N was attenuated by less than a) 10% and b) 5%; both for different numbers of detectors contributing to the track.

the intensity and the correct identification of the triggering particle. Figures 5.28a) an b) help us understand how this is possible. In these figures the reconstructed S/N is shown as a function of the probability that the track with the highest mean S/N was attenuated by less than a) 10% and b) 5%[13]. This is equivalent to saying that the track with the highest mean S/N arrived in a time interval [-19.6ns,26.6ns] and [-14.4ns,17.8ns] respectively, around the peaking time of the premux chip. This means that if, on average, the track with the highest mean S/N lies within these time intervals, a good estimation of the real S/N value can be given. For this to be possible the rate must be small, or the number of detectors must be large.

One can reinterpret the result as follows: upon increasing the number of detectors, the selection will be able to select particles that are less and less out of time. However, due to the shaping function of the electronics, a number of equivalent tracks will remain. These equivalent tracks are only slightly out of time with respect to the trigger and can therefor not be distinguished from each other by the electronics.

In conclusion to the Monte Carlo study of the set-up, we would expect that, using the above defined cut, a constant signal enhancement of 5% in MI and 10% in HI should be found.

5.7.4.2 Dependence on the algorithm used

Trying the above described method on real data, did not result in a increase of 10% of the S/N in HI and 3% in MI as predicted by the Monte Carlo. Therefore, the possible reasons were investigated.

In order to investigate the dependence of the S/N reconstruction on the algorithm used, the tracking was performed in two directions. Once taking detector 33 as a seed and trying to find a track ending in detector 65, and reversely, starting off at detector 65 as a seed and then proceeding towards detector 33 as the end point.

The relative difference of these two S/N determinations (i.e $(S/N_{65} - S/N_{33})/S/N_{33}$) in the 3 studied intensities is shown in figure 5.29. At LI, both algorithms determine the same values for the S/N, within $\pm 2\%$. At MI and HI the determination is the same within $\pm 5\%$. However, the S/N determination seems to give an increased value for the seed detector in both algorithms of roughly 10%. This can again be explained by the choice the algorithm can make. Indeed, all

[13]This probability is calculated as the number of events in which the track with the highest mean S/N value was attenuated by less than 10% (5%) divided by the total number of events generated.

the clusters found in the seed detector are labeled as seeds. If 2 seeds are found within a space window of 25 strips from each other, only the cluster with the highest S/N is taken into account. This is done to reduce the number of tracks that share most of their hits. Due to this choice the seed detector has a slightly higher S/N value.

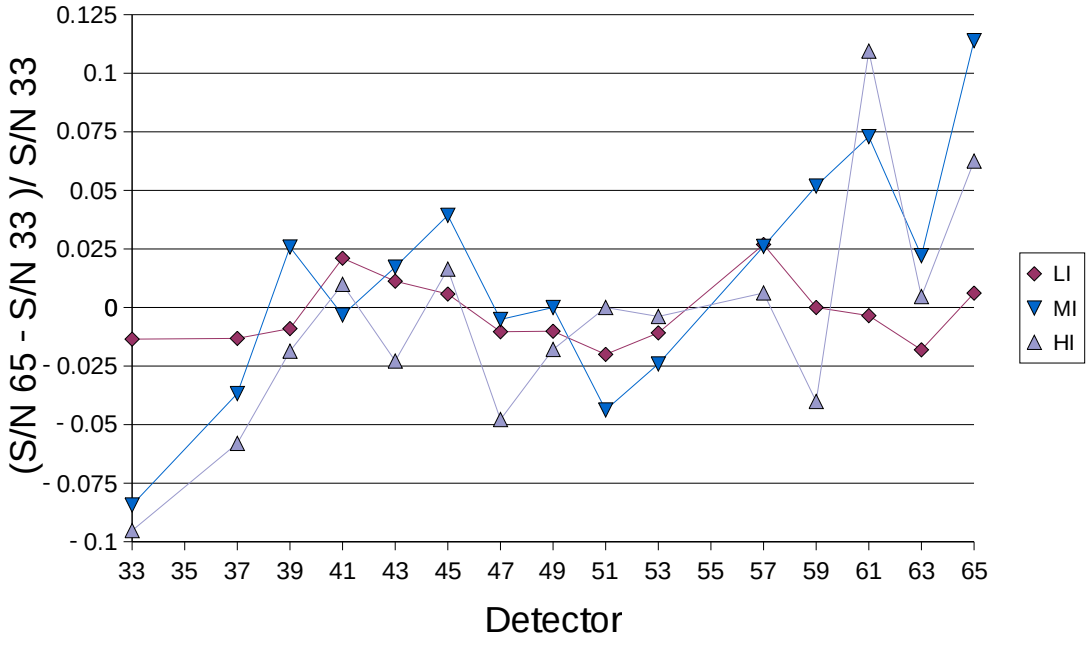

Figure 5.29: $(S/N_{65} - S/N_{33})/S/N_{33}$ for all detectors in LI, MI and HI.

5.7.4.3 Gain uniformity and stability

In this section we will investigate the gain uniformity (across strips) and stability (in time) of the detectors. To do so, only runs at LI will be used, as here the track identification is easy and there is no mistake possible in the identification of the triggering particle because, on average, there is only one track per event (see figure 5.23a)).

Figure 5.30 shows the S/N recorded in 3 different LI runs. The time interval between the first and the last run was approximately 12 hours. Fluctuations as large as 10% between the 3 determinations are noticed. The two possible causes for these variations are the uncertainty on the determination of the maximum of the Landau distribution and non-uniformities of the gain along the strips. Both will now be further examined.

To estimate the error on the Landau fit parameter, a resampling method[109] was used. This method consists in choosing randomly n measurements out of the available m (n<m) measurements and determining the relevant properties of the obtained distribution. This procedure is repeated several times in order to have an estimate of the variation of the quantities involved. In our case we choose n events and put them in a S/N distribution for which the maximum probability is computed through a fit to a Landau. The distribution of all these maximum probability values is distributed as a Gaussian with a standard deviation that represents the error on the fit.

The errors obtained in this manner for the 3 different intensities can be seen in figure 5.31. As is noticed, the average error on the S/N is 3% at LI, 6.5% at MI and 4.5% at HI. The difference between LI and MI,HI errors is understood by an increased number of noise clusters in the distributions. These are the result of a bad tracking. It is estimated that 10% of the clusters are affected. The difference between MI and HI errors is due to the reduced amount of events present in the MI distributions as this beam was used only for a short period of time.

To study the uniformity of the gain across the strips, the three LI runs mentioned in the

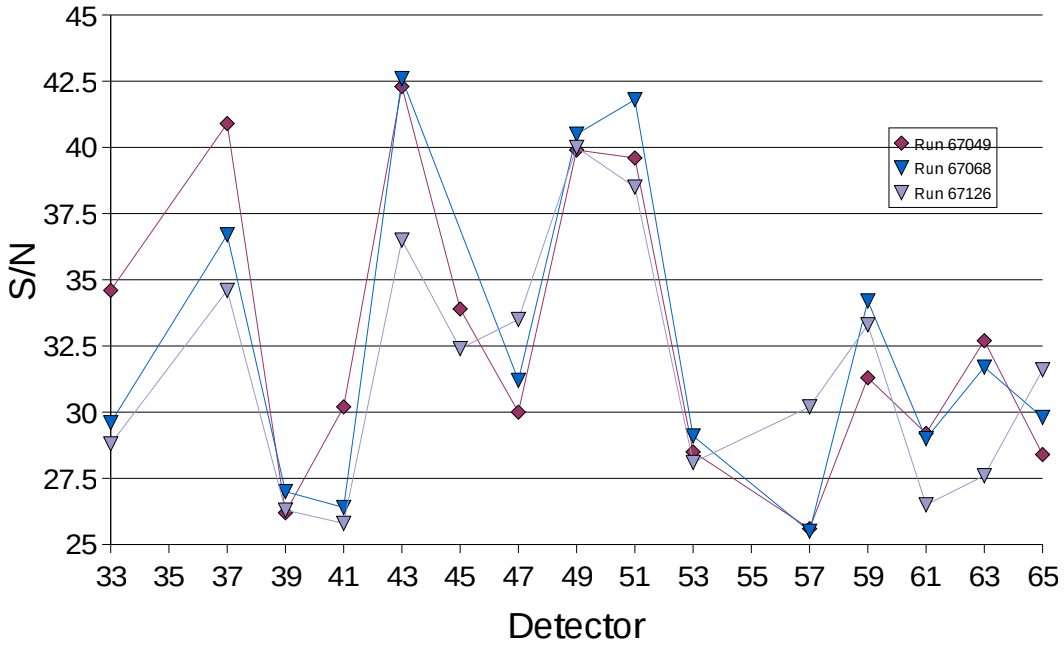

Figure 5.30: S/N for all detectors under study, for 3 different LI runs.

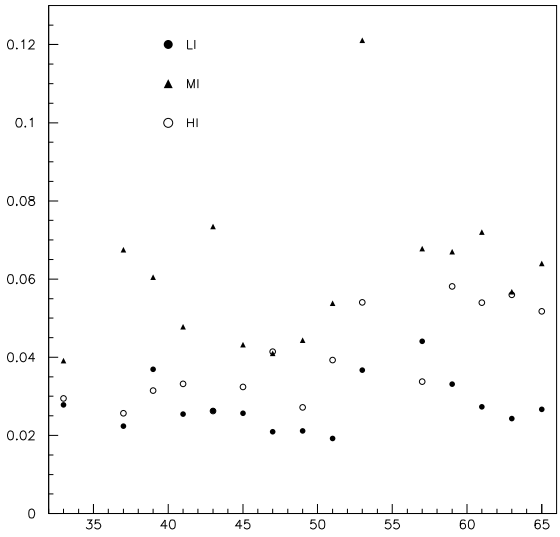

Figure 5.31: Error estimation on landau fit for all the detectors under study.

previous paragraph were combined into one. Tracks were formed and for every cluster belonging to a track, its position and S/N value were recorded. Next, histograms were formed containing the S/N values of a certain detector for clusters whose center of gravity was in the interval $]x_0 x_1]$. As no information was available about the position of the cluster along the strip, this defines a surface of $(x_1 - x_0) * 10cm$. Here, we cannot use the strategy followed in section 5.3 were we determined the average S/N value for every strip. Indeed, to be able to fit a Landau distribution at least 800 data points should be present, whereas per strip, only 7 to 10 data points are present in the data samples used. Therefore a value of $\Delta x = 100\, strips$ was chosen.

Figure 5.32 shows the S/N for all detectors under test for $\Delta x = 100\, strips$, roughly corresponding to an area of $20cm^2$. The spread on the obtained values (i.e. their standard deviation divided by their mean) are represented in figure 5.33.

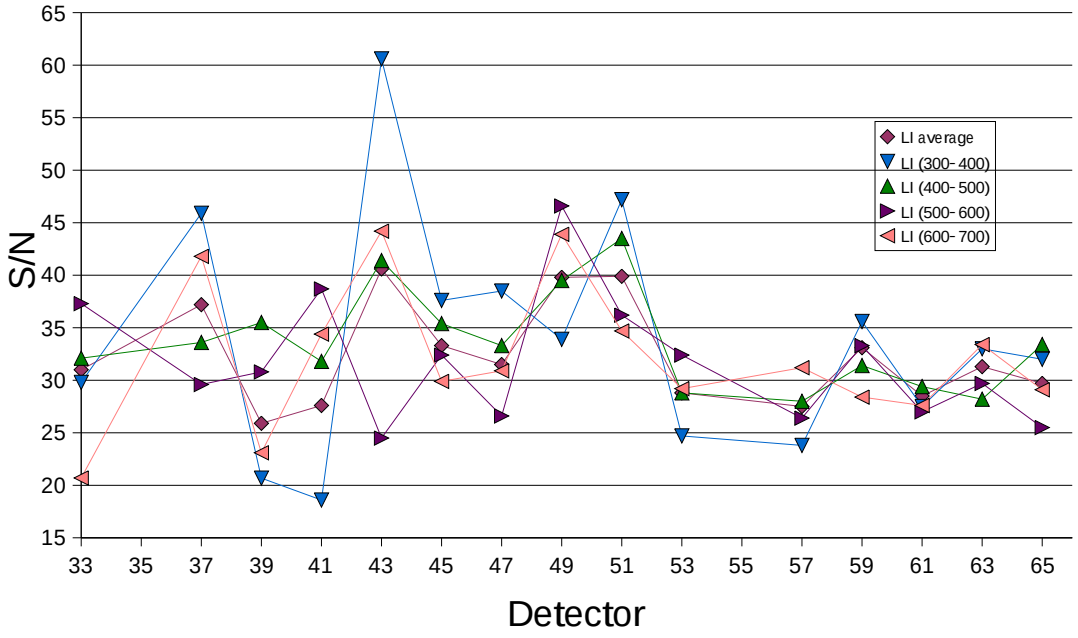

Figure 5.32: S/N for all detectors, for different areas of the detector that were irradiated. The considered surface was approximately $20cm^2$. The numbers in the legend represent the strips used for.

Huge variations in gain are noticed. Detector 43 for instance has gain variations over its surface that are over a factor 2 (minimum S/N=25; maximum S/N=60). It has been proved that MSGCs (including wedge shaped MSGCs) have a good gain uniformity over their surface ($\pm 10\%$) (see for instance [55]). It has also been shown that the gain of a well stretched GEM foil can have a gain uniformity of $\pm 10\%$ over its entire surface[70]. However, small variations in the GEM hole diameter give rise to large gain variations. Actually, the gain of the GEM increases exponentially with the hole diameter[69]. A measurement of the diameter of the GEM holes of the GEMs in our detectors revealed diameter fluctuations of $5\mu m$ from hole to hole. This is expected from the the manufacturing procedure which is based on PCB (Printed Circuit Board) techniques. When hole diameters in a region of approximately $1mm^2$ are compared, difference of $2\mu m$ on the average diameter were observed. Therefore gain fluctuations of 20 to 30% are to be expected. However, to account for the observed variations in gain a difference in the mean hole diameter of $15\mu m$ is needed. It is very unlikely that this was the case.

The probable cause is a GEM sag which was, as discussed in section 5.3, discovered by the different timings of the detectors. However, if one looks at the S/N as a function of the center position of the considered strip interval (see figure 5.34) one can see that the most general form the GEM foil is taking, is not a clear sag. Some GEMs seem to have folds in them. It is not clear whether this is due to a bad stretching or to aging of the foil through contact with the DME.

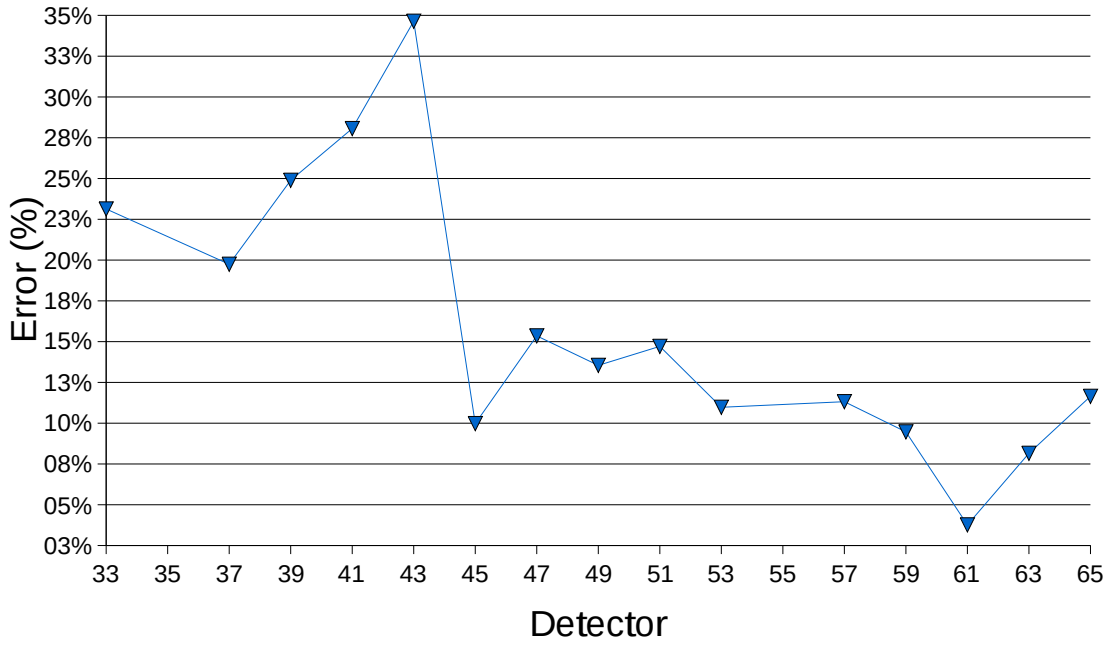

Figure 5.33: Spread on S/N values over the entire surface, for all detectors under study.

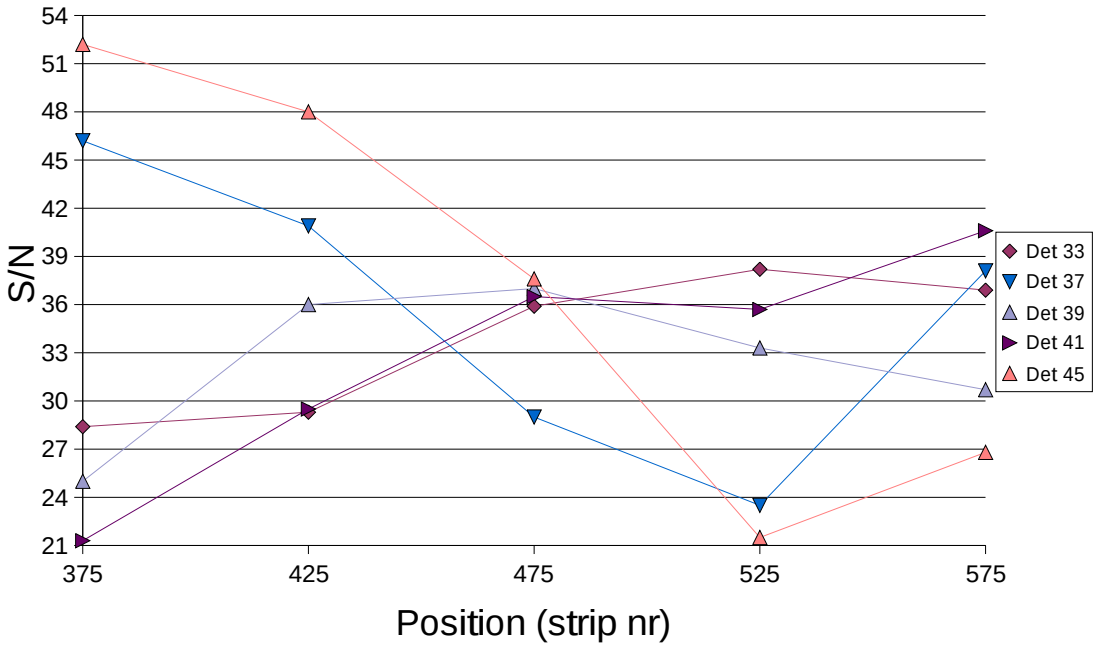

Figure 5.34: S/N as a function of the center position of the considered strip interval (intervals are 50 strips broad).

Due to the large non uniformity in the gain, one needs the beam profiles in the different intensities to be the same in order to correctly reconstruct the real LI S/N. The beam profile as defined in the following sections only includes clusters contained in the track with the highest mean S/N value after tracking.

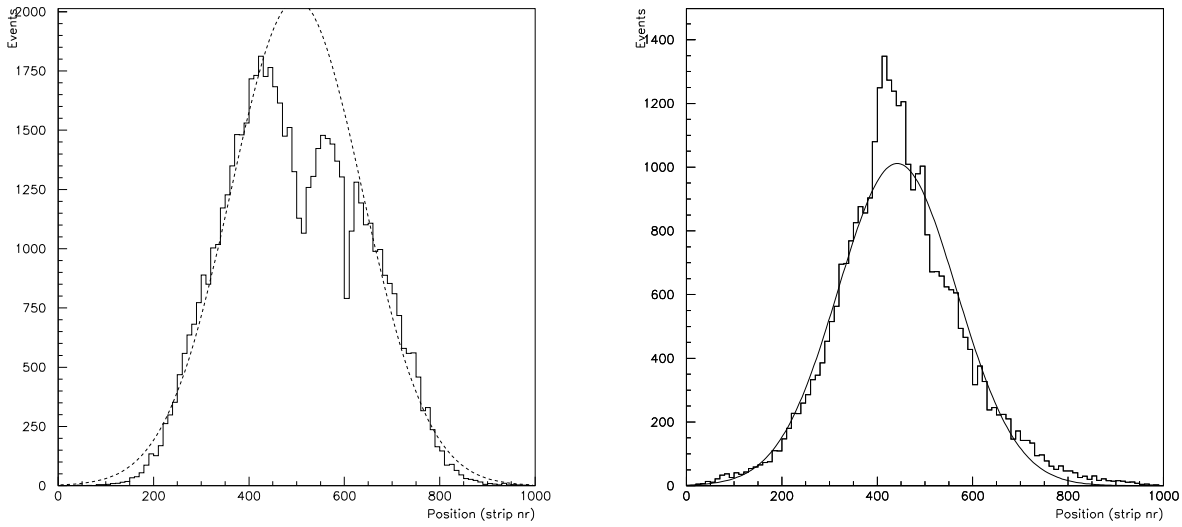

Figure 5.35: Beam profile at a) LI and b) MI, integrated over all detectors.

The LI beam profile is shown in figure 5.35a). According to reference [71], this beam profile should be Gaussian, as suggested by the dashed line. However, two holes appear prominently in this profile: one around strip number 512 and one around strip number 640. The hole around strip 512 can be explained by the mechanics of the detectors. Indeed, as seen in figure 5.3, the outer frame covers the central region of the detectors. This means that over the central region of strips (strip 502 to 522) an additional layer of 2mm PEEK is located. This will act as an additional source of Coulomb scattering, and thus make it less probable to find clusters in this region. It is however far less clear what is causing the hole around strip 640. No reason in the detector construction could be found in order to explain what is observed. It is most likely an unknown source of material somewhere along the beam path.

Figure 5.35b) represents the MI beam profile. Its features are very different from what is noticed at LI. A Gaussian shape can, again, be guessed as suggested by the full line, but its maximum is shifted to the left compared to what is found in LI. Furthermore, there is an excess around the maximum of the Gaussian. These differences in features are explained by the use of different scintillators to make make the trigger in both intensities. At LI, the trigger is performed by two $5cmx5cm$ scintillators, one placed in front of the detectors and one placed behind. At MI and HI the trigger is performed by two $1cmx5cm$ scintillators. The emplacement of all the scintillators can be seen in figure 5.4.

As at MI the particle causing the trigger has a 60% change to be correctly identified (see section 5.7.4.1) the beam profile is enhanced in the region of the scintillators.

Figure 5.36 shows a superposition of the LI, MI and HI beam profiles. It is noticed that the HI beam profiles recovers the shape of the LI beam profile, even though the small scintillators were used. This can be understood by the Monte Carlo study which predicts that, in HI, only in 40% of the cases the track with the highest mean S/N is the triggering particle. This means that in 60% of the cases the selection will be statistics driven, and one should find back the real particle distribution.

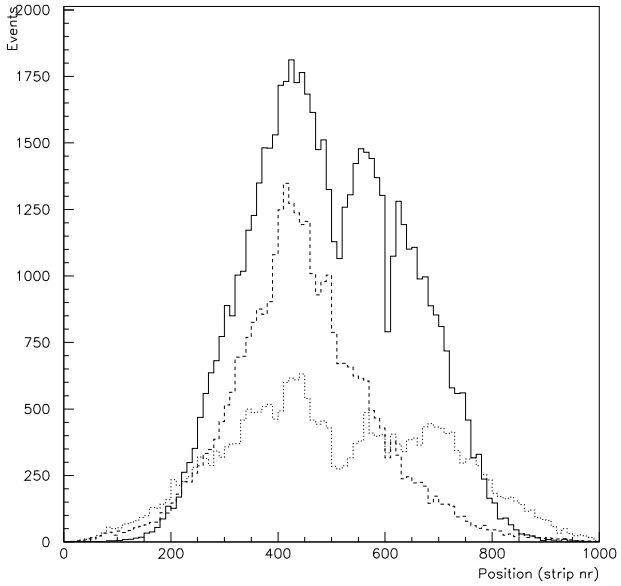

Figure 5.36: Superposition of the LI (full line), MI (dashed line) and HI (dotted line) beam profiles.

5.7.4.4 Localised approach

From the simulations one would expect a signal increase of 5% (MI) and 10% (HI) for all detectors. However, due to the large non uniformity of the gain over the detector surface and the intensity dependent beam profiles, it is very difficult to reconstruct the LI S/N using a HI run when trying to select the triggering particle out of all reconstructed tracks. However, one can restrict the search for particles to a smaller area of the detector. Over these smaller areas, the gain non uniformity should be less pronounced and S/N enhancements due to choices made should play a far less important role. A natural choice is to restrict the search for tracks to the area defined by the small scintillators as here at least one of the tracks found should be in time. This area can only be guessed by looking at the MI beam profile as no precise measurement of their location was performed. The excess over the Gaussian profile pinpoints the area. It is delimited by strips number 380 and 460, corresponding to 80 strips or 1.6cm, in good agreement with the dimensions of the scintillators.

In figure 5.37 the average S/N for the track with the highest average S/N is shown for all three intensities studied. The central value of these 3 distributions now agree within 0.5%. However, it is noticed that the MI and HI contain more events with an average S/N value below 40 than their LI counterpart. These events are therefore more likely to be the result of bad tracking. Based on the number of events with an average S/N below 40, we estimate the number of noise clusters to be 11% at HI and 9% at MI.

When looking at the reconstructed S/N value for the individual detectors, one expects to find a good agreement with the LI S/N. This is confirmed in figure 5.38 for MI and in figure 5.39 for HI. The figure represent the reconstructed S/N divided by the LI S/N. The errors are depicted by the error bars. The average signal enhancements are -0.027 ± 0.57 and 0.006 ± 0.38 for MI and HI respectively. The errors on the MI data are larger than errors on the HI data because only 5 runs were taken in the MI beam. Therefore the number of events used is much less than in the HI case.

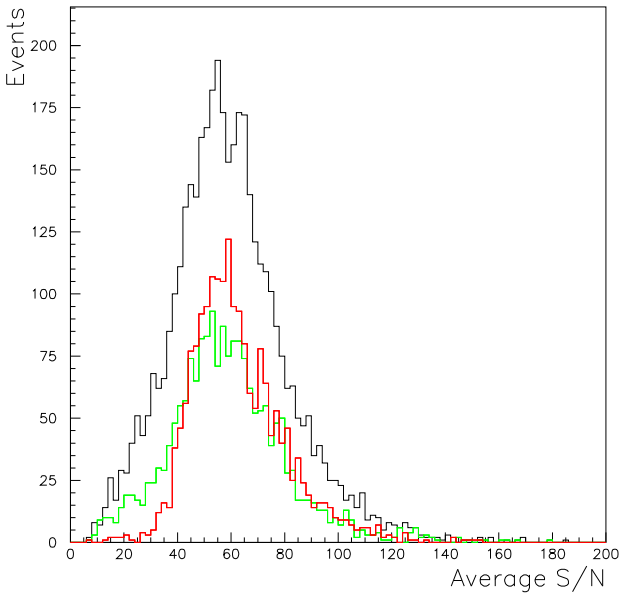

Figure 5.37: Average S/N for the track with the highest average S/N for LI (red), MI (green) and HI (black), when the search for tracks was restricted to the scintillator surface.

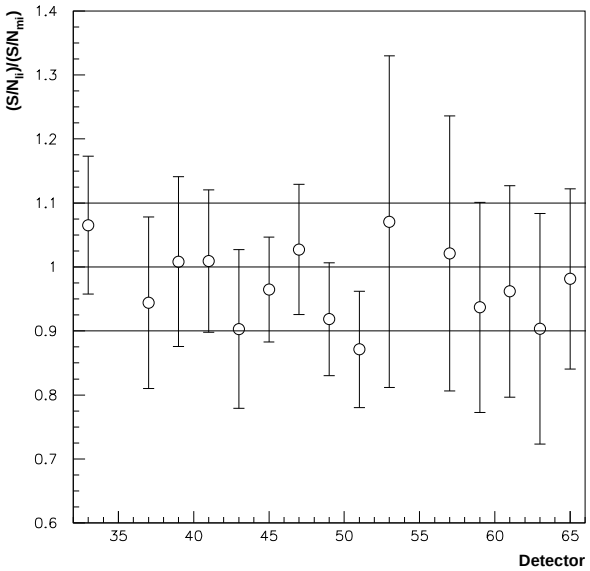

Figure 5.38: Reconstructed S/N divided by the LI S/N for all detectors under study in MI.

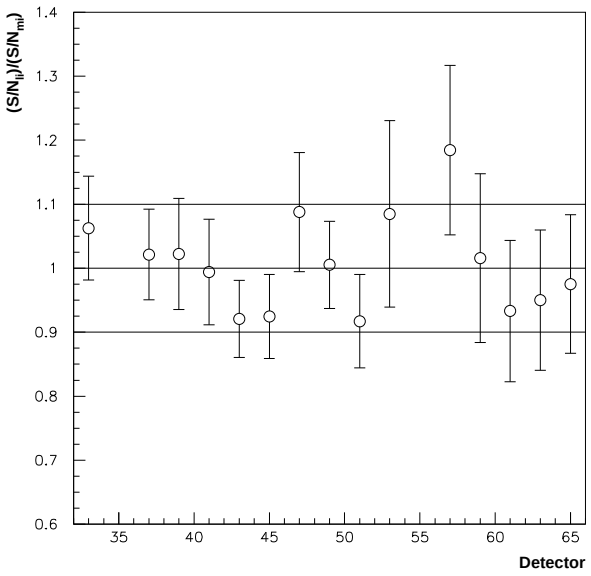

Figure 5.39: Reconstructed S/N divided by the LI S/N for all detectors under study in HI.

5.7.5 Efficiency

The minimum S/N value needed for 98% detection efficiency was established in a low intensity beam and was ascertained to be 17. The question arises if this value is still correct when the detector is subjected to a much increased beam intensity.

Unfortunately, no systematic voltage scan was performed around the S/N value for 98% detection efficiency for premux as the aim of the MF2 test was to establish the stability of the detector under a high particle flux, at a S/N value twice the one needed for 98% detection efficiency with the used electronics.

5.7.5.1 A new approach

A new approach was therefore tried. We tried to emulate the reduction of the gain by an increase threshold on the S/N for cluster formation. If this threshold is increased, more and more clusters will be excluded from the Landau curve and consequently, the efficiency will drop. The only thing needed is a relation between this increased threshold and the S/N we want to emulate.

Increasing the threshold by a factor x can be seen as if the threshold had not changed, but as though the noise had increased by a factor x. And thus as though the S/N had dropped by this same factor x. Indeed, from the point of view of the efficiency, the two statements are equivalent: if the S/N threshold for cluster formation is 4, a cluster with a S/N of 7.5 will be accepted. If its noise doubles, it will have a S/N of 3.75 and will not be accepted. If conversely, we double the threshold on cluster formation, this threshold becomes 8 and the cluster will not be accepted either.

The assumption was tested via the gas simulation program by Tom Beckers[73] and via tracking in a LI run. All these results are summarized in figure 5.40.

Both for simulation and data, two curves are shown. One labeled 'gain' and one labeled 'threshold'. An almost perfect agreement of the two methods is seen. A small discrepancy between data and simulation at lower S/N values is probably due to some physical effects not taken into account in the simulation.

The S/N needed for 98% detection efficiency is determined through a fit of the data points to the function: $efficiency(S/N) = A + Bexp(C * S/N)$. The intersection to the straight line:$efficiency = 98$ then yields the sought value. In all cases a value of 17 is found.

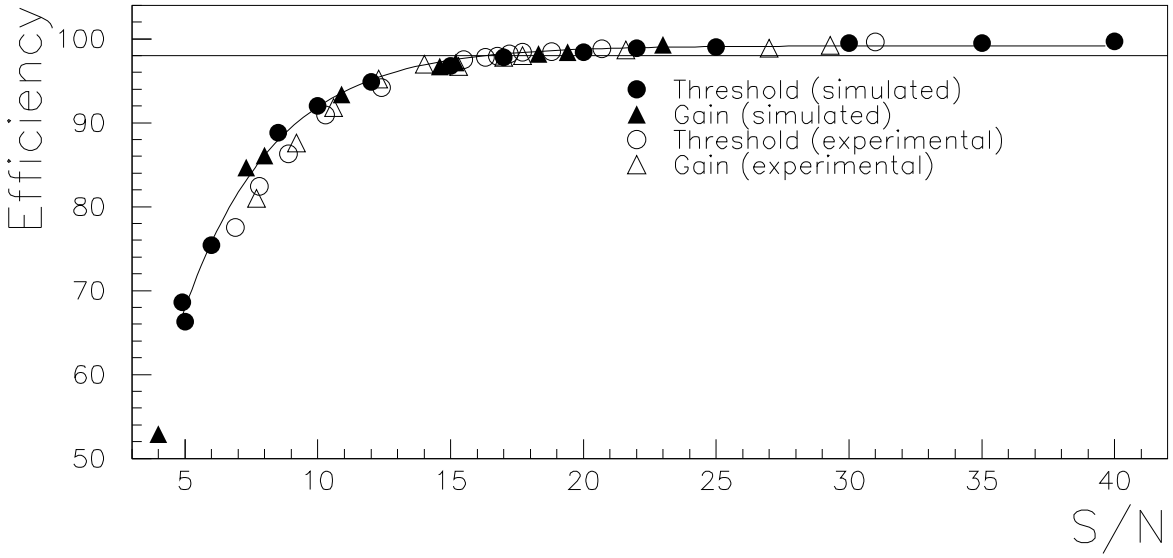

Figure 5.40: Efficiency versus S/N at low intensity, for both simulated and experimental data.

Now that the validity of this new method is proven, it is possible to retrieve the efficiency curve out of one run of data.

5.7.5.2 Results

In figure 5.41 the application of the method to data obtained in MI and HI can be seen. For reference, the curve obtained at LI is also added. The nominal value of the S/N at MI and HI is determined in a LI run, taken less than 4 hours before or after the MI or HI run.

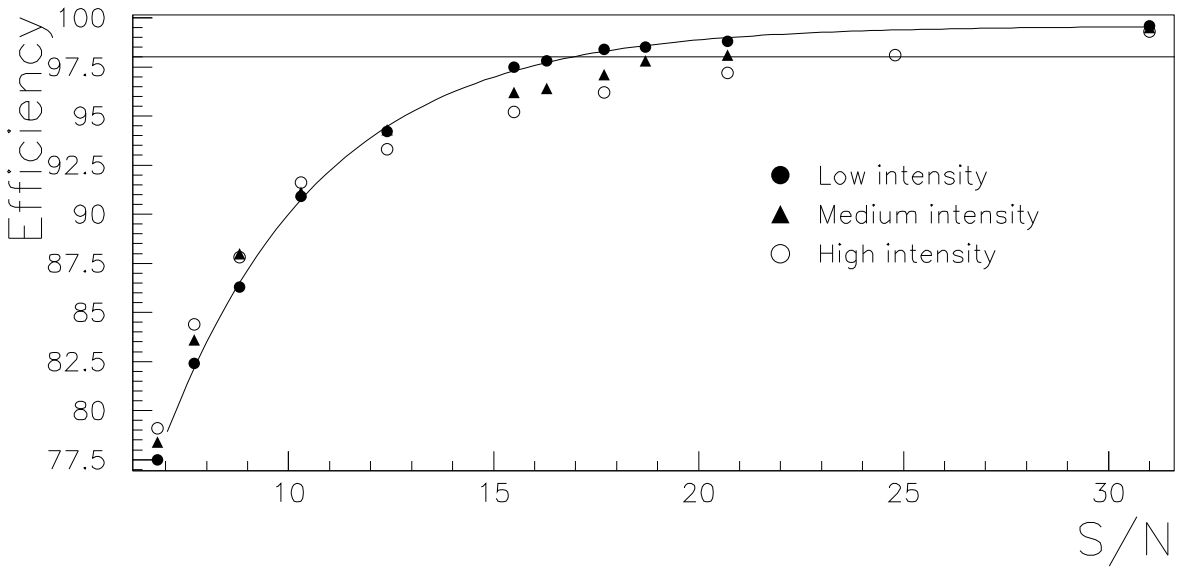

Figure 5.41: Efficiency versus S/N for three different beam intensities, using the threshold method.

Two differences are observed between the three curves. First, the minimal S/N value for 98% detection efficiency seems to increase upon raising the intensity, and second, the efficiency at a S/N lower than 12 seems to increase with the intensity.

To resolve the apparent contradiction, all the events in which the efficiency loss is observed were scanned manually. In some of these events, due to a sudden bending of the tracks, it is wrongly reconstructed. These events have then been discarded from the analysis. Furthermore, in some events, a track is reconstructed, but the algorithm misses the detector under test (due to MCS). These events were then counted as though the detector was present in the track.

A last inefficiency was introduced by definition of the mean S/N value as defined in formula 5.13. As the threshold is increased, some clusters no longer pass the selection criterion and aren't any more available for the track reconstruction. The track, previously containing n clusters, now only contains n-1 clusters. The mean value consequently raises, making it possible for the track to be assigned to the triggering particle. The problem can be overcome by stating that, as all our detectors are supposed to be 90% efficient, it is likely that the particle leaves tracks in all of them. Formula 5.13 can then be rewritten as $\overline{S/N} = \sum_i (S/N)_i/16$, were 16 is the number of detectors participating in the analysis.

The result of this manual scanning and change in the definition of $\overline{S/N}$ is shown in figure 5.42. The three curves are now in agreement with respect to the minimum S/N ratio needed to obtain 98% detection efficiency: namely 17.

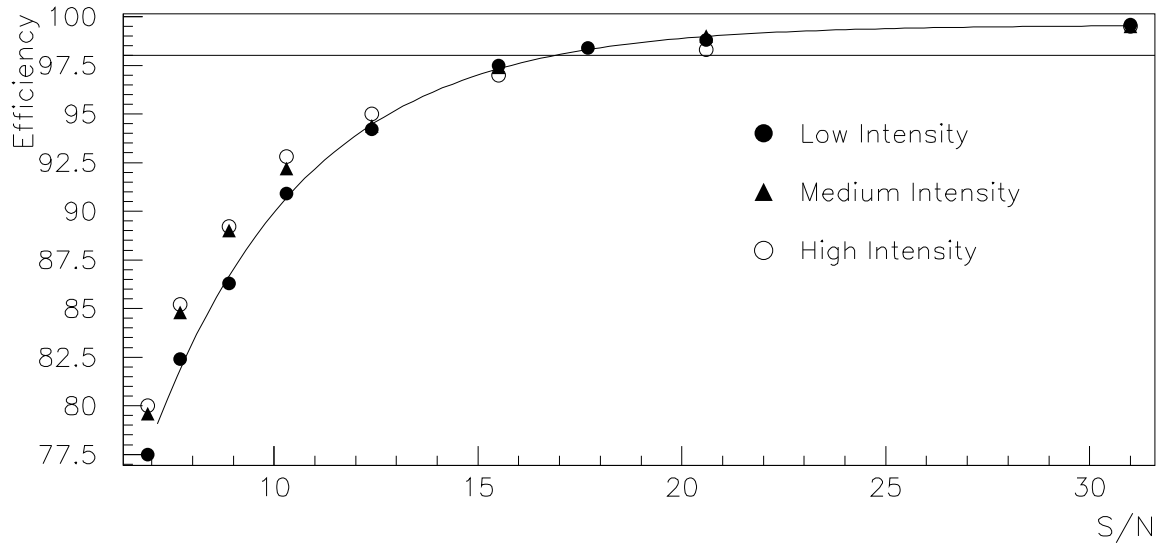

Figure 5.42: Efficiency as a function of the S/N, corrected for algorithm inefficiencies.

The higher efficiency observed at low S/N values, however, is becoming even more pronounced. Therefore the efficiency scan in a high intensity beam was simulated. Also here, the threshold on the cluster acceptance is increased for the detector under study.

The difference between the efficiency obtained by using the track belonging to the the triggering particle and the efficiency obtained when using the track with the highest mean S/N was studied. The result can be seen in figure 5.43. When the S/N is larger than 12, corresponding to an efficiency above 92%, the two values are the same. However, due to the track selection procedure, at lower S/N values, an apparent higher efficiency is noticed. The onset of this effect corresponds roughly to what is noticed in the data coming from the MF2 set-up.

A last point with respect to efficiency is given in the number of detectors contained in the tracks associated to the triggering particle. Figure 5.44 shows the histograms for LI, MI, and HI. They all have the same appearance and very similar mean values (LI: 15.26; MI:15.38; HI:15.35). At MI and HI a few tracks (10-20) appear that have less than 14 detectors in them. This are probably out of time tracks with a HIP contained into them

The probability to reconstruct all the impact points in the tracks can then be estimated to be 95.4% for Low intensity, 96.1% for medium intensity, and 95.9% for high intensity. These

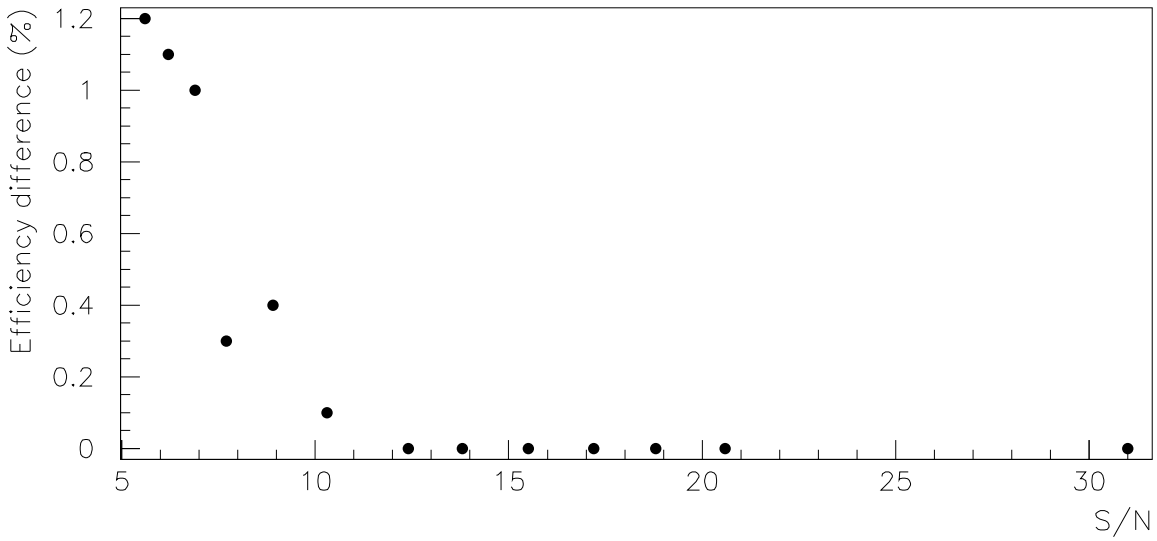

Figure 5.43: Difference in efficiency due to the tracks selection procedure as a function of S/N.

numbers correspond with an individual efficiency of each of the participating detectors of 99.7%. The slightly higher global efficiency for MI and HI is again due to the selection of the track with the highest average S/N value.

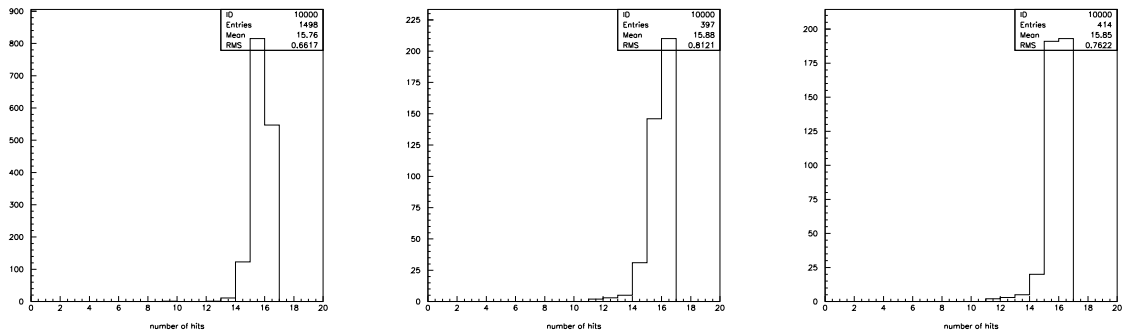

Figure 5.44: Number of detector contained in a track at a)LI, b)MI and c)HI

5.8 Conclusions

A large scale test of MSGC+GEM detectors was set up in the Paul Sherrer Institute in Villigen, Switzerland. Eighteen detector modules, consisting of 4 MSGC substrates, from which 2 were read out, were tested for more than 360hours in the πM1 beam.

The detectors were kept at a S/N value of 37 ensuring 98% detection efficiency with APV, the electronics foreseen to be used in CMS. During this time, only 25 out of 13325 read-out channels were lost, which would result in a loss of 10% of the strips when extrapolated tot 10 years of operation at the LHC.

The properties under a high intensity irradiation were extensively studied. It was proven that it is possible to follow the tracks of charged particles through the entire set-up, even with a multiple Coulomb scattering angle as high as $0.00229\,rad$ per detection plane.

It was the first time that such a large number of MSGC+GEM detectors were tested together in a high intensity beam and thus the first time that its tracking capabilities were studied. A

tracking algorithm was developed in order to investigate the functioning of the detectors under high intensity.

Using this algorithm is was possible to prove that the signal to noise ratio (S/N) of the detectors is unaltered when switching to high intensity. As the efficiency in this type of devices is usually only dependent on the signal to noise value, one expects that the S/N at which the detector detects minimum ionising particles with an efficiency of 98% remains unaltered. As no scan in signal to noise was present, a new technique was developed to overcome this problem. It was proven that, from the point of view of the efficiency, increasing the threshold for cluster formation is equivalent to reducing the gain in the detector. This point was proven both via a simulation and an analysis on low intensity data. via this method we were able to prove that indeed the minimum S/N needed for 98% detection efficiency remains unaltered in LHC conditions.

All the studies that were performed indicate that the MSGC+GEM technology is both apt and mature to be used in high rate environments like the one found around the HERA and LHC accelerators. However, special care must be taken in the mounting procedure as this has led to most of the min points of the test.

Chapter 6

Primary vertex reconstruction

6.1 Introduction

This chapter deals with the development and implementation of two algorithms that find and reconstruct the primary vertex. The algorithms use the information provided by a full reconstruction of all the tracks within the central tracker. It is most probable that full tracking will not be possible in the trigger of CMS. Therefore the algorithm could be used in an offline analysis. The concrete implementations are tested using various Monte Carlo samples (§ 6.4). The issue of CPU usage will be investigated in section §6.4.5. The tracker layout used for the simulations is the full silicon tracker as described in section 1.4.7.4.

The principal task of primary vertex finding is to identify the particles produced by the pp collision that caused the trigger and to separate them from tracks produced in superimposed minimum-bias events. This is not an easy task as in each bunch crossing there will be 3.4 (luminosity=$2.10^{33} cm^{-2} s^{-1}$) or 17.3 (luminosity=$10^{34} cm^{-2} s^{-1}$) primary vertexes on average.

Therefore a good resolution of the position of the primary vertex is needed. In CMS a reconstruction of the primary vertex is foreseen at the L2 stage. In this algorithm only the information from the pixel detectors will be used. The data from the pixels represents only 10% of the total data in the central tracking system and will thus be available at this early stage of the trigger.

The whole analysis chain in the CMS detector will be performed within the ORCA (**O**bject **O**riented **R**econstruction for **C**MS **A**nalysis) framework. The framework is intended to be used for final detector optimisations, trigger studies, event reconstruction and global detector performance evaluation[117]. The choice was made to adopt an object oriented model in the software development. The implementation language was chosen to be C^{++}[120], the object oriented extension of the C programming language.

6.2 The CMS simulation chain

6.2.1 Event Generation

The performance of the CMS detector is evaluated via the ORCA program as mentioned before. As ORCA is only intended to reconstruct the physics events, a number of steps need to be performed before ORCA can start.

Foremost, the physics events under study must be generated. PYTHIA[118] takes care of that. It generates the pp interactions as well as all the secondary particles emanating from the vertex.

Next CMSIM, the CMS simulation program, sets in. It is based on GEANT[119] which is a general simulation program that simulates the passage of particles through matter. Using CMSIM, the particles are followed through the CMS detector taking into account the energy lost by interactions with the different detector materials.

The third step is performed by ORCA itself: the digitisation. In this step, the signals induced

by the particles traversing the different sub-detectors, are generated. Next, electronic noise is added, after which a clustering algorithm, used to determine the location at which the particle traversed the detector[1], is performed. All these hits serve as input to the track reconstruction chain described in the next section. In the digitisation of the signals in Si detectors, the signal is taken to be proportional to the energy deposited in the Si layer, as computed by CMSIM.

6.2.2 Track reconstruction

The main challenge of the track reconstruction is the huge number of hits present in the tracker detectors: typically 5.10^3 at low luminosity and ten times more at high luminosity. This causes severe combinatorial problems. Different solutions were investigated. In the tracker the choice was to adopt an algorithm based upon a Kalman filter.

The track reconstruction is done in 4 steps:

1. Generation of seeds
2. Construction of trajectories for a given seed
3. Ambiguity resolution
4. Final fit of the trajectories

The algorithm used to produce track seeds is usually the following: a pair of seed layers are chosen (in ORCA these are the 1^{st} and 2^{nd} pixel layers). All hits in the outer seed layer are identified. Next, for each hit found, all the hits on the inner seed layer that are compatible with a beam spot of a given size and a minimal p_T cut are identified (see figure 6.1). All pairs found in this way are considered to be track seeds.

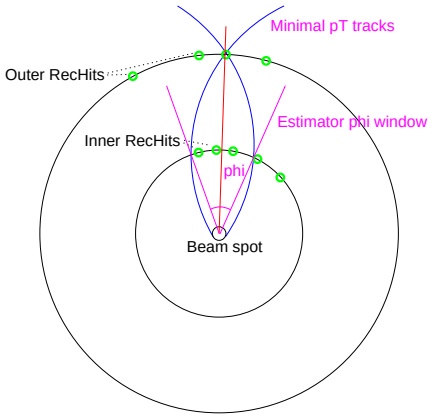

Figure 6.1: Graphical representation of the seed generation algorithm.

The next stage in the track reconstruction is performed by the Kalman filter procedure. This iterative procedure was introduced in 1960 in the framework of signal filtering in linear systems. The technique was first applied to track fitting by P. Billoir[122] and is now used by several CERN experiments.

The filter is given an initial guess of the track (the seed) and then extrapolates from this guess to the next layer. Here compatible hits are identified and added to the track. Next, the track parameters are updated, taking into account multiple scattering in the detector material, and the procedure can be repeated on the next layer with a better estimate of the track parameters. At each iteration step, the track parameters as well as the errors are calculated. The best precision is therefore reached when all measurements have been added to the track.

[1] An algorithm much like the one described in §4.3.5 is used. However, its implementation differs for the different detectors.

In the presence of a magnetic field, the trajectory of a particle can be defined at each detection layer by five independent parameters: the particle momentum p, the polar angle complement λ, the azimuthal angle ϕ between then CMS x-axis and the track projected onto the transverse plane, and the two coordinates of the track crossing point in the detection plane. The parameters are grouped into a 5-component state vector $\mathbf{x} = (p, \lambda, \phi, x, y)$. It is this set of parameters that is updated at each step of the Kalman filter.

After the filter step, one is left with a number of tracks that might share a number of hits. Typically, a single seed results in one or two possible trajectories, mostly sharing a large fraction of their hits. A trajectory cleaning step is therefore needed. Per seed, it retains only one track. The choice is based on the χ^2, number of hits and number of missing hits of the tracks. As several seeds may result in the same track, a global cleaning is performed after all seeds have been processed as described above.

The filter method, however, has some drawbacks. In the first step of the filter, the prediction accuracy is poor and therefore the rejection power for outliers (hits that do not belong to the track) is also poor. A filter, as used in ORCA, only yields a good estimate at the outer tracker layers, which makes it easy to connect the tracks to the possible hits in the calorimeters or muon chambers. However, the estimate of the tracks parameters in the pixel layers is bad. They do not estimate well the impact point of the track which is needed for vertex reconstruction. Here, the impact point of the track is defined as the point of closest approach of the track to CMS z-axis. Furthermore, an optimal precision of the estimate of the particle crossing points is needed at any detection layer to allow a precise inter alignment of the tracker elements. The process that takes care of finding the best estimate in each point of the track, using all the information available, is called smoothing. The most widely used smoothing implementation uses a reverse Kalman filter.

6.2.3 Vertex finding and reconstruction

Vertex finding consists in associating tracks that come from a common vertex. A fit of all these tracks into a vertex can then be performed, resulting in a vertex position and error. A next step to discard or include new tracks from the vertex also can performed. Two concrete implementations of vertex finding procedures will be discussed in sections 6.3.1 and 6.3.2.

The vertex fitting in ORCA is performed by an algorithm based on a straight line approximation of the tracks in the vicinity of the vertex[123]. In the neighbourhood of the vertex, the tracks can be approximated by a straight line. For instance, the sagitta of the arc with length $l \approx 2mm$ and with radius of curvature $R = \rho^{-1} = 0.5m$ is about $\frac{1}{8}\rho l^2 \approx 1\mu m$. In CMS the half meter radius of curvature corresponds to $600MeV$ in p_T. Similarly, the contribution of the direction uncertainty $\Delta\varphi$ to the position is $l\Delta\varphi$ which is only $2\mu m$ for $l = 2mm$ and $\Delta\varphi = 1mrad$.

In this approximation, the minimisation of the χ^2 has an explicit solution involving only 3×3 matrix algebra.

6.3 Primary vertex reconstruction

Within the ORCA framework, no real level 3 algorithm for primary vertex reconstruction was present. Therefore we developed 2 particular algorithms based upon the ideas from F. Jackson [124]. The next sections describe these algorithms.

6.3.1 Clusterisation

The clusterisation algorithm tries to cluster tracks into a vertex based upon the z coordinate ($\equiv z_c$) of the point of closest approach ($= (x_c, y_c, z_c)$) of the track to the CMS z-axis. However, in a first step, all tracks whose transverse displacement ($= \sqrt{x_c^2 + y_c^2}$) is larger than the three times the error on this parameter are discarded from the analysis. This is a crude method to exclude tracks that are not compatible with the beam profile, and that might originate from a displaced (secondary) vertex.

Next, the remaining z_c values are sorted ascendingly. Then, a first cluster is started with the first z_c (i.e. the smallest) value. If the second z_c value is less than a distance d apart from the first one, the track is added to the cluster. If the distance is larger than the specified value, a new cluster is started with the last value under test. The procedure is repeated iteratively with the last added track serving as the reference for the track to be added.

In this way a number of clusters are formed. Then a vertex is fitted for each cluster using the algorithm described in section 6.2.3. The selection of the primary vertex among these candidates will be based upon the number of tracks associated to the vertex or the sum of the transverse momenta of all the tracks contributing to the track, as will be outlined in section 6.4.2.

In a next iteration outliers can be rejected. In the case of vertexes, outliers are tracks that were added to the vertex, but do not belong to that vertex. All tracks with a z_c that is further than 3 standard deviations apart from the fitted vertex position are discarded, and a refit is performed

6.3.2 Gauss summation method

An other way of finding the primary vertex consists in finding the maximum of the Gaussian sum probability function.

All z_c values are returned with an error σ that is Gaussian. The probability that the z-impact parameter is a value z is then given by $p(z) = \frac{1}{\sqrt{2\pi}\sigma} e^{-[(z-z_c)^2/2\sigma^2]}$. Given n such impact points $z_{c,i}$ with their respective error σ_i, the average probability that the vertex is at a certain position z will then be given by:

$$P(z) = \frac{1}{n}\sum_{i=1}^{n} p_i(z) = \frac{1}{n}\sum_{i=1}^{n} \frac{1}{\sqrt{2\pi}\sigma_i} e^{-[(z-z_{c,i})^2/2\sigma_i^2]} \tag{6.1}$$

A graphical representation of this function constructed with 19 tracks can be seen in figure 6.2a).

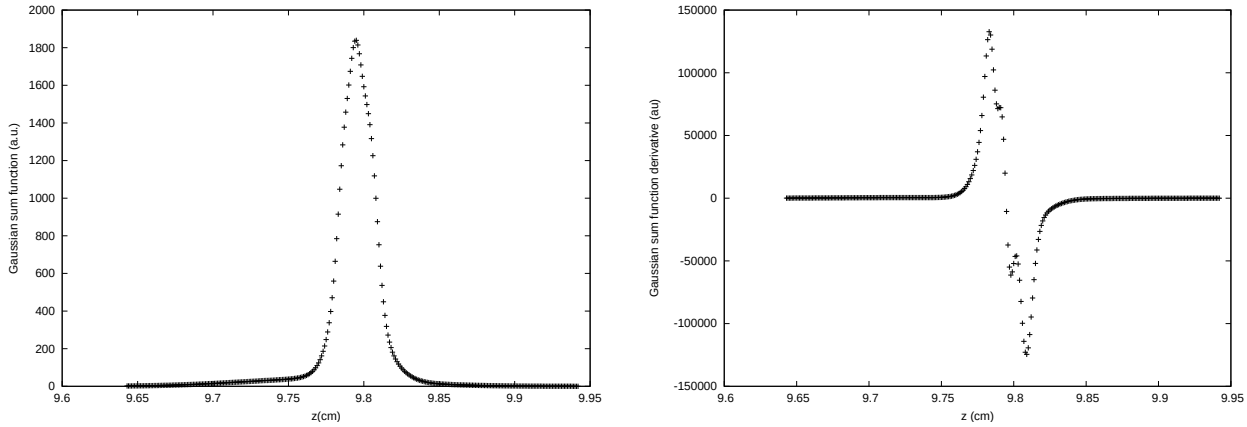

Figure 6.2: a) Sum of 19 Gaussians and b) derivative of the function shown in the left pane. The maximum of the function in the left pane is associated with the primary vertex.

The maximum of the probability function determines the position of the vertex. Finding this maximum is a typical problem of function maximisation. Two different methods were implemented: a 'brute force' method and a more elegant solution based on Brents algorithm[128].

The 'brute force' algorithm relies on the fact that the function to maximise is known analytically, its first derivative is known analytically and the fortunate appearance of this first derivative. In figure 6.2 one can see the shape the derivative of equation 6.1 takes in a particular case where $n = 19$. The maximum of the Gaussian sum function is easily found by finding the zero of its

derivative as the derivative crosses the $y = 0$ plane. Requesting that the evaluation of $\frac{\partial P}{\partial z}(z)$ in z_i (the i^{th} evaluation point) has an opposite sign than the evaluation in z_{i+1} easily finds all the extrema. The maxima are then separated from the minima by an evaluation of the second derivative of equation 6.1 in the found extremum.

This method has the disadvantage of having to compute a large number of times the expression $\frac{\partial P}{\partial z}(z)$ in order to find all the extrema. The used CPU time will rise as $n \times m$ where n is the number of tracks and m the number of times the expression is evaluated.

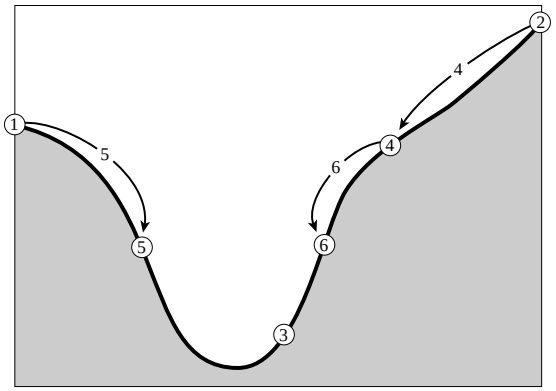

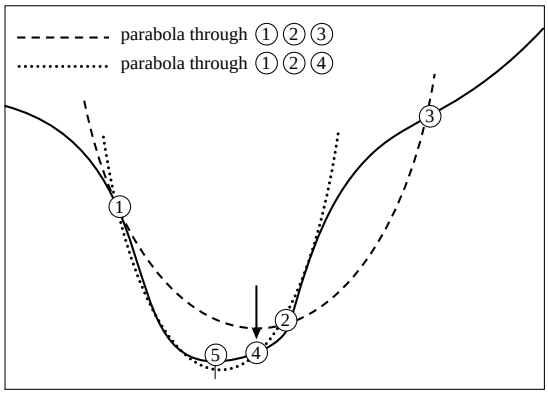

Figure 6.3: Left: Successive bracketing of a minimum. The minimum is originally bracketed by points 1,2,3. The function is evaluated at 4, which replaces 2, then at 5, which replaces 1; then at 6, which replaces 4. The rule at each stage is to keep a center point that is lower than the two outside points.

Figure 6.4: Right: Convergence to a minimum by inverse parabolic interpolation. A parabola (dashed line is drawn through the three original points 1,2,3 on the function to be minimised (solid line). The function is evaluated at the parabola's minimum, 4, which will now replace 3. A new parabola (dotted line) is drawn through points 1,4,2. The minimum of this parabola is at 5, which is close to the minimum of the function.

The second algorithm under investigation relies on an implementation of Brents[129] method for finding minima[2] and is described in the next paragraphs.

Most minimisation algorithms rely on the bracketing of minima. A minimum of a function $f(x)$ is said to be bracketed if there exists a triplet of points, $a < b < c$ such that $f(b)$ is less than both $f(a)$ and $f(c)$. In this case we know that the function (if it is nonsingular) has a minimum in the interval (a, c).

Once this interval is known, we want to locate the real minimum. An obvious approach is to choose a new point, either between a and b or b and c, and evaluate $f(x)$. if $f(b) < f(x)$, then the new bracketing triplet of point is (a, b, x); contrariwise, if $f(b) > f(x)$, then the new bracketing triplet is (b, x, c). In all cases the middle point of the triplet is the abscissa whose ordinate is the best minimum achieved so far. The process of bracketing is continued until the distance between the two outer points of the triplet is tolerably small. The successive narrowing of the bracketing interval is graphically represented in figure 6.3. The choice of where to choose the point x is not obvious. It can be proven that the optimal bracketing interval (a, b, c) has its middle point b a fractional distance $\frac{3-\sqrt{5}}{2} \approx 0.38197$[3] from one end and $1 - \frac{3-\sqrt{5}}{2} \approx 0.61803$ from the other end. Using this rule throughout the whole bracketing procedure makes the algorithm converge in the fastest way possible by this kind of method, usually called the 'golden section method'.

This algorithm has the advantage of always finding the minimum (if one exists) but has the disadvantage of being only linear (meaning that successive significant figures are won linearly with additional function evaluations).

[2]The algorithm computes the minimum of $-P(z)$ which is the maximum of $P(z)$

[3]This is the golden mean or golden section to which the Pythagoreans ascribed aesthetic properties.

However, for functions that are parabolic near their minimum (as a Gaussian is), then the parabola fitted through the three points takes us very near to the minimum in one go. The formula for the absica x that is the minimum of a parabola through the three points $f(a), f(b)$, and $f(c)$ is

$$x = b - \frac{1}{2}\frac{(b-a)^2[f(b)-f(c)] - (b-c)^2[f(b)-f(a)]}{(b-a)[f(b)-f(c)] - (b-c)[f(b)-f(a)]}$$

The formula only fails if the three points are collinear. The so found minimum will be the new point for bracketing the minimum as explained in the golden section method. For a graphical representation of the algorithms logic one can look at figure 6.4.

Brents algorithm consists in combining both methods. Parabolic interpolation is first attempted. If the parabola takes us out of the bracketed interval, does not converge fast enough, or the minimum just jumps around without converging, the algorithm moves to a golden section search. In this way a fast algorithm that is guaranteed to converge is constructed.

6.4 Results

All results are obtained with a simulation of CMS with a full silicon tracker as described in section 1.4. All tests were performed using ORCA version 6_1_1 using the cms121 layout as described in section 1.4.7.4. Note also that the results obtained in this chapter are obtained with a detector whose detecting elements are perfectly aligned.

6.4.1 Characterisation of the data samples used

6.4.1.1 Nomenclature

In all used samples, each event contains one hard p-p interaction (with a large momentum transfer between the protons) to which a number of minimum bias events (soft) can be superposed. The samples are further characterised by three quantities:

1. The luminosity: three different luminosities were simulated: one with only the signal event is generated, one including minimum bias events corresponding to low luminosity ($2\ 10^{33} cm^{-2} s^{-2}$), and a last with minimum bias events corresponding to high luminosity ($10^{34} cm^{-2} s^{-2}$)

2. The average transverse energy E_t[4]: samples with $E_t = 50\,GeV$, $100\,GeV$ and $200\,GeV$ were used.

3. The average pseudorapidity of the particles: two regions were considered: $|\eta| < 1.4$ and $1.4 < |\eta| < 2.4$

6.4.1.2 Impact point

For tracks originating at the primary vertex, the impact point is defined as the point of closest approach to the CMS z-axis.

A few derived quantities are introduced in order to compare the simulated and reconstructed tracks. These are called impact parameters and are computed relative to the vertex. The transverse impact parameter, R_{ip}, with respect to a given vertex is defined as the point of closest approach to that vertex in the transverse plane. It has a sign: for positively charged particles, it is negative when the vertex is inside the trajectory circle and positive when it is outside. The reverse holds for negatively charged particles.

The longitudinal impact point parameter, z_{ip}, is defined as the distance in z between the impact point and the primary vertex.

[4] $E_t = E * sin(\theta)$, where E is the sum of the energy of the decay products.

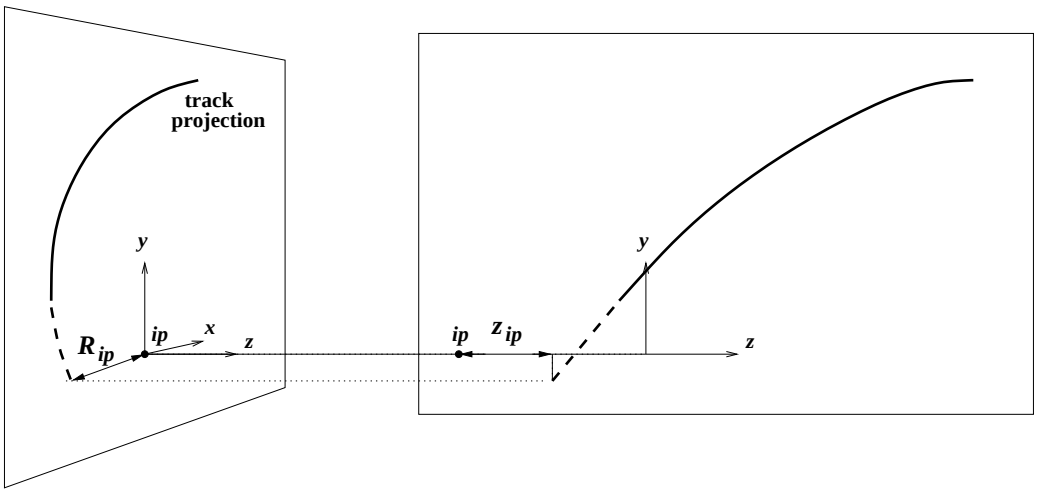

Figure 6.5: Definition of the transverse and longitudinal impact parameters R_{ip} and z_{ip} with respect to the proton interaction point ip.

Figure 6.5 illustrates these definitions in the case where the considered vertex is the primary vertex.

In figure 6.6 the resolution of these parameters is shown as a function of the pseudorapidity for isolated muons of different p_T[21].

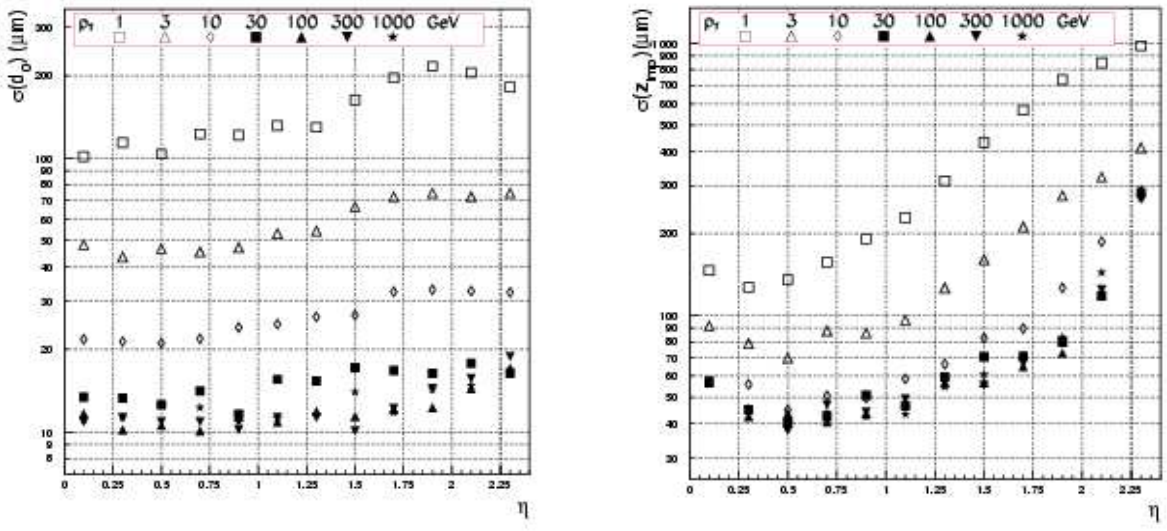

Figure 6.6: Left: Transverse impact parameter (R_{ip}) resolution as a function of the pseudorapidity. Right: Longitudinal impact parameter (z_{ip}) resolution as a function of the pseudorapidity. Both resolutions are shown for isolated muons of different p_T.

6.4.1.3 Quality checks

The quality of the reconstruction can be verified using the pulls of the track parameters. The pull for a parameter p is given by

$$Pull(p) = \frac{p_{rec} - p_{sim}}{\sigma(p_{rec})} \tag{6.2}$$

In this, p_{rec} is the reconstructed value of the parameter p, p_{sim} its simulated value and $\sigma(p_{rec})$ is the error on the fitted parameter.

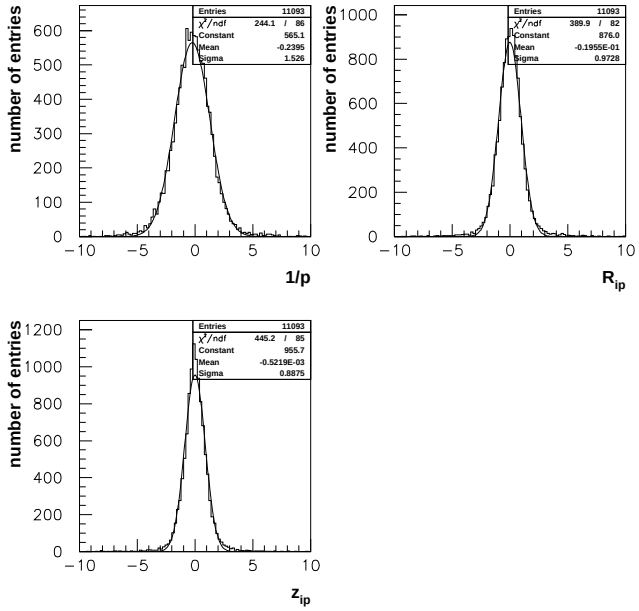

Figure 6.7: Pull distributions for the following parameters: $1/p$, R_{ip}, z_{ip}

Figure 6.7 shows the distributions of the pulls of $1/p$, R_{ip}, z_{ip} for tracks with no pile up, $E_t = 100GeV$ and $|\eta| < 1.4$. The average values are not compatible with zero, pointing to a small bias in the reconstruction of the parameters. The standard deviations of the Gaussian curves fitted to the central part of the distributions are close to 1 (for the R_{ip} and z_{ip} distributions), indicating that the covariance matrix of the track parameters is correctly estimated. The width of the $1/p$ distribution is too large, pointing to an underestimation of the error on this parameter. Furthermore, the peak of the pull distribution departs from 0 as η increases. This is due to the way the magnetic field is simulated inside ORCA. The magnetic field is simulated to be constant in the z direction, which is a good approximation in the barrel part (small $|\eta|$), but becomes worse in the forward region.

For our analysis, the most important parameter is the z_{ip}. The distribution of $z_{ip,sim} - z_{ip,rec}$ can be seen in figure 6.8a). The distribution seen is the sum of different Gaussians with different σ that correspond to different bins in η, and for tracks with different p_T. Therefore the resulting distribution is not a perfect Gaussian. The momentum distribution of the tracks used is shown in figure 6.8b). The cut at 1GeV was imposed by hand.

Table 6.1 shows the z_{ip} resolution for different bins of p_t and η. The numbers quoted are the widths of the Gaussian fitted to the $z_{ip,sim} - z_{ip,rec}$ distributions. A strong degradation of the resolution with increasing η is observed. This can be explained by the increased amount of material traversed by the particle as the pseudorapidity increases. The improved resolution with increasing momentum can be understood by the influence of the multiple coulomb scattering that becomes more important as the p_t of the particle decreases. From a p_t of $10GeV/c$ onwards, the resolution becomes constant.

p_t (GeV/c)	z_{res} (μm)	η	z_{res} (μm)
1-3	110	0-0.8	61.8
10-14	42	0.8-1.6	89
20-25	42	1.6-2.4	447

Table 6.1: Resolution of z_{ip} for 3 different bins of p_t, averaged η in and for 3 different bins in $|\eta|$, averaged in p_T.

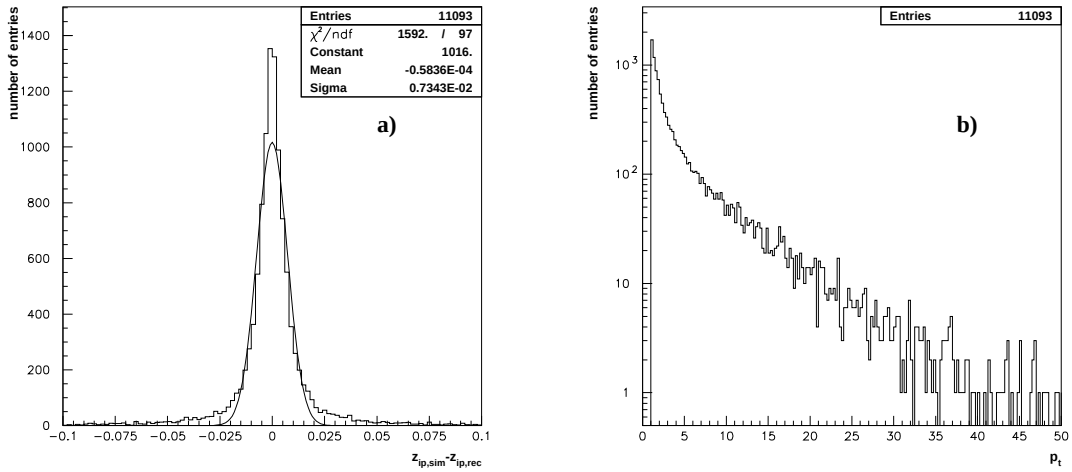

Figure 6.8: a) $z_{ip,sim} - z_{ip,rec}$ distribution for a sample with no pile-up, $E_t = 100GeV$ and $|\eta| < 1.4$ b) Momentum distribution of the used tracks.

6.4.2 Clusterisation

6.4.2.1 Resolution

As explained in §6.3.1, the clusterisation groups together tracks having z_c's less than a distance d apart. Figure 6.9 shows the resolution of the z-coordinate of the primary vertex as a function of the parameter d, when the clusterisation algorithm is used. The different curves are labeled with their E_t bin and the direction in which the primary particles departed (SE stands for $\overline{\eta} < 1.4$ and BE stands for $1.4 < \overline{\eta} < 2.4$, $\overline{\eta} = \sum |\eta|$ where the sum runs over all tracks associated to the vertex). At small values of d $(5 - 30\mu m)$ the resolution improves with d. When the distance that can be overcome by the algorithm is too small, the cluster will be broken in several parts. For each part, a vertex is fitted. The vertex with the largest $\sum p_T$ is associated to the primary vertex. However, none of the parts give the ideal approximation of the vertex. For instance at $d = 5\mu$ the algorithm reconstructs 2.4 vertexes on average. When $d = 75\mu m$, the algorithm only reconstructs 1.4 vertexes. As the sample contains $u\overline{u}$ events with no pile-up, only one vertex is expected. The extra 0.4 vertexes are due to badly reconstructed tracks.

When d is large enough, a plateau is reached. The exact value of d at which the plateau starts varies with the energy and $\overline{\eta}$ bin. However, at a value of $d = 75\mu m$, the plateau is reached in nearly all the cases.

Also, as expected from dependence of the resolution of the z_{ip} on the p_t and $\overline{\eta}$, the resolution degrades when the energy is lowered and, for a same energy, the resolution in the low $\overline{\eta}$ bin is better than in the high $|\eta|$ bin. Moreover, it is noticed that in the high energy case, more particles are produced in the signal event. In these samples, on average, 18.01, 15.62, and 10.62 tracks were found in the primary vertex, for the $200GeV$, $100GeV$, and $50GeV$ sample respectively. The best resolution obtained (i.e. in the $200GeV$, $\eta < 1.4$ sample) was $22\mu m$.

In order to determine the best achievable resolution with this method of vertex fitting, we associated the tracks using the Monte Carlo information. In this way, all reconstructed tracks pointing to the vertex are found. A fit performed with vertexes created in this way yielded the same spatial resolution as when associating the tracks with the clusterisation method ($d = 75\mu m$), validating the algorithm.

A more detailed study of the dependence of the resolution of the z-component of the primary vertex (PV) is shown in figure 6.10. A clear dependence on $\overline{\eta}$ is observed. In the lowest $\overline{\eta}$ bin $(0 < \overline{\eta} < 0.2)$, the obtained resolutions are: $17.9\mu m$, $20.3\mu m$ and $22.5\mu m$ for $E = 200, 100$ and $50GeV$ respectively. The values cited were obtained with $d = 75\mu m$.

The resolution in presence of the pile-up events can be seen in figure 6.11. The dependence on

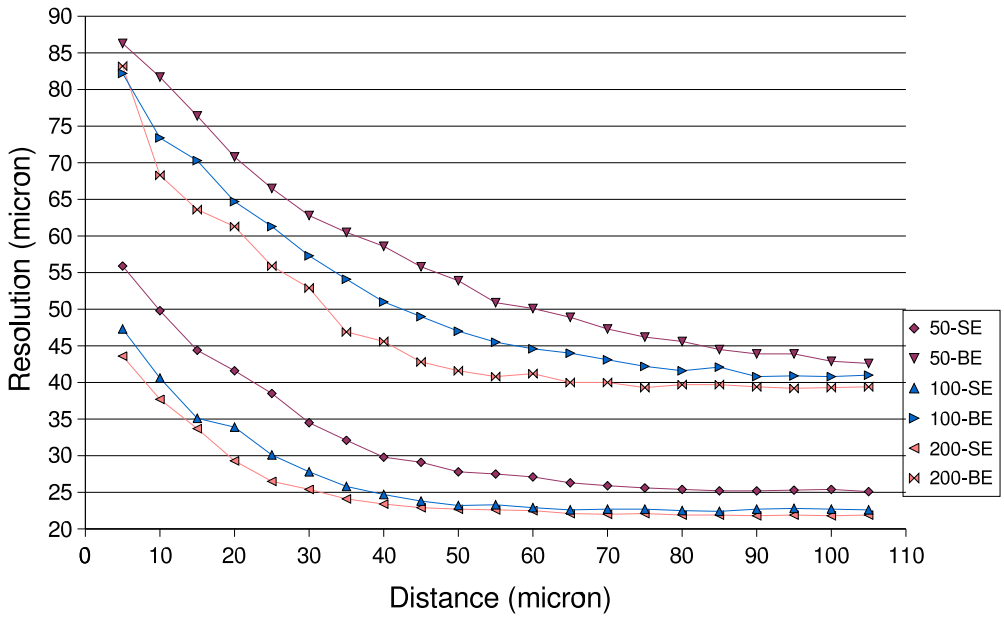

Figure 6.9: Resolution of the z-coordinate of the vertex for the clusterisation algorithm as a function of the parameter d for different bins of E_t and $\overline{\eta}$. The used Monte Carlo samples did not contain any pile-up events. The different curves are labeled with their E_t bin and the direction in which the primary particles departed (SE stands for $\overline{\eta} < 1.4$ and BE stands for $1.4 < \overline{\eta} < 2.4$

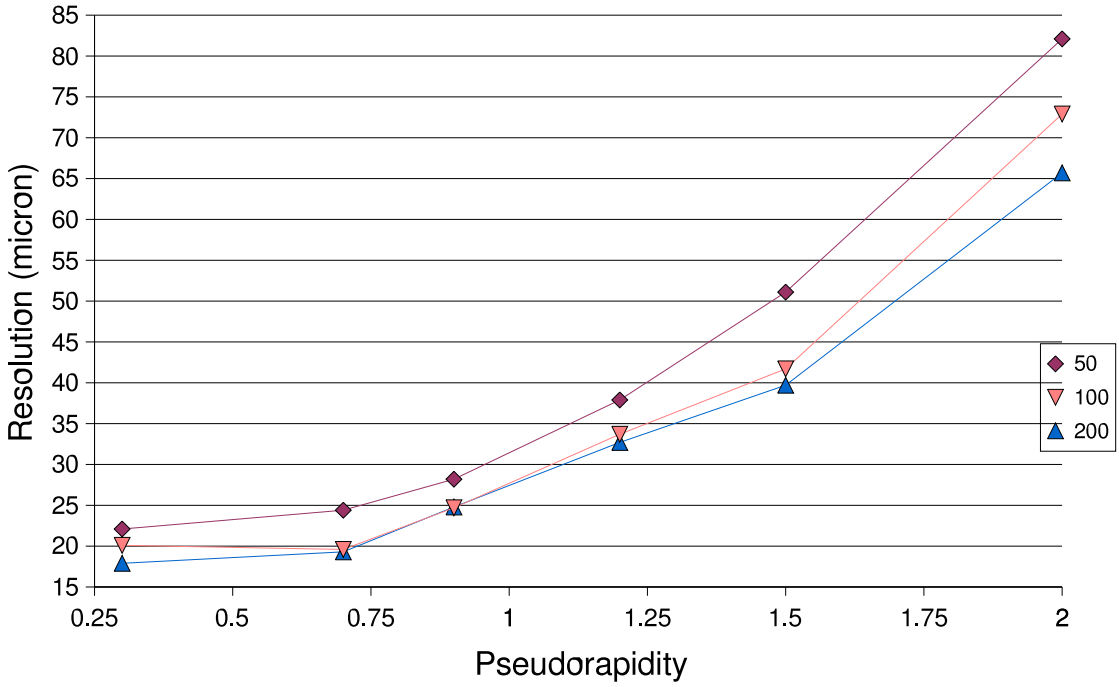

Figure 6.10: Resolution of the z-component of the primary vertex as a function of $\overline{\eta}$. The center of the bin is shown as the label of the x-axis.

the parameter d is qualitatively the same as in the case where no pile-up is present. Furthermore, the plateaus are reached around the same value of d ($d = 75\mu m$). Even the best achievable resolution for the different cases remains unaltered when adding pile-up events.

This is expected when the vertexes are separated enough. As the interaction region will have a spread of 5cm ($L = 2.10^{33} cm^{-2} s^{-1}$) or 30 cm ($10^{34} cm^{-2} s^{-1}$)[5] and there will be 3.4 and 17.3 interactions on average per bunch crossing, an average spread of 1cm between the vertexes is expected. As the extend of the particles coming from the same vertex is roughly $1mm$, few or no overlap is to be expected between primary vertexes.

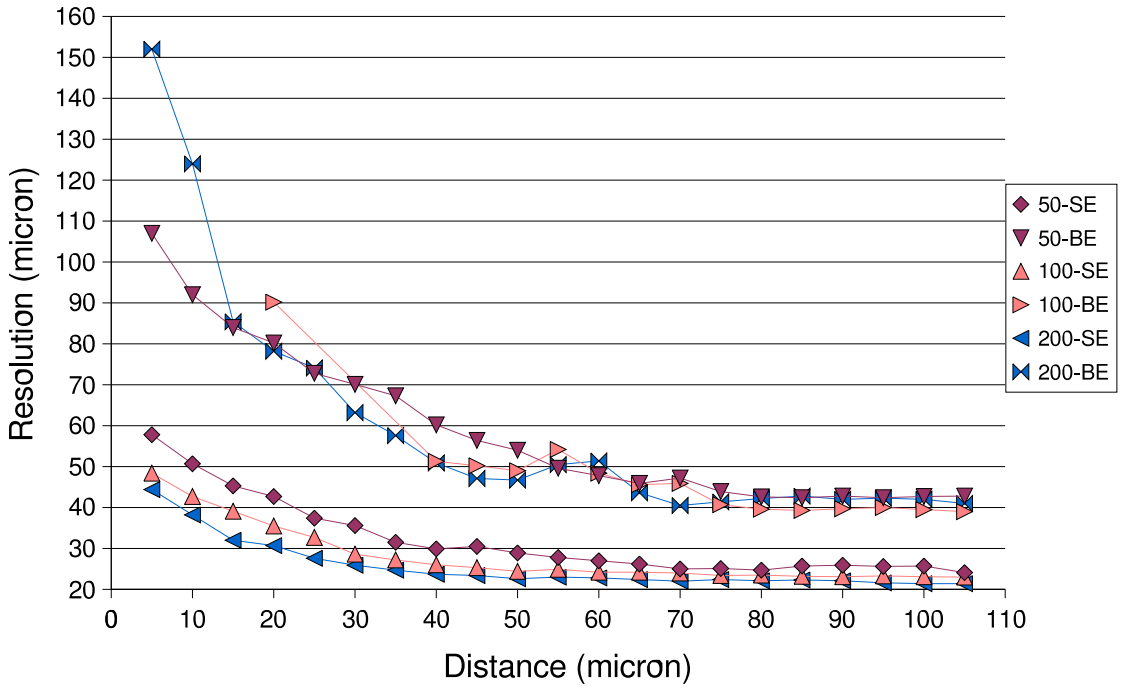

Figure 6.11: Resolution of the z-coordinate of the vertex for the clusterisation algorithm as a function of the parameter d for different bins of E and η. The simulated luminosity amounts to $2.10^{33}/cm^2 s$.

6.4.2.2 Efficiency

As mentioned before, the signal primary vertex is reconstructed by selecting the vertex for which $\sum p_T$ over all tracks is the largest. The efficiency of the reconstruction based upon this criteria can be estimated. The results are summarized in table 6.2. All cited numbers were obtained with $d = 75\mu m$. The primary vertex is said to be well reconstructed if it is within $0.5mm$ from the signal vertex.

2.10^{33}	$\overline{\eta} < 1.4$	$1.4 < \overline{\eta} < 2.4$
50 GeV	83%	91%
100 GeV	92%	93%
200 GeV	94%	96%

Table 6.2: Efficiency of correctly identifying the PV for two different bins of $|\eta|$.

The efficiency is around 90% for all cases. Somewhat surprisingly, the PV identification efficiency is better at larger pseudorapidity. This is due to the definition of the E_t. In the used sample, the E_t is kept constant, meaning that the Energy in the center of mass of the collision increases with $\overline{\eta}$. Therefore more particles are produced in these $\overline{\eta}$ bins, increasing the probability

[5]These values represent the 3σ luminous region.

that the vertex is designated as being the signal vertex as this is solely dependent on the number of particles associated to it.

6.4.3 Gaussian sum method

As in any maximisation algorithm, initial values need to be given. As the plateau of constant resolution starts at $d = 75\mu m$, the position of the PV returned by the clusterisation algorithm for this particular value of d, is taken as a starting value. The range to be scanned (brute force) or bracketing interval (Brent) is chosen to be $[(estimate - 0.1)mm, (estimate + 0.1)mm]$.

A comparison of the results obtained with the different methods is shown in figure 6.12a) and b).

In figure 6.12a), the points are constructed as follows: the x-coordinate represents the residue obtained with the brute force Gaussian method, whereas the y-coordinate represents the residue computed with the clusterisation method ($d = 75\mu m$).Figure 6.12b) is constructed in the same manner, however, the y-coordinate represents the residue obtained with Brents method.

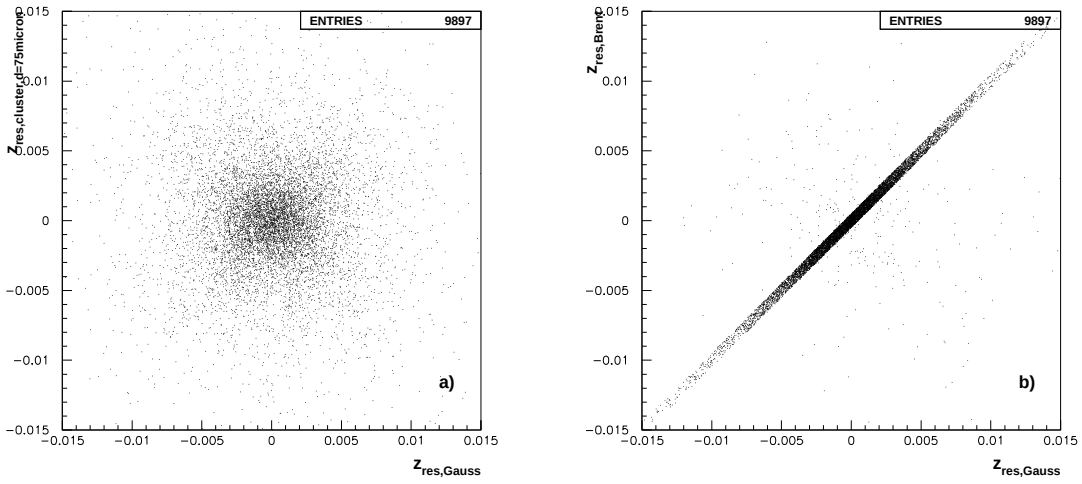

Figure 6.12: a) Residue using the Gaussian method versus the residue when using the clusterisation algorithm with d=$75\mu m$. b) Residue using the Gaussian method versus the residue when using Brents method.

As expected, Brents method and the brute force method agree within 4 microns. Both methods are correlated by the Gaussian sum function (equation 6.1) and only differ in the way they reconstruct the maximum of this function. The difference observed is in accordance with the required resolution for the determination of the minimum: $2\mu m$ in both cases.

When comparing the brute force method with the clusterisation approach, differences of the order of the resolution are observed. Both methods seem to be uncorrelated.

As both methods based upon equation 6.1 yield comparable results on the resolution (all obtained resolutions agree to within $0.5\mu m$) only results for Brents method will be given.

Figure 6.13 shows the obtained resolution for Brents method and the clusterisation algorithm as a function of the pseudorapidity. For the clarity of the representation, only the results for $E = 50GeV$ and $E = 200GeV$ are shown.

As noticed, Brents methods yields an improvement of $1\mu m$ (small $\overline{\eta}$) to $5\mu m$ (large $\overline{\eta}$). The improvement is most prominent for $E = 50GeV$ $\overline{\eta} = 2$, where the resolution is improved by $8.5\mu m$.

The best resolutions obtained now are: $16.8\mu m$, $20,1\mu m$ and $22,1\mu m$ for $E = 50, 100$ and $200GeV$ respectively.

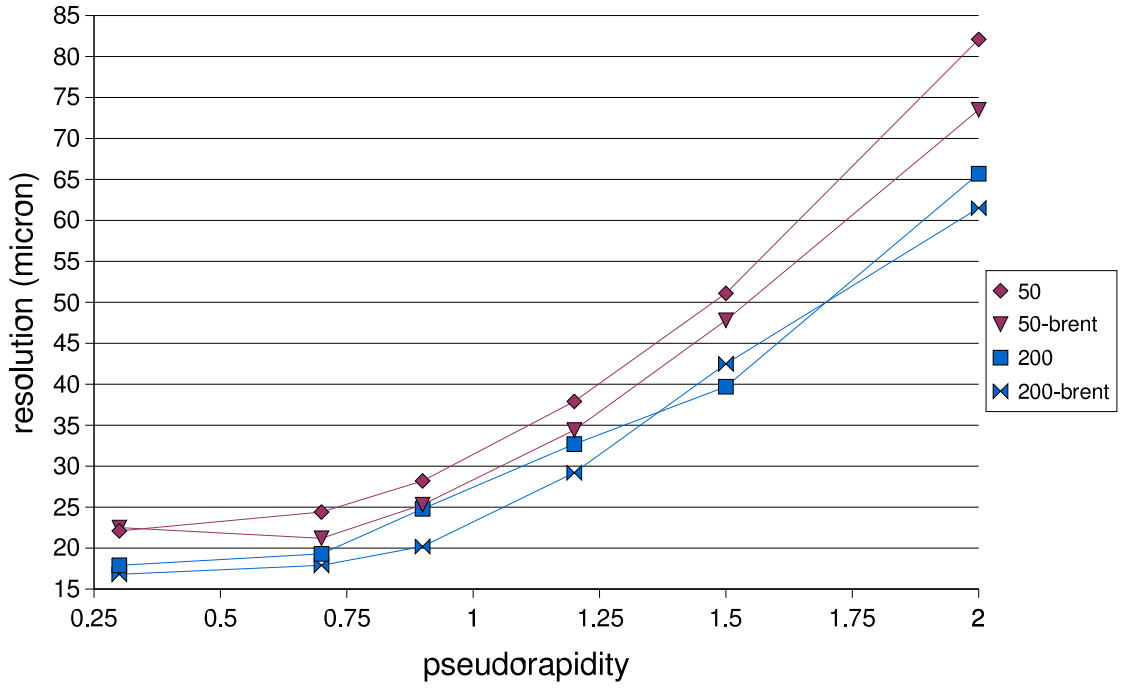

Figure 6.13: Resolution as a function of the pseudorapidity for 2 different jet energies and 2 different methods used.

6.4.4 Higgs disintegration channels

The clusterisation algorithm was also tried on several Higgs disintegration channels. A summary of the results for $d = 75\mu m$ can be seen in table 6.3. The efficiency is still defined as the number of events where the alleged primary vertex is within $0.5mm$ from the true primary vertex, divided by the total number of events generated. The error is $\sqrt{(efficiency) * (1 - efficiency)/N}$, with N the number of generated events.

For some channels, we compare our results to the work of D.Kotlinski[126, 127]. He uses only the pixel data. As the pixel data only constitutes less than 10% of the inner tracker data volume, an algorithm based upon it is very attractive and is envisaged for the L2 trigger. When 2 entries are found in a column they are separated by a /. The first entry was obtained with the clusterisation method, using the full tracker information. The second entry was obtained using only the pixel data. In the case of the pixel data, 500 events were generated for each channel.

Event type	Efficiency (%)	Error (%)	resolution (μm)
H (500GeV)$\rightarrow \tau\tau$ + low-lumi	99/96	0,3/0.9	37/55
H (500GeV)$\rightarrow \tau\tau$ + high-lumi	94/88	0,9/1,4	42/63
H(115/120GeV)$\rightarrow \gamma\gamma$+ low-lumi	95/71	0,3/2	30/63
H(115/120GeV)$\rightarrow \gamma\gamma$+ high-lumi	90/35	1,4/2,1	36/66
H(200GeV)$\rightarrow \tau\tau$+ low-lumi	98,9	0,3	30
H(200GeV)$\rightarrow \tau\tau$+ high-lumi	93,5	1,4	34
H(200GeV)$\rightarrow ZZ \rightarrow 4\mu$+ low-lumi	99,7	0,1	19
H(200GeV)$\rightarrow ZZ \rightarrow 4\mu$+ high-lumi	98,1	0,6	21
H(200GeV)$\rightarrow WW \rightarrow 2\mu$+ low-lumi	99,4	0,3	24
H(200GeV)$\rightarrow WW \rightarrow 2\mu$+ high-lumi	96,2	1,1	37

Table 6.3: A compilation of primary vertex finding efficiencies and spatial resolution of the vertex. For some channels, a comparison is made with the work of D.Kotlinski[126, 127].

As can be seen, the algorithm works quite well in all channels studied. All finding efficiencies are above 90%. A clear improvement is also observed when compared to 'pixel data' method.

The improvement is considerable in th $H \rightarrow \gamma\gamma$ channel[6] where the efficiency in high luminosity is almost tripled and the spatial resolution is improved by a factor 2.

6.4.5 Timing

As the algorithms that were developed might serve for the High Level Trigger (HLT), the time used by each algorithm is of special interest. The time taken by the different algorithms used is shown in figure 6.14. Although the brute force algorithm performs a lot of needless calculations, it is still almost 6 times faster than the clusterisation algorithm. Here the main part of the time used is due to the fitting of the vertex. Only a small fraction of the time is used by the clusterisation itself. As an algorithm based upon the STL[7] (She standard Template Library[121]) is used, this part is optimized.

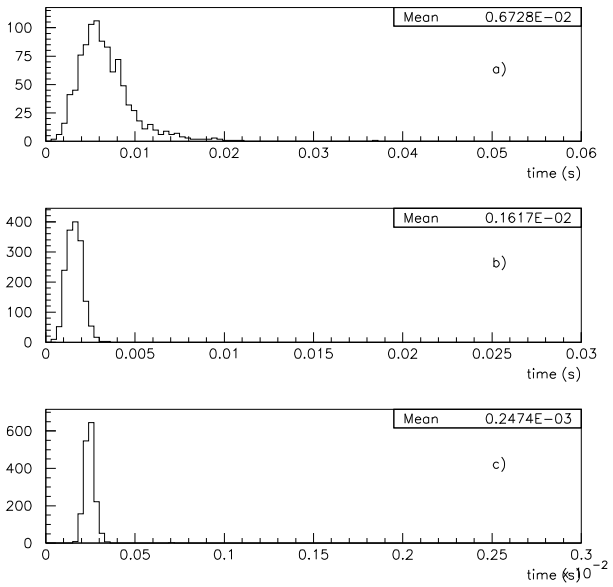

Figure 6.14: Time taken by the algorithms used. a) Clusterisation ($d = 75\mu m$) b) Gauss 'brute force' c) Brents method.

The algorithm based on Brents method is almost a factor 10 faster than the brute force method and consequently a factor 60 on the clusterisation method. However, none of the methods based upon the Gauss sum function (equation 6.1) can be used without a prior estimate on the location of the vertex. Therefore some lightweight algorithm based upon a clusterisation, where the estimate of the vertex position is given by the average position in the beam, maybe weighted by their p_t, followed by the Gauss Sum approach, maximised by Brents method, will be CPU friendly and yield very good results from the point of view of the resolution of the PV position.

6.5 Conclusions

In this chapter we developed, implemented and tested 2 methods for primary vertex finding. In the first method, tracks are associated based upon their distance to the most nearby track. A suitable distance for this distance was found to be $75\mu m$. Using this value, spatial resolutions as good as $17\mu m$ were obtained.

[6]For this channel, the 'pixel data' numbers were obtained using a Higgs with a mass of 200GeV, whereas the full tracker simulation was performed with a Higgs with a mass of 115GeV.

[7]The standard template library is a C^{++} library containing (amongst others) sorting algorithms that were optimised for speed and efficiency.

A second algorithm tested is based upon the Gaussian sum method. As all the z-impact parameters are returned with a position z_i and a Gaussian error σ_i, the probability that the primary vertex is in a position z can be expressed as: $P(z) = \frac{1}{n}\sum_{i=1}^{n} p_i(z) = \frac{1}{n}\sum_{i=1}^{n} \frac{1}{\sigma_i} e^{-[(z-z_i)^2/2\sigma_i^2]}$. The maximum of this function is computed via 2 different, numerical, methods. The first method computes $P(z)$ for every z position in a certain range. The second methods uses Brents algorithm. The 2 methods yield the same spatial resolution. However, Brents method is 10 times faster than the scanning (also called 'brute force') method. The spatial resolution is however $1\mu m$ (small $\overline{\eta}$) to $8\mu m$ (large $\overline{\eta}$) better than in the clusterisation case.

The clusterisation method was also tried on some Higgs decay channels. The efficiency for finding the primary vertex exceeds 90% in all tested cases, including cases in high luminosity. The signal vertex is separated from the minimum bias vertexes by selecting the vertex where the sum of the p_T of the contributing tracks is the largest.

When compared to an algorithm using only the pixel data, a clear improvement of both the efficiency and the spatial resolution is observed. This is most prominent in the $H \rightarrow \gamma\gamma$ channel, where the efficiency is improved by a factor 2.6 and the spatial resolution by a factor 1.8 in the high luminosity case.

Conclusions

The main subject of this thesis is the Micro Strip Gas Counter (MSGC), whether or not equipped with a Gas Electron Multiplier (GEM). As these detectors were foreseen to be used in the central tracking detector of the Compact Muon Solenoid (CMS) , their design and development focused on a correct operation in the experimental conditions present inside this experiment. CMS is designed to operate at the Large Hadron Collider (LHC), the new proton-proton collider under construction in CERN, near Geneva. It is designed for a wide range of Physics studies and optimised for the discovery of the Higgs boson in the mass range between $114 GeV/c^2$ and $1 TeV/c^2$, range not covered by the LEP experiments. To be able to perform these studies, the interaction energy will be raised to $14 TeV$ and the luminosity will be as high as $10^{34} cm^{-2} s^{-1}$.

The MSGC detectors should be able to detect particles with an efficiency of 98%. Also, the occupancy should be as low as 1%. The choice of the detection gas is therefore of utmost importance. A Ne/DME 40/60 mixture was chosen for its good properties: the drift speed amounts to $50 \mu m/ns$ at a field of $5 kV/cm$ and a minimum ionising particle produces 38 primary electrons within 1cm of gas traversed.

We have participated to the optimisation of the process-flow for electroless plated MSGC substrates at imec. This technique is commonly used in the area of Multi Chip Modules. The technique yields thick strips ($1.6 \mu m$) and naturally round off edges, feature believed to reduce the rate of discharges between anodes and cathodes. The details of the processing needed to be adapted in order to meet the stringent design criteria: 98% of the anodes were to be operational. At the level of individual substrates, we were able to meet these requirements. However, due to the lack of time and interest in the field, no large scale production scheme was tried.

Next, we took part in the testing of detectors containing an imec made substrate in different particle beams. Tests in an $8 GeV/c$ pion beam revealed the excellent properties of the technology: signal to noise (S/N) values up to 4 times the minimum for 98% detection efficiency for minimum ionising particles (MIPs) were observed. However, gain fluctuation up to 50% were ascertained. These fluctuations remained unexplained.

The detectors were also tested in a high intensity beam of $350 MeV/c$ pions. These pions can interact via the strong interaction with the detector material. Due to this, nuclear fragments can enter the gas volume and create up to 1000 times more primary ionisation than MIPs. They are consequently called Highly Ionising Particles (HIPs). Furthermore, it was shown via a simulation that this beam reproduces the experimental conditions inside CMS at 10cm from the beam pipe, location at which the MSGCs were foreseen.

Also in this beam, the MSGCs made with the imec technology showed encouraging results. It was possible to operate the detectors at 3 times the S/N needed for 98% detection efficiency. When compared to a detector made in ALENIA with the lift-off technique, the imec detectors show a sparking rate that is 10 to 50 times higher. However, due to the increased thickness of the strips, almost no anodes become nonoperational due to this behaviour. It was also proven that the detection inefficiency due to this increased sparking rate is $2.4\, 10^{-5}$.

In the fall of 1998 a large amount of MSGC+GEM detectors was operated for 365 hours in this same $350 MeV/c$ pion beam. It was proven that the technology was mature and able to cope with the experimental conditions. The detectors were operated at twice the S/N needed for 98% detection efficiency with the used electronics, i.e. premux. All detector operated with a sparking rate that was less than $10^{-3} Hz$. Out of the 18696 irradiated channels, only 24 became nonoperational during operation. Extrapolated to 10 years of operation in CMS, this would lead

to a reduced spatial resolution in 5% of the MSGC surface.

It was also shown that the properties of the MSGC+GEM remained unaltered when the detectors are irradiated with a high flux of charged particles. It was possible to show that the S/N as well as the minimum S/N needed for achieving 98% detection efficiency remain unaltered by the changed experimental conditions. For this last point, a new method was developed to determine the detection efficiency for a wide range of S/N values if, due to a lack of time, a S/N scan was not performed. This method was verified via a simulation and data taken in a low intensity beam. The method was then applied to a run in a high intensity environment.

In the last part of this work, we developed and implemented algorithms for primary vertex finding. The first algorithm clusters together tracks whose z-impact parameter differs by less than a distance d. A suitable value for d was found to be $d = 75\mu m$. When using this value of d, an optimal spatial resolution of $17.9\mu m$ was obtained in $u\overline{u}$ events to jets with an average transverse energy of $200GeV$. This result was obtained in the $0 < |\eta| < 0.2$ region.

A second algorithm tested is based upon the Gaussian sum method. As all the z-impact parameters are returned with a position z_i and a Gaussian error σ_i, the probability that the primary vertex is in a position z can be expressed as a sum of these Gaussians. The primary vertex is then associated with the maximum of this function. As no direct analytical way of finding this maximum exists, it was determined via numerical methods. One method using a scanning of all the possible vertex positions, and a more elegant solution based on Brents algorithm were implemented and evaluated.

The two methods yield the same spatial resolution as they are correlated by the Gaussian sum probability function. However, the algorithm based upon Brents method is a factor 10 faster than the scanning algorithm. Both methods yield an improvement of the spatial resolution by 1 to $8\mu m$ when compared to the clusterisation method. The improvement is most pronounced at large $|\eta|$

The clusterisation method was also tried on some Higgs decay channels. The efficiency for finding the primary vertex exceeds 90% in all tested cases, including cases in high luminosity. The signal vertex is separated from the minimum bias vertexes by selecting the vertex where the sum of the p_T of the contributing particle tracks is the largest.

When compared to an algorithm using only the pixel data, a clear improvement of both the efficiency and the spatial resolution is observed. This is most prominent in the $H \rightarrow \gamma\gamma$ channel, where the efficiency is improved by a factor 2.6 and the spatial resolution by a factor 1.8 in the high luminosity case.

Acknowledgements / Dankwoord

De tijd vliegt voorbij, dat merk je wanneer je collega's krijgt aan dewelke je nog les hebt gegeven toen zij in de eerste kandidatuur zaten. Vijf jaar heeft mijn doctoraat in beslag genomen. Het waren zeer vruchtbare en leerrijke jaren. Met droeve momenten omdat de simulaties de werkelijkheid weer eens niet beschreven, en vele euforische momenten omdat, na het verwijderen van bug nummer 13097, alles toch nog in z'n plooi valt.

Het is dan ook de hoogste tijd om een woord van dank uit te spreken. Vooreerst aan professor Jacques Lemonne omdat hij mij opgenomen heeft in z'n dienst en mij zo de mogelijkheid heeft geboden om aan dit werk te beginnen.

Ik heb het genoegen gehad om onder de leiding van twee promotoren te staan. Vooreerst stond ik onder de leiding van professor Walter Van Doninck, die mij heeft ingewijd in het mooie onderzoeksdomein dat de MSGCs vormen en in het harde leven van een experimentator die deelneemt aan een 'beam test'. Toen Walter naar Genève vertrok werd hij vervangen door professor Fred Udo die steeds weer de juiste (=lastige) vraag wist te stellen om mij weer een stapje verder te helpen. Ik dank hen beide van harte, want zonder hen had ik de klus zeker niet geklaard.

Je suis reconnaissant au professeur Catherine Vander Velde pour toutes les suggestions faites lors d'inombrables meetings. Professor Catherine De Clercq dank ik om de leiding van mijn bijstelling op zich te hebben genomen.

Ook mijn collega's fysici wil ik bedanken. Pascal Vanlaer voor het superviseren van het gedeelte over de trigger. Jorgen D'Hondt voor de begeleiding van mijn bijstelling en de vele wijntips. Tom Beckers die mij een grote dienst heeft bewezen door de simulaties over de efficientie studie uit te voeren. Gilles De Lentdecker voor de vele boeiende gesprekken en uren doorgebracht in zijn bureau. Maar ook de anderen, die een meer indirecte bijdrage hebben geleverd: Caroline, Xavier, Laurent, Lionel, Benoit, Othmane, Daan, Roel, Sofie, Steven voor de informatica discussies, Philip en Chunxu Yu die mij al heel wat heeft geleerd over de chinese cultuur.

Ik heb ook het genoegen gehad om met vele buitenlandse collega's te kunnen samenwerken. Ik dank Anette Zander, Andreas Nowack, Stéphanie Moreau en Valery Zhukov om de vele constructieve (en soms verhitte) discussies.

Au début de ma carrière, j'ai aussi eu le plaisir de travailler avec Rolande Pins, qui m'a beaucoup aidé dans l'optimisation du procesus pour produire les MSGC. Ook Francesca Iacopi wens ik hier voor de samenwerking en de vele uren die we doorbrachten in de clean room, te danken.

Ook de vele andere leden van het IIHE hebben er voor gezorgd dat mijn verblijf in hun midden zeer aangenaam is verlopen. Ik denk hierbij in het bijzonder aan Rosine, Annie, Marleen, Luc en Christian.

Als laatste dank ik mijn familie voor de geboden kansen en steun en mijn vriendin Tinne om haar steun en het geduld dat zij met mij heeft gehad gedurende deze drukke jaren.

Bibliography

[1] P.C.W. Davies, The forces of nature, **Cambridge university press** (1986)

[2] M.K. Sundaresan, Handbook of particle physics, **CRC press** (2001)

[3] The LHC study group, *The Large Hadron Collider*, Conceptual design, **CERN/AC/95-05** (1995)

[4] D.Denegri, *Standard model physics at the LHC*, Proc. ECFA workshop for LHC, Aachen (1990) **CERN 90-10**, Vol. I, p56

[5] DONUT Collaboration, Observation of tau neutrino interactions, Phys Let. B504, 218 (2001)

[6] F. Englert and R. Brout, Phys. Rev. Lett. **13** (1964) 321

[7] P.W. Higgs, Phys. Rev. **145** (1966) 1156

[8] A.Zee Red., *Unity of forces in the universe*, vol II, **World Scientific** (1982)

[9] U. Mosel, Fields, symmetries and quarks, **Mc Graw-Hill** (1989)

[10] D.P. Roy, *Higgs and SUSY searches at LHC*, **TIFR/TH/98-08**, (1998)

[11] LEP Higgs Working Group, 'Search for the standard model Higgs boson at LEP', hep-ex0107029 (2001)

[12] 'Search for the SM Higgs boson at LEP in the year 2000', Phys. Lett. B 499, 23 (2001)

[13] CDF,Nucl. Phys., B64 (406-410) (1998)

[14] F. Sauli,*CERN lectures* **77-09** (1977)

[15] A. Oed,*Nucl.Instr. and Meth.* **A263** (351-359) (1988)

[16] CMS Collaboration, *The magnet project*, **CERN/LHCC 97-10** (1997)

[17] CMS Collaboration, *The muon project*, **CERN/LHCC 97-32**, (1997)

[18] CMS Collaboration, *The electromagnetic calorimeter project*, **CERN/LHCC 97-33**, (1997)

[19] CMS Collaboration, *The hadron calorimeter project*, **CERN/LHCC 97-31** (1997)

[20] CMS Collaboration, *The Tracker project TDR.* **CERN/LHCC 98-C,CMS TDR 9** (1998)

[21] CMS Collaboration, *Addendum to the CMS Tracker TDR.* **CERN/LHCC 2000-16**, CMS TDR5 addendum 1

[22] J.P. Peigneux, Nucl. Instr. and Meth. A 378, 410 (1996)

[23] M. Spira, QCD effects in Higgs physics, CERN-TH/97-68 (1997)

[24] CMS tracker layout optimization group, *V3 CMS tracker layout - Detector break-up*, **CMS NOTE 1996/013** (1996)

[25] W.Blum and L. Rolandi, Particle detection with drift chambers, Accelerator Physics, Spinger-Verlag (1994)

[26] D.L. Landau, On the energy loss of fast particles by ionisation, J. Phys. USSR 8 201 (1944)

[27] U. Fano, Phys. Rev. 72, 26 (1947)

[28] J.H. Cobb et al., The ionisation loss of relativistic charged particles in thin gas samples and its use for particle identification, Nucl. Instr. and Meth. A 133, 315 (1976)

[29] V.A. Chechin et al, The ionization loss distribution at very small absorber thickness, Nucl. Instr. and Meth. A 136, 551 (1976)

[30] V.C. Ermilova, Fluctuations and the most probable values of charged particle energy loss in thin gas layers, Nucl. Instr. and Meth. A 145, 555 (1977)

[31] E.P. Lima et al., Nucl. Instr. and Meth. A192, 575 (1982)

[32] Review of particle physics, Eur. J. Phys. 3, 1 (1998)

[33] Particle Data Group, Rev. D54, 1. (2000)

[34] CERN Courier Vol. 37 No7, 26 (sept 1997)

[35] E.B. Wagner et al., Time of flight investigations of electron transport in some atomic and molecular gases, J. Chem. Phys. 47, 3138 (1967)

[36] G. Charpak et al., Nucl. Instr. and Meth. A 62, 262 (1968)

[37] J.H. Parker et al., Theory of electron diffusion parallel to electric fields, Phys. Rev. 181, 290 (1969)

[38] J. Byrne, Proc. Roy. Soc. A 66, 33 (1962)

[39] A. Lansiart, J.P. Morucci, J. Phys. Radium 23, suppl. nr. 6, 102A (1962)

[40] H. Reather, Electron avalanches and breakdown in gases, Butterworks, Washington (1964)

[41] P. Rice-Evans, Spark, streamer, proportional and drift chambers, Richelieu (1974)

[42] S.A. Korff, Electrons and nuclear counters, Van Nostrand, New York (1946)

[43] S. Ramo, Currents induced in electron motion, Proc IRE 27, 584 (1939)

[44] ATLAS MSGC, ATLAS internal note INDET-NO-076 (1994).

[45] J. Schmitz, Results on Monte-Carlo simulations of an MGC, Nucl. Instr. and Meth. A323, 638 (1992)

[46] F. Sauli, Nucl. Instr. and Meth.A386, 531 (1998)

[47] M. Della Negra (spokesperson),em **CERN/LHCC 94-38** (1994)

[48] L.L. Jones, *Premux128 Specification version 2.3 chip specifications* (1995)

[49] M. French, *APV6 use manual*, **Rutherford Aplleton Laboratory** (1997)

[50] F.G. Sciaccia, Study of analogue signal processing algorithms for MSGC signals in CMS. CMS NOTE/1997-22 (1997)

[51] F.G. Sciaccia, Readout of an MSGC prototype with the APV6 front-end chip. CMS NOTE/1998-093 (1998)

[52] F.G. Sciaccia, Impact of fast shaping at the front-end on signals from MSGCs. CMS-NOTE1997-105 (1997)

[53] B. Baiboussimov et al., *Readout and slow control system for the forward MSGC prototype*, **CERN Documentation** (1997)

[54] E. Daubie, *Physicalia Mag. vol. 18 nr 2* **109-123** (1996)

[55] O. Bouhali et. al., *CMS Forward-Backward MSGC Milestone*, **CMS NOTE-1998/095** (1995)

[56] W. Beaumont et al.,*Beam test results with MSGCs with thick metal strips,* **CMS NOTE 1999/059** (1999)

[57] Othmane Bouhali *Contribution to the study of the MSGC tracker of the CMS detector, at the future proton collider LHC* **PhD thesis** (1999)

[58] Othmane Bouhali et al., *Proceedings of the International Workshop on Micro Strip Gas Counters* Lyon (1995) p. 101

[59] Particle Data Group: Phys. *Rev D* (1994)

[60] J. van der Marel,A silicon microstrip gas chamber, Nucl. Instr. and Meth. A,348, 383, (1994)

[61] Yu.N. Pestov and L.I. Shekhtman, *Influence of the bulk resistivity of glass with electronic conductivity on the performance of microstrip gas chambers,* Nucl. Instr. and Meth. A **338** (1994) 368

[62] R. Bouclier et al., *On some factors affecting discharge conditions in micro strip gas chambers,* Nucl. Instr. and Meth. A **365** (1995) 65

[63] R. Bouclier et al., *Development of MSGCs on thin plastic supports,* Nucl. Instr. and Meth. A **315** (1992) 512

[64] R. Bellazzini and M.A.Spezziga, *Electric field, Avalanche growth and signal development in MSGCs and MGCs* ***Rivista del Nuovo Cimento*** **17** 12 (1994)

[65] G.D. Akhazov, Mean value and variance of gas amplification in proportional counters, Nucl. Instr. and Meth. A75, 161 (1969)

[66] G.D. Akhazov, Statistics of electron avalanches and ultimate resolution of proportional counters, Nucl. Instr. and Meth. A89, 155 (1970)

[67] J.E. Bateman et al., The experimental characterization of gas microstrip detectors, RAL 94-114 (1994)

[68] J.J. Florent, The electric field in MSGCs and its influence on detector performance, Nucl. Instr. and Meth. **A, 329,** 125 (1993)

[69] S. Bachmann et. al., Nucl. Instr. and Meth. A, **438**, 376 (1999)

[70] R. Bouclier et.al, The Gas Electron Multiplier (GEM), IEEE Nuclear science Symposium (Anaheim), November 3-9 (1996).

[71] R. Bellazzini et al. *The CMS Micro-Strip Gas Chamber project- Development of a high resolution tracking detector for harsh radiation environments.* Nucl. Instr. and Meth. **A 457** 22 (2001)

[72] F. Udo, private communication

[73] T. Beckers, PhD thesis, to be published.

[74] M.Ageron et al. *Robustness test of a system of MSGC+GEM detectors at the cyclotron facility of the Paul Scherrer institute,* Nucl. Instr. and Meth. A, **471,** 380 (2001)

[75] M.Ageron et al., *Experimental an simulation study of the behaviour and operation modes of MSGC+GEM detectors*, Nucl. Instr. and Meth. A, **489,** 121 (2002)

[76] M. Pentia et al., *A fast procedure for geometric parameter determination of a silicon vertex tracker* Nucl. Instr. and Meth. A, **369** *101-106* (1996)

[77] Dirk Macke, *MSGC with GEMs and their application in the CMS experiment,* **PhD thesis 01/00** PITHA

[78] G. De Lentdecker, *Etude d'un compteur à gaz à grille microscopique (micromégas) pour un traceur au LHC*, End of study thesis, (1998)

[79] D. Macke, Micro Strip Gas Chambers with Gas Electron Multipliers and their application in the CMS experiment, PhD thesis

[80] A. Zander, Experiences with a pre-series of MSGCs with GEMs for high rate applications, PhD thesis.

[81] A. Nowack, Investigations of a Pre-Series of Micro Strip Gas Chambers with Gas Electron Multipliers for High Rate Environments, PhD thesis

[82] G. Delentdecker, Contribution to the study of the central tracking system of the CMS detector at the LHC collider and to the elaboration of its online triggering system, PhD thesis (2002)

[83] T. Beckers et al., Nucl. Instr. and Meth. **A 346**, 95, (1994)

[84] P. Fonte et al., *Streamers in MSGCs and other gaseous detectors*, **ICFA Instrum. Bull**, Spring 1997

[85] Yu. Ivaniouchenkov et al., Breakdown limit studies in High rate Gaseous Detectors, Nucl. Instr. and Meth. **A 422**, 243, (1997)

[86] V. Peskov et al., A study of breakdown in micro strip gas counters, presented at the 4th international conference on position sensitive detectors, University of Manchester, 9-13 September 1996

[87] P. Fonte et al., A study of breakdown limits in microstrip gas counters with pre-amplification structures, Nucl. Instr. and Meth. **A416,** 23 (1998)

[88] W.G Gong, *MSGCs with Pestov glass coatings*, Nucl. Instr. and Meth. **A 374**, 144 (1996)

[89] V.Mack et al., *A study of various coatings for MSGCs*, Nucl. Instr. and Meth. **A 423** 369 (1999)

[90] Gary E. McGuire (ed.), *Semiconductor materials and process technology handbook* **Noyes Publications** (1988)

[91] Berryl, Hall, Harris *Thin Film Technology* **Van Nostrand Reinhold Company** (1968)

[92] W.M. Moreau *Semiconductor lithography: principles, practices and materials* **Plenum Press** (1988)

[93] G.W.W. Stevens *Microphotography* **Chapman and Hall** (1968)

[94] K. Morita, *Fujitsu* ***Sci. Tech. J.*** **43** (1978)

[95] M. Honore, Personal communication

[96] D. Meyerhofer, **J. Appl. Phys. 49**, 3393 (1978)

[97] S. Bachmann et al., *Spatial resolution of a wedge shaped MSGC module*, **CMS NOTE 1997/077** (1997)

[98] P. Dierckx, 'Curve and surface fitting with splines', **Clarendon, Oxford** (1995)

[99] D. Ebbing, *General Chemistry*, **Hougton Mifflin Company**, 3rd edition (1990)

[100] G.Berger et al. CYCLONE- A multipurpose heavy ion, proton and neutron SEE test site RADECS (1997)

[101] E.L. Florian et al., **CERN/ECP/95-15**

[102] W. Beaumont et al. MSGC test with fast neutrons., **CMS NOTE 98/014** (1998)

[103] E.L. Florian et al.,**CERN/TIS-CFM/IR/93-03**

[104] J.P.Meulder et al., **Phys. Med. Biol. 20**, 235 (1975)

[105] S.J. Lindenbaum, Particle-interaction physics at high energies, **Clerendon press** (1973)

[106] M.Huhtinen, Factors to scale higly ionising particle rates in MSGC irradiation tests to the LHC radiation environment, **CMS NOTE 98/014** (1998)

[107] O.Bouhali et al., TDR: A possible approach for the construction of the CMS Forward-Backward MSGC Tracker, **CMS-NOTE 97/081**.

[108] S. Bachmann et al., The closed MSGC design: detectors and mechanical structure, PITHA 98/19, RWTH Aachen (1998)

[109] R. Barlow, SLUO Lectures on Statistics and Numerical Methods in HEP, http://hep.man.ac.uk/~roger/sluo6.ps

[110] A. Brez, Personal Communication

[111] L. Mirabito, http://infodan.in2p3.fr/delphi/mirabito/tbeam/tbeam.html

[112] F. Drouhin et al., A Unix SRV4-OS9 Distributed Acquisition for High Energy Physics, **IEEE transactions on nuclear science, Vol 45** (1998)

[113] B. Schwaller et al., The trigger system of the first CMS beam tests, **IEEE transactions on nuclear science, Vol** 45, No. 5 (1998)

[114] L. Yuan,C-H Wu (ed.), Nuclear Physics, volume 5, Academic Press (1961)

[115] CN/ADS Group and J.Zoll/ECP, Zebra user's guide, **Program library Q121,**CERN (1993)

[116] CN/ADS group, PAW user's guide, **Program library Q100**, CERN (1993)

[117] CMS Software and Computing Group ,Object Oriented Reconstruction for CMS Analysis, **CMS-IN 1999/001 (1999)**

[118] T. Sjöstrand, PYTHIA.6.152 Comp. Phys. Comm., 135 (2001) 238

[119] R. Brun et al, GEANT, Detector description and simulation tool, CERN program library W5013 (1994)

[120] B. Stroustrup, The C^{++} programming language (third edition), Addison-Wesley, (1997)

[121] D. R. Musser, A. Saini, 'STL tutorial and Reference Guide', Addison-Wesley (1996)

[122] P. Billoir, Track fitting with multiple scattering: a new method, Nucl. Instr. and Meth. **A** 225, 352-366 (1984)

[123] V. Karimaki, Effective Vertex Fitting, CMS NOTE-1997/051 (1997)

[124] D. J. Jackson, A topological vertex reconstruction algorithm for hadronic jets, Nucl. Instr. and Meth. **A 388**, 247 (1997)

[125] P.J. Rousseeuw, A.M. Leroy, Robust Regression and outlier detection, John Wiley (1987)

[126] D. Kotlinski, Track reconstruction and primary vertex finding using the pixel detector data, CMS IN-2000/022 (2000)

[127] http://www.hip.fi/btau/talkDK.pdf

[128] R.P. Brent, Algorithms for minimisation without derivatives, Englewood Cliffs, NJ: Prentice Hall (1973)

[129] W.H. Press, S.A. Teukolky, W.T. Vetterling, and B.P. Flannery, Numerical recipes in C, second edition, Cambridge University Press (1992). Electronically available at http://www.ulib.org/webRoot/Books/Numerical_Recipes/